Development of Advanced GaAs Based Quantum Dot Devices

By

Kejia Zhou

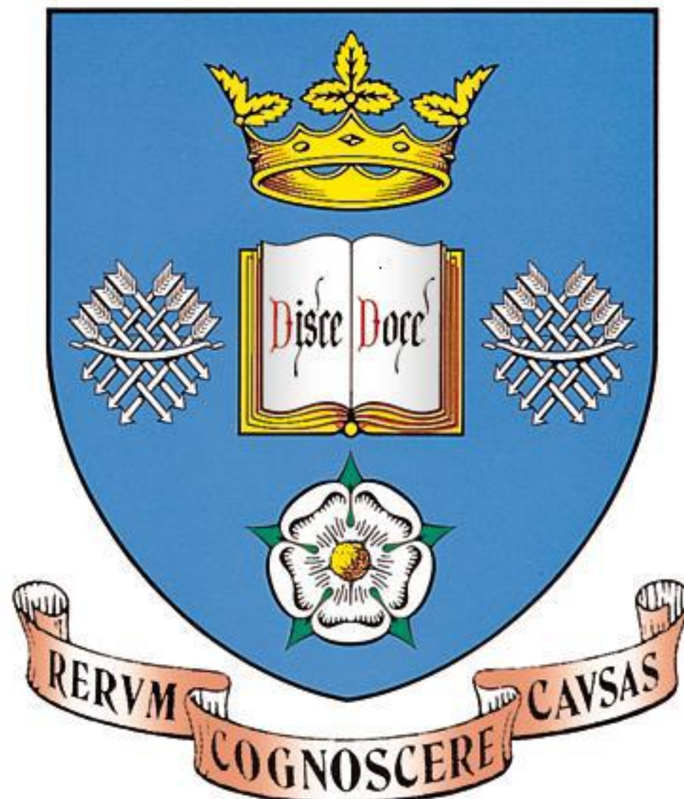

Department of Electronic and Electrical Engineering

Thesis submitted to the University of Sheffield for the degree of Doctor of Philosophy

April 2014

Intentionally Blank

Abstract

This thesis details research on the development of ~1.3μm quantum dot (QD) devices. QD devices which are theoretically ideal for the realisation of temperature insensitive lasers. A method to measure the recombination coefficients in a semiconductor laser is developed, and the role of Auger recombination in the realisation of temperature insensitive lasers is discussed.

Moreover, due to a broad spectral linewidth and strong state-filling effects, QD structures are promising for application as broadband light sources.

It is reported that the Auger recombination coefficient decreases with increasing device temperature, as measured by several complicated experimental techniques. In chapter 2, a simple analysis method (small signal modulation) to measure all of the recombination coefficients is introduced and discussed. In chapter 3, experimental data based on the small signal modulation technique is analysed. Which shows that all of the recombination coefficients, including the Auger coefficient, are a function of temperature and modulation doping in QD lasers.

Following on from chapter 3, in chapter 4 the dynamic characteristic (differential carrier lifetime) of a 3μm-ridge QD laser device fabricated from commercial QD material is investigated. The modelled GS peak gain as a function of current density is determined based on the recombination coefficients, the random population model and the measured gain (via the

Hakki-Paoli method). Then, by comparing the modelled GS gain to the experimental results, the carrier thermal escape parameter is determined. Finally in chapter 4, the variation of the Auger coefficient is explored to investigate the possibility of a temperature independent current density.

The selective intermixing technique can be used in order to achieve broadband light source devices. In chapter 5, the intermixing method is introduced based on both quantum well and quantum dot structures. Then, a number of different capping materials on samples with different active region structures are discussed based on photoluminescence measurements from intermixed structures. The potential for selective area intermixing of an integrated device with a TiO_2 and SiO_2 cap annealed on a p-doped sample is demonstrated at the end of the chapter.

Finally, in chapter 6, two integrated devices are fabricated based on this TiO_2 and SiO_2 cap. These devices demonstrate a broad emission bandwidth, and by applying a fast Fourier transform to the spectra in order to determine the point spread function of the instrument, and application of the Rayleigh criterion for resolution, an estimation of the resolution in an OCT system is made.

In loving memory of my Granny (1935-2012)

Acknowledgements

Firstly, I would like to thank dear Professor Richard Hogg for his enthusiastic help, without his insight, guidance and support, I would “drown in the research ocean”.

Secondly, I would like to thank all the senior members in our group who helped me and guided me to the right direction during this work. Deep thanks to ZZ and Qi for their help for not only research but also my life in Sheffield. Thank to “Big” Dave for tolerating my ignorance and for all the invaluable setups he built up in our group. Thank to Ken, who is the most handsome guy in the *III-V* centre, for his patient and accommodating help during my tedious fabrication processes.

I would like to thank all my colleagues especially: Xiao, Jon, Nasser, Kris, Kristof, Little Dave, Negin, Majid, Hifsa, Richard, Hongchi, Saurabh, Omar, Luke, Bret, Avan, Noura, and Amilia. Also a massive thanks to my “Sheffield family” members: Siming and Wei.

Finally, I would like to thank my parents and my wife for their unacknowledged support. They are always there for me when I am down. I hope I make you proud.

List of Publications

Journal & proceeding papers:

- ***K. J. Zhou***, Q. Jiang, Z. Y. Zhang, S. M. Chen, H. Y. Liu, Z. H. Lu, K. Kennedy, S. J. Matcher, and R. A. Hogg, "**Quantum dot selective area intermixing for broadband light sources**," Opt. Express, vol. 20, pp. 26950-26957, Nov 19 2012.

- ***K. J. Zhou***, S. M. Chen, D. T. D. Childs, and R. A. Hogg., "**Effect of modulation p-doping on the differential carrier lifetime of quantum dot lasers**," Proc. SPIE, **8277**, 827720-1 (2012)

- Z. Y. Zhang, A. E. H. Oehler, B. Resan, S. Kurmulis, ***K. J. Zhou,*** Q. Wang, M. Mangold, T. Suedmeyer, U. Keller, K. J. Weingarten, and R. A. Hogg, "**1.55 m InAs/GaAs Quantum Dots and High Repetition Rate Quantum Dot SESAM Mode-locked Laser**," Sci. Rep. , **2**, 477 (2012).

- S. M. Chen, ***K. J. Zhou***, Z. Y. Zhang, D. T. D. Childs, M. Hugues, A. J. Ramsay, and R. A. Hogg., "Ultra-broad spontaneous emission and modal gain spectrum from a hybrid quantum well/quantum dot laser structure," Appl. Phys. Lett. 100, 041118 (2012).

- S. M. Chen, ***K. J. Zhou***, Z. Y. Zhang, O. Wada, D. T. D Childs, M. Hugues, and R. A. Hogg., "**Room temperature simultaneous three-state lasing in hybrid quantum well/quantum dot laser**," Electron. Lett. **48**, 644 (2012).

- Siming Chen, ***Kejia Zhou***, Ziyang Zhang , Jonathan R. Orchard, David T. D. Childs, Maxime Hugues, Osamu Wada, and Richard A. Hogg, "**Hybrid Quantum Well/Quantum Dot Structure for Broad Spectral Bandwidth Emitters**," IEEE J. Sel. Topics Quantum Electron. . vol. 19, pp. 1900209, 2013.

- A. Choudhary, A. A. Lagatsky, Z. Y. Zhang, ***K. J. Zhou***, Q. Wang, R. A. Hogg, K. Pradeesh, E. U. Rafailov, W. Sibbett, C. T. A. Brown, and D. P. Shepherd, "**A diode-pumped 1.5µm waveguide laser mode-locked at 6.8GHz by a quantum dot SESAM,**" Laser Physics Letters, vol. 10, p. 105803, 2013.

- S. M. Chen, ***K. J. Zhou***, Z. Y. Zhang, D. T. D. Childs, J. R. Orchard, R. A. Hogg, K. Kennedy, and M. Hugues, "**Hybrid quantum well/ quantum dot structure for broad spectral bandwidth devices**," Proc. SPIE. 8255, 82550E (2012).

- Mehrdad Irannejad, Gin Jose, Paul Steenson, Qi Jiang, ***Kejia Zhou***, Ziyang Zhang and Richard Hogg, Animesh Jha, "Pulsed laser deposition of glass on GaAs and channel waveguide fabrication," Photon10, 23-26, August, 2010.

Submitted paper:

- ***K.Zhou***, S.Chen, David T. D. Childs, O.Wada, Z.Y.Zhang, K.Kennedy, Xiao Jin and Richard A. Hogg, "Characterization of recombination processes in quantum dot lasers using small signal modulation" (submitted to Journal of Applied Physics)

Conference papers and presentations:

- B. Resan, A. E. Oehler, Z. Zhang, S. Kurmulis, ***K. Zhou***, Q. Wang, M. Mangold, T. Suedmeyer, U. Keller, R. A. Hogg, and K. J. Weingarten, "**10GHz Pulse Repetition Rate ERGO Laser Modelocked by a 1550nm InAs/GaAs Quantum-Dot SESAM**," 2012, p. JTh2A.23.

- ***K. Zhou***, D. T. D. Childs, S. Chen and R. A. Hogg, "**Measurement of Differential Carrier Lifetime of Un-doped and Modulation p-doped Quantum Dot Lasers**"（Oral）

  UK Semiconductor conference, University of Sheffield, UK, July (2011).

- ***K. Zhou***, S. Chen, D.T.D. Childs, R.A. Hogg, "**Effect of Modulation p-Doping on the Differential Carrier Lifetime of Quantum Dot Lasers**"（Poster）

  UK Semiconductor conference, University of Sheffield, UK, July (2012).

- ***K. J. Zhou***, S. M. Chen, D. T. D. Childs, and R. A. Hogg., "**Effect of modulation p-doping on the differential carrier lifetime of quantum dot lasers**," (Poster)

  Photonics West conference, San Francisco, California, United States, January （2012）

- ***K. J. Zhou***, Q. Jiang, Z. Y. Zhang, S. M. Chen, H. Y. Liu, K. Kennedy and R. A. Hogg, "**Broadband Quantum Dot Light Source Based on Selective Area Intermixing Process**"（Poster）

  The Celebration of the 50th Anniversary of the Laser Diode, University of Warwick, Coventry, UK, September (2012)

- ***K. J. Zhou***, O. Wada, S. M. Chen, Z. Y. Zhang, D. T. D Childs, K. Kennedy and Richard A. Hogg, "**Characterization of Recombination Processes in Quantum Dot Lasers Using Small Signal Modulation**" (Poster)

  International Semiconductor Laser Conference (ISLC), San Diego California, United States, October（2012）.

- Z. Y. Zhang, A. Oehler, B. Resan, ***K. J. Zhou***, M. Mangold, T. Suedmeyer, U. Keller, K. J. Weingarten, and R. A. Hogg, "**1.55μm InAs/GaAs Quantum Dot Semiconductor Saturable Absorber Mirror**" (Oral)

  Photonics West conference, San Francisco, California, United States, January（2012）

- S. Chen, ***K. Zhou***, Z. Zhang, D. T. D. Childs, O. Wada, M. Hugues, and R. A. Hogg, **"Hybrid Quantum Well/Quantum Dot Active Element for Broad Spectral Bandwidth Source"** (oral)

  UK Semiconductor conference, University of Sheffield, UK, July (2012).

- S. Chen, ***K. Zhou***, Z. Zhang, D. T. D.Childs, O. Wada, M. Hugues, and R. A. Hogg, **"Hybrid Quantum Well/Quantum Dot Laser Structure for Broad Spectral Bandwidth Source"** (Poster)

  The Celebration of the 50th Anniversary of the Laser Diode, University of Warwick, Coventry, UK, September (2012)

- S. Chen, ***K. Zhou***, Z. Zhang, D. T. D. Childs, J. Orchard, M. Hugues, K. Kenneth, and R. A. Hogg, "**Hybrid Quantum Well/Quantum Dot Structures for Broad Spectral Bandwidth Devices**" (Oral)

  Photonics West conference, San Francisco, California, USA, Jan（2012）

- Siming Chen, ***Kejia Zhou***, Ziyang Zhang, Osamu Wada, David Childs, Kenneth Kennedy, Max Hugues and Richard Hogg, "**Hybrid Quantum Well/Quantum Dot Active Element for Broad Spectral Bandwidth Emitters and Amplifiers**" (Poster)

  International Semiconductor Laser Conference (ISLC), San Diego California, United States, October（2012）.

- S. Chen[1], N. Peyvast[1], ***K. Zhou[1]***, N. Babazadeh[1], Z. Zhang[1], D. T. D. Childs[1], M. Hugues[2], O. Wada[1], and R. A. Hogg[1, 2], T. Kageyama[3], K. Nishi[3], K. Takemasa[3], and M. Sugawara[3], "**Broad Bandwidth Emission from Hybrid QW/QD Structures**" (Oral)

  The 18th Opto-Electronics and Communications Conference / Photonics in Switching 2013 (CLEO-PR&OECC/PS 2013)

- S. Chen, N.Peyvast, ***K. Zhou***, N. Babazadeh, Z. Zhang, D. T. D. Childs, M. Hugues and R. A. Hogg **"Broad Bandwidth Emission from Hybrid Quantum Well/Quantum Well Structure"** (Oral)

  UK Semiconductor conference, University of Sheffield, UK, July (2013).

Contents

Development of Advanced GaAs Based Quantum Dot Devices i
Abstract iii
Acknowledgements vi
List of Publications vii
Thesis Outline xiv
1. Background Introduction 1
1.1. Quantum Dots (QDs) Materials 1
1.2. Recombination Processes in Semiconductors 5
1.3. Molecular Beam Epitaxy (MBE) 7
1.4. Temperature Independent Laser 9
1.5. Broadband Emitters 12
Reference 16
2. Device Fabrication & Experimental Techniques 20
2.1. Device Fabrication 20
2.1.1. Mesa Diode Device Fabrication 20
2.1.2. Multi-section Device Fabrication 28
2.1.3. Tilted Ridge Emit Device Fabrication 42
2.2. Experimental Techniques 42
2.2.1. Small signal modulation (SSM) 43
2.2.2. Light-Current (L-I) measurement 46
2.2.3. Hakki-Paoli Gain Measurement 47
2.2.4. Photoluminescence Spectroscopy (PL) 50
2.2.5. Photocurrent Spectroscopy (PC) 52
Reference 54
3. Characterization of Recombination Processes in QD Lasers Using Small Signal Modulation 56
3.1. Introduction 56
3.2. Devices – Epitaxy, Fabrication and Temperature Insensitivity (T_0) 59
3.2.1. Epitaxy 59
3.2.2. Fabrication 60
3.2.3. Temperature Insensitivity (T_0) 61
3.3. Experimental Method 62

3.4. Results and Discussion 66
3.4.1. Un-doped device 66
3.4.2. Modulation p-doped device 68
3.5. Discussion 72
3.6. Conclusion 73
3.7. Future work 74
Reference 75
4. Temperature Sensitivity of Commercial QD Laser Material 78
4.1. Growth and Fabrication Details 78
4.2. Static Characteristics 80
4.2.1. I-V and EL Spectrum 80
4.2.2. Temperature Dependent L-I 81
4.3. Temperature Dependent Differential Carrier Lifetime 86
4.4. Gain vs. Temperature 88
4.4.1. Gain Measured by Hakki-Paoli Method at 20°C 89
4.4.2. Gain Measured by Hakki-Paoli Method at 60°C 90
4.5. Modelling and Analysis 91
4.5.1. Random Population and Fermi Distribution 91
4.5.2. Peak Gain Model 94
4.5.3. Empirical Fit 96
4.5.4. Explore Possibility of Obtaining Infinite T_0 102
4.6. Conclusion 105
4.7. Future Work 106
Reference 107
5. Quantum Dot Selective Area Intermixing for Broadband Light Sources (Material Investigation) 110
5.1. Introduction of Selective Intermixing Technique 110
5.2. QW Intermixing 111
5.3. QD Intermixing 113
5.3.1. Introduction & Theory 115
5.3.2. Intermixing of Un-doped QD sample 121
5.3.3. Intermixing Based on DWELL Samples 126
5.4. Conclusion 134
5.5. Future work 134

Reference 135
6. Quantum Dot Selective Areas Intermixing for Broadband Light Sources (Device Investigation) 139
6.1. Introduction to Broadband Sources 139
6.1.1. Broadband Emission Discussion Based on PL 141
6.1.2. Power-Dependent PL & Analysis 142
6.1.3. PC Measurement & Analysis 146
6.1.4. Device Fabrication and Result 147
6.2. Conclusion 156
6.3. Further work 156
Reference 158
7. Summary 161
Reference 164
8. Appendix i
8.1. 5µm and 15µm Narrow Ridge Lasers i
8.2. 3µm trench lasers v
8.3. QD Multi-section SLDs ix

Thesis Outline

This thesis will discuss the characteristics of QD based semiconductor devices including both dynamic and static characteristics. This covers the temperature sensitivity of QD lasers and the manufacture of broad spectral band-width devices by intermixing.

As fabrication process development has played a significant part of my work, chapter 2 will firstly discuss the device fabrication process for three different device structures: mesa-diode device, narrow ridge multi-section device and the 7 degree off normal ridge device. The process will be discussed step by step, and the relevant recipes are introduced. Then, four experimental techniques, relevant to the remainder of the thesis, will be introduced and discussed in the second section of chapter 2, they are small signal modulation, photocurrent (PC) spectroscopy, light-current (L-I) measurement and the Hakki-Paoli gain measurement. The experimental apparatus for all the measurements will be shown as well as some examples of results.

Chapter 3 reports on spectrally resolved differential carrier lifetime measurements of un-doped and modulation p-doped 1300nm quantum dot lasers. It is found that the differential carrier lifetime is significantly reduced for p-doped samples compared to essentially identical un-doped samples in line with enhanced Auger recombination. With increasing temperature, the impedance corrected results from the un-doped sample are slightly increased and an increase in impedance corrected differential carrier lifetime is also observed for the p-doped sample. Based on the plot of $1/\tau^2$ versus J, I

deduce a reducing Auger rate with increasing temperature. The recombination rate of the excited state is also discussed. At the end of the chapter, all the recombination coefficients are deduced and found to be a function of temperature.

Chapter 4 will firstly discuss the static characteristics of a 3μm narrow ridge laser device (fabricated from an 8 layer QD wafer), for example, current-voltage (I-V), electroluminescence (EL) spectrum and temperature dependent L-I. Based on the temperature dependent L-I result, the efficiency of laser device with different lengths will be investigated. Then the dynamic characteristic will be discussed to determine the differential carrier lifetime. The recombination coefficients A, B and C are also obtained for this sample. According to the random population model, the modelled GS peak gain vs. current density is determined. By comparing the modelled gain to the measured gain by using the Hakki-Paoli method, the carrier thermal escape coefficient is obtained. Finally, the Auger coefficient C is varied in order to theoretically achieve infinite T_0.

In chapter 5, the selective area intermixing technique will be introduced and discussed including both QW and QD intermixing processes. Based on photoluminescence (PL) measurement, a number of key parameters will be discussed. Then, different capping materials used during the intermixing process will be introduced, such as TiO_2, SiO_2, Al, Si_3N_4. All these caps will be firstly investigated based on an un-doped 8 layer QD sample. Then a comparison of un-doped and p-doped 5 layer DWELL structures is made**.** By

comparing all the data from three different samples, modulation p-doped samples are shown to have beneficial properties in the intermixing process.

Chapter 6 will briefly introduce the broadband source used in the OCT system. Then the intermixing process of the modulation p-doped sample with several capping materials will be further investigated based on PL measurements. PC data is also measured and analysed in order to confirm the location of the energy levels. After a comparison of capping materials, a TiO_2 cap and a SiO_2 cap are chosen to manufacture broad-band devices. A two-section device with spectral bandwidth of ~240nm is achieved as a first step and then a three-section device with a spectral bandwidth of ~310nm is obtained. If both devices are used in an OCT system, the axial resolution will be ~3.5μm and ~2.4μm when the Rayleigh criterion is satisfied.

Lastly, a summary of my work in this thesis will be presented, along with proposals for future work.

1. Background Introduction

1.1. Quantum Dots (QDs) Materials

By the end of 1980s, the main properties of quantum wells (QWs) were well understood and researchers started to shift their interest toward the structure with further reduced dimensionality – quantum dots (QDs). QDs are semiconductor nanocrystals (<100 nm) and were first realized by Rocksby in 1932. Many applications have been predicted such as single electron transistors or QD lasers [1].

In QDs, carriers are confined in all three dimensions which break the classical band structure model of a continuous dispersion of energy related to momentum. This resulting a highly discrete energy level (density of states) in QDs. Figure 1.1 shows the density of states (DOS) of the system where the carrier has various degrees of freedom: 3D (bulk), 2D (QW), 1D (quantum wire) and 0D (QD) [2].

In the last two decades, nanostructures, including QD, have been successfully realized using self-organization effects. For the ideal self-assembled quantum dots (SAQDs) layer, dots have the uniform size distribution which results in highly discrete energy states with fixed photon energies. However, in the real case, SAQDs typically grown by using Stranski-Krastanow (S-K) mode where SAQDs are formed due to the large lattice constant mismatch between two materials such as InAs and GaAs. During the growth process, the size and composition of the dot cannot be perfectly controlled which leads to a

naturally inhomogeneous broadening of the DOS, as shown in Figure 1.2 [3].

Moreover, due to the three-dimensional quantum confinement of charge carriers, laser device based on QD structures should provide low threshold current density, reported J_{th}~11.7A/cm^2 at room temperature under continue-wave mode (CW) [4] and reduced temperature sensitivity (T_0=161K from 0°C to 80°C [5], T_0=213K from 0 to 81°C [6]).

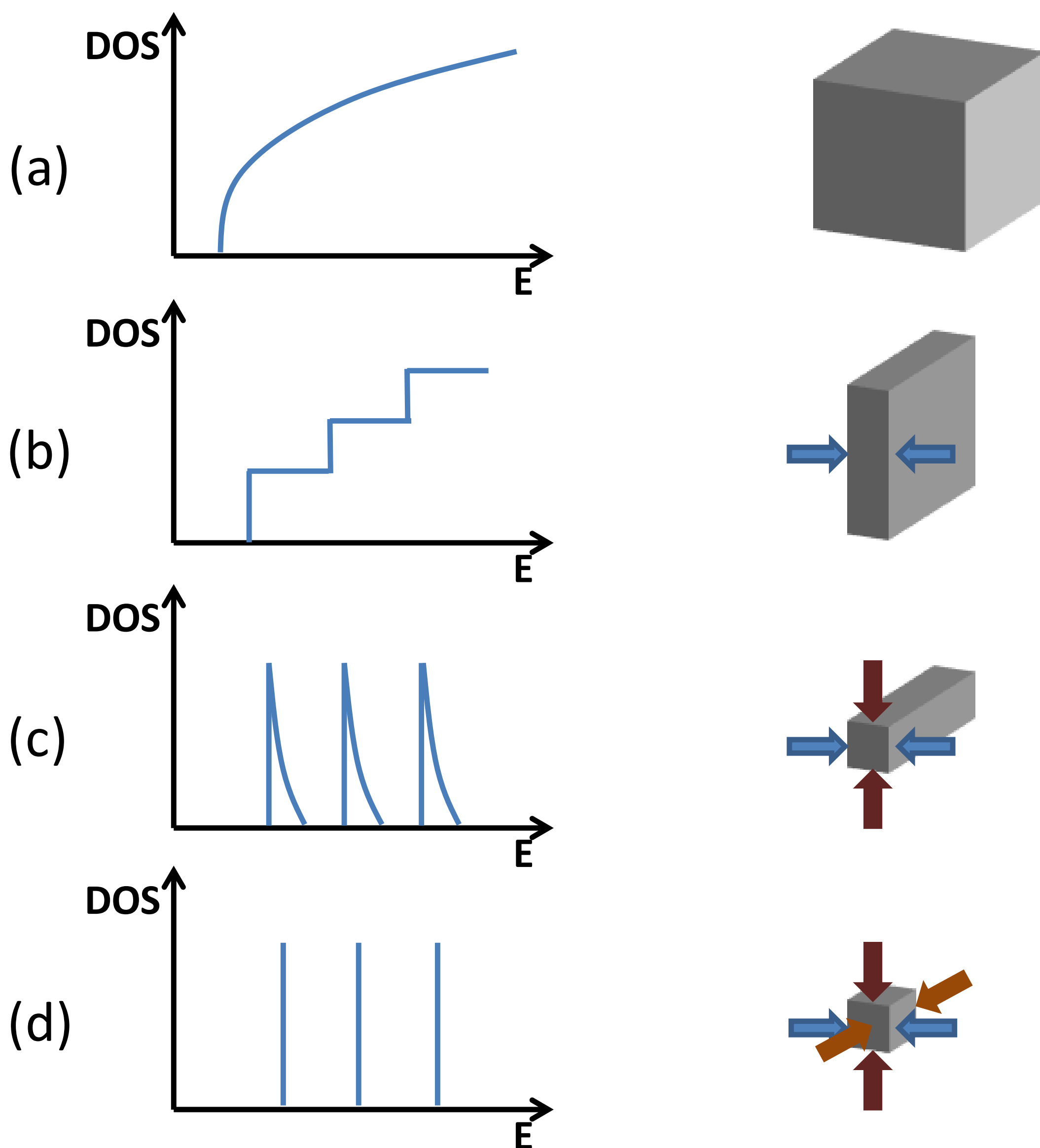

Figure 1.1. Active region and its corresponding DOS of (a) bulk semiconductor, (b) QWs, (c) quantum wires, and (d) QDs [2].

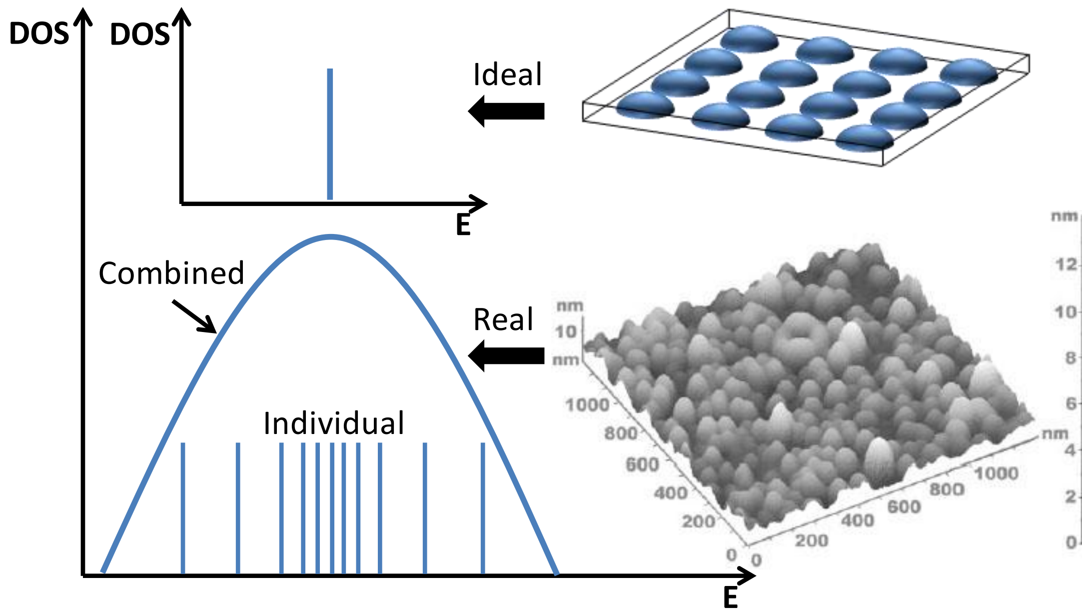

Figure 1.2 Density of state of the ideal QD and the real QD ensemble [3].

Broadband light source is a light source with a broad optical full-width of half-maximum (FWHM) [7], usually ≥100nm. Typically, the broadband light source exhibit a high spatial coherence, making it easy to couple with fibre, and due to its broad FWHM the temporal coherence is low (discussed in detail in chapter 6). Some applications of broadband source are attractive, such as white light interferometer [8], fibre optic gyroscopes (FOG) [9], wavelength division multiplexing (WDM) and especially the optical coherence tomography (OCT) systems which is discussed in chapter 2&6.

For the QDs grown by S-K mode, the typical size uniformity is ~10% [10], due to its broad inhomogeneous linewidth, it becomes popular for realizing the broadband light source. Furthermore, in SAQDs the gain is relatively small compared to QWs due to the limited number of energy states which means the GS is saturated at low current density. This saturation of the GS is also a benefit for broadband light source, as the appearance of the exited state (ES)

can further broaden the linewidth of the emission spectrum.

Recently, several different methods have been used to broaden the emission linewidth. By using chirped multi-layer stack of QDs, which has different emission wavelengths in each layer due to the indium composition variation, a device with 121nm emission bandwidth and corresponding 1.3mW output power has been obtained under pulse operation [11]; A dot-in-well (DWELL) structure was studied, by varying the indium composition in each QW layer where the QD layers are capsule and carefully engineering the wavelengths of each layer to compensate each other, a device with 85nm FWHM and corresponding output power of 2.5mW was achieved under continues-wave (CW) operation [12]; By investigating the QW/QD hybrid structure, in which a QW layer is carefully grown with several QD layers to emit light at the same wavelength of the ES_2 of the QDs, device with 213nm 3dB linewidth and corresponding output power of 1.1mW was obtained under pulse operation [13]; The selective area intermixing technique was also used to realize the broadband emission. By using different capping materials during the annealing process, due the Gallium vacancy interdiffusion process the emission wavelength varies laterally on the sample surface. If the emission spectrum from each capped area compensate each other, the broadband spectrum can be achieved [14]. Although in [14] the emission bandwidth is only 60nm due to the spectrum overlap at the centre wavelength, its corresponding output power under pulse operation is relatively high (79mW). It shows the potential of this intermixing technique for realizing the broadband source.

1.2. Recombination Processes in Semiconductors

At steady state, the carrier lifetime is the rate of the carrier recombination process. Initially, for bulk semiconductor the rate equation regarding carrier lifetime can be written as [15]:

$$R(N) = \frac{N}{\tau_c} = A(N) + B(N)^2 + C(N)^3 \qquad 1\text{-}(1)$$

Where *R(N)* is the total recombination rate, *N* is carrier density, τ_c is carrier lifetime. *A* is considered to be non-radiative coefficient related to defects, *B* is the spontaneous emission and *C* is the Auger recombination coefficient. Recently, equation 1-(1) was assumed the case for QD system [16], then equation 1-(1) can be written regarding to the dot occupancy volume V_{dots} as:

$$R(N) = \frac{\frac{<n>}{V_{Dots}}}{\tau_c} = A\left(\frac{<n>}{V_{Dots}}\right) + B\left(\frac{<n>}{V_{Dots}}\right)^2 + C\left(\frac{<n>}{V_{Dots}}\right)^3 \qquad 1\text{-}(2)$$

here *<n>* is the carriers per dot.

In QD device, coefficient *A* in equation 1-(2) possibly related to the carriers recombine at the non-radiative recombination centre caused by defects; the coefficient *B* is considered to be spontaneous emission: an electron in the conduction band recombining with a hole in the valence band spontaneously to generate a photon, shown in Figure 1.3(a). If a number of this recombination process should occur, due to the random emission time and direction, it would result an incoherent emission. The recombination rate of the spontaneous emission is proportional to the carrier density of electrons and holes (N^2 when the density of the electron and the hole are equal);

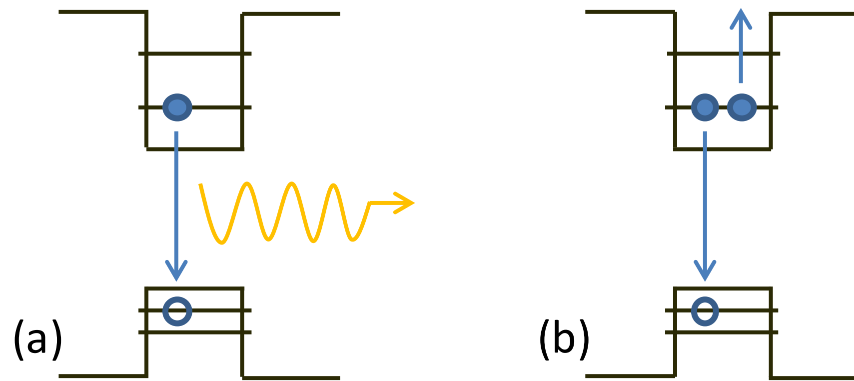

Figure 1.3 Recombination process (a) spontaneous emission process, (b) Auger recombination process.

The Auger recombination process is typically a process has three particles involved, as shown in Figure 1.3(b), an electron in the GS of the conduction band and a hole in the GS of the valence band recombines with each other, instead of emitting a photon the energy is transferred to another electron in the conduction band, this electron is then exited to a higher energy level. In equation 1-(2) the coefficient *C* is called Auger coefficient in this thesis, but there is some debate in the field [17], due to complicated structure of the dots and their inhomogeneous size distribution, each of the recombination coefficients (*A, B, C*) may depend on the carrier density causing strong deviations from the assumed simple form. For example, in such localized/inhomogeneously broadened structures some defect levels above the bandgap are possible which may cause a strong temperature/carrier density dependence of *A* coefficient leading to an Auger – like behavior of (*AN*) term. Due to lack of thermal equilibrium and carrier redistribution effects *B* – coefficient may also depend on carrier density. Therefore, in the following chapters, the *C* coefficient will be referred to as Auger, but that this is a term which relates to cubic and higher order terms, not restricted to Auger alone.

1.3. Molecular Beam Epitaxy (MBE)

Molecular beam epitaxy (MBE) is one of the major epitaxial growth techniques in both research and industry. All the samples investigated in this thesis were grown by MBE. In this section, the MBE technique is briefly introduced.

MBE was developed in the early 1970s for the purpose of growing high-purity compound semiconductor layers [18]. In the last 40 years, it has been one of the most popular techniques for growing *III-V* compound semiconductors. Because of the high degree of control of the MBE system, it can produce abrupt layer interfaces and precise thickness, composition and doping level control. The MBE system is widely used in developing high quality optoelectronic and electronic devices.

In the MBE system, in order to achieve high-purity compound semiconductor layers, the material source must be extremely pure and the entire growth process is done in an ultra-high vacuum environment. There are three main chambers in the MBE system: a growth chamber, a buffer chamber (preparation and storage chamber), and a load lock which is used to send the sample in and out of the vacuum environment. Figure 1.1 illustrates a growth chamber and several subsystems of the MBE system.

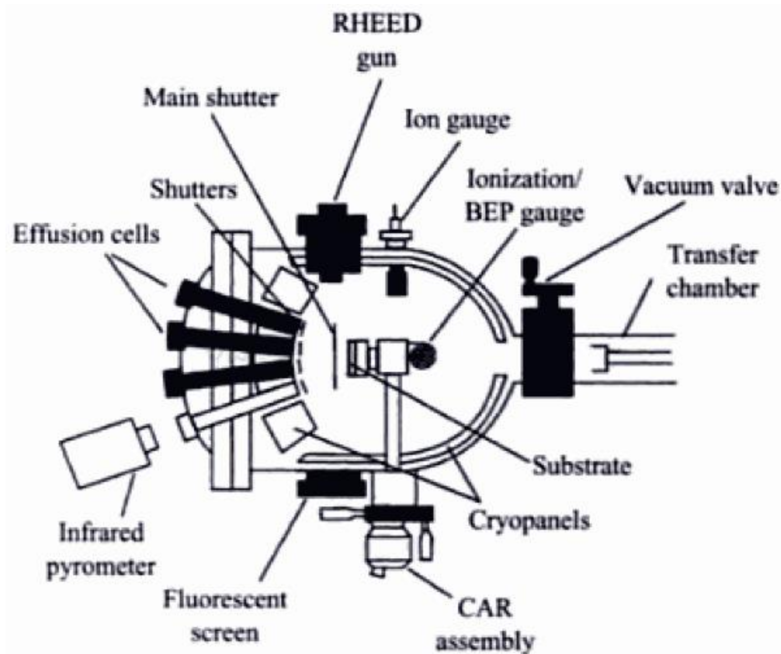

Figure 1.1. Diagram of a typical MBE system growth chamber and several subsystems [19].

The wafers are loaded into the growth chamber via a magnetically coupled transfer rod. When the sample is loaded, the rotatable sample holder is flipped around from the loading position, in order to place the sample to face the material sources. The material sources from the effusion cells are heated independently to the sample to achieve the desired material flux. In the research type MBE system, the effusion cells are normally placed 10-15cm in front of the sample in the growth position, this distance would be extended if we grow larger wafers. Also, there is a chilled panel to separate each of the effusion cells in order to prevent thermal cross-talk. Shutters controlled by the computer are placed in front of the effusion cells to shutter the molecular beams reaching to the sample surface.

A clean sample surface is crucial for the epitaxial growth process, since contaminants from the atmosphere can easily cause defects in the epitaxial layer. At the initial stage of the MBE growth, Auger electron spectroscopy was

used to check the cleanliness of the wafer [20]. Currently, “epi-ready” wafers are widely used, which have a protective oxide layer deposited on the sample surface after a pre-clean process in a controlled environment. There is no wafer cleaning procedure needed for the “epi-ready” samples.

Reflection high energy electron diffraction (RHEED) is an important tool for monitoring the growth rates, the removal of oxides from the sample surface, the substrate temperature and the arsenic overpressure. It can be seen in Figure 1.1 the RHEED gun is located on top of the growth chamber, it emits electrons to strike the sample surface at a shallow angle of ~0.5-2° [19]. There is a phosphor screen which shows the reflection and diffraction patterns of the electrons reflected from the sample surface. The patterns provide information related to the surface crystallography.

1.4. Temperature Independent Laser

The characteristic temperature T_0, is a very important factor for the laser devices, which indicates how sensitive the laser device is to temperature [21]. Equation 1-(3) shows the definition of T_0, which is related to the change of the temperature and the change of the natural logarithm of the threshold current density.

$$T_0 = \frac{\Delta T}{\Delta \ln(J_{th})} \qquad 1\text{-}(3)$$

T_0 is derived by measuring the threshold current density of a laser with increasing device temperatures. It is discussed with experimental data in chapter 4. When T_0 is infinite, it means the threshold current does not change with temperature.

It is well known that the temperature sensitivity of a semiconductor laser is of particular importance in optical communications [22]. Data is encoded as a series of high and low intensities as shown in Figure 1.2. An eye diagram [23] in a practical communication system is also shown in Figure 1.2.

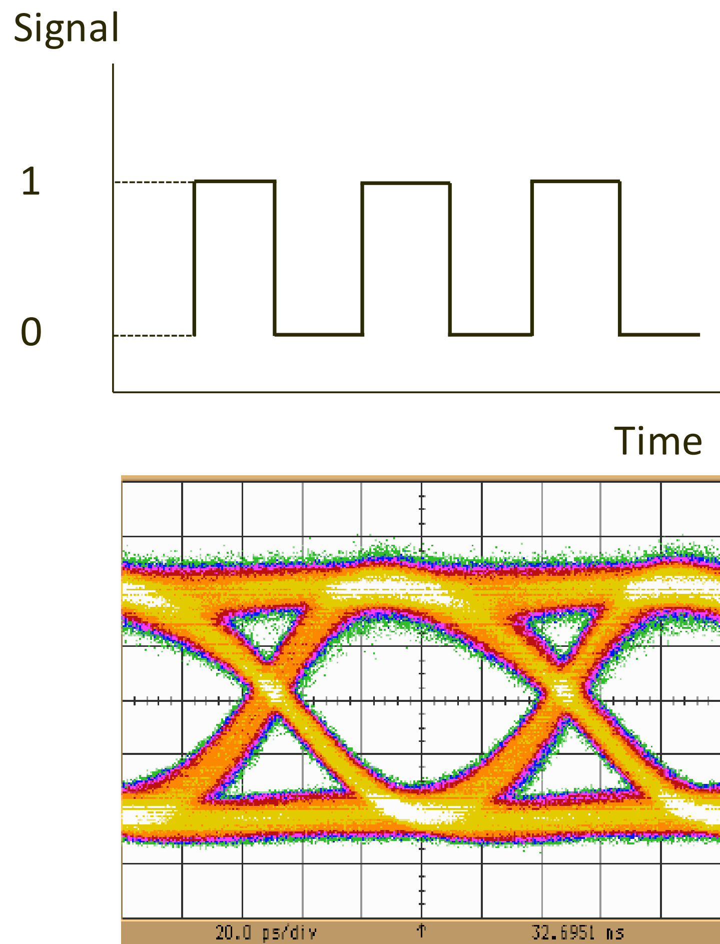

Figure 1.2. The time domain transmission signal and an eye diagram in communication process [23].

Moreover, in optical communication systems, the signal “0” does not correspond to zero optical power, it is a low power when the laser is turned on (i.e. operating above threshold), and the signal “1” is chosen with higher laser output power as demonstrated in Figure 1.3. This is because the “ON” and “OFF” process of the laser diode would be the speed limitation in the transmission system.

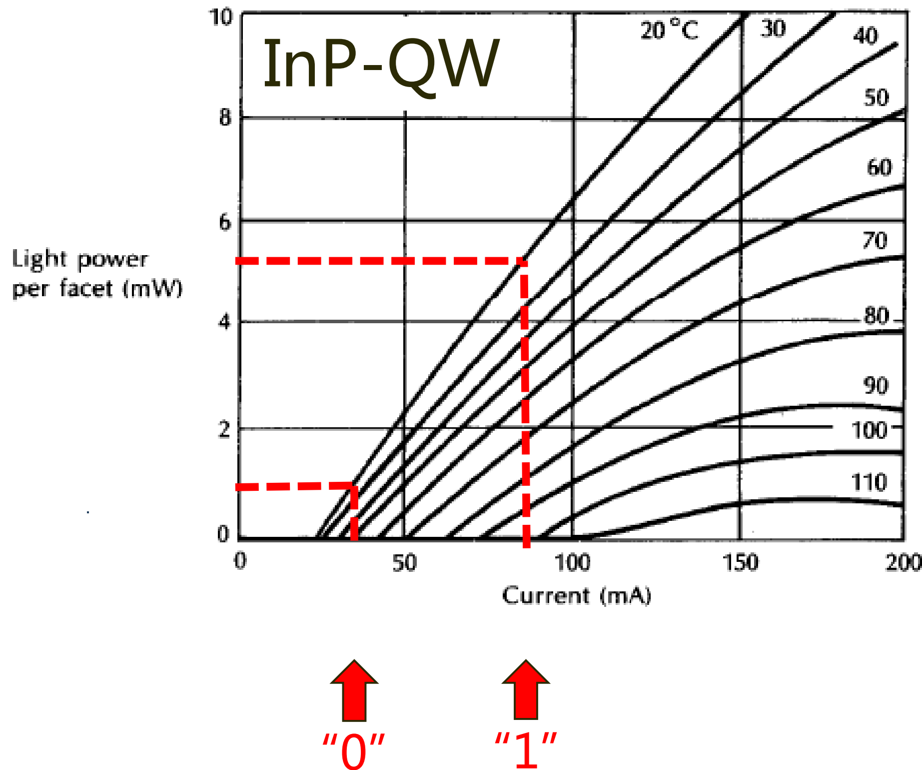

Figure 1.3. The temperature dependent light power vs. current curve of an InP QW device [24].

A temperature sensitive laser, such as an InP QW laser, requires cooling, which adds to module costs and the cost of ownership as it increases energy consumption. Recently, GaAs based QD devices have been commercialized [25], which have considerably improved temperature sensitivity compared to an InP QW device [26].

In the ideal case, due to the 3D confinement of charge carriers, the delta-like DOS and the increased exciton binding energy, and deep confinement potentials, the QD laser device should perform well at high temperature. The temperature independent QD laser was theorised by Arakawa and Sakaki [26], if the energy separation between the lasing state and the next quantised state is bigger then k_BT. Figure 1.5 shows the numerical example of the threshold current calculated in [26].

In most real QD systems, the separation of the energy spacing is just a few meV in the valence band. Therefore, the threshold current is particularly sensitive to a thermal distribution of holes because of the promotion of carriers out of the ground (lasing) state.

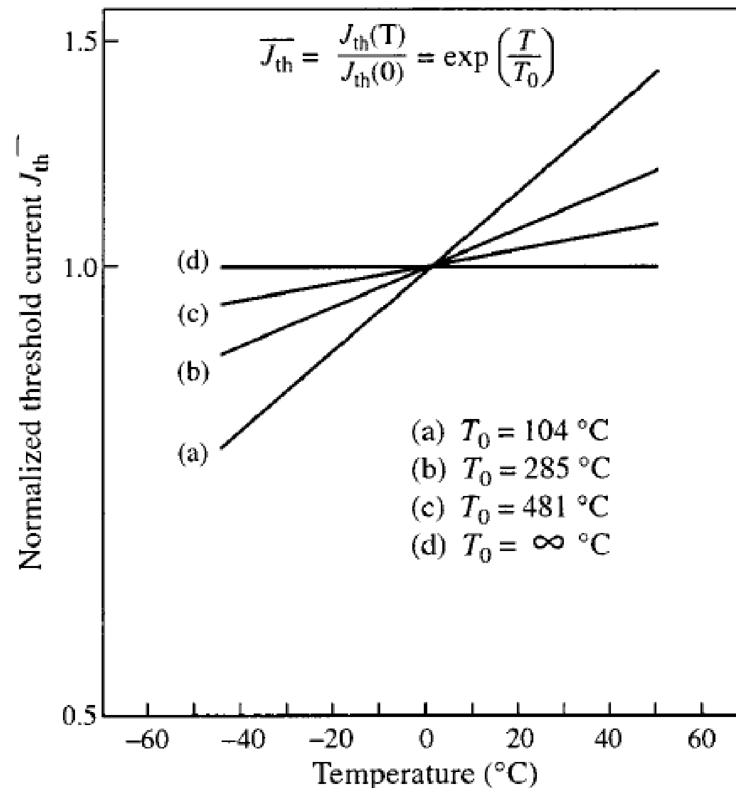

Figure 1.5. Normalized temperature dependence of the threshold current for various lasers: (a) Bulk (b) with 1D confined QWs (c) with 2D confined QWs, (d) with 3D confined QWs [26].

As a result, with increasing temperature, the gain cannot be maintained due to the decreased GS occupancy at a fixed injection current. However, modulation p-doped sample have been shown to reduce the temperature sensitivity of QD lasers [5] by counteracting the effect of hole broadening [27, 28].

1.5. Broadband Emitters

Broadband light sources have attracted significant interest in medical imaging

applications, such as optical coherence tomography (OCT) systems. The system was firstly invented and developed by Prof. James G Fujimoto and his colleagues [29]. It is a three dimensional (3D) imaging technique which enables *in-situ* and *in-vivo* imaging of living cells [30]. The OCT system is based upon a Michelson interferometer which measures the interference pattern created by two beams (split from one beam) travelling in different paths. Two wavelengths are promising for the OCT system, one is ~1050nm which has zero dispersion in aqueous tissue such as human eyes, and the other is ~1300nm which has a minimum absorption and scattering in the skin [31].

There are two main typical OCT systems: the time domain (TD)-OCT system and the Fourier domain (FD) OCT system including the swept source (SS)-OCT which uses a wavelength sweeping laser source. In both OCT systems the final image is made up from individual axial scans (completed by a single scan of the reference mirror in the TD-OCT or one sweep of the laser in the FD-OCT) taken by scanning optics during the lateral scan. The lateral and axial resolution of the OCT system is independent to each other, the lateral resolution of the system is limited by the scanning optics and the limitation of diffraction. The axial resolution is directly related to the coherence length of the light source as shown in equation 1-(4):

$$L_c \approx 0.44 \times \frac{\lambda_0^{\ 2}}{\Delta\lambda} \qquad \text{1-(4)}$$

where λ_0 is the centre wavelength and $\Delta\lambda$ is the full-width at half maximum (FWHM) of a light emitting source in Gaussian shape. Based on equation 1-

(4), it is known that the broadband light source is a crucial component in obtaining high axial resolution in the OCT system [32, 33].

Figure 1.6 shows the schematic diagram of the typical TD-OCT system.

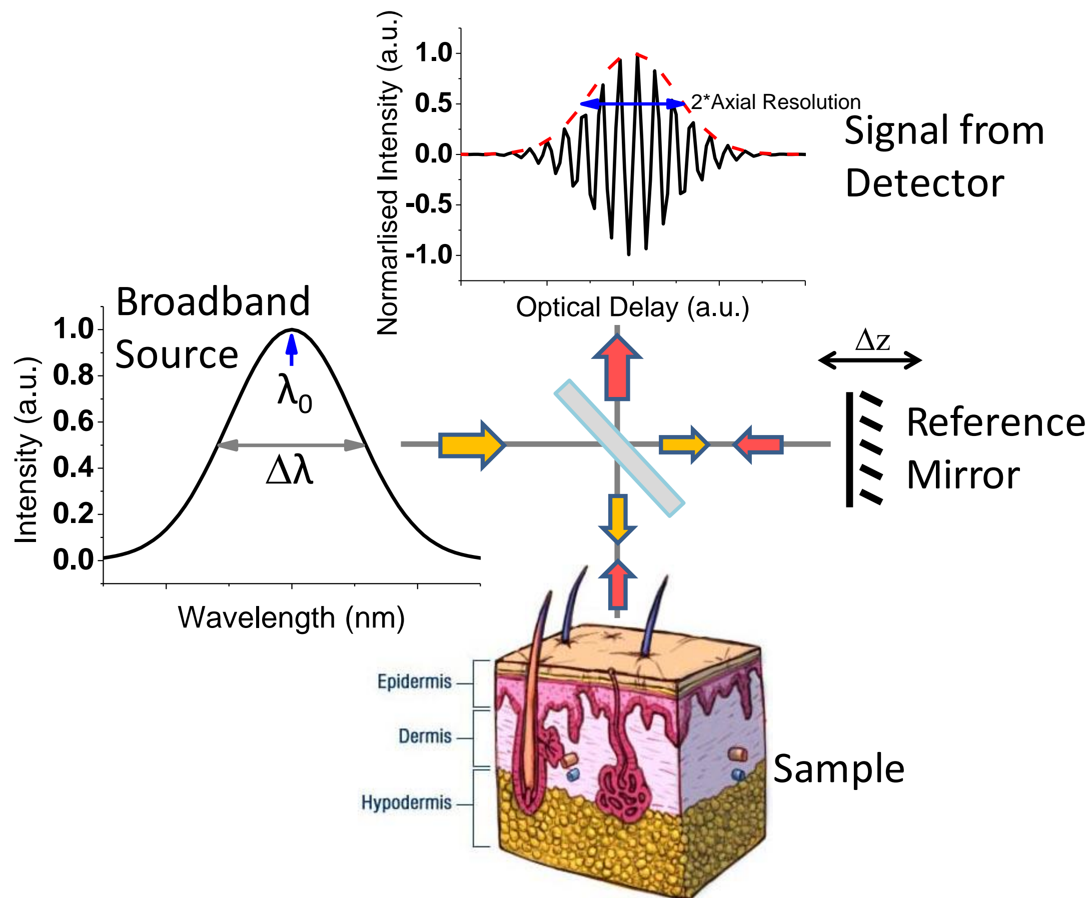

Figure 1.6. A schematic diagram of time-domain OCT system.

Low coherence light is emitted from the broadband light source, it is then split by the beam splitter and sent to the sample and the reference mirror separately. The two reflected light signals then interfere with each other forming an interference pattern which is measured by a detector. In the TD-OCT systems, the A-scan is achieved by scanning the reference arm, which is a one-dimensional amplitude modulation scan. The A-scan gives one dimensional information about the sample of interest. Compared to an A-scan,

the B-scan (cross-sectional tomography) is a two-dimensional view of the sample, it is achieved by laterally combining a series of A-scans.

In the SS-OCT system, instead of scanning the reference mirror, the light source is swept through a range of frequencies. Figure 1.7 shows the schematic diagram of a SS-OCT system.

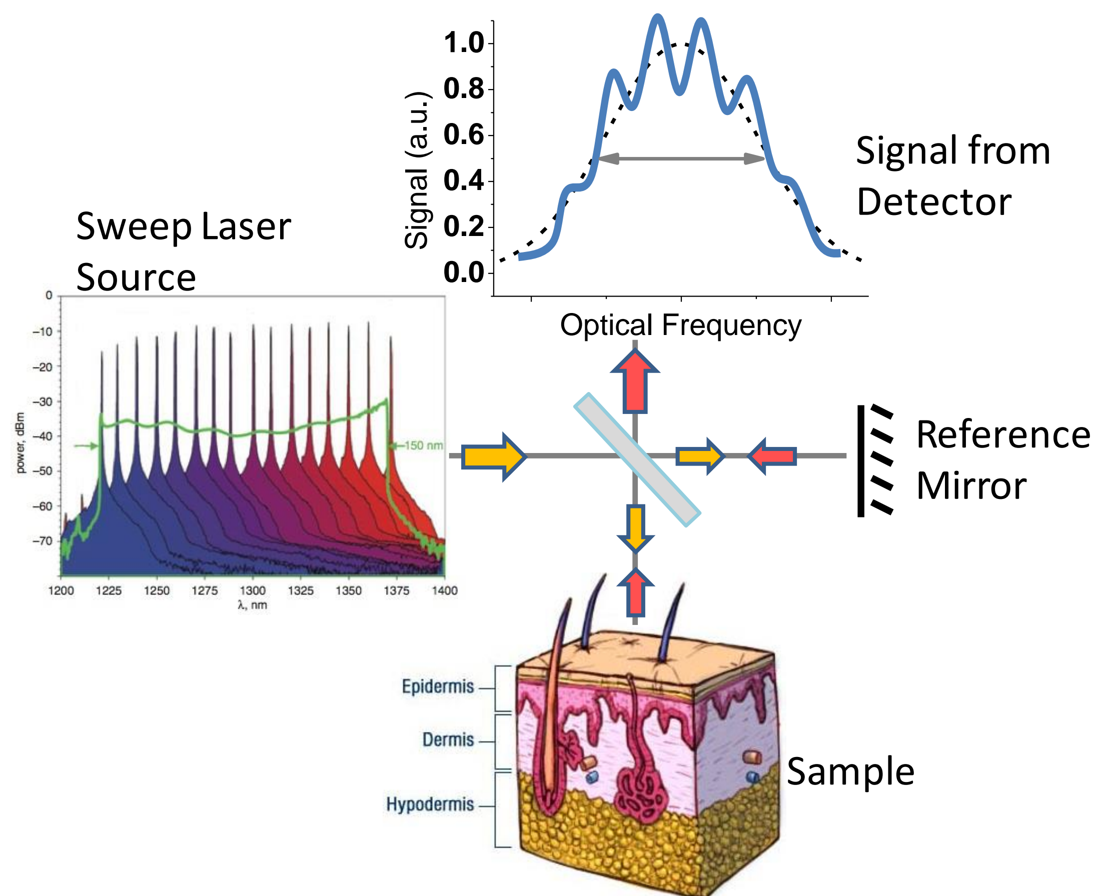

Figure 1.7. A schematic diagram of a SS-OCT (it belongs to the Fourier domain OCT) system.

In this system, a swept laser light source is used instead of the broadband source used in the TD-OCT system. It encodes the spatial information in frequency rather than time and it also have higher sensitivity than the TD-OCT system [34].

Reference

1. D. Bimberg, M. Grundmann, and N. N. Ledentsov, Quantum dot heterostructures (John Wiley Chichester, 1999), Vol. 471973882.
2. S. Chen, "Hybrid Quantum Well/Quantum Dot Structure for Broad Spectral Bandwidth Emitters," (Sheffield University, Sheffield, 2013).
3. Z. Y. Zhang, R. A. Hogg, X. Q. Lv, and Z. G. Wang, "Self-assembled quantum-dot superluminescent light-emitting diodes," Adv. Opt. Photon. 2, 201-228 (2010).
4. X. Huang, A. Stintz, C. P. Hains, G. T. Liu, J. Cheng, and K. J. Malloy, "Very low threshold current density room temperature continuous-wave lasing from a single-layer InAs quantum-dot laser," IEEE Photon. Technol. Lett. 12, 227-229 (2000).
5. O. B. Shchekin and D. G. Deppe, "1.3μm InAs quantum dot laser with To=161 K from 0 to 80 degrees C," Appl. Phys. Lett. 80, 3277-3279 (2002).
6. O. B. Shchekin, J. Ahn, and D. G. Deppe, "High temperature performance of self-organised quantum dot laser with stacked p-doped active region," Electron. Lett. 38, 712-713 (2002).
7. R. Paschotta, Encyclopedia of Laser Physics and Technology (Wiley-VCH, Berlin, 2008), p. 844.
8. K. Naganuma, K. Mogi, and H. Yamada, "Group-delay measurement using the Fourier transform of an interferometric cross correlation generated by white light," Opt. Lett. 15, 393-395 (1990).
9. W. Burns, C. Chin-Lin, and R. Moeller, "Fiber-optic gyroscopes with broad-band sources," J. Lightwave Technol. 1, 98-105 (1983).
10. Y. Ebiko, S. Muto, D. Suzuki, S. Itoh, K. Shiramine, T. Haga, Y. Nakata, and N. Yokoyama, "Island Size Scaling in InAs/GaAs Self-Assembled Quantum Dots," Phys. Rev. Lett. 80, 2650-2653 (1998).
11. L. H. Li, M. Rossetti, A. Fiore, L. Occhi, and C. Velez, "Wide emission spectrum from superluminescent diodes with chirped quantum dot multilayers," Electron. Lett. 41, 41-43 (2005).
12. S. K. Ray, K. M. Groom, M. D. Beattie, H. Y. Liu, M. Hopkinson, and R.

A. Hogg, "Broad-band superluminescent light-emitting diodes incorporating quantum dots in compositionally modulated quantum wells," IEEE Photon. Technol. Lett. 18, 58-60 (2006).

13. S. M. Chen, K. J. Zhou, Z. Y. Zhang, J. R. Orchard, D. T. D. Childs, M. Hugues, O. Wada, and R. A. Hogg, "Hybrid quantum well/quantum dot structure for broad spectral bandwidth emitters," IEEE J. Sel. Topics Quantum Electron. 19, 1900209-1900209 (2013).
14. Z. Y. Zhang, Q. Jiang, M. Hopkinson, and R. A. Hogg, "Effects of intermixing on modulation p-doped quantum dot superluminescent light emitting diodes," Opt. Express 18, 7055-7063 (2010).
15. L. A. Coldren, S. W. Corzine, and M. L. Mashanovitch, Diode Lasers and Photonic Integrated Circuits (Wiley, 2012).
16. A. Dikshit, V. Vangapally, and J. Pikal, "Carrier lifetime in 1.3μm InAs quantum-dot lasers using small-signal modulation technique," Proc. SPIE 6017, 60170L (2005).
17. G. Ozgur, A. Demir, and D. G. Deppe, "Threshold Temperature Dependence of a Quantum-Dot Laser Diode With and Without p-Doping," IEEE J. Quantum Electron. 45, 1265-1272 (2009).
18. A. Y. Cho, "GaAs epitaxy by a molecular beam method: observations of surface structure on the (001) face," J. Appl. Phys. 42, 2074-2081 (1971).
19. V. M. Ustinov, Quantum Dot Lasers (Oxford University Press, 2003).
20. A. Y. Cho and J. R. Arthur, "Molecular beam epitaxy," Progress in Solid State Chemistry 10, Part 3, 157-191 (1975).
21. R. R. Alexander, D. Childs, H. Agarwal, K. M. Groom, H. Y. Liu, M. Hopkinson, R. A. Hogg, M. Ishida, T. Yamamoto, M. Sugawara, Y. Arakawa, T. J. Badcock, R. J. Royce, and D. J. Mowbray, "Systematic study of the effects of modulation p-doping on 1.3μm InAs/GaAs dot-in-well lasers," IEEE J. Quantum Electron. 43, 1129-1139 (2007).
22. M. Wasiak, R. P. Sarzala, T. Czyszanowski, P. Mackowiak, W. Nakwaski, and M. Bugajski, "(InGa)As/GaAs quantum-dot diode lasers for 1.3um optical fibre communication," in Transparent Optical Networks, 2002. Proceedings of the 2002 4th International Conference on, 2002), 144-147 vol.141.

23. F. I. Lai, T. H. Hsueh, Y. H. Chang, H. C. Kuo, S. C. Wang, L. H. Laih, C. P. Song, and H. P. Yang, "10 Gb/s single-mode vertical-cavity surface-emitting laser with large aperture and oxygen implantation," Semiconduct. Sci. Technol. 19, L86-L89 (2004).
24. N. Yokouchi and A. Kasukawa, "High-performance 1.3µm GaInAsP/InP tensile-strained quantum well lasers," in 1997), 378-381.
25. S. Today, "QD Laser commercializes 10Gb/s 1310nm quantum dot laser for telecoms" (2009), retrieved 02 April, 2009, http://www.semiconductor-today.com/news_items/2009/APRIL/QDLASER_020409.htm.
26. Y. Arakawa and H. Sakaki, "Multidimensional quantum well laser and temperature-dependence of its threshold current," Appl. Phys. Lett. 40, 939-941 (1982).
27. K. Otsubo, N. Hatori, M. Ishida, S. Okumura, T. Akiyama, Y. Nakata, H. Ebe, M. Sugawara, and Y. Arakawa, "Temperature-insensitive eye-opening under 10-Gb/s modulation of 1.3µm p-doped quantum-dot lasers without current adjustments," Jpn. J. Appl. Phys. 43, L1124-L1126 (2004).
28. S. Fathpour, Z. Mi, P. Bhattacharya, A. R. Kovsh, S. S. Mikhrin, I. L. Krestnikov, A. V. Kozhukhov, and N. N. Ledentsov, "The role of Auger recombination in the temperature-dependent output characteristics ($T_0=\infty$) of p-doped 1.3µm quantum dot lasers," Appl. Phys. Lett. 85, 5164 (2004).
29. J. G. Fujimoto, C. Pitris, S. A. Boppart, and M. E. Brezinski, "Optical coherence tomography: an emerging technology for biomedical imaging and optical biopsy," Neoplasia 2, 9-25 (2000).
30. W. Drexler, U. Morgner, F. X. Kartner, C. Pitris, S. A. Boppart, X. D. Li, E. P. Ippen, and J. G. Fujimoto, "In vivo ultrahigh-resolution optical coherence tomography," Opt. Lett. 24, 1221-1223 (1999).
31. W. Drexler, "Ultrahigh-resolution optical coherence tomography," J. Biol. Opt. 9, 47-74 (2004).
32. P. D. L. Greenwood, D. T. D. Childs, K. Kennedy, K. M. Groom, M. Hugues, M. Hopkinson, R. A. Hogg, N. Krstajic, L. E. Smith, S. J.

Matcher, M. Bonesi, S. MacNeil, and R. Smallwood, "Quantum Dot Superluminescent Diodes for Optical Coherence Tomography: Device Engineering," IEEE J. Sel. Topics Quantum Electron. 16, 1015-1022 (2010).

33. Krstajic, x, N., L. E. Smith, S. J. Matcher, D. T. D. Childs, M. Bonesi, P. D. L. Greenwood, M. Hugues, K. Kennedy, M. Hopkinson, K. M. Groom, S. Macneil, R. A. Hogg, and R. Smallwood, "Quantum Dot Superluminescent Diodes for Optical Coherence Tomography: Skin Imaging," IEEE J. Sel. Topics Quantum Electron. 16, 748-754 (2010).

34. M. A. Choma, M. V. Sarunic, C. H. Yang, and J. A. Izatt, "Sensitivity advantage of swept source and Fourier domain optical coherence tomography," Opt. Express 11, 2183-2189 (2003).

2. Device Fabrication & Experimental Techniques

In this chapter, device fabrication processes are described for all the devices manufactured and measured as part of my thesis. Experimental methods are then discussed.

2.1. Device Fabrication

2.1.1. Mesa Diode Device Fabrication

The mesa diode is very basic semiconductor device, which can be used for several measurements such as PL, EL, and PC. Figure 2.1 shows a pictorial representation of the epitaxial structure of the wafer, the QD active region can be seen in the middle. The epitaxial growth of a wafer is carried out by MBE. In this schematic, there are 3 QD layers sandwiched by the p-type AlGaAs and n-type AlGaAs to form the p-i-n junction.

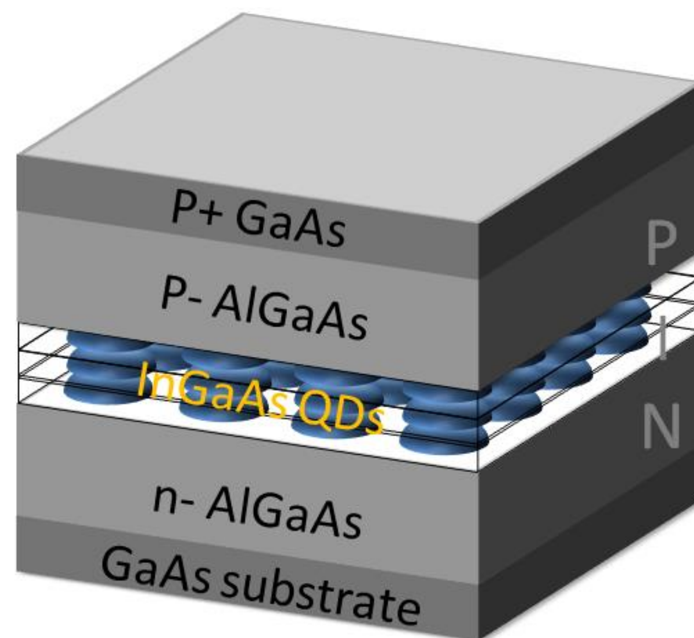

Figure 2.1 Epitaxial structure of the wafer grown by MBE.

The beginning of the fabrication process is to cleave ~¼ out of the wafer using a diamond tipped hand-scribe tool. This is followed by an inspection of the sample under the microscope to check the growth defect density and the sample surface condition. The next step is to clean the wafer with a three stage clean process. The first stage is to put the sample in warm n-butyl acetate (placed on a 300°C hotplate), then to remove it and use an n-butyl acetate dipped cotton bud to wipe the surface of the wafer in order to remove any big particles on the sample surface. This process can be repeated several times until there is no obvious particle on the surface. The second stage is to place the sample into acetone, this is followed by isopropyl alcohol (IPA) and then blown dry the sample using a nitrogen gun. All subsequent 3-stage cleaning process did not including the cotton bud wipe step. This 3-stage process can be repeated until the sample is clean, determined by looking at the sample under the microscope by the operator.

Once the surface is cleaned, the sample is then placed onto a 100°C hotplate for 1 minute as a dehydration bake, this is to remove any of the cleaning solvents remained on the sample. The sample is then placed on a small piece of blue tacky paper in order to protect the backside of the sample, and then put it onto the vacuum chuck of a spinner. On top of the sample, a photoresist named BPRS100 is deposited and spun at 4000 rpm for 30 seconds. It is then followed by a 1 minute hotplate bake in order to stiffen the surface of the photoresist, it is shown in Figure 2.2, and the pink thin layer is the photoresist layer.

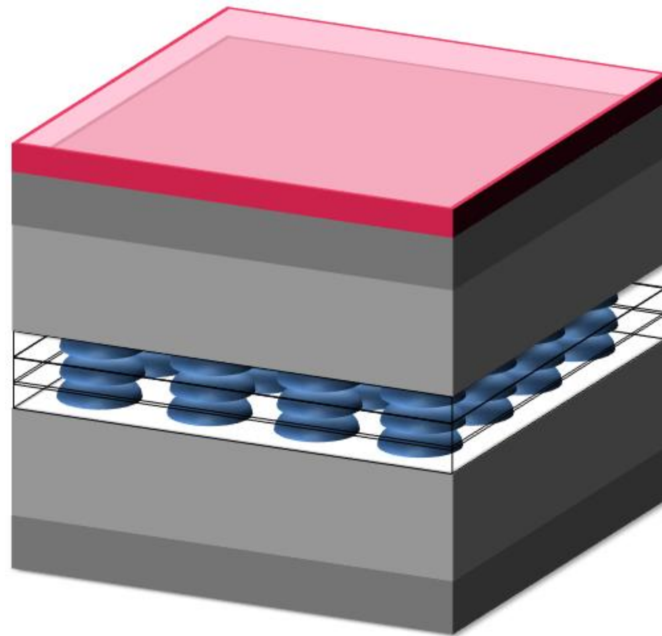

Figure 2.2. Cleaned the sample with a thin layer of photoresist on the top.

There is thickness non-uniformity in the resist across the sample, known as an edge bead, an area of ~1.5mm around the edge of the sample has to be removed before the mask alignment process. The edge bead procedure is done by masking the sample with a piece of scrap wafer and then exposing the sample for 30 seconds (much longer than the actual exposure time for that resist) using aligner “UV300”. The edge bead process is followed by a 1 minute development in 3:1 H_2O: PLSI, is then rinsed in DI water, followed by blow drying the sample.

Then, the sample is placed on the chuck of a mask aligner and positioned so that the pattern on the surface aligned with that of the metallisation pattern on the mask. The sample is then exposed and developed in 3:1 H_2O: PLSI for 1 minute to produce a pattern on the resist, and then rinsed in DI water followed by blow drying the sample. The pattern on the photoresist is plotted in Figure 2.3. The photolithography pattern is checked under the microscope and then

the sample is given a 1 minute oxygen plasma ash to make sure all the photoresist has been removed in the patterned area. Now the sample is ready for the top metallisation stage.

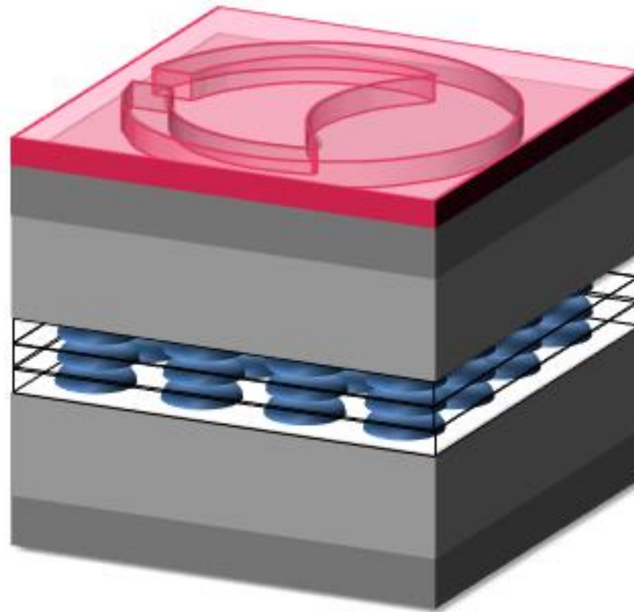

Figure 2.3 Wafer after patterning on the photoresist.

A thermal evaporator is used to deposit an Au/Zn/Au metallic contact onto the front side of the device. A tungsten coil/heating element and a tungsten coil/heating element basket are placed at a position of 6cm above the crystal thickness monitor in the thermal evaporator. A 2cm length of gold wire is folded and 3-stage cleaned, and then placed in the tungsten coil/heating element. The tungsten coil/heating element basket is filled with ~10mg of zinc wire. Before the sample is placed in the thermal evaporator, it is dipped in 19:1 H_2O: Analar Ammonia solution for 30 seconds in order to remove of the surface oxide, followed by a rinse in DI water and a blow dry. Next, the sample is placed into the evaporator underneath the coils, close to the crystal thickness monitor. The chamber of the evaporator is then sealed and pumped

down to a pressure of ~1.5x10^{-6}mbar, it takes usually ~2 hours. Once the aimed pressure has been reached, a thin layer of gold ~20nm is firstly deposited onto the sample surface, this layer helps promote adhesion of the zinc. During the deposition process, the thickness of each metal is measured using the crystal thickness monitor. Next, ~10nm of zinc is deposited on top of the thin gold layer. The final step is to deposit another ~200nm of gold layer on the top for electrical contact. Once the deposition process is done, ~10 minutes is given to the evaporator to cool down, followed by venting the chamber back to atmosphere, and then remove the sample and the coils. An example of the sample after gold deposition process is shown in Figure 2.4.

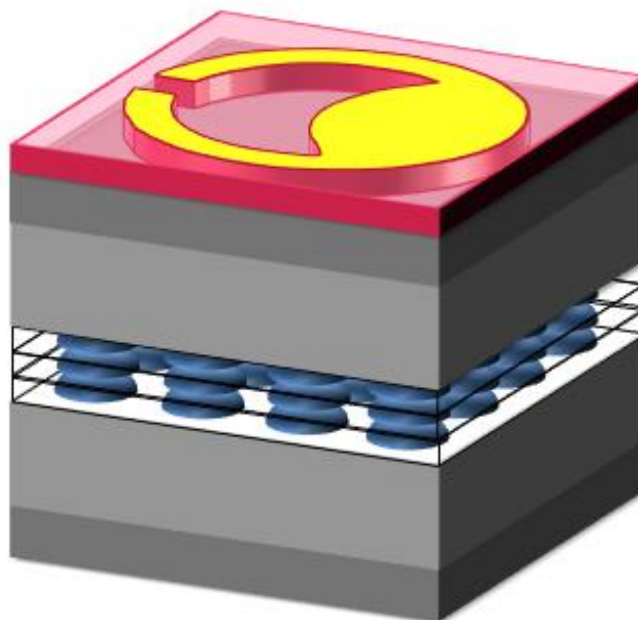

Figure 2.4 Device after metallisation process.

The sample is then placed in a beaker of acetone, in order to soften the photoresist and lift off the gold on top of the photoresist in the areas which is not required. The lift off process can be promoted by spraying additional acetone onto the sample surface from a squeezy bottle. The spraying process is repeated until all the unwanted gold has been removed, followed by a

microscope inspection. A 2 minutes O_2 plasma ash is given to the sample to remove any residual resist. When the sample is cleaned, it is then placed in the rapid thermal annealing (RTA) annealed at 360°C for 30 seconds ramp time and a 3 second dwell. This annealing process allows the formation of a low resistance electrical contact. The sample after annealing is shown in Figure 2.5.

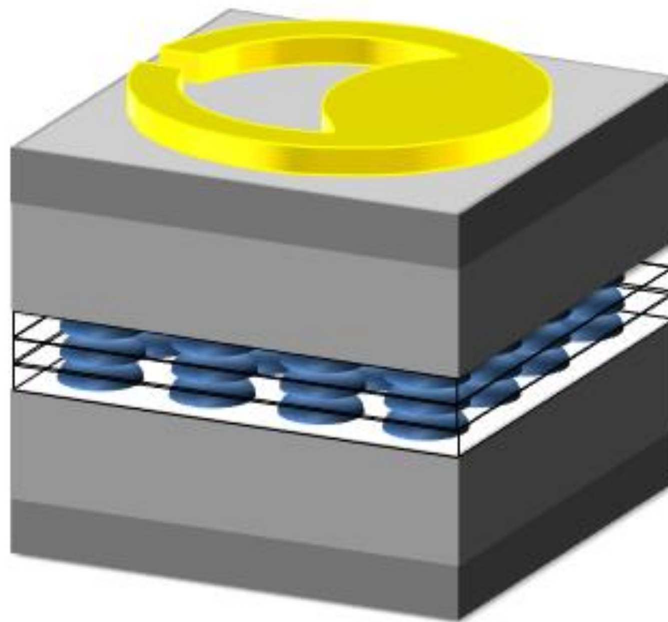

Figure 2.5 Sample after lift off and thermal annealing procedure.

Next, the sample is prepared for a wet etch step by spinning the SPR350 photoresist on top of the sample. It is then followed a 1 minute hotplate bake in order to stiffen the surface of the photoresist. An edge bead step is given to the sample following the bake process. Then, the sample is placed on the aligner and positioned it so that the pattern on the surface is aligned with that of the mesa etch pattern on the mask, and then exposed. This is followed by development in MF26A for 1 minute to produce the pattern in the resist, before being rinsed in DI water and blown dry, as shown in Figure 2.6.

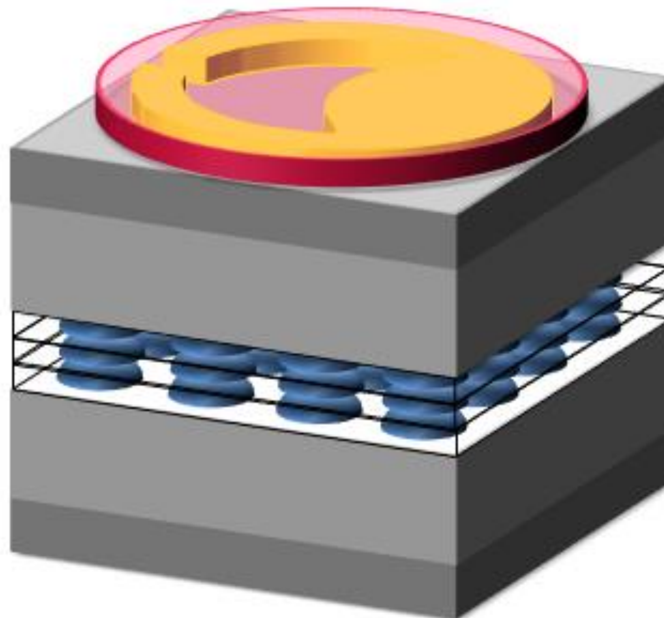

Figure 2.6 Photolithograph on the sample for mesa etch by 1:1:1 wet etch.

A 1:1:1 mixture of acetic acid, hydrobromic acid and potassium dichromate is used to wet etch the device through the active region, to a depth of ~5μm, shown in Figure 2.7.

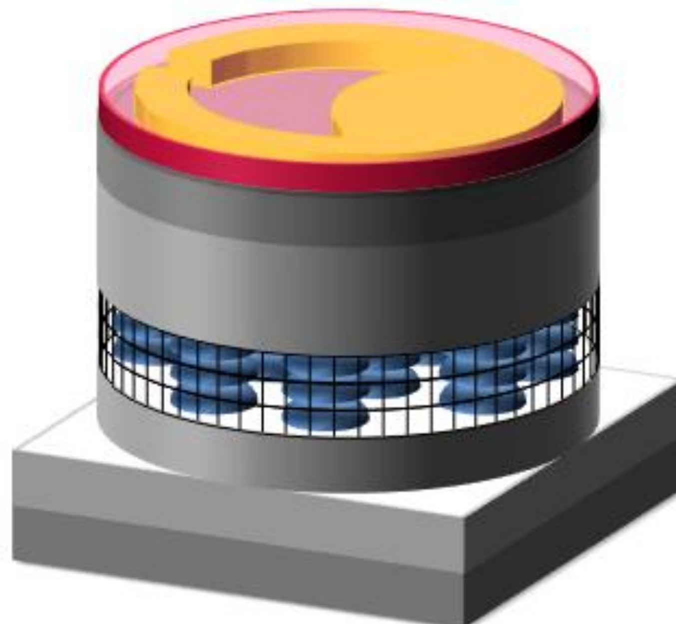

Figure 2.7 Device after mesa wet etch process.

After the wet etching process, the device is rinsed in DI water and blown dry.

Then, a beaker of acetone is used to remove the photoresist on top of the gold. When the photoresist has been removed, as shown in Figure 2.8, a 1 minute 30 seconds O_2 plasma ash is given to the sample to clean any residual photoresist.

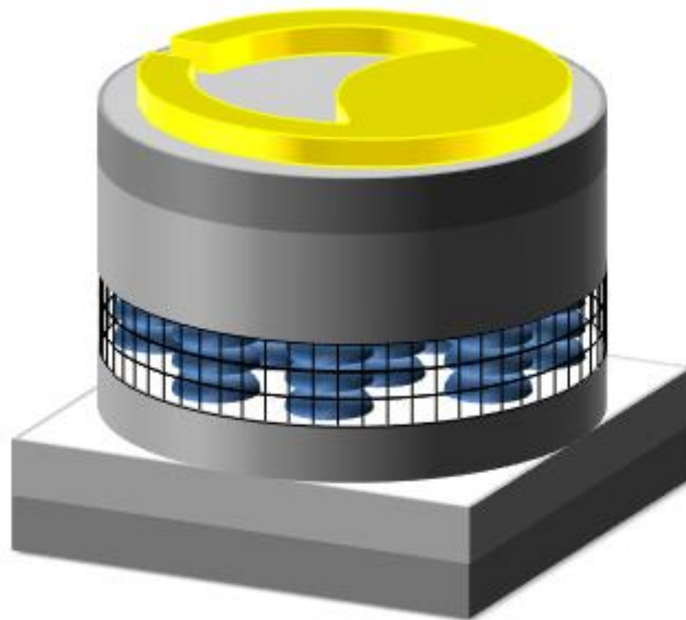

Figure 2.8 Device after lift off process.

The sample is now ready for the finally step, deposition of backside metal contact. This is In/Ge/Au and is carried out using a thermal evaporator. The evaporator is set up by placing a tungsten coil/heating element and a tungsten coil/heating element basket at 6cm from the stage of the chamber. The tungsten coil/heating element basket is filled with a small piece (~10mg) of indium and a ball (~10mg) of germanium. The tungsten coil/heating element is filled with two 2cm length of folded gold wires. Before the evaporation process, the sample is rinsed in 19:1 Analar Ammonia solution for 30 seconds to remove the surface oxide. It is followed by a rinse in DI water and blown dry. Then sample is placed in the thermal evaporator, which then pumped down to a pressure of ~$1.5x10^{-6}$mbar. When the pressure is reached, 20nm of

indium/germanium alloy is firstly deposited onto the surface, this is followed by a 400nm gold deposition. Once the deposition process is completed, the sample is annealed in the RTA at 340°C for 30 seconds. This produced a low resistance n-type contact on the backside of the sample, depicted in Figure 2.9.

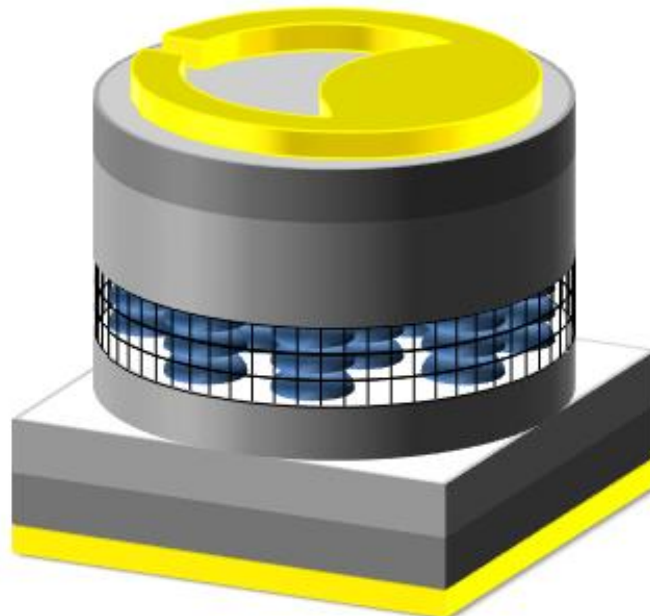

Figure 2.9 Metallisation on backside of the device.

Now the mesa diode device is done, ready for the characterization.

2.1.2. Multi-section Device Fabrication

Multi-section device is the complex device, which can be used to measure the EL, gain by Hakki-Paoli method and multi-section method. Figure 2.10 shows a pictorial representation of the epitaxial structure of the wafer, the active region normally including QW (QD) layers.

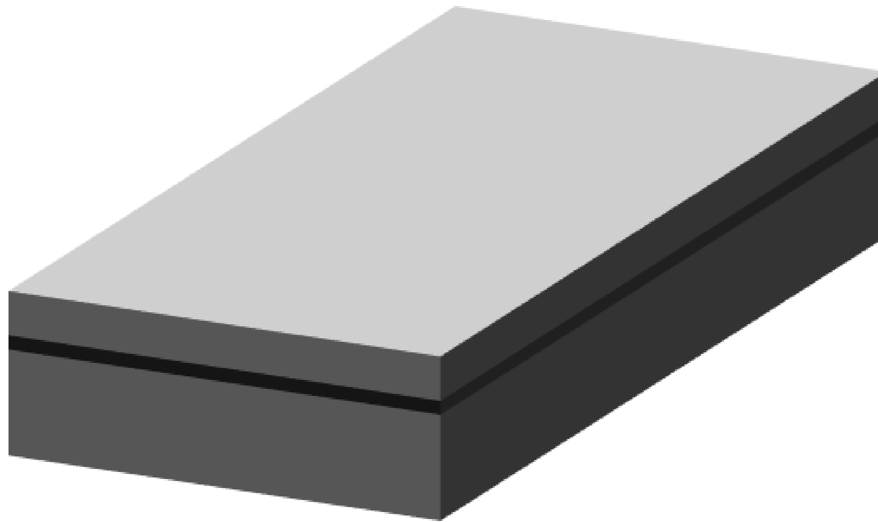

Figure 2.10 Epitaxial structure of the wafer grown by MBE.

The first step is to cleave ~¼ out of the wafer using a diamond tipped hand-scribe tool. This is followed by an inspection of the sample under the microscope to check the growth defect density and the dirt area. Then a three stage cleaning is given to the sample which is described in details in section 2.1.1, paragraph two.

Once the surface is cleaned, the sample is then placed onto a 100°C hotplate for 1 minute in order to remove any of the cleaning solvents remained on the sample. The BPRS100 photoresist is then spun onto the sample surface followed by a 1 minute hotplate bake in order to stiffen the photoresist. It is shown in Figure 2.11, and the pink thin layer is the photoresist layer.

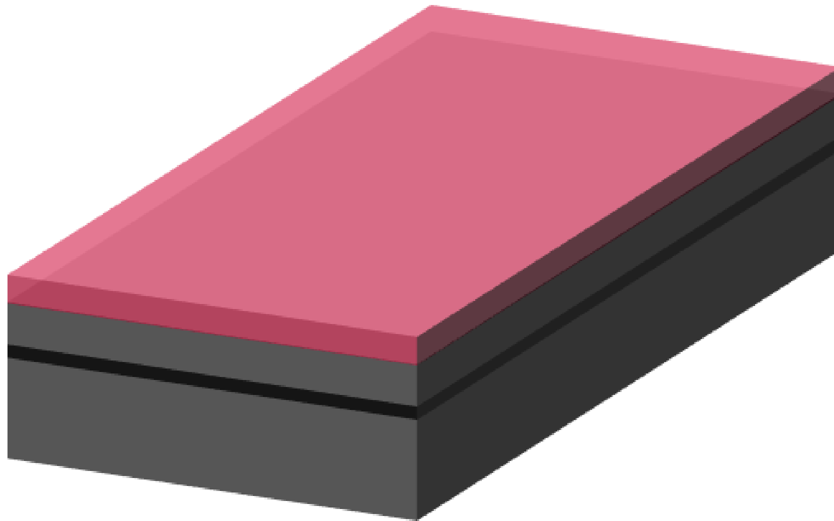

Figure 2.11 Cleaned the sample with a thin layer of photoresist on the top.

Because of the non-uniformity of the photoresist across the sample mentioned in section 2.1, an edge bead removal process is carried out before mask aligning. Then, the sample is placed on the chuck of a mask aligner and positioned so that the pattern on the surface is aligned with that of the 3μm ridge pattern on the mask. After exposing, the sample is then developed in 3:1 H_2O: PLSI for 1 minute to form a 3μm straight ridge structure in the photoresist. It is then rinsed in DI water followed by blow drying the sample. The sample after exposure is shown in Figure 2.12.

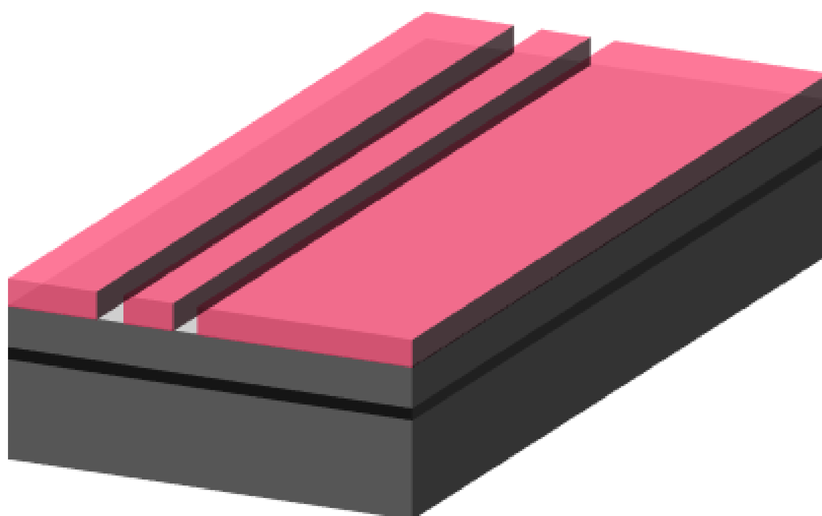

Figure 2.12 Sample after exposing, in order to form the laser ridge.

Before dry etching of the sample, it is given a 1 minute oxygen plasma ash to remove any of the residual photoresist. In the meantime the inductively coupled plasma (ICP) is set up by running the etch recipe for 30 minutes with no sample in the chamber to condition the chamber for the etch process. A test sample is used to determine the etch rate before the actual sample is used. This is an important process which helps us to control the etch rate accurately when we deal with the actual sample.

To etch the test sample, it is loaded into the ICP chamber with the end point laser focused on an exposed semiconductor area. The etch recipe used in this case is 5sccm $SiCl_4$ combined with 2sccm Ar, a chamber pressure of 2mT, a RF power of 150W and an ICP coil power of 250W. The test sample is etched for 10 minutes, then by using Dektak surface profiler to measure the relative heights of features before and after etching. The etch rate can be defined by the change in the relative height of the semiconductor area on the sample divided by the etch time. Since the trench width (3μm) is too narrow to be directly probed, the alignment key area is measured to determine the etch rate.

When the etch rate is determined, the actual sample is loaded into the chamber in the same way as for the test sample. It is required that the sample to be etched through the active region, ~3μm in this case. The typical etch rate of the recipe for semiconductor is ~600nm/min, giving an etch duration time of ~5 minutes. Once the etching is completed, the sample is removed and measured the depth using the Dektak. It is also checked under the microscope to ensure the etch process has proceeded as expected. Then the

photoresist stripper is used to remove the photoresist on the sample surface. The device structure after trenches etch is shown in Figure 2.13.

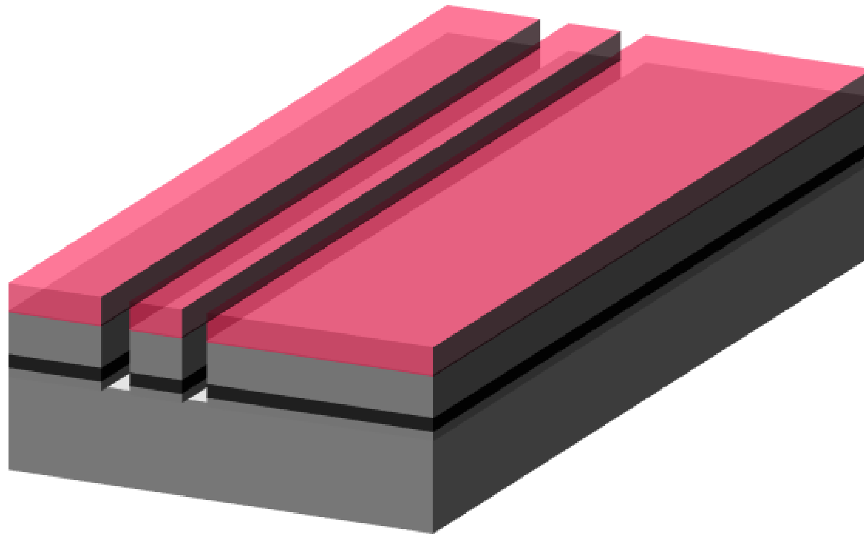

Figure 2.13 The device structure after trenches etch.

The next step is to deposit 500nm of Si_3N_4 on top of the sample to form an insulating dielectric layer. The sample is placed in the plasma-enhanced chemical vapor deposition (PECVD) and 500nm of silicon nitride is deposited on the surface of the sample, which is illustrated by the light blue layer in Figure 2.14.

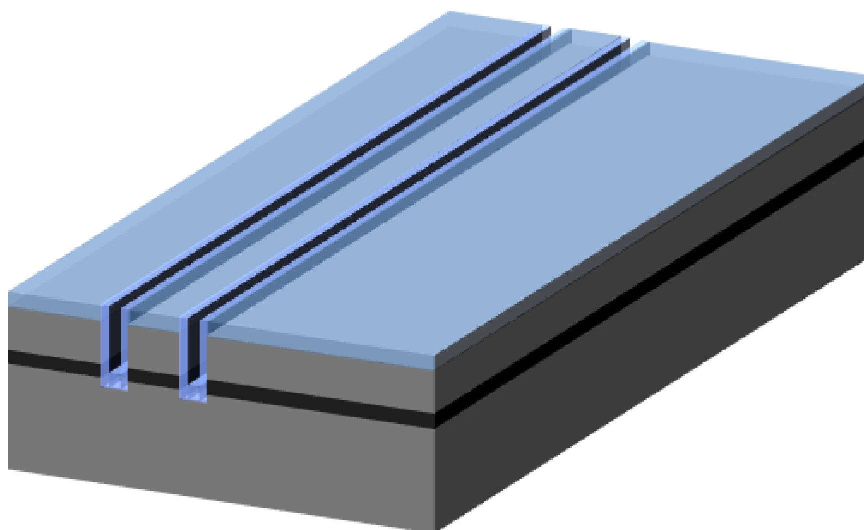

Figure 2.14 Deposition of the dielectric layer on the surface of the sample.

The sample is inspected under the microscope after the deposition process,

to check the quality of the dielectric layer and ensure there are no fragments embedded in the layer caused by “drop off” from the chamber.

The next step is to open a window on top of the ridge for the metallisation process. The sample is placed onto a 100°C hotplate for 1 minute as a dehydration bake, in order to remove any residual solvents. On top of the sample, SPR350 photoresist is deposited and spun at 4000 rpm for 30 seconds. It is then followed a 1 minute hotplate bake in order to stiffen the surface of the photoresist. Then the sample is placed on a chuck of a mask aligner and exposed under the “open window” mask. After exposing, the sample is then developed in MF26A for 1minute, followed by rinsing in DI water and drying the sample. This sample is loaded into the ICP chamber (the pre-run process is completed), with the point end laser interferometer spot focused on the edge bead area (the open window area is too narrow to be focused). The etch recipe is set up of 20sccm of CHF_3 combined with 20sccm of Ar, a RF power of 200W and chamber pressure of 35mTorr. During the etch process, the dielectric layer on the sample surface is traced by the End Point system which would go flat when there is no layer thickness change (all the Si_3N_4 is etched out in the open window area). For 500nm of silicon nitride layer, the etch time is ~40 minutes.

Then the sample is removed from the chamber and inspected under the microscope to ensure all the dielectric material has been etched out in the unmasked areas. If there is still some residual dielectric material remaining in the unmasked area, the sample would be placed back in the ICP and etched

further until all the unwanted dielectric has been removed.

When the window on the ridge is fully opened, the sample is placed in photoresist stripper solvent on a 100°C hotplate for 2 minutes, rinsed in water, then IPA, and blown dry. This is followed by a 1 minute of O_2 plasma ash to remove any residual photoresist, the structure is plotted in Figure 2.15.

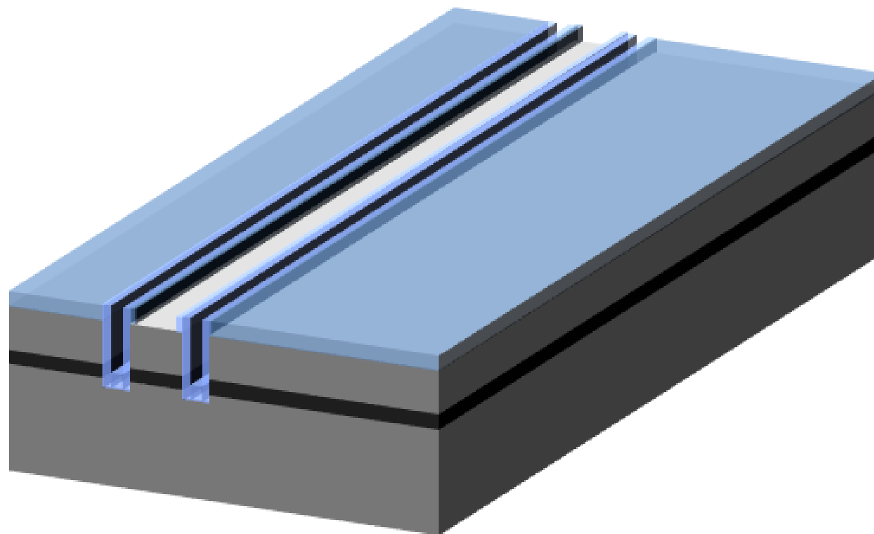

Figure 2.15 Open window process is done on top of the laser ridge.

The next step is metallisation photolithography. The BPRS100 photoresist is spun on top of the sample, and then placed in mask aligner to expose under the mask “metallisation”. The wafer is developed in 3:1 H_2O: PLSI for 1 minute and rinsed in DI water followed by blow drying the sample.

Before metal deposition, the sample is dipped in 19:1 H_2O: Analar Ammonia solution for 30 seconds in order to remove of the surface oxide, followed by a rinse in DI water and a blow dry. Now the sample is ready for Au/Zn/Au metal deposition, followed by a 360°C annealing process to make the metal secure, the deposition and annealing processes are described in detail in section

2.1.1, after metallisation the sample status is shown in Figure 2.16.

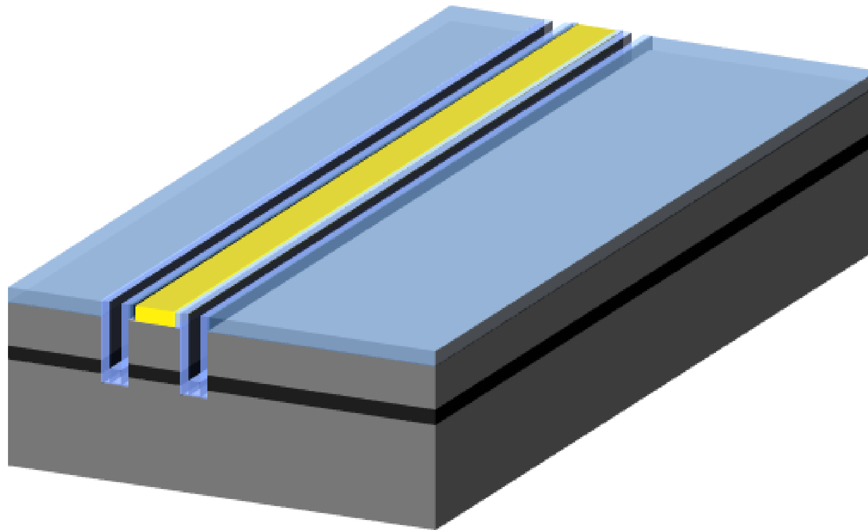

Figure 2.16 Metal deposition is done on top of the ridge structure.

The next step is to use a reactive ion etcher (RIE) to etch out the dielectric layer in the n-contact area first, and then to etch a 4μm depth square area in semiconductor material for the top n-contact window. As the ridge surface is covered in gold, the process could not be done in ICP because of the chamber contamination by gold. Here, photoresist BPRS220 is spun on the sample surface, followed by the exposure under the mask of “N-contact”. Then the sample is rinsed in DI water and blown dry.

As mentioned previously, a conditioning run with no sample in the RIE chamber is carried out for 30 minutes. The etch recipe includes 35sccm of CHF_3 and 5sccm of O_2 with a chamber pressure of 35mTorr and a RF coil power of 60W. When the actual sample is loaded into the RIE chamber, the End Point system is used to trace the etch process. After etching out the dielectric layer, the sample is inspected under the microscope to ensure all the unmasked area is free of Si_3N_4. Another conditioning run for

semiconductor etch is done for 30 minutes with the recipe consists of 35sccm CHF_3 and 5sccm O_2 with a chamber pressure of 35mTorr and a RF coil power of 100W. After conditioning run, the actual sample is etched by RIE to achieve a 4µm depth top n-contact. The depth of the etched area is measured by the Dektek system. The sample status is shown in Figure 2.17 after top n-contact etch.

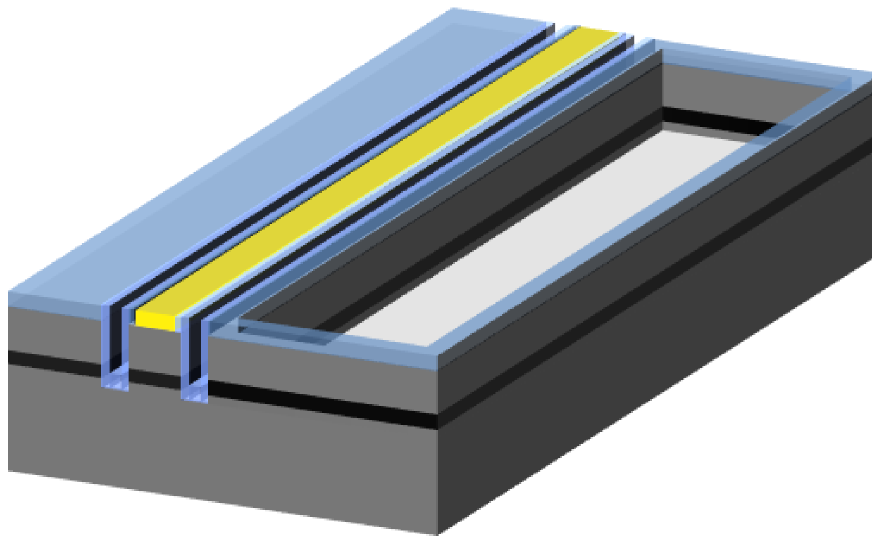

Figure 2.17 Dry etched top n-contact areas on the sample.

Now the sample is ready for the bond pad metallisation photolithography. Photoresist BPRS100 is used and the sample is exposed under the mask “bond pads”. When the bond pad pattern is ready after inspecting under the microscope, the sample is given a 30 seconds rinse in 19:1 H_2O: Analar Ammonia solution before put into the thermal evaporator chamber. Once the pressure is ready in the chamber, 20nm of titanium is deposited on the sample, followed by 200nm of gold. Then the sample is given a lift off process to remove the photoresist, after lift off the structure is shown in Figure 2.18.

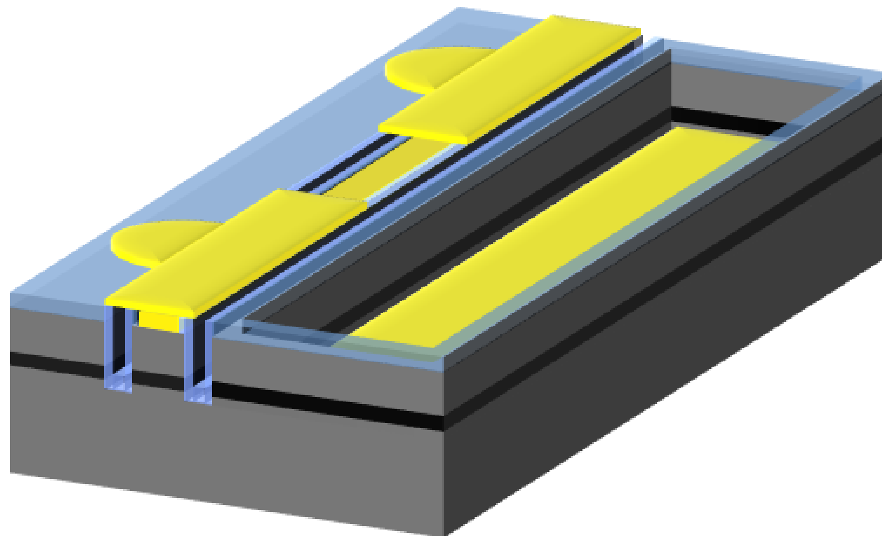

Figure 2.18 Bond pads metallization process on the sample.

There are several advantages when the sample is electroplated: one is to achieve a good connection between probe pins and the bond pads when the bond pads on the sample are electroplated; another is this gold electroplating could provide a pure gold layer of a few microns, which helps the wire bonding of the devices. It also improves the extraction of heat in optoelectronic devices. The photoresist BPRS220 is spun onto the sample, then the sample is aligned and patterned with the mask “electroplate”. Then the sample is exposed and developed, followed by rinsing the sample in DI water and blown dry. Now the sample is ready for the electroplate process.

During the electroplate procedure, the first step was to fill up the beaker with 75ml of Aurofab BP RTU, followed by setting the sample on gold plated glass slide. The sample and the platinum mesh were rinsed with DI water then with IPA and blown dry. The gold plated glass was then tight into the beaker; a lid was used to hold it in place. Then place the beaker onto the hotplate set at 70°C, which corresponded to 40°C in the solution. A magnetic stirrer in the

beaker was set to 200rpm to achieve the temperature uniformity in the solution. The thermometer was placed in the solution to trace the temperature before electroplating. Once the solution reaches 40°C, the thermometer was then removed. Put the lid on the beaker with the sample and the platinum mesh, and make sure the lid was fitted securely to minimize evaporation of the solution. The electrodes were connected with galvanometer, and the current source was preset to 30 minutes of galvanostat mode with 2mA of current. These settings gave us approximately 1.5μm of gold plated above the bond pads. After 30 minutes the setup was stopped by itself, then removed the sample from the solution and rinsed with DI water and blown dry. Sample after electroplate procedure is shown in Figure 2.19 (a) and the experimental apparatus of electroplating is shown in Figure 2.19 (b).

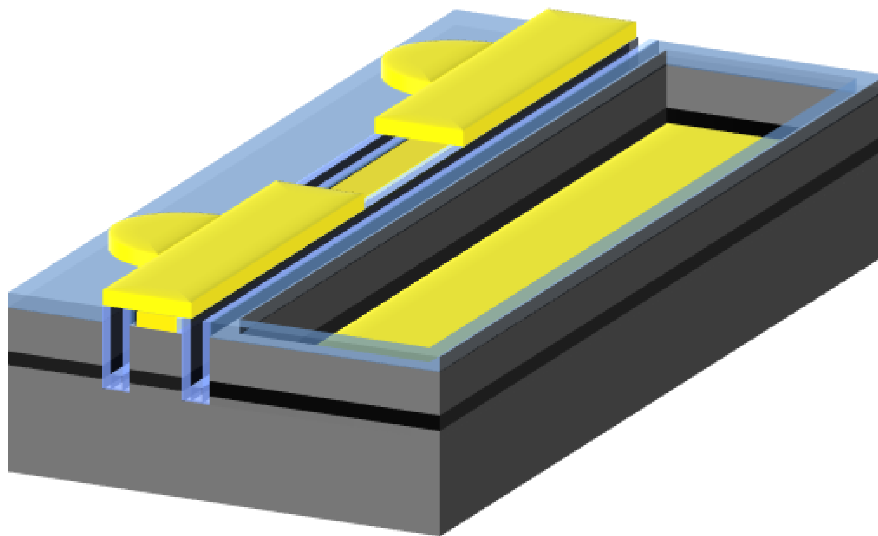

Figure 2.19 (a) Electroplate of the bond pad on the sample.

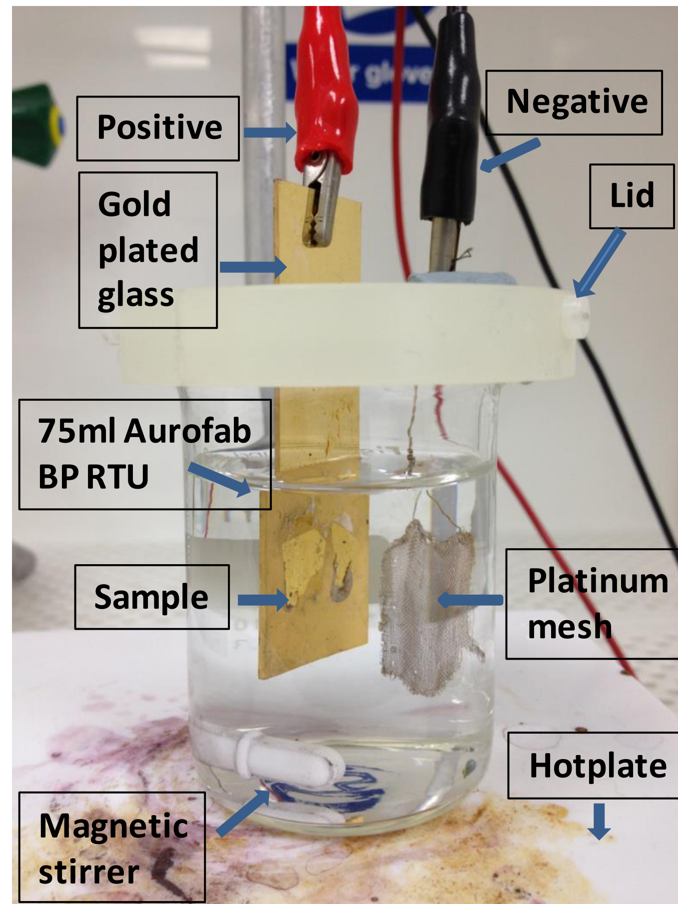

Figure 2.19 (b) Experimental setup of the electroplating.

For multi-section devices, all the sections should be electrical isolated from each other, so gold on the laser ridge between bond pads needs to be etched out by using KI/I_2 solvent. BPRS220 is used and then the sample is exposed under the “multi-section etch” mask and developed for 1 minute, followed by rinsed in DI water and blown dry. The sample is then placed into the KI/I_2 liquid for 12 seconds to remove the gold between sections, followed by rinsed in DI water and blown dry. Next, the sample is placed into the 5:1 H_2O_2: Citric acid to selectively etch out the highly p-doped GaAs layer between sections on top of the ridge, followed by being rinsed in DI water and blown dry. After multi-section etch the structure is shown in Figure 2.20.

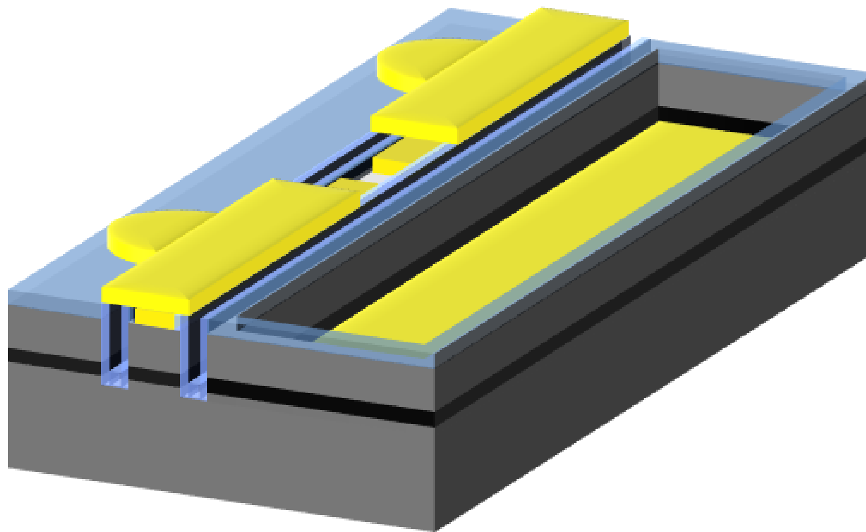

Figure 2.20 The multi-section etch on top of the ridge.

The next step is to thin the substrate in order to achieve a good thermal extraction. Easy for cleaving is another additional benefit of thinning the sample. Firstly, the sample is spun with BPRS220 photoresist and baked for 1 minute, to form a protective layer on top of the sample surface. A special wax is used to cover a circular glass block on the 100°C hotplate, and the wax is allowed to flow for 5 minutes to create a uniform layer. Then the sample is mounted upside down on the glass block and 3 small pieces of GaAs material of the same thickness are also mounted around the sample. The glass block is then removed from the hotplate and left to cool until the wax has set firm. The relative height of different positions is then measured across the sample with an allowable average deviation of 10µm. If the deviation is too large then the glass block has to be placed back on the hotplate to level out the samples again.

When level out is done the glass block is then placed in a vacuum jig of a Logitech LP50 lapper/polisher in the semi-clean room. The lapping wheel is

set to 20RPM, and the glass wheel is constantly being covered with a mixture lapping media of 1:9 3µm aluminium oxide particles: water. The jig, which contains a spring to vary the force on the glass block, is then placed onto the glass wheel, it is adjusted to give a lapping rate of 1~2µm/min. The jig is removed from the glass wheel when the substrate is thinned down to ~150µm. Then the glass block is removed from the jig and rinsed with DI water to remove any remaining GaAs slurry on the sample and then blown dry. To remove the sample from the glass block, it is placed in a beaker of warm n-butyl acetate to break down the wax, allowing the sample to be removed. The sample then is inspected under the microscope to check if there are any contaminants.

The sample is now ready for the InGe/Au backside metallisation. The metal is deposited by a thermal evaporator. The process is described in detail in the last paragraph of section 2.11. After deposition, the sample is annealed in RTA at 360°C, shown in Figure 2.21.

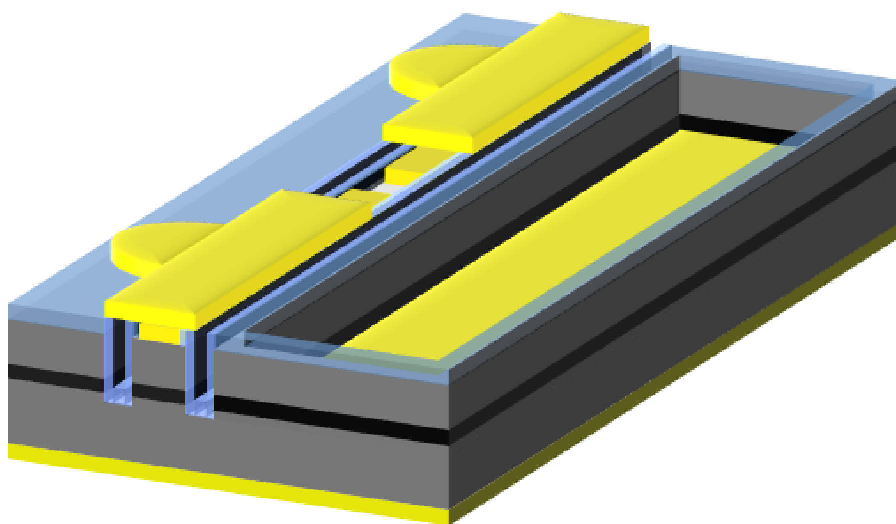

Figure 2.21 Sample after thinning and backside gold contact deposition.

Now, the multi-section device fabrication is done and the sample is ready for

testing. During the measurement, the top n-contact described in Figure 2.17&2.18 does not work as I expected. Its contact resistance is higher than the normal back n-contact described in Figure 2.21, this may due to the imperfect etching process or insufficient n-doping level in the layer underneath of the top n-contact layer [1]. Due to the high ohmic contact of the top n-contact, it is not utilised in the characterisation in the following chapters.

2.1.3. Tilted Ridge Emit Device Fabrication

The tilted device fabrication is very similar to the multi-section device, the only differences are: (1) instead of the 3μm straight ridge, it is the 5μm and 15μm 7 degree off to the normal ridge; (2) there is no isolation etch; (3) there is no top n contact. The completed tilted device is shown in Figure 2.22.

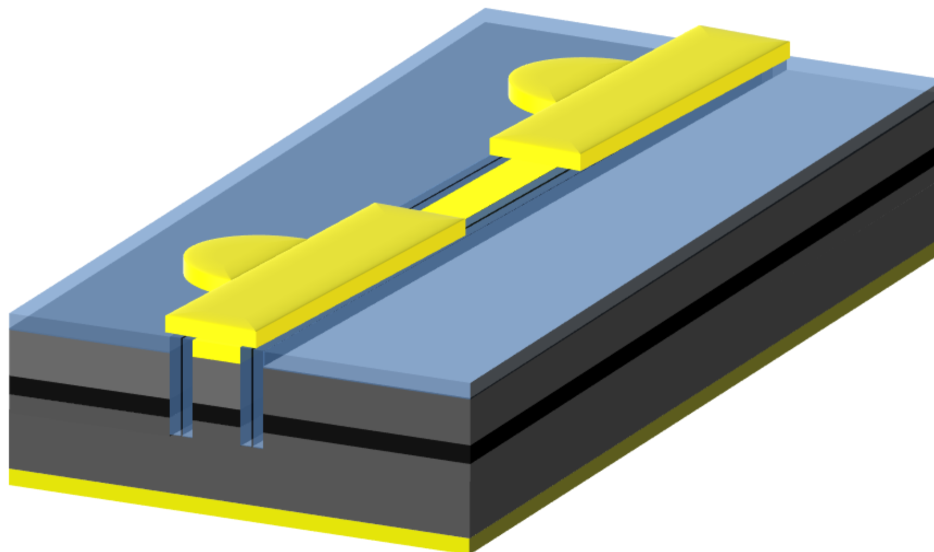

Figure 2.22 The tilted ridge emit device structure after fabrication process.

All the process sheets for the fabrication process discussed above are shown in the appendix.

2.2. Experimental Techniques

In this section, four experimental measurements, which are used in the

following chapters, are introduced and discussed.

2.2.1. Small signal modulation (SSM)

Small signal modulation is a useful technique, which when applied above threshold it gives an idea of the maximum modulation frequency which the real laser is capable to response, below threshold it allows us to derive the recombination coefficients. This thesis covers such measurement, and the result is discussed in chapter 3 and 4.

The schematic illustration of the experimental setup is shown in Figure 2.23

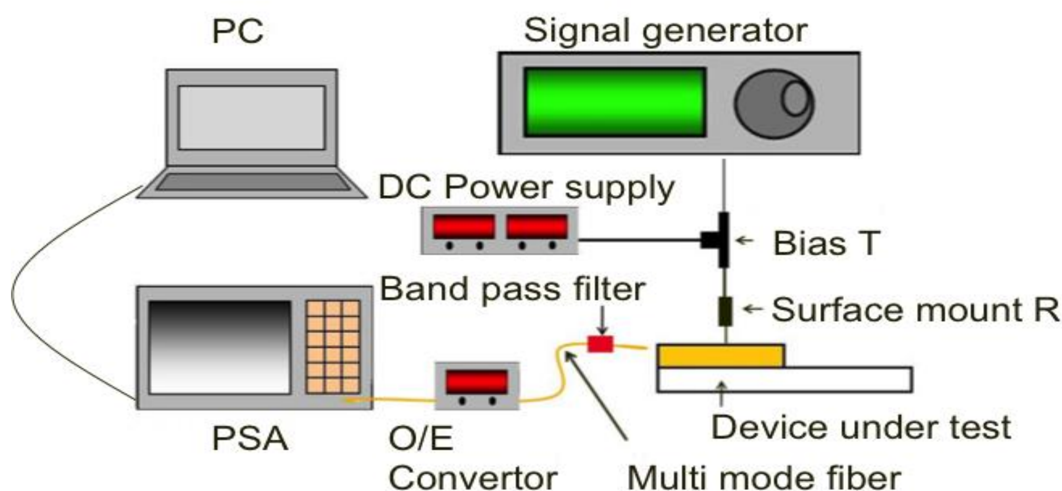

Figure 2.23 Circuit diagram of the experimental system.

A surface mount resistor is mounted as close to the laser device as possible, in order to optimize the impedance match between source and load. A bias T allowed the combination of AC and DC to allow the differential carrier lifetime to be deduced at various current densities. The RF signal generator allowed the laser device to be modulated between 10MHz and 20GHz although practically, modulation frequencies are typically < 2GHz. Emission is collected from the laser facet using a multi-mode fibre. This is then passed through an

optical band-pass filter (coupling efficiency 85% without filter), and is subsequently fed into an O/E (optical to electrical) converter (Agilent 11982A). The electrical signal is finally measured by a power spectrum analyzer (PSA). The modulation current used here is much smaller than the DC current to avoid parasitic capacitance and resistance.

A thermo-electric cooler (TEC) beneath the ceramic tile is used to vary the temperature, with LabView used to capture the frequency response from the PSA. Based on the theory mentioned in [2], there is no need to fit the raw optical response curves; the only parameter needed is the -3dB frequency measured from the experimental data. In this way the complexity of the problem is reduced and the data analysis is simplified. Error bars are determined by measuring the difference between the experimental data and the average value, they are approximately 5% of the differential carrier lifetime value.

Figure 2.24 is a schematic plot of the IV characteristic of the laser diode. A small sinusoidal signal is used to modulate the DC current. By modulating the current, the spontaneous light intensity is modulated and the modulation response at each frequency is measured by the PSA. The response over the whole frequency range is taken using LabView (the inset of Figure 2.24).

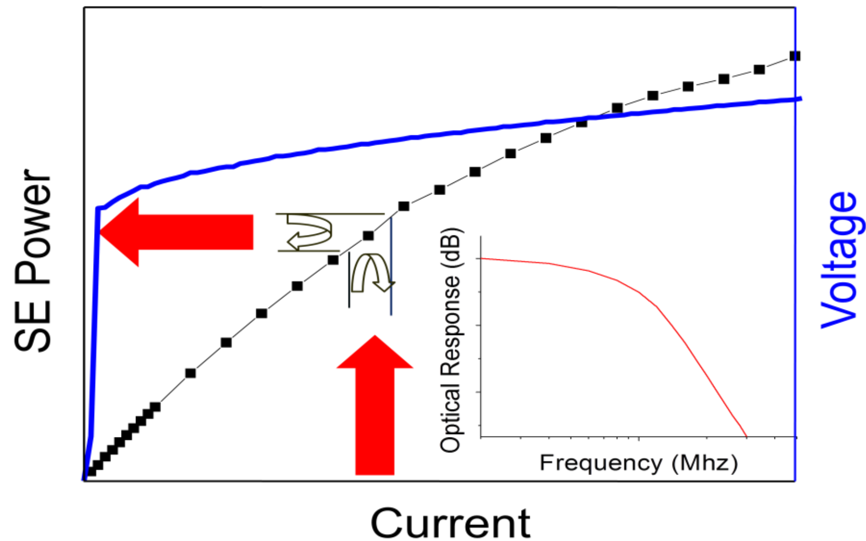

Figure 2.24 Modulate the spontaneous emission by modulating the DC current, the inset is the frequency response of the modulation signal.

Also it should be pointed out that the low current density data may not be ideal due to non-linearity of the diode, as can be seen in Figure 2.24, during the low current density region the impedance is varying non-trivially. An impedance correction method is used to solve this problem [3] [4]. Based on the simple equivalent circuit of the laser diode below threshold, a series resistance R_s (introduced by the contacts and cladding layers) and R_d (which is the static differential resistance of the p-n junction) are used to correct the data, along with the output impedance of the drive circuitry *r*. As shown in equation 2-(1):

$$\tau_{corrected} = \tau_{optical} \times (1 + \frac{R_d}{R_s + r}) \qquad \text{2-(1)}$$

Where the corrected lifetime $\tau_{corrected}$ is larger than the raw experimental value τ_{optical}. R_s can be obtained by extrapolating the above-threshold value of *dV/dI* to threshold and R_d can be achieved by measuring the sub-threshold value of

dV/dI(I) – R_s [5]. The differential carrier lifetime used in chapter 3 and 4 is this $\tau_{corrected}$.

2.2.2. Light-Current (L-I) measurement

The L-I curve gives the basic idea of the performance of a laser diode, it is the relationship between the inject current and the output power. Figure 2.26(a) shows the apparatus of the measurement and 2.26(b) shows an example of the L-I curve.

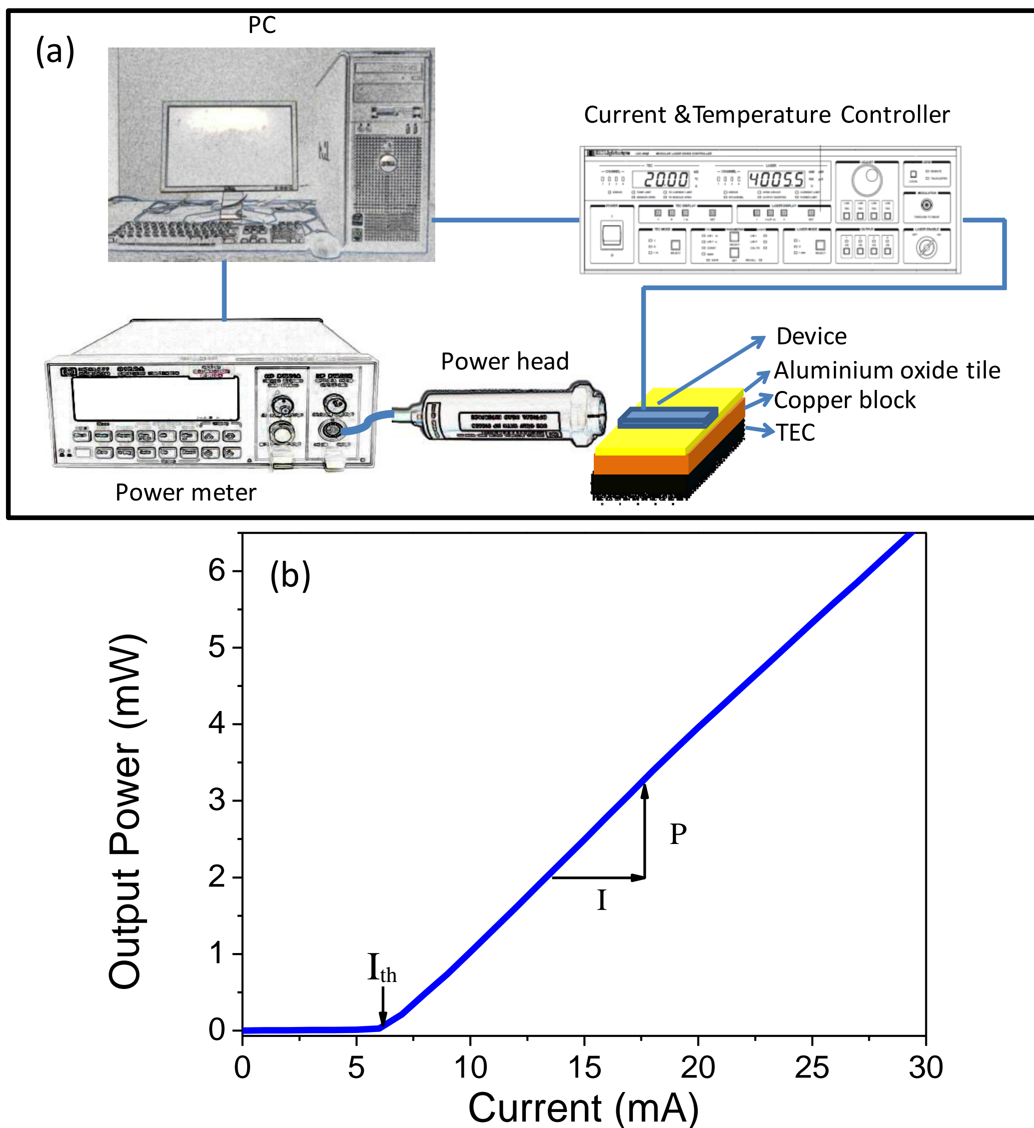

Figure 2.25 (a) Setup of the LI measurement, (b) output light vs. current curve for a 2mm cavity device. Threshold is marked ~6mA.

Normally, the laser device is placed on a copper block, and a TEC is placed underneath of the copper block in order to vary the device temperature. During the measurement, a power-head is moved to maximise the signal to the power meter. A LabView program is used to step the current and measure the output power at each step. Based on the L-I curve, several important parameters can be extracted, such as threshold current density J_{th} when the dimension of the device is known; the external efficiency η_d is calculated from equation 2-(2):

$$\eta_d = 2\frac{\Delta P}{\Delta I}\left[\frac{q\lambda}{hc}\right] \qquad \text{2-(2)}$$

Where $h = 6.6262\times10^{-34} J.\sec$, $q = 1.6022\times10^{-19} C$, $c = 2.99\times10^{8} m/\sec$, $\lambda = 1.3\times10^{-6} m$ in this case. $\Delta P/\Delta I$ is the gradient of the L-I curve.

Moreover, based on the temperature dependent L-I, T_0 is derived by measuring the threshold current density of a laser with increasing device temperatures. When T_0 is infinite it means the threshold current does not change with temperature. The definition of T_0 was shown in equation 1-(3), it is the change of the temperature over the change of the natural logarithm of the threshold current density.

2.2.3. Hakki-Paoli Gain Measurement

In a single-mode Fabry-Perot (F-P) laser device, the Hakki-Paoli technique can be utilised to determine the net model gain. In edge-emitting EL spectra, spectral modulation is caused by the round trip interference of the emitted light. The gain spectrum by using Hakki-Paoli method can be derived from the peak to valley ratio of the modulation. Figure 2.27 shows the experimental

setup of the Hakki-Paoli measurement. The device under test is a 3µm wide strip laser device with the length of 250µm. It is mounted on a ceramic tile and then put on top of a copper block to achieve good thermal contact. A TEC is placed underneath the copper block in order to vary the temperature from 20 degree C to 60 degree C. The laser device is driven below threshold by the HP 4145 semiconductor analyser, the spontaneous emission from the device is collected by a lensed single mode fibre and measured by an Advantest OSA Q8384. Finally, the data is plotted using a LabView program on a PC. During the measurement, the temperature is varied using a LDC3900 laser diode driver which includes a temperature controller.

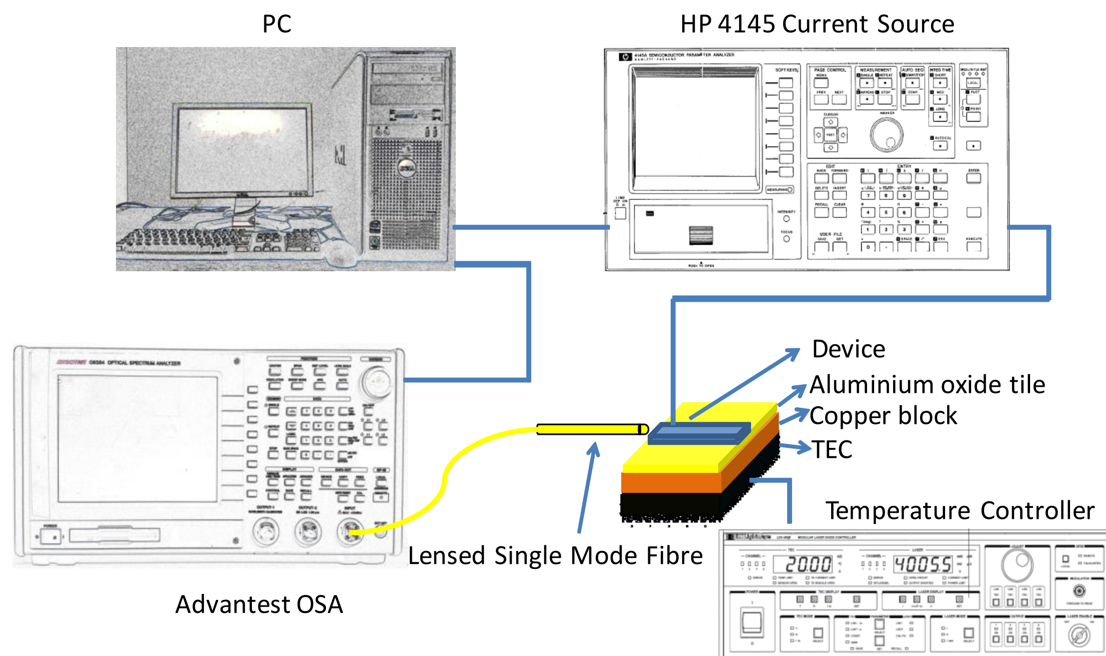

Figure 2.26 Setup for optical spectrum measurements.

The Hakki-Paoli gain measurement is normally applied below threshold, because it does not give much useful information above threshold due to the gain clamping effect. In order to achieve the net model gain, the peak (P_i) and valley (V_i) of each F-P mode must be measured as shown in Figure 2.28 and

the gain is then calculated based on equation 2-(3) and 2-(4) [6].

$$r_i = \frac{P_i + P_{i+1}}{2V_i} \tag{2-(3)}$$

$$gain = \frac{1}{L}\ln\left(\frac{r_i^{\frac{1}{2}}+1}{r_i^{\frac{1}{2}}-1}\right) + \frac{1}{L}\ln R \tag{2-(4)}$$

Peak to valley ratio can be achieved by fitting the envelope of the maxima and minima of the entire spectra or calculated based on each individual modal basis. Here, the peak to valley ratio is extracted by a MS Excel program which finds the peak and the valley in each sampling window. At the beginning of the scan process (at shorter wavelength), the signal collected from the sample is noisy and the peaks and valleys are not well defined. I set the program to find the minimum value in the first 50 data points and then set the sampling window from the valley wavelength.

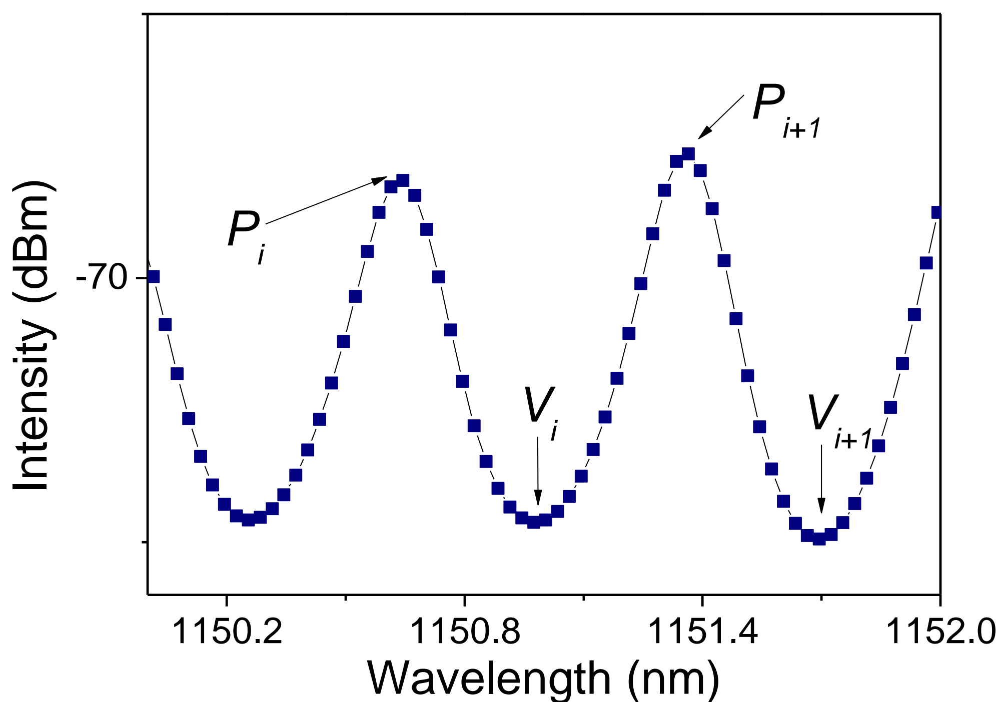

Figure 2.27 F-P modes of a laser spectrum including peaks (P_i) and valleys (V_i).

Based on the mode spectrum in Figure 2.28, it is single mode in this sampling window of the device. The single mode device can avoid mode overlapping in the emission spectrum which is helpful for the Hakki-Paoli gain measurement.

Moreover, for both lasing and non-lasing cases, the essentially identical shifts of the F-P peak position of the mode indicate that the shift in lasing wavelength is dominated by thermal expansion of the cavity and thermal change in refractive index, rather than a change in refractive index due to free carriers [7]. Based on this observation, the wavelength of an individual F-P mode below threshold can be used as a reference to achieve the constant junction temperature of the device. This allows the removal of the Joule heating effect by reducing the heat-sink temperature.

2.2.4. Photoluminescence Spectroscopy (PL)

Photoluminescence (PL) is a powerful tool to investigate the optical characteristics of the unfabricated semiconductor wafers. It is achieved by shining a laser onto the targeting sample and due to the absorption and re-radiation process in the sample the emitted light is collected by a detector. The process is shown in Figure 2.29 schematically. By absorbing the incoming light, an electron and a hole are generated higher in the conduction band and valence band. Before recombining, the carriers relax to the bottom of the bands by scattering with phonons.

The experimental setup of the PL measurement is shown in Figure 2.29. A diode pumped solid state laser (DPSSL) is used as the excitation source, the standard laser power density shined on the sample is 50W/cm^2. In the system

an optical chopper is used to provide a reference for the two-phase lock-in amplifier. The PL signal from the sample is fed into a DM 150 double monochromator, which gives the wavelength information to the detector. An InGaAs detector is used in this system for device emit near infrared. On the computer, a LabView program is used to combine the wavelength data (from the monochromator) with the corresponding intensity data (from the detector) to obtain the PL intensity versus wavelength plot.

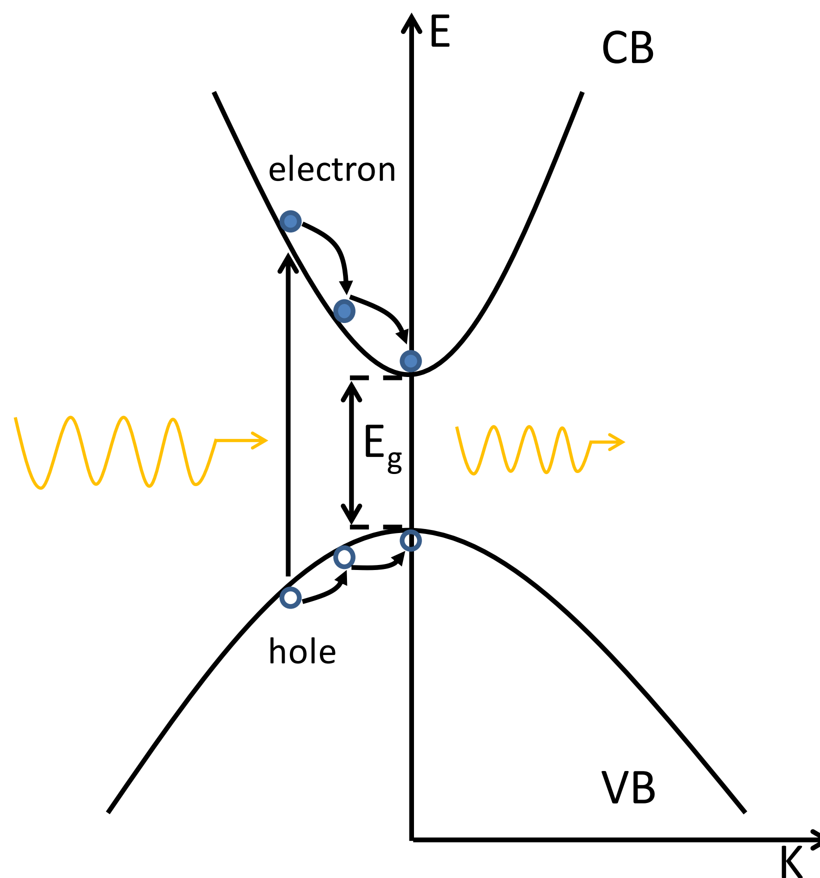

Figure 2.28 The absorption and recombination process during the PL measurement [8].

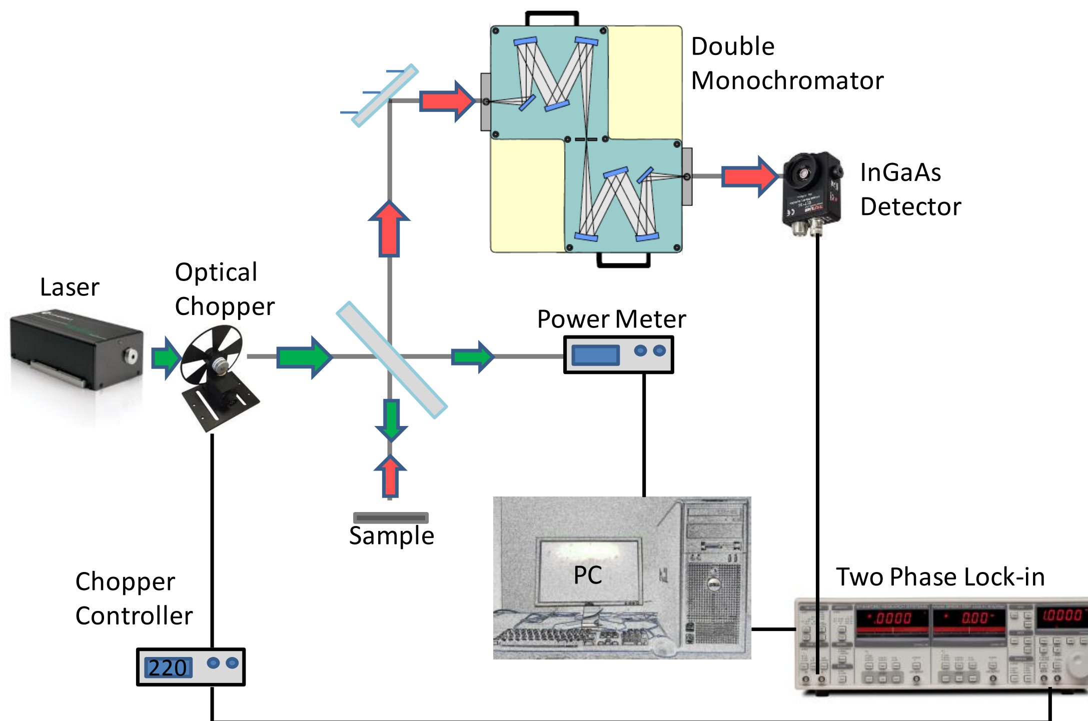

Figure 2.29 Schematic diagram of Photoluminescence setup.

2.2.5. Photocurrent Spectroscopy (PC)

PC spectroscopy is reported to be a simple, highly sensitive, quantitative technique to measure the interband absorption spectrum. It has been used to investigate QWs [9, 10] and SAQDs [11]. The PC spectrum is based on the experiment, it not only reflects the absorption in QWs and QDs, but also the electron-hole pairs (which can be calculated from the measured PC signal) generated from the absorbed photons. Therefore, the intensity of the PC peaks are important when investigating the recombination and escape rates of photo-generated carriers [12]. The PC spectrum investigated and discussed in this thesis are all measured based on the 400μm diameter mesa diode device.

The setup of the photocurrent spectroscopy system is shown in Figure 2.25.

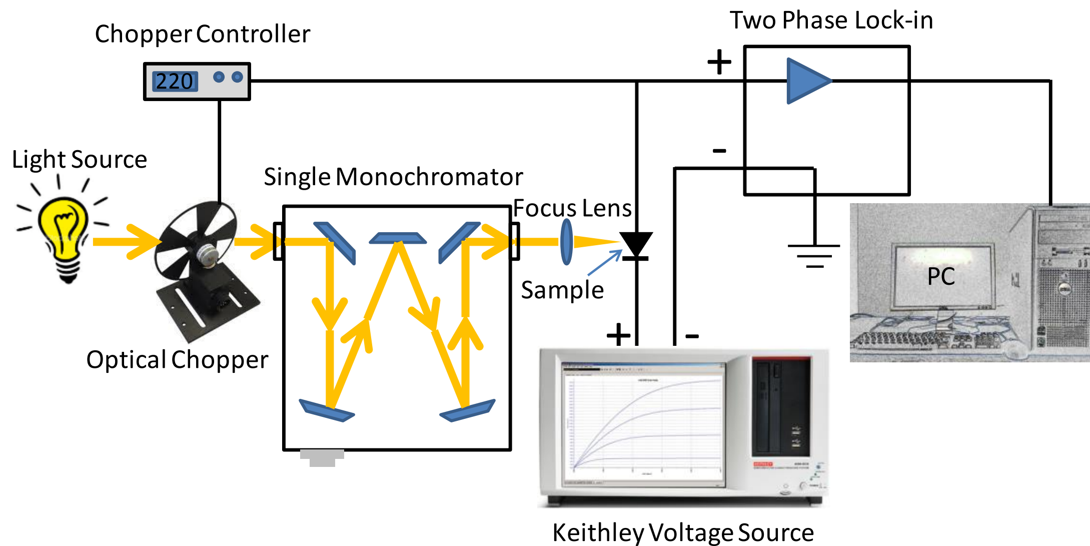

Figure 2.30 Schematic diagram of photocurrent experimental setup.

A tungsten lamp is the light source of the system. Light is collected and dispersed in a monochromator. There is an optical chopper between the light source and the monochromator, which is used to modulate the intensity of a light beam. A lock-in amplifier is normally used in combination with the chopper to improve the signal-to-noise ratio. The light beam out of the monochromator is then focused onto the p-type surface of the sample. A reverse bias can be applied to the sample by the Keithley voltage source. The current signal is collected by the lock-in, and the PC spectrum is plotted on the computer by using a LabView program.

Reference

1. R. Corporation, "Method of forming ohmic contacts," (1975).
2. A. Dikshit, V. Vangapally, and J. Pikal, "Carrier lifetime in 1.3µm InAs quantum-dot lasers using small-signal modulation technique," Proc. SPIE 6017, 60170L (2005).
3. G. E. Shtengel, D. A. Ackerman, P. A. Morton, E. J. Flynn, and M. S. Hybertsen, "Impedance-corrected carrier lifetime measurements in semiconductor lasers," Appl. Phys. Lett. 67, 1506-1508 (1995).
4. G. E. Shtengel, R. F. Kazarinov, G. L. Belenky, M. S. Hybertsen, and D. A. Ackerman, "Advances in measurements of physical parameters of semiconductor lasers," J. High Speed Electron. Syst. 09, 901-940 (1998).
5. W. B. Joyce and R. W. Dixon, "Electrical characterization of heterostructure lasers," J. Appl. Phys. 49, 3719-3728 (1978).
6. B. W. Hakki and T. L. Paoli, "Gain spectra in GaAs double-heterostructure injection lasers," J. Appl. Phys. 46, 1299-1306 (1975).
7. H. Shahid, D. T. D. Childs, B. J. Stevens, and R. A. Hogg, "Negative differential gain due to many body effects in self-assembled quantum dot lasers," Appl. Phys. Lett. 99(2011).
8. M. Fox, Optical Properties of Solids (OUP Oxford, 2010).
9. K. Yamanaka, T. Fukunaga, N. Tsukada, K. L. I. Kobayashi, and M. Ishii, "Photocurrent spectroscopy in GaAs/AlGaAs multiple quantum wells under a high electric field perpendicular to the heterointerface," Appl. Phys. Lett. 48, 840-842 (1986).
10. R. T. Collins, K. v. Klitzing, and K. Ploog, "Photocurrent spectroscopy of GaAs/$Al_{(x)}Ga_{(1-x)}As$ quantum wells in an electric field," Phys. Rev. B. 33, 4378-4381 (1986).
11. P. W. Fry, I. E. Itskevich, S. R. Parnell, J. J. Finley, L. R. Wilson, K. L. Schumacher, D. J. Mowbray, M. S. Skolnick, M. Al-Khafaji, A. G. Cullis, M. Hopkinson, J. C. Clark, and G. Hill, "Photocurrent spectroscopy of InAs/GaAs self-assembled quantum dots," Phys. Rev. B. 62, 16784-16791 (2000).

12. P. N. Brunkov, A. Patanè, A. Levin, L. Eaves, P. C. Main, Y. G. Musikhin, B. V. Volovik, A. E. Zhukov, V. M. Ustinov, and S. G. Konnikov, "Photocurrent and capacitance spectroscopy of Schottky barrier structures incorporating InAs/GaAs quantum dots," Phys. Rev. B. 65, 085326 (2002).

3. Characterization of Recombination Processes in QD Lasers Using Small Signal Modulation

In this chapter, a method to determine the recombination coefficients of a semiconductor laser is described and applied to 1.3μm QD laser materials. This comparatively simple method, relying on the spectral resolution of a small signal modulation of the laser, allows the extraction of recombination coefficients in a direct manner. It is found that all recombination coefficients are a function of both temperature and modulation p-doping. The results indicate that the temperature insensitivity of modulation p-doped QD lasers is due to all recombination coefficients reducing with increasing temperature, which compensates the carrier thermal escape process. Here a reducing Auger recombination coefficient plays the main role.

3.1. Introduction

The recombination processes of a semiconductor hetero-structure play a key role in determining the threshold current density of a laser and how it varies with temperature. For three decades, QD lasers have attracted significant attention due to the prediction of temperature insensitive operation [1]. However, this temperature insensitivity (infinite characteristic temperature, T_0) at practical operating temperatures has only been observed with modulation p-doping [2] [3]. The origin of the infinite T_0 has been discussed at length in the literature, with several models having been proposed. These include, circumvention of thermal hole broadening [4], Auger process with 1/T dependence of the scattering rate [3], Coulombic attraction increasing the

confinement potential for electrons within the QDs [5], [6], mixed Auger recombination [7], and a photon coupling mechanism [8]. A simple and robust method to measure these coefficients therefore presents a powerful tool in the characterization of laser diodes.

A reduction in the Auger coefficient with increasing temperature for QD lasers was previously deduced by fitting modelled radiative currents in the QD, barrier, and wetting layer states. Non-radiative recombination, attributed to Auger recombination in 1260nm QD lasers was discussed in [3]. Figure 3.1 (taken from [3]) shows the threshold current density and Auger recombination component as a function of temperature in both un-doped and modulation p-doped samples.

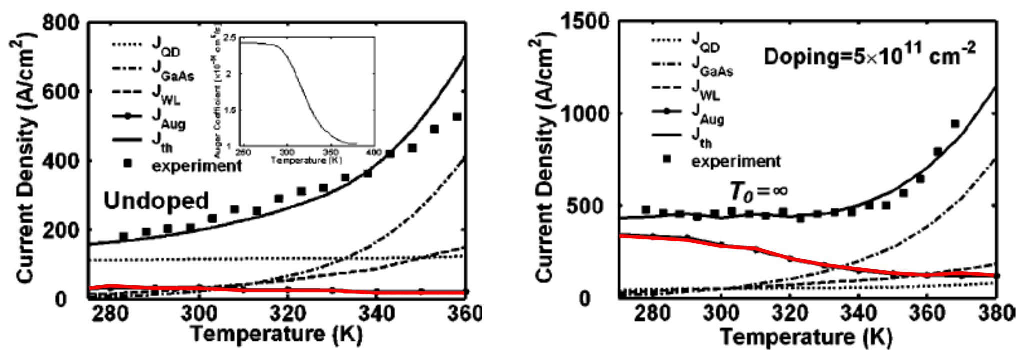

Figure 3.1 Variation of calculated and measured threshold current density, J_{th}, in p-doped (right), and un-doped (left) self-organized QD lasers. The red line shows the Auger component in the dots (J_{Aug}), from Fathpour *et al* [3].

In addition, fitting the experimental turn on delay time for the large signal modulation of 1040nm QD lasers [9] has allowed the Auger coefficient at threshold to be deduced. By analyzing the threshold current under hydrostatic pressure, a reduction in threshold current of 1300nm QD lasers with increasing pressure has been observed. It was shown that the radiative efficiency of 1300nm QD lasers drops much more quickly with increasing

temperature compared to 980nm QD lasers [10]. This is contrary to what one would expect as 1300nm lasers have larger confining energies, suggesting reduced thermal loss. This result indicated that Auger recombination is the likely mechanism which causes 1300nm QD lasers to be more temperature sensitive than 980nm QD lasers.

A range of samples with varying levels of modulation p-doping have been investigated using time-resolved PL at low excitation densities corresponding to <<1 e-h pair per QD [11]. At 10K, the carrier lifetime was observed to decrease with increasing doping level, which is attributed to an enhancement of the Auger-type recombination due to the presence of extrinsic holes in the QDs. However, for practical applications the laser material should be studied at typical operating temperatures and carrier densities (dot occupancies).

In this chapter, I detail a method to measure all recombination coefficients over a wide range of practical temperatures and carrier densities. This method combines various elements of small-signal modulation with spectral resolution of the emission to provide a comparatively simple method, which will be of use in characterizing various semiconductor laser materials. Beyond the use of standard laser structures, modest RF modulation and detection equipment, no specialist apparatus is required. By contrast to other methods, no theoretical modelling is required, with the recombination coefficients being determined by simple fitting procedures.

A study is presented of the un-doped and modulation p-doped (18

acceptors/QD) dot-in-well (DWELL) laser materials operating at ~1310nm in the temperature range of 0°C to 60°C (The same samples were studied in [11, 12]). The measurement allows the differential carrier lifetime at a range of carrier densities to be deduced. Analysis of the differential carrier lifetime data allows all the recombination coefficients to be determined (A-defect, B-spontaneous emission, and C-Auger) at various temperatures. Furthermore, the spectral resolution of the emission allows the ES and GS differential carrier lifetime to be independently determined. The importance of the spectral filtering of the optical emission is highlighted, due to the observation of a difference in the differential carrier lifetime for the GS and ES transitions.

3.2. Devices – Epitaxy, Fabrication and Temperature Insensitivity (T_0)

3.2.1. Epitaxy

Epitaxial growth was carried out on 3-inch Si-doped n+ GaAs (100) substrates using a VG Semicon V90H solid source MBE reactor by Prof. Huiyun Liu. Seven-layer DWELL laser structures were grown, with each DWELL consisting of three monolayers of InAs grown on 2nm of $In_{0.15}Ga_{0.85}As$ before capping with 6nm of $In_{0.15}Ga_{0.85}As$. Following each DWELL layer was a 50nm GaAs spacer layer, the first 15nm of which was deposited at the DWELL growth temperature of 510°C, with the remaining 35nm grown at 620°C. This high-temperature step increases the surface mobility of gallium adatoms thereby replanarizing the growth front, which in turn, reduces the likelihood of defective QD growth on successive layers [13]. Optical confinement was achieved using 1500nm-thick $Al_{0.4}Ga_{0.6}As$ cladding layers. The upper (p-type)

and lower (n-type) cladding layers were doped with beryllium and silicon respectively. Further growth parameters can be found elsewhere [14]. The growth of the present devices was based on earlier growth studies [15].

Two wafers were studied with structures normally identical being grown in successive runs of the same growth campaign, except for the beryllium doping concentration in a 6nm-wide modulation p-doped layer located in the spacer layer 9nm below each DWELL. These doped layers were grown at 620°C with nominal concentrations corresponding to 18 acceptors per QD. Figure 3.2 shows a schematic of the position of the doped layer on a transmission electron microscope (TEM) image of the DWELL region.

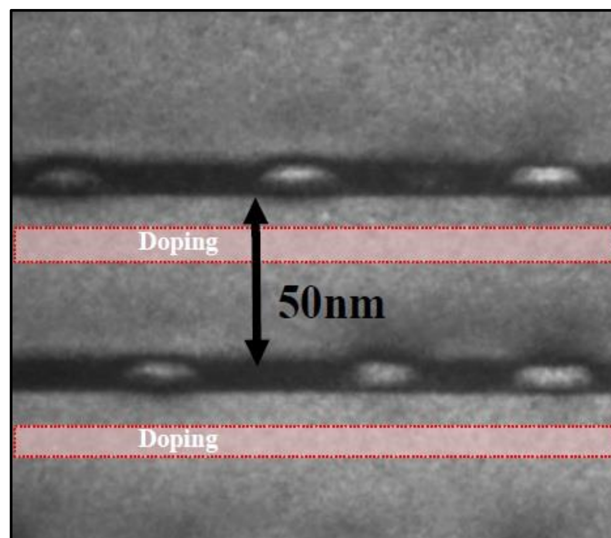

Figure 3.2 TEM image of modulation p-doped QD sample, in which beryllium is used for the p-type modulation adjacent (the red bars are only guides for the eye) [16].

3.2.2. Fabrication

Both samples were fabricated into 15μm wide broad area lasers by standard photolithographic techniques. The ridge was wet chemical etched through the p-side AlGaAs cladding layers, stopping 100nm above the active region. Au-

Zn-Au and In-Ge-Au were thermally evaporated on the top and bottom of the wafer to provide p and n side ohmic contacts, respectively. Laser bars were cleaved and the bars were mounted on gold plated Al_2O_3 ceramic tiles using InAgPb solder. The mirror facets were left as cleaved.

3.2.3. Temperature Insensitivity (T_0)

Figure 3.3(a) plots the threshold current density of 3mm long 15µm-wide ridge waveguide F-P lasers of the modulation p-doped and un-doped material [12]. These measurements were performed under pulsed operation to minimise the effects of self-heating at high current densities. This cavity length was chosen as all samples exhibit GS lasing at this length at all temperatures.

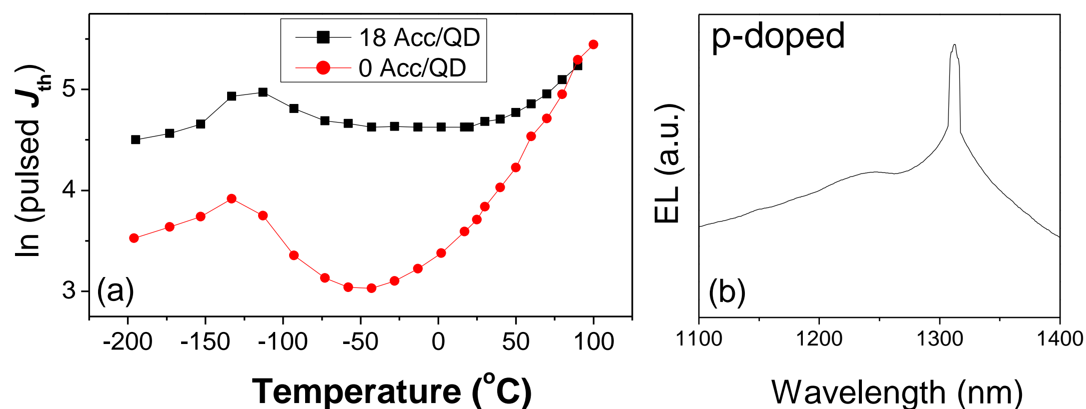

Figure 3.3 (a) Pulsed threshold current density as a function of temperature (b) lasing spectrum of modulation p-doped sample [12].

The modulation p-doped sample shows infinite T_0 from -75°C to 25°C, whilst over this range the un-doped sample exhibits quite strong temperature sensitivity. Figure 3.3(b) shows a lasing spectrum from a 1mm long modulation p-doped device at room temperature, which indicates the lasing wavelength is ~1310nm.

3.3. Experimental Method

In order to analyse the recombination process of the GS and ES separately, band-pass filters were introduced into the system. The function of these optical band-pass filters are shown in Figure 3.4, which shows a typical emission spectrum from the un-doped sample at 200 $\mathrm{A/cm^2}$. In addition, emissions recorded using 1200nm and 1300nm band-pass filters are shown. Whilst not perfect, efficient rejection of the GS and ES emission can be obtained, allowing the study of the differential carrier lifetime of the ES and GS, respectively.

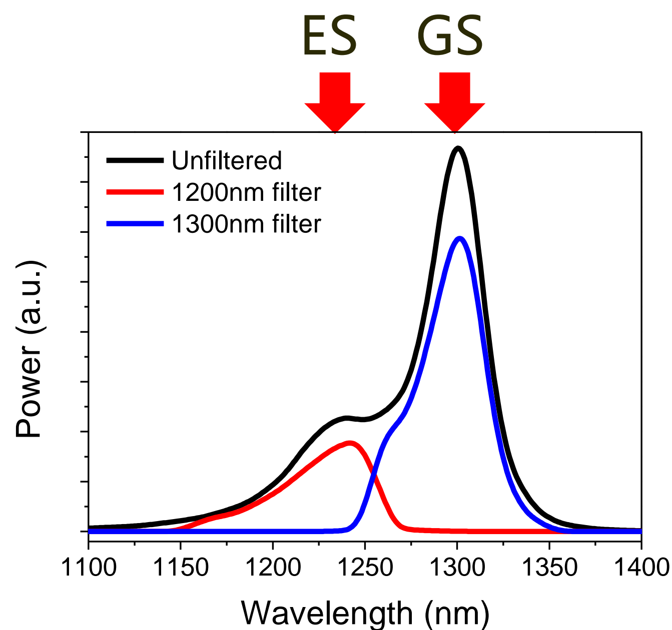

Figure 3.4 Unfiltered and filtered EL spectrum of the un-doped device at an inject current density of 200A/cm^2.

By analyzing the sub-threshold single level rate equations, the relationship relating the carrier density and lifetime to the current is derived. The carrier rate equation is given as followed:

$$\frac{dN}{dt} = \eta_i \frac{I}{q} - R(N) \qquad \text{3-(1)}$$

Here, all injected carriers are assumed to be in the reservoir until they recombine, *I* is the injected current, *N* is the carrier density, η_i is the injection efficiency and *R(N)* is the total recombination rate which is normally written in the following form, including a carrier lifetime component (thermal escape process of the carriers are not considered in this chapter, will be discussed in the next chapter):

$$R(N) = \frac{N}{\tau_c} = A(N) + B(N)^2 + C(N)^3 \qquad \text{3-(2)}$$

The steady state solution of equation 3-(1) and 3-(2) through the recombination coefficients relating the lifetime and injected current is written as

$$I = eVR(N) = eV\left[A(N) + B(N)^2 + C(N)^3\right] \qquad \text{3-(3)}$$

Here the analysis of this differential carrier lifetime is the derivative of the total recombination rate related to the carrier lifetime [17].

$$\frac{1}{\tau'} = \frac{dR(N)}{dN} = A + 2B(N) + 3C(N)^2 \qquad \text{3-(4)}$$

The differential carrier lifetime is obtained from the small signal modulation response, the measurement was introduced in section 2.2.1. Figure 3.5 shows an example of the small signal modulation response from the experimental system.

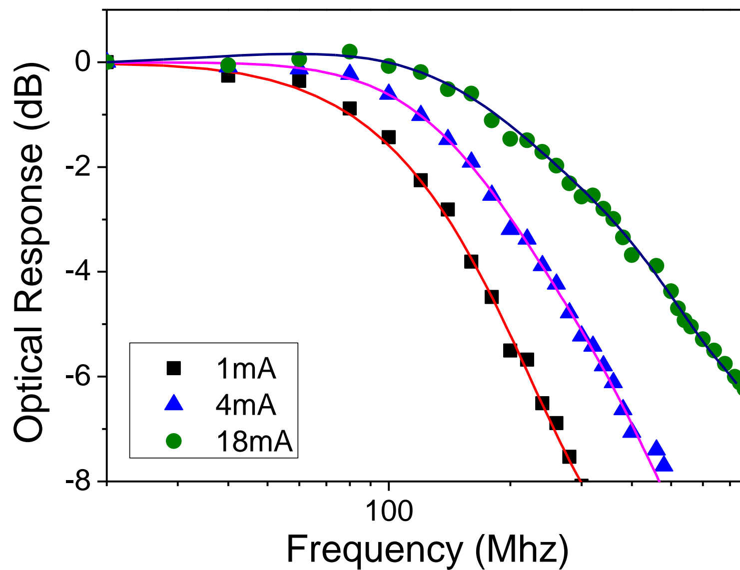

Figure 3.5 Small signal modulation response data of the dynamic system with fitting using equation 3-(4).

The sub-threshold optical response |S| is expressed as [17]:

$$|S| \propto 20\log\frac{1}{\sqrt{1+(2\pi f)^2\tau'^2}}\cdot\frac{1}{\sqrt{1+(RC)^2}} \qquad 3\text{-}(5)$$

Where: f is the modulation frequency, τ' is the differential carrier lifetime of the device without impedance correction. Equation 3-(5) describes the modelled optical response of the device and is an accumulation of the inherent differential lifetime response and the low pass filter response of the *RC* parasitic. In this case, because the device is driven in a low frequency regime, the *RC* term is assumed to be equal to one. But when the system is operating at a high frequency, the *RC* term may be significant and cannot be ignored. The fitting plot based on equation 3-(5) to the experimental data is also shown in Figure 3.5 (solid line) by using a least square method.

Based on [18], the above equations 3-(4) can be simplified when linear and quadratic terms dominate the recombination process

$$\frac{1}{\tau'^2} = A^2 + \frac{4B}{eV}I \qquad 3\text{-}(6)$$

A demonstration of equation 3-(6) is shown in Figure 3.6. Figure 3.6(a) plots a set of differential carrier lifetime data versus current density and Figure 3.6(b) recasts this data by plotting the $\tau^{'2}$ as a function of current density. It can be seen from Figure 3.6(b), coefficient A is derived from the intercept ($=A^2$) and coefficient B is derived from the gradient of the plot ($=4B/eV$). If coefficient A and B are known then the Auger coefficient C can be fit from the model based on equation 3-(4).

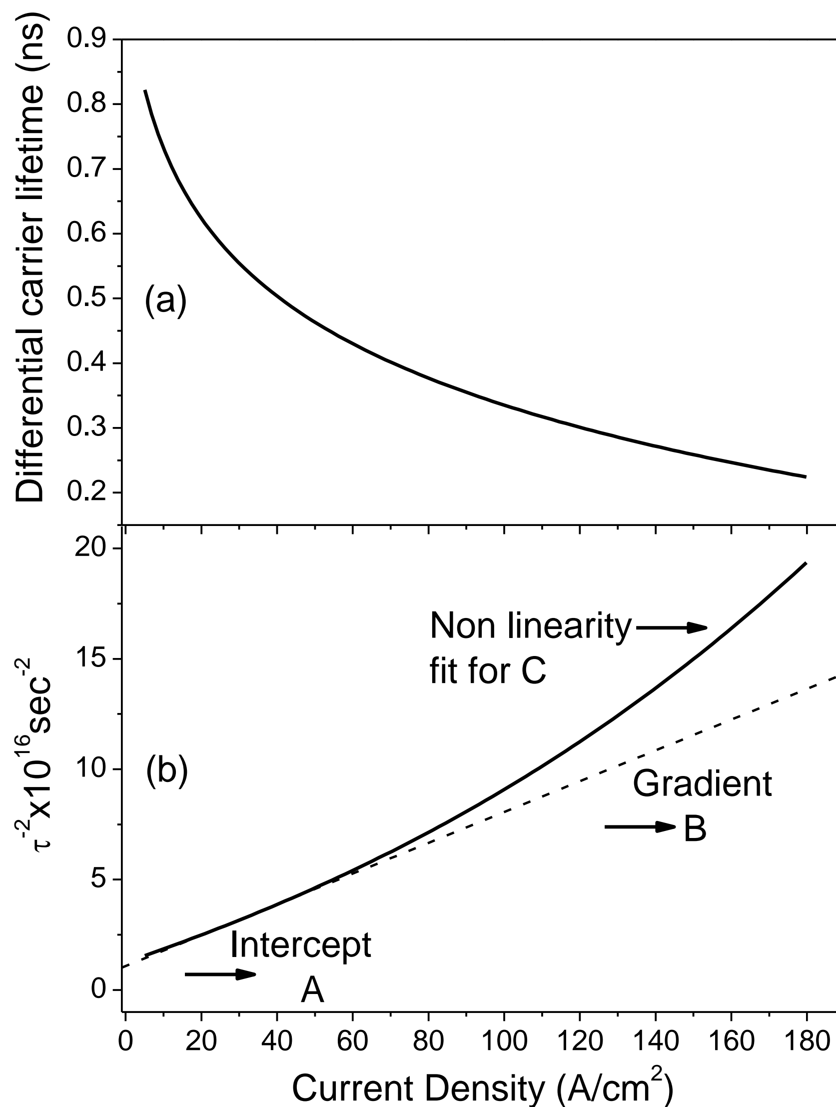

Figure 3.6 (a) A set of differential carrier lifetime data as a function of current density (b) a demonstration of the derivation of the coefficient A, B and C.

3.4. Results and Discussion

3.4.1. Un-doped device

Because of an impedance change during the low current density region, in order to fit the coefficient C accurately, an impedance correction method is used as discussed previously in section 2.2.1 [19]. The corrected differential carrier lifetime data is slightly larger than the raw optical response.

Figure 3.7 plots the impedance corrected differential carrier lifetime as a function of current density for the un-doped sample. Spectral resolution of the optical signal allows the differential carrier lifetime of the GS and ES emission to be measured independently. Data at heat-sink temperatures of 20°C and 60°C is shown. With regard to the GS, a reduction in differential carrier lifetime is observed. The observed sensitivity of laser devices to temperature over this region may therefore be attributed to thermal excitation of carriers out of the QDs.

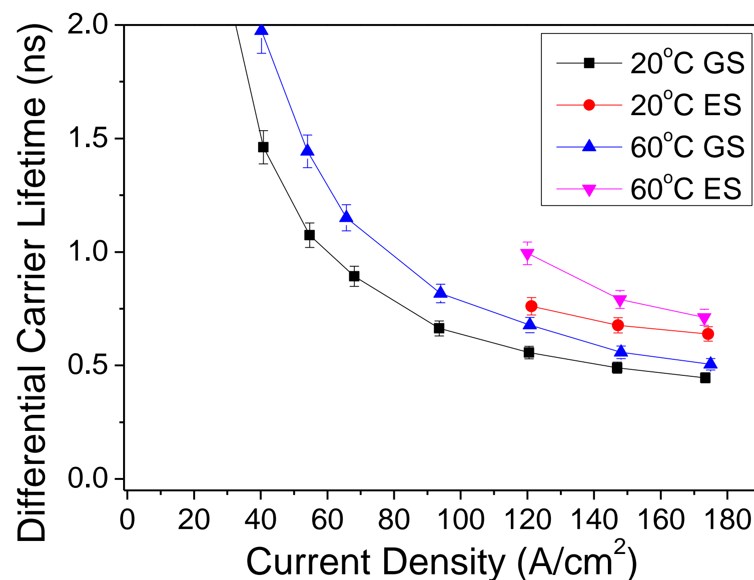

Figure 3.7 The impedance corrected GS and ES differential carrier lifetime of un-doped sample below threshold at 20 degree C and 60 degree C with band pass filters.

For the ES emission (only observed at high current density), at 20°C the differential carrier lifetime is higher than that of the GS. At 60°C, the ES differential carrier lifetime is observed to be significantly higher than that of the GS. As temperature increases the carrier lifetime is increasing, leading to higher QD occupancy. As a result, relaxation from the ES to GS will be blocked more readily. As a consequence, ES recombination will no longer be dominated by ES to GS relaxation (driven by GS recombination) and will decay radiatively. This is therefore suggestive of a longer radiative decay time of the ES as compared to the GS, in agreement with theory [20].

Figure 3.8 shows the plot of $1/\tau^2$ versus *J* [18], as discussed in Figure 3.6, it is a useful method to determine if higher order terms contribute (such as the cubic Auger term).

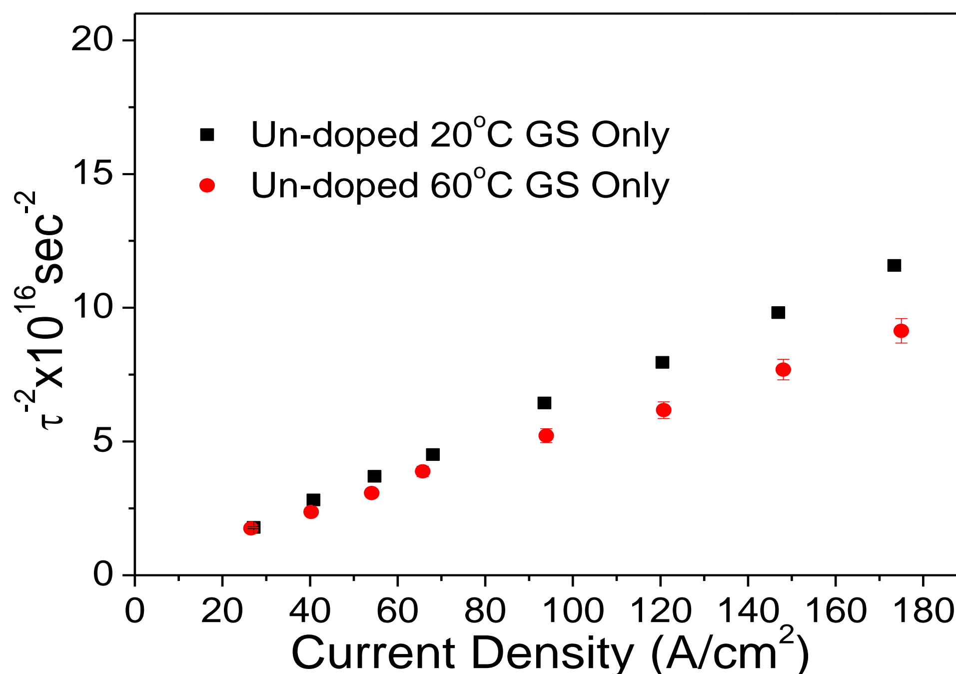

Figure 3.8 $1/\tau^2$ as a function of current density for the un-doped sample.

If only linear and quadratic terms contribute, the data is nearly a straight line

and the coefficient A and B can be deduced from the fitted intercept and the slope as described previously. By the calculation based on the low *J* data in Figure 3.8, values for A and B can be obtained, high *J* data is fitted in Figure 3.7 to obtain C.

It can be seen that for the un-doped sample at both temperatures, the $1/\tau^2$ versus *J* plot is essentially a straight line over the current densities studied. This indicates that for the un-doped sample there is limited contribution from Auger recombination in this temperature region.

3.4.2. Modulation p-doped device

Figure 3.9 is a similar plot for the modulation p-doped sample with 18 acceptors per QD. It shows the differential carrier lifetime as a function of current density. Because of the impedance change during the low current density region, in order to fit coefficient C accurately, the impedance correction method is applied in Figure 3.9 [19], as discussed previously. Data at heat-sink temperatures of 0^oC, 20^oC and 60^oC is shown. With regard to the GS, a reduction in differential carrier lifetime is again observed in line with Auger non-radiative recombination becoming dominant at high carrier densities.

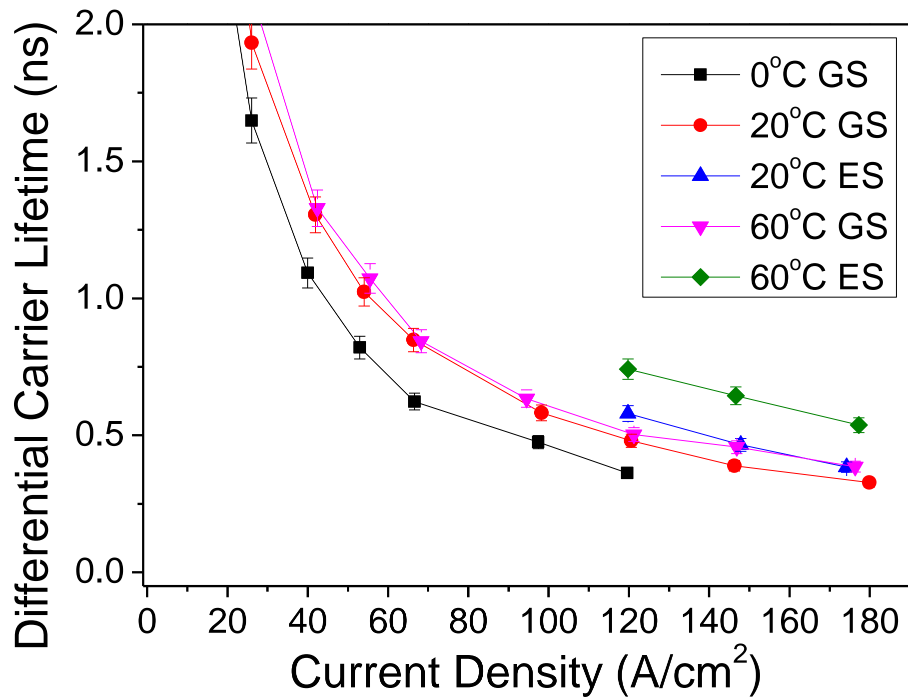

Figure 3.9 The impedance corrected GS and ES differential carrier lifetime of modulation p-doped laser below threshold at 20 degree C and 60 degree C with band pass filters.

By comparing to the un-doped device, a shorter differential lifetime is observed for the modulation p-doped device, in line with enhanced Auger recombination due to the modulation p-doping. For the same current density the GS emission differential carrier lifetime is observed to increase with increasing temperatures. This is suggestive that the Auger C coefficient (as Auger recombination is dominant) is changing in this temperature region. For the ES emission (only observed at high current density), at 20°C the differential carrier lifetime is close to that of the GS. At 60°C however, the ES differential carrier lifetime is significantly higher than that of the GS.

Figure 3.10 shows the similar $1/\tau^2$ versus J plot for the modulation p-doped sample. The observation here is different from the un-doped sample. From the plot we observe that additional higher order terms (not only linear and quadratic but cubic terms) contribute to the recombination process.

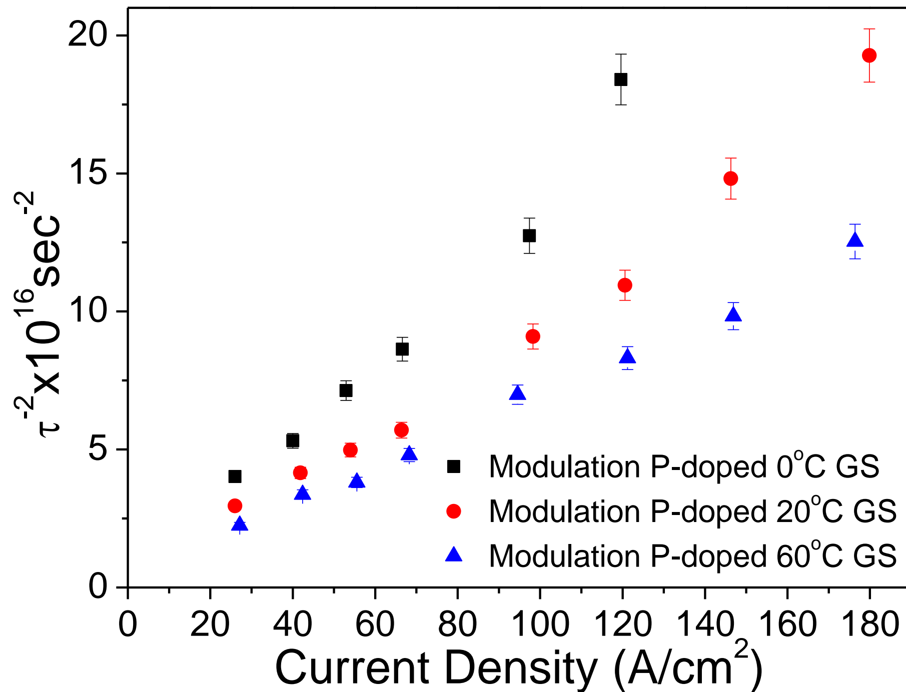

Figure 3.10 $1/\tau^2$ as a function of current density for the modulation p-doped sample.

A, B, and C coefficients are deduced as described above and plotted in Figure 3.11. The Figure shows that for the modulation p-doped sample the Auger recombination rate decreases with increasing temperature which is in agreement with previous work [3].

In addition, all recombination coefficients are a function of both temperature and modulation p-doping. The mono-molecular recombination (A coefficient) can be treated as non-radiative recombination centre [21] which traps carriers. With increasing temperature, the carrier thermal escape process compensates the effect of the non-radiative recombination centre, which is a possible reason for A coefficient decreasing with increasing temperature in Figure 3.11(a). The A coefficient increases for the p-doped sample as compared to that of the un-doped sample (shown in Figure 3.11(a)). In Figure 3.11(b), the decrease of the B coefficient with increasing temperature is due to

the carrier thermal escape process. The higher B coefficient for the un-doped sample is because in p-doped samples the carrier-carrier scattering process is enhanced, which in turn will decrease the recombination rate. In the p-doped sample, due to its rich hole environment, the Auger rate is higher than it is in the un-doped sample.

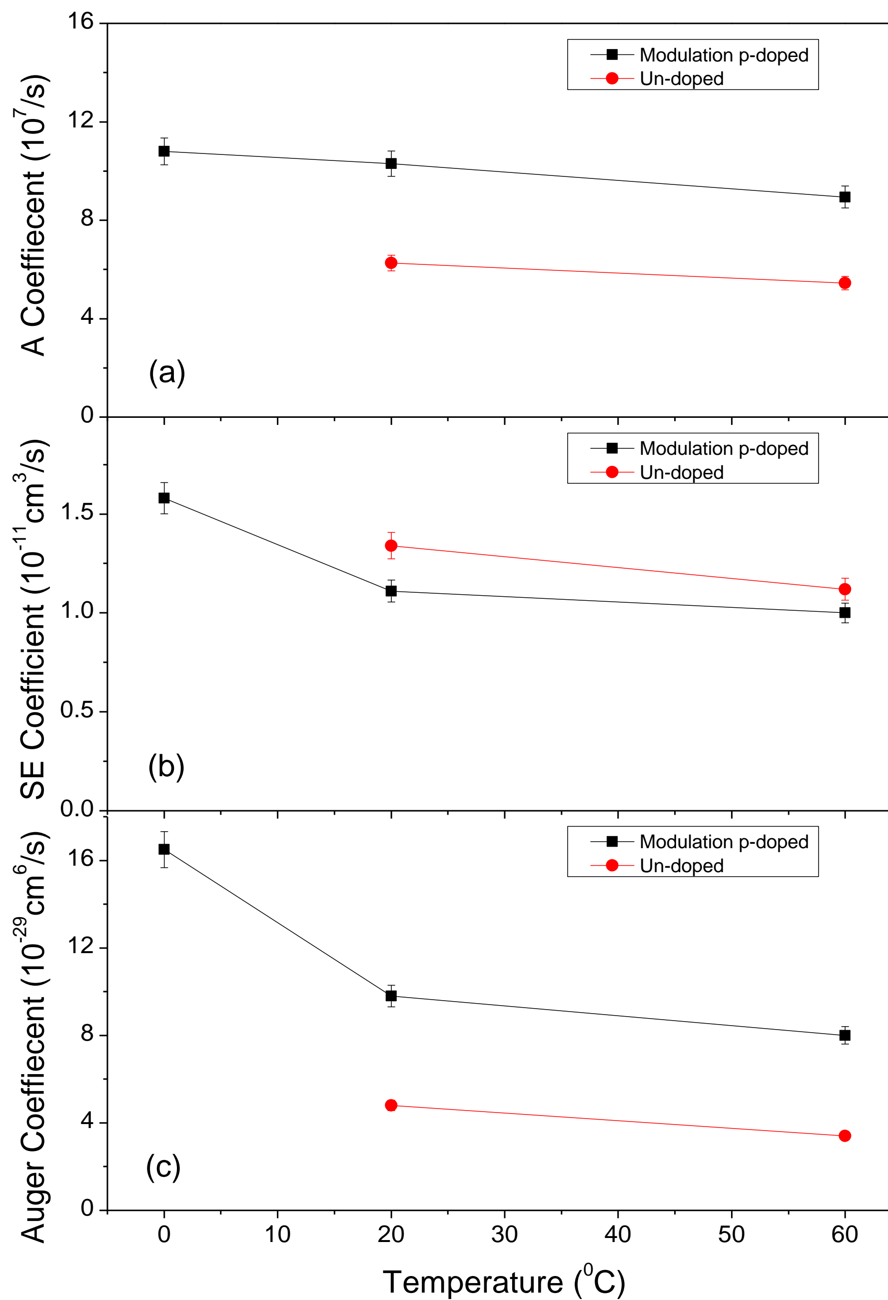

Figure 3.11 A, B, C coefficients of the un-doped sample and modulation p-doped sample as a function of heat-sink temperature.

Moreover, the decrease of the Auger coefficient with increasing temperature is possibly a direct consequence of the temperature dependence of the GS hole occupation. With increasing temperature, the thermal excitation of holes from the lowest energy level will decrease the relaxation rate from the ES to GS, which in turn lower the GS hole occupation. Since there are less holes in the GS to scatter with electrons, the Auger rate based on electron-hole scattering decreases [9]. Finally, a reducing Auger rate with increasing temperature plays the main role in creating a threshold current reducing process to counter threshold current increasing processes (carrier thermal escape).

3.5. Discussion

The precision and ease by which this data can be directly extracted from the small signal modulation response, along with the taking into account the change in impedance (differential resistance) makes this technique a powerful tool for the characterization of laser media, particularly QDs. By contrast, the analysis of the turn on delay of QD lasers allows only the Auger coefficient to be determined following comparatively complex calculations and measurements. Including the calculation of the gain, spontaneous emission rates, carrier distributions in wetting layer and barriers and the optical confinement factor. Moreover, need the measurement of the internal loss and solution of multi-mode rate equations along with calibration of the model (varying the inhomogeneous broadening) against the threshold current density [9]. The application of hydrostatic pressure requires highly specialist test apparatus and allows the relative contributions of radiative and non-radiative recombination to the threshold current. First principle calculations

are then required in order to determine the relative strengths of the recombination coefficients at threshold [10].

3.6. Conclusion

In summary, I have presented a small-signal modulation method to allow the measurement of all recombination coefficients in a semiconductor laser material over a range of current densities and temperatures. Using this method, I have discussed differential carrier lifetime measurements of un-doped and modulation p-doped (18 acceptors/QD) DWELL lasers operating at ~1310nm. I spectrally resolved the emission from the QD device in order to observe the ES and GS emission independently. This technique, which is applied to a standard laser structure, allows the recombination coefficients to be deduced, and may act as a useful tool in the characterization of a range of semiconductor laser materials.

For the current densities and temperatures studied (around room temperature), I deduced that all recombination coefficients are slightly reduced with increasing temperature for the un-doped sample over this temperature range.

For the modulation p-doped device, I deduced that modulation p-doping result in an increase in coefficient A and C and a reduction in the radiative B coefficient, as compared to the un-doped sample. Auger recombination is observed to be significantly enhanced in the modulation p-doped sample. All recombination coefficients for the p-doped sample are observed to reduce with increasing temperature, making this a strong candidate for the origin of

the infinite T_0 observed in modulation p-doped QD lasers. Due to the spectral resolution of the optical signal, the ES and GS differential carrier lifetimes are observed to be different. The larger ES lifetime is in line with theoretical predictions.

3.7. Future work

Future possible work is to investigate samples with varied doping level using the techniques discussed in this chapter, in order to plot the Auger and other recombination coefficients as a function of doping levels and temperatures. It would also be interesting to study a device from 10 to ~400K, where the effect of homogeneous linewidth on J_{th} [22, 23] and emission could be studied in conjunction with recombination coefficients of QD laser.

Reference

1. Y. Arakawa and H. Sakaki, "Multidimensional quantum well laser and temperature-dependence of its threshold current," Appl. Phys. Lett. 40, 939-941 (1982).
2. K. Otsubo, N. Hatori, M. Ishida, S. Okumura, T. Akiyama, Y. Nakata, H. Ebe, M. Sugawara, and Y. Arakawa, "Temperature-insensitive eye-opening under 10-Gb/s modulation of 1.3μm p-doped quantum-dot lasers without current adjustments," Jpn. J. Appl. Phys. 43, L1124-L1126 (2004).
3. S. Fathpour, Z. Mi, P. Bhattacharya, A. R. Kovsh, S. S. Mikhrin, I. L. Krestnikov, A. V. Kozhukhov, and N. N. Ledentsov, "The role of Auger recombination in the temperature-dependent output characteristics ($T_0=\infty$) of p-doped 1.3μm quantum dot lasers," Appl. Phys. Lett. 85, 5164 (2004).
4. O. B. Shchekin and D. G. Deppe, "Low-threshold high T0 1.3μm InAs quantum-dot lasers due to P-type modulation doping of the active region," IEEE Photon. Technol. Lett. 14, 1231-1233 (2002).
5. I. P. Marko, N. F. Masse, S. J. Sweeney, A. D. Andreev, A. R. Adams, N. Hatori, and M. Sugawara, "Carrier transport and recombination in p-doped and intrinsic 1.3μm InAs/GaAs quantum-dot lasers," Appl. Phys. Lett. 87(2005).
6. T. J. Badcock, R. J. Royce, D. J. Mowbray, M. S. Skolnick, H. Y. Liu, M. Hopkinson, K. M. Groom, and Q. Jiang, "Low threshold current density and negative characteristic temperature 1.3μm InAs self-assembled quantum dot lasers," Appl. Phys. Lett. 90(2007).
7. S. Mokkapati, M. Buda, H. H. Tan, and C. Jagadish, "Effect of Auger recombination on the performance of p-doped quantum dot lasers," Appl. Phys. Lett. 88(2006).
8. C.-Y. Jin, T. J. Badcock, H.-Y. Liu, K. M. Groom, R. J. Royce, D. J. Mowbray, and M. Hopkinson, "Observation and modeling of a room-temperature negative characteristic temperature 1.3μm p-type modulation-doped quantum-dot laser," IEEE J. Quantum Electron. 42,

1259-1265 (2006).

9. S. Ghosh, P. Bhattacharya, E. Stoner, J. Singh, H. Jiang, S. Nuttinck, and J. Laskar, "Temperature-dependent measurement of Auger recombination in self-organized In0.4Ga0.6As/GaAs quantum dots," Appl. Phys. Lett. 79, 722 (2001).
10. I. P. Marko, A. D. Andreev, A. R. Adams, R. Krebs, J. P. Reithmaier, and A. Forchel, "The role of Auger recombination in InAs 1.3μm quantum-dot lasers investigated using high hydrostatic pressure," IEEE J. Sel. Topics Quantum Electron. 9, 1300-1307 (2003).
11. Y. D. Jang, T. J. Badcock, D. J. Mowbray, M. S. Skolnick, J. Park, D. Lee, H. Y. Liu, M. Hopkinson, R. A. Hogg, and A. D. Andreev, "Enhanced nonradiative Auger recombination in p-type modulation doped InAs/GaAs quantum dots," Appl. Phys. Lett. 93, 101903 (2008).
12. R. R. Alexander, D. Childs, H. Agarwal, K. M. Groom, H. Y. Liu, M. Hopkinson, R. A. Hogg, M. Ishida, T. Yamamoto, M. Sugawara, Y. Arakawa, T. J. Badcock, R. J. Royce, and D. J. Mowbray, "Systematic study of the effects of modulation p-doping on 1.3μm InAs/GaAs dot-in-well lasers," IEEE J. Quantum Electron. 43, 1129-1139 (2007).
13. C. L. Walker, I. C. Sandall, P. M. Smowton, D. J. Mowbray, H. Y. Liu, S. L. Liew, and M. Hopkinson, "Improved performance of 1.3μm In(Ga)As quantum-dot lasers by modifying the temperature profile of the GaAs spacer layers," IEEE Photon. Technol. Lett. 18, 1557-1559 (2006).
14. Z. Y. Zhang, I. J. Luxmoore, C. Y. Jin, H. Y. Liu, Q. Jiang, K. M. Groom, D. T. Childs, M. Hopkinson, A. G. Cullis, and R. A. Hogg, "Effect of facet angle on effective facet reflectivity and operating characteristics of quantum dot edge emitting lasers and superluminescent light-emitting diodes," Appl. Phys. Lett. 91(2007).
15. H. Y. Liu, D. T. Childs, T. J. Badcock, K. M. Groom, I. R. Sellers, M. Hopkinson, R. A. Hogg, D. J. Robbins, D. J. Mowbray, and M. S. Skolnick, "High-performance three-layer 1.3μm InAs-GaAs quantum-dot lasers with very low continuous-wave room-temperature threshold currents," IEEE Photon. Technol. Lett. 17, 1139-1141 (2005).
16. R. R. Alexander, "GaAs based quantum dot lasers for 1.3μm optical communications," (University of Sheffield, Sheffield, 2009).

17. A. Dikshit, V. Vangapally, and J. Pikal, "Carrier lifetime in 1.3μm InAs quantum-dot lasers using small-signal modulation technique," Proc. SPIE 6017, 60170L (2005).
18. R. Olshansky, C. B. Su, J. Manning, and W. Powazinik, "Measurement of radiative and nonradiative recombination rates in InGaAsP and AlGaAs light sources," IEEE J. Quantum Electron. 20, 838-854 (1984).
19. G. E. Shtengel, R. F. Kazarinov, G. L. Belenky, M. S. Hybertsen, and D. A. Ackerman, "Advances in measurements of physical parameters of semiconductor lasers," J. High Speed Electron. Syst. 09, 901-940 (1998).
20. M. T. Crowley, I. P. Marko, N. F. Masse, A. D. Andreev, S. Tomic, S. J. Sweeney, E. P. O'Reilly, and A. R. Adams, "The Importance of Recombination via Excited States in InAs/GaAs 1.3μm Quantum-Dot Lasers," IEEE J. Sel. Topics Quantum Electron. 15, 799-807 (2009).
21. T. Sugahara, H. Sato, M. S. Hao, Y. Naoi, S. Kurai, S. Tottori, K. Yamashita, K. Nishino, L. T. Romano, and S. Sakai, "Direct evidence that dislocations are non-radiative recombination centers in GaN," Jpn. J. Appl. Phys. 37, L398-L400 (1998).
22. M. Sugawara, K. Mukai, Y. Nakata, H. Ishikawa, and A. Sakamoto, "Effect of homogeneous broadening of optical gain on lasing spectra in self-assembled $In_{(x)}Ga_{(1-x)}As$/GaAs quantum dot lasers," Phys. Rev. B. 61, 7595-7603 (2000).
23. G. Ozgur, A. Demir, and D. G. Deppe, "Threshold Temperature Dependence of a Quantum-Dot Laser Diode With and Without p-Doping," IEEE J. Quantum Electron. 45, 1265-1272 (2009).

4. Temperature Sensitivity of Commercial QD Laser Material

The origin of an infinite T_0 related to modulation p-doping of a QD sample was discussed in chapter 3. In this chapter, devices fabricated from a commercial QD laser wafer are analysed and discussed, with a view to determining optimised modulation p-doping levels for an infinite T_0. Firstly, the temperature and length dependent L-I is plotted and discussed. The characteristic temperature, T_0 is calculated from this data, which shows the T_0 value is not high for these devices. The differential carrier lifetime is measured from a 250μm long device in order to obtain the A, B and C coefficients, and then the relationship between carrier occupancy <n> and current density is deduced. The GS peak gain versus <n> is calculated based on the random population model. Then, the modelled GS peak gain as a function of the current density is determined without consideration of the carrier thermal escape process. The gain is measured afterwards by using the Hakki-Paoli method at both 20°C and 60°C, in order to plot the experimental GS peak gain as a function of current density. This is then compared to the modelled GS peak gain plot to estimate the carrier thermal escape coefficient. Finally, by varying the recombination coefficient C, I found if the doping level is high enough to give a C coefficient of ~1×10^{-27}cm^6/s, the infinite T_0 may be achieved at some threshold current densities.

4.1. Growth and Fabrication Details

The wafer was grown by QD Laser Incorporated (Japan). Eight layers of InAs

quantum dot were grown in a MBE system on an n-GaAs substrate. The thickness for each QD layer repeat (barrier and QD) is 40nm. The whole QD active region was sandwiched by a 1400nm thick Si-doped lower n-$Al_{0.4}Ga_{0.6}As$ cladding layer and a 1440nm upper p-$Al_{0.4}Ga_{0.6}As$ cladding layer with varying doping levels. The schematic of the wafer structure is shown in Figure 4.1.

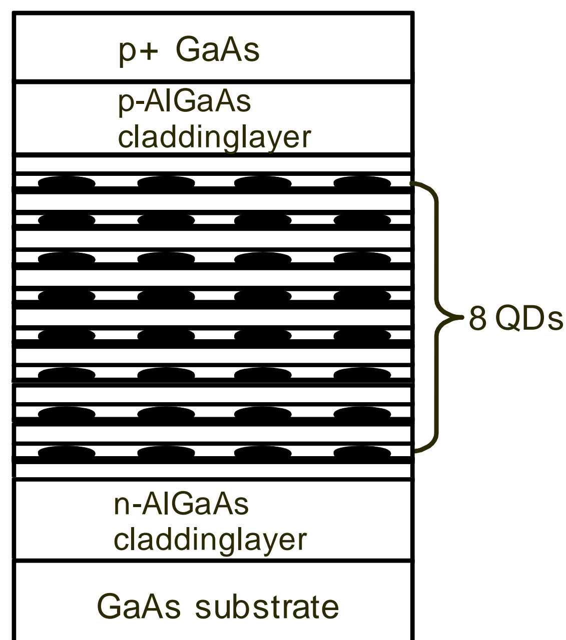

Figure 4.1 The schematic diagram of the wafer growth structure.

The QD sample was then fabricated into 3μm wide ridge waveguide devices with segmented contacts by a dry etch through the QD active region. Thin layers of Au-Zn-Au and In-Ge-Au were thermally evaporated on the top and the bottom of the device respectively, to provide p and n-side ohmic contacts. The fabrication details were described in chapter 2. The multi-section laser devices were then cleaved into bars with different lengths, such as 250μm, 500μm, 750μm, 1mm, 2mm, and 5mm. The facets of the devices were left as cleaved.

4.2. Static Characteristics

Initially, the device was investigated by measuring the room temperature I-V and the room temperature EL spectrum. Then, based on the temperature dependent L-I, T_0 and the differential external efficiency are analysed.

4.2.1. I-V and EL Spectrum

The voltage vs. current is plotted in Figure 4.2 and the differential resistance is determined to be ~3.5ohm. In the following sections, for the dynamic measurement, a 46.5ohm surface mount resistor is used to make the device 50ohm impedance matching. The inset is the CW EL spectrum of the device at low current, showing the emission wavelength is ~1286nm at 26.7A/cm^2. Lasers based on this sample are currently used in the telecommunication area.

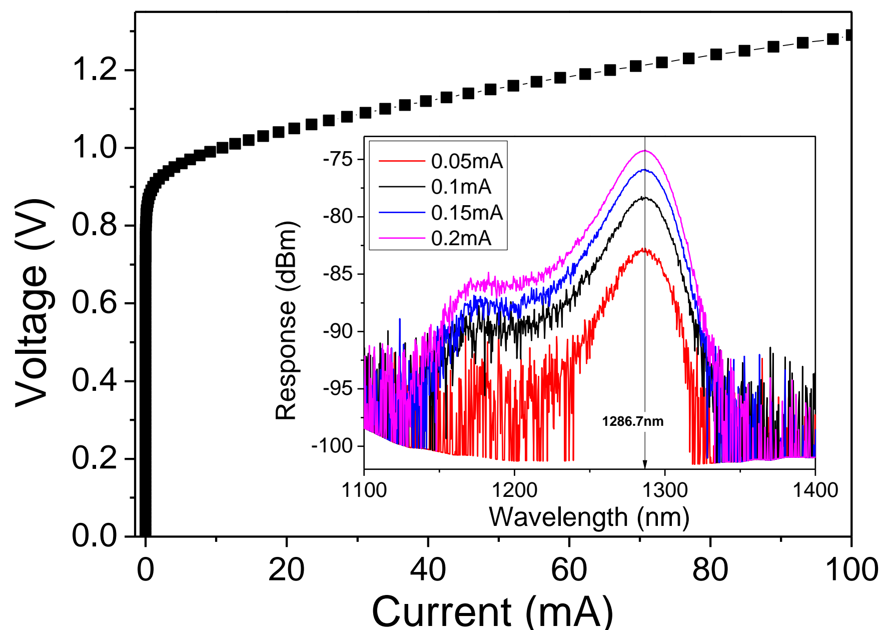

Figure 4.2 Voltage-current characteristics of a 500μm cavity length 3μm wide ridge laser. The inset shows its emission spectrum at low injection current density.

4.2.2. Temperature Dependent L-I

To further investigate the performance of these laser devices, the temperature dependent L-I was measured for different lengths. Figure 4.3 shows the threshold current of different device lengths with increasing device temperature from 10°C to 60°C.

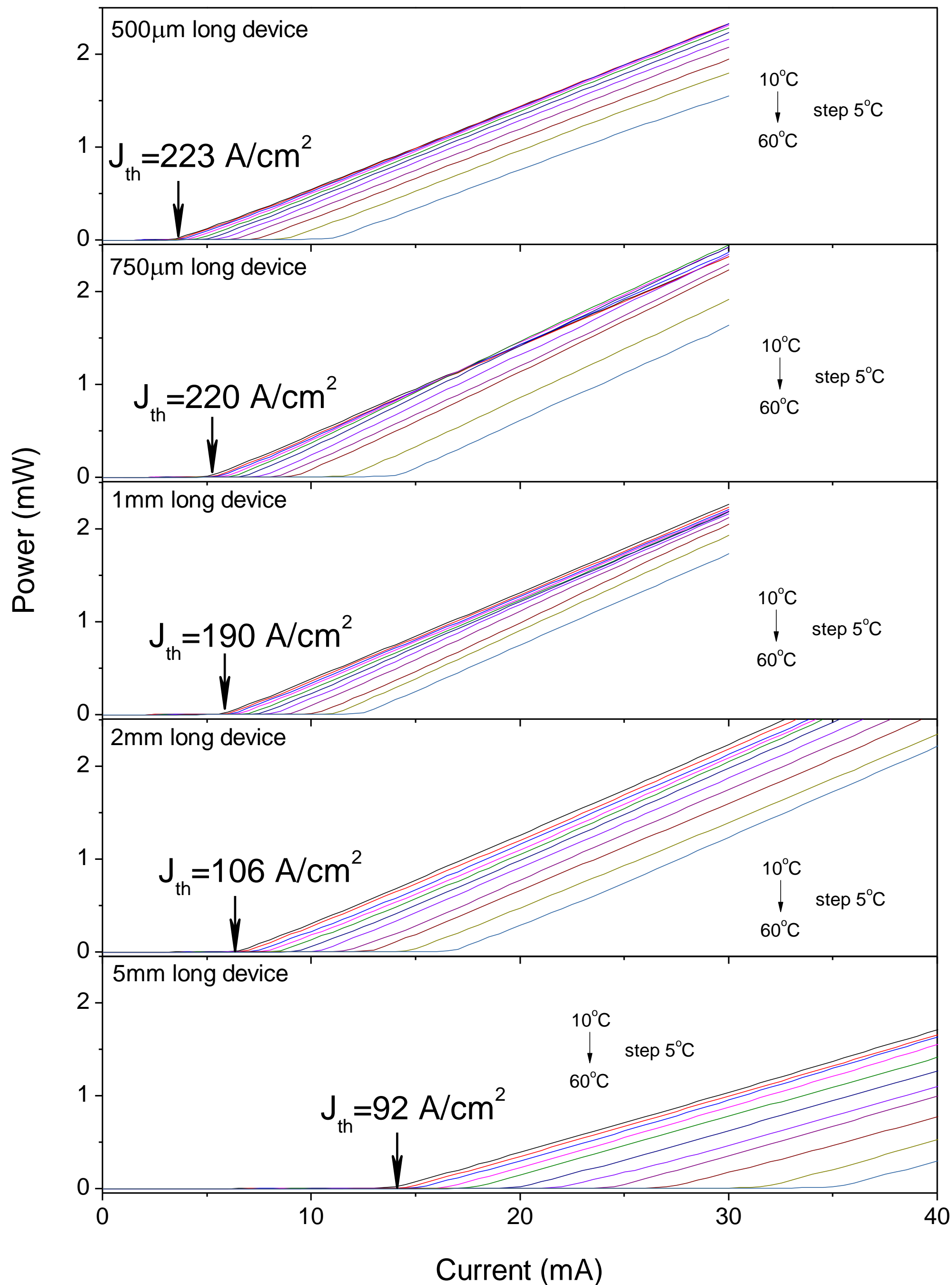

Figure 4.3 Temperature dependent L-I of different device lengths, the temperature is varied from 10 degree C to 60 degree C with a step of 5 degree C.

We can see from the graph that the threshold current density is decreasing with increasing device length, which is due to the decrease of the mirror loss. However, as the total volume is increasing, the threshold current is increasing with increasing cavity length. Based on the L-I data in Figure 4.3, the natural log of the threshold current density (ln_{Jth}) for different lengths at a range of temperatures can be plotted. Based on the temperature dependent ln_{Jth} plot in Figure 4.4, the characteristic temperature T_0 is calculated using equation 1-(1).

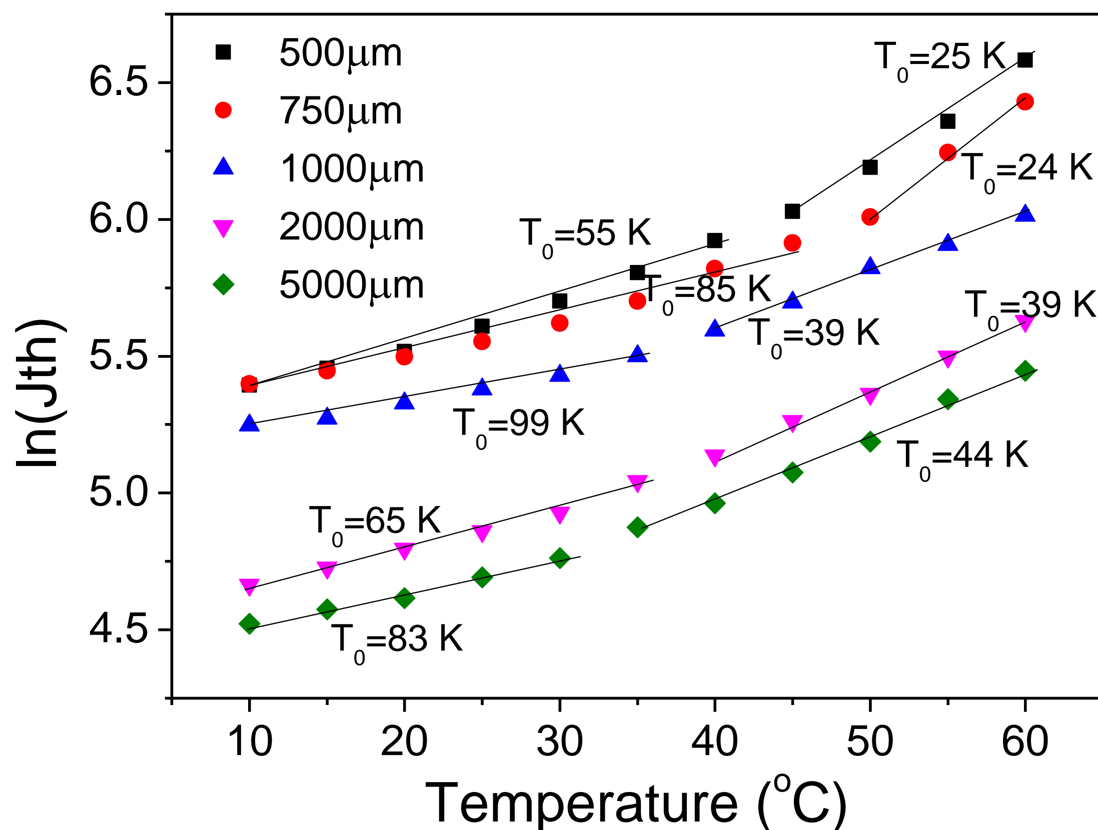

Figure 4.4 T_0 of different device lengths as a function of device temperatures.

In Figure 4.4, for the temperature range from ~10°C to ~40°C, T_0 is nearly two times the value of the T_0 in temperature range from ~40°C to ~ 60°C. Various lines of best fit are shown in Figure 4.4 which illustrate the difficulty in using a single T_0. The 1mm long device has the highest T_0 value around room temperature of ~100K. The T_0 value achieved here is small compared to the

result reported by other groups [1, 2]. In the following sections, the optimisation of p-doping which can improve T_0 performance of the device is discussed based on the small signal modulation measurement associated with Hakki-Paoli gain measurement.

In addition, based on the data in Figure 4.3 and equation 2-(2), the external efficiency of the devices of different lengths at various temperatures is also plotted in Figure 4.5.

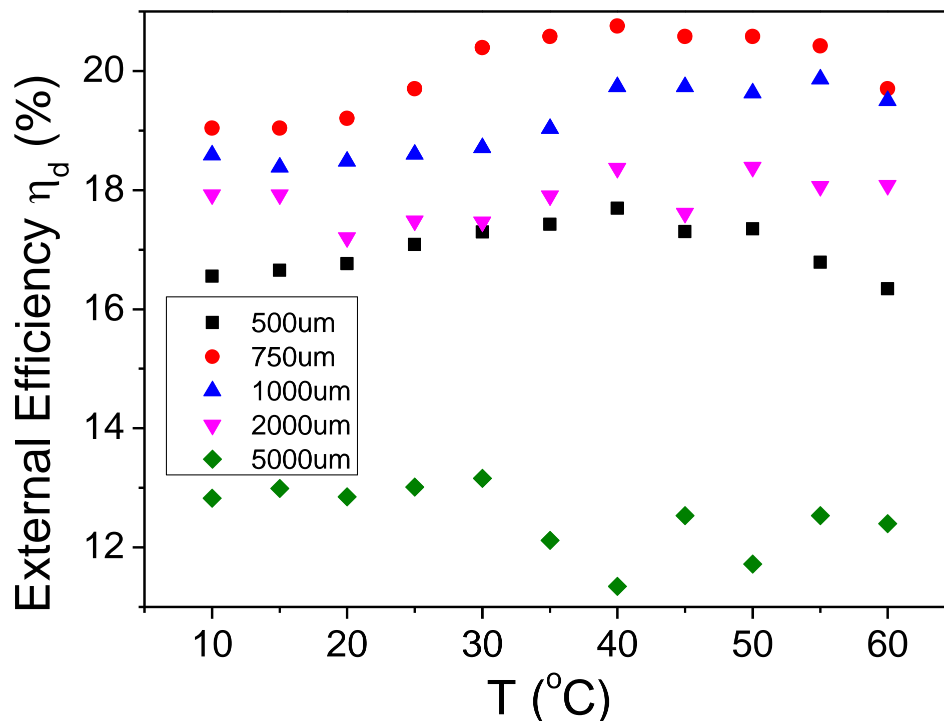

Figure 4.5 External efficiencies as a function of device temperatures for different device lengths.

It can be seen that, there are two competing processed, one is acting to increase slope efficiency, and another process acting to decrease slope efficiency. Devices with various lengths in Figure 4.5 all show this. The external efficiency is increasing slightly with increasing device temperature (10°C~40°C). This is suggestive that the increased homogeneous linewidth with increasing temperature is playing the role [3]. With increasing

temperature, due to the increase of the homogeneous linewidth, more dots may contribute to the lasing process. The efficiency decreased slightly from about 40°C~60°C. The reduction in efficiency may due to the increased non-radiative recombination (such as Auger recombination process) [4] and the carrier thermal escape process.

Figure 4.6 shows the EL spectra from a 1mm long device at three different temperatures, 10°C, 20°C and 40°C respectively.

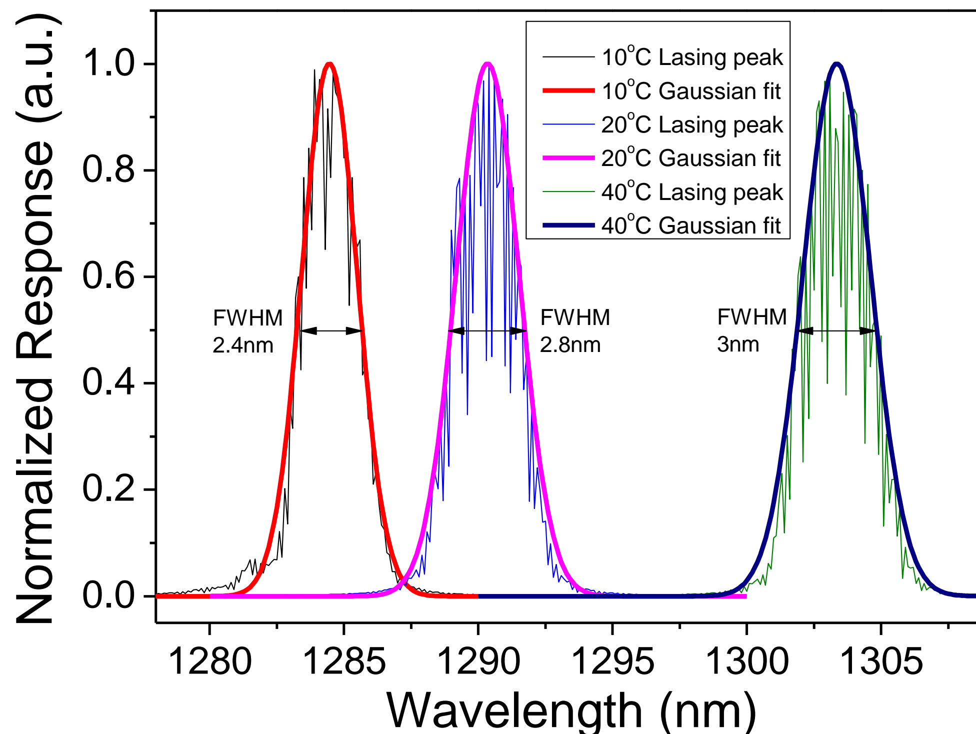

Figure 4.6 Lasing spectra from a 1mm long 3μm ridge width device under a fixed output power at 10°C, 20°C and 40°C respectively.

The spectra were taken at a fixed output power ~2J_{th}. The lasing spectra are plotted in a linear scale and fitted by the Gaussian peak. The FWHMs of the fitted Gaussian peak increase slightly from ~2.4nm to ~3nm in agree with the argument that the linewidth is dominated by the homogeneous linewidth [3]. Furthermore, to confirm this increase in linewidth with increasing sample

temperature, spectra at $1.2J_{th}$ were taken and fitted by Gaussian peak, as shown in Figure 4.7. This also shows the increased lasing FWHM linewidth with increasing temperature.

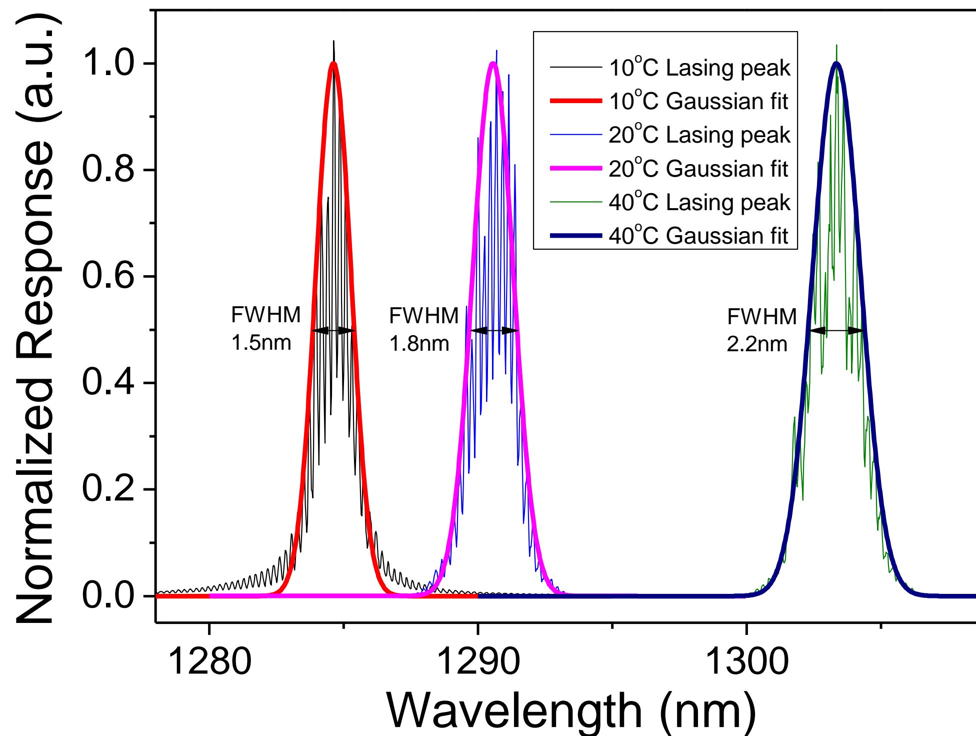

Figure 4.7 Lasing spectra from a 1mm long 3μm ridge width device at 10°C, 20°C and 40°C with bias current of $1.2J_{th}$.

Furthermore, from equation 4-(1):

$$\frac{dP}{dI} \propto \frac{\partial_m}{\partial_i + \partial_m} \qquad 4\text{-}(1)$$

here, ∂_i is the internal loss, ∂_m is the mirror loss. Without gain saturation or thermal issues, then a large ∂_m (e.g. small cavity length L) is required to achieve high efficiencies. However, gain saturation is significant in QDs [5]. Experimentally, a maximum in efficiency is observed for the 750μm device. The external efficiency for different device lengths decreases from device length of 750μm to 5000μm gradually. The decrease of the external efficiency is suggestive to the decrease of the differential gain in the device.

Figure 4.8 plots the QD peak modal gain calculated using a random population model [6]. The lower efficiency of the 500μm device as compared to the 750μm one may be due to the increase of the ES carrier population in the 500μm long device, which acts as a form of non-radiative recombination and reduces η_i. 500μm long device has positive gain on both GS and ES when it is lasing, which may cause its low external efficiency due to a strong excited state occupancy.

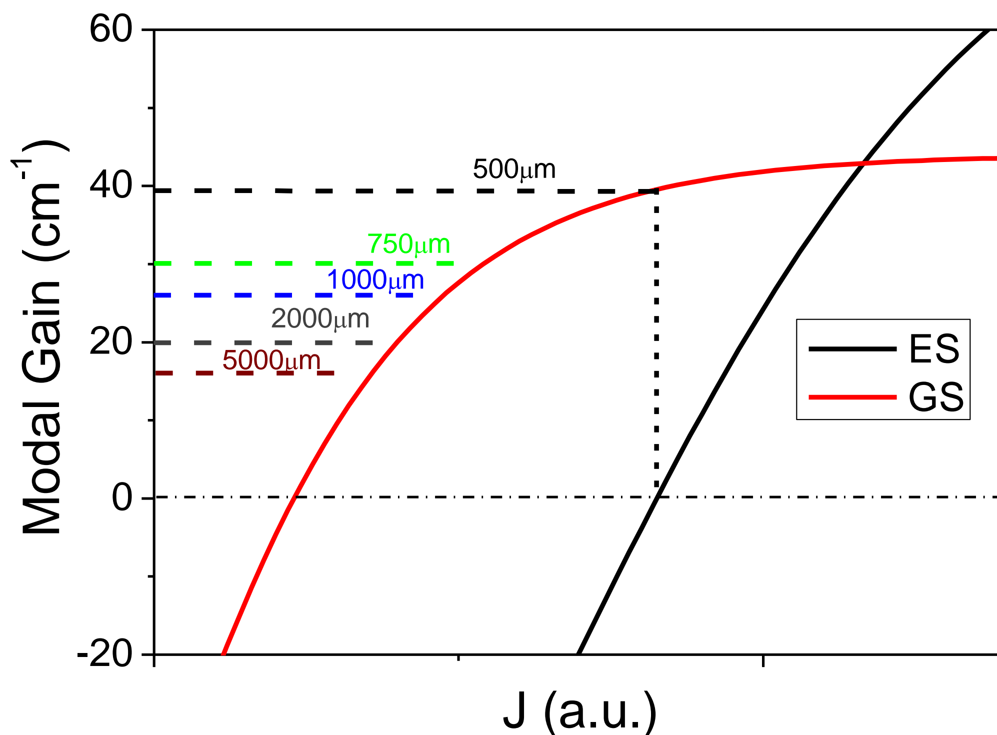

Figure 4.8 GS and ES modal gain as a function of current density, the dish line in different colours indicate the threshold modal gain for device of different lengths.

4.3. Temperature Dependent Differential Carrier Lifetime

The 3μm wide ridge device is cleaved into 250μm length and the facet is left as cleaved. By using the small signal modulation method discussed in chapter 2&3, the differential carrier lifetime is measured and shown in Figure 4.9. The inset shows the L-I curve of this device, as super luminescence occurs at

~1500A/cm^2 the differential carrier lifetime is measured where the stimulated rate is low, <1200A/cm^2. The differential carrier lifetime is observed to decrease with increasing current density which is similar to the previous results in chapter 3. And the differential carrier lifetime at 60°C is observed to be longer compared to the one at 20°C, it may due to the increase in the electron relaxation time from the ES to the GS with increasing temperature [7].

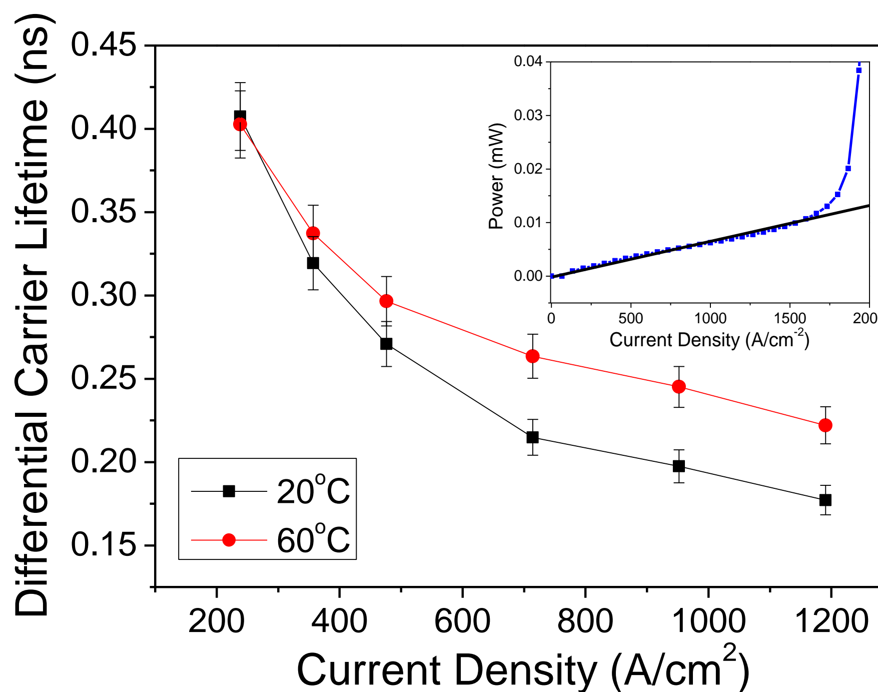

Figure 4.9 Temperature dependent differential carrier lifetime measured from a 3μm wide 250μm long device.

As mentioned in chapter 3, based on equation 3-(4) the coefficient *A*, *B* and *C* can be deduced by fitting the experimental data in Figure 4.9. The coefficients are shown in Figure 4.10. It can be observed that all recombination coefficients reduce with increasing temperature, it has the same trend for *A*, *B*, *C* as compared to the results in chapter 3, and the order of magnitude for the *A*, *B*, *C* coefficients agrees with the previous result in chapter 3. However, the values of the recombination coefficients *A*, *B* and *C* discussed in this chapter are quite different from the values discussed in chapter 3. This may due to the

samples investigated in different chapters have different epitaxy structures (5 layers of DWELL structure in chapter 3 and 8 layers of QD structure in chapter 4).

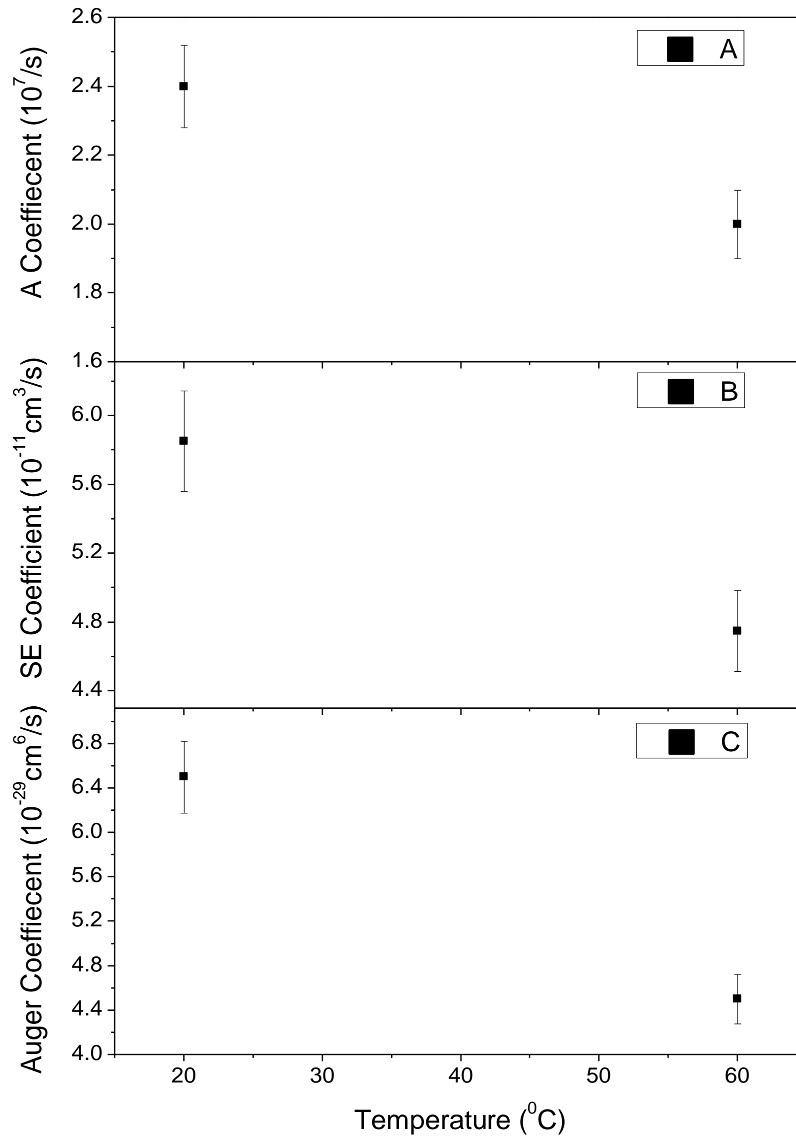

Figure 4.10 Temperature dependant A, B, C coefficients from a 250μm long device.

4.4. Gain vs. Temperature

In this section the gain is measured using Hakki-Paoli method [8] from a 250μm long device at 20°C and 60°C, respectively, with a constant junction temperature. The experimental details were introduced and discussed in chapter 2.

4.4.1. Gain Measured by Hakki-Paoli Method at 20°C

The gain spectra measured using the Hakki-Paoli method at 20°C is plotted in Figure 4.11.

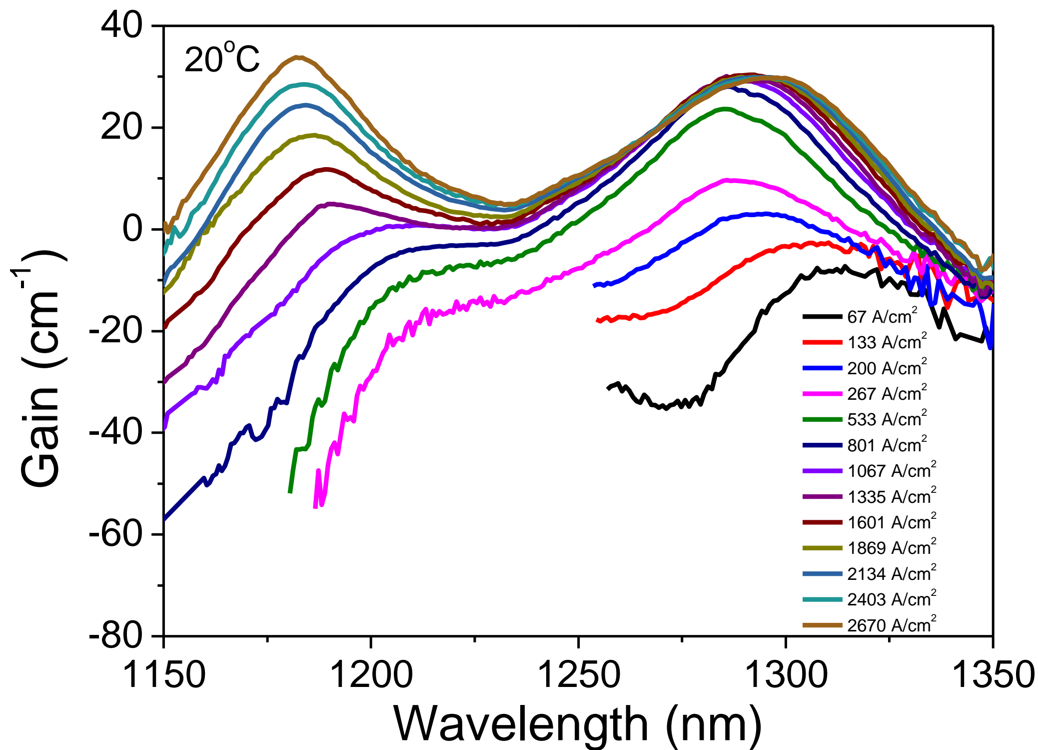

Figure 4.11 The gain spectra measured using Hakki-Paoli method for the laser with 8 QDs layers, 250μm cavity length and 3μm ridge width at 20°C.

From the gain spectrum, the maxima gain before lasing threshold (from ES at ~1180nm) is ~34cm^{-1} for this sample at 20 degree C. Moreover, the internal loss can be estimated from the asymptote of the long wavelength tail on the gain plot (Figure 4.11) which is approximately 10cm^{-1}. Due to the removal of self-heating effects (discussed in chapter 2), the effects of free-carriers alone can be observed on the gain spectra at current densities up to 2.67kAcm^{-2}, which is beyond the saturation of the GS gain.

Furthermore, in Figure 4.11, it can be observed at low current injection levels

the GS gain peak blue shifts prior to remaining fixed in wavelength while the peak gain value saturates. After the GS gain saturation, the GS net modal gain peak broadens with increasing injection current, along with a reduction observed in peak net modal gain [9]. This is because of the free carrier effect based on increased dot occupancy. For the ES, the peak position is continuously blue-shifting with increasing injection level [9].

4.4.2. Gain Measured by Hakki-Paoli Method at 60°C

Figure 4.12 shows the net modal gain spectra measured at 60 degree C.

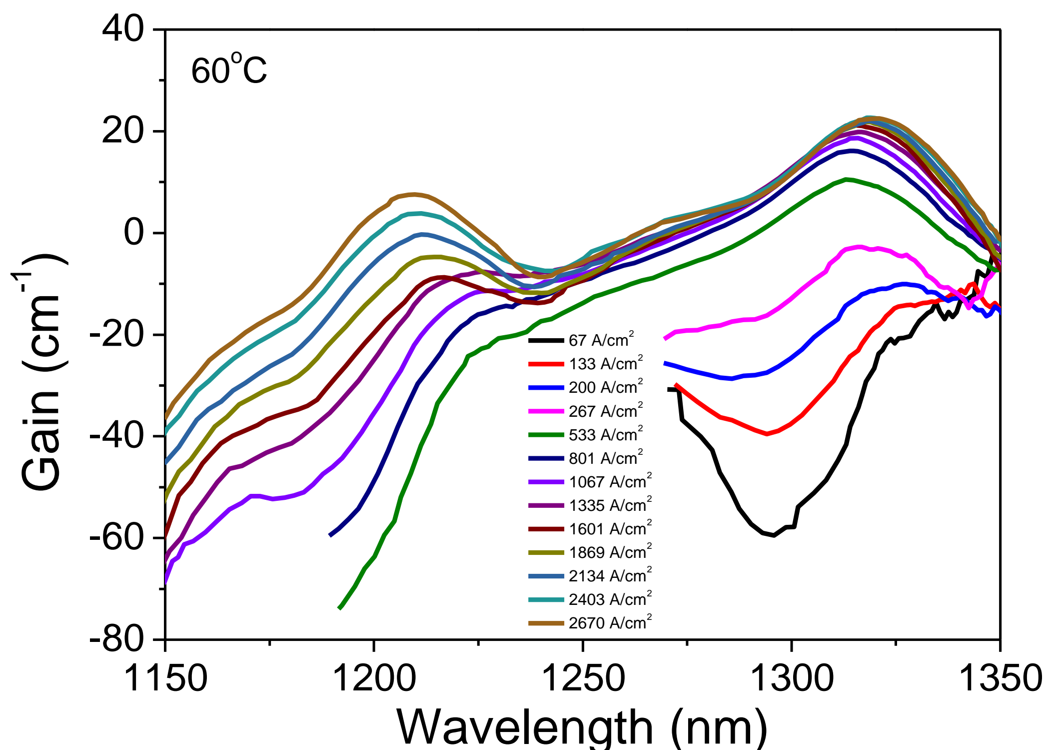

Figure 4.12 The gain spectra measured using Hakki-Paoli method for the laser with 8 QDs layers, 250μm cavity length and 3μm ridge width at 60°C.

The gain spectra at 60°C have a similar shape as compared to the result at 20°C. The peak gain values are reduced at 60°C compared to the value at 20°C. This is attributed to the thermal escape of carriers.

4.5. Modelling and Analysis

4.5.1. Random Population and Fermi Distribution

There are two models describing the carrier filling process, one is the random population process [6], the other is the Fermi distribution [10], as shown in Figure 4.13 (simulated by Dr. David Child). In the model, a C++ program is coded to simulate the optical gain in a single QD and the spontaneous emission emitted from a single QD under Fermi carrier distribution or random carrier distribution. The result from a single QD is then integrated by the number of QDs assumed in the active region. The fitting parameters used in the simulator are listed in table 4.1:

Fitting Parameters	Value
Homogeneous linewidth	5meV (at 300K)
Energy shift factor	0.09 (volume to carriers per dot conversion)
State separation	106nm (from Figure 4.2)
GS wavelength	1286nm (from Figure 4.2)
Inhomogeneous linewidth of ensemble	32meV
Number of QDs	100000
Barrier energy	250meV

Table 4.1 Fitting parameters used in the gain and spontaneous emission model under Fermi and random carrier distribution.

It can be seen in Figure 4.13(a) and (c), the spontaneous emissions as a function of carrier occupancy for Fermi/random occupation are very similar. Figure 4.13 (b) and (d) show the peak gain from both Fermi distribution and random population models vs. carrier occupancy.

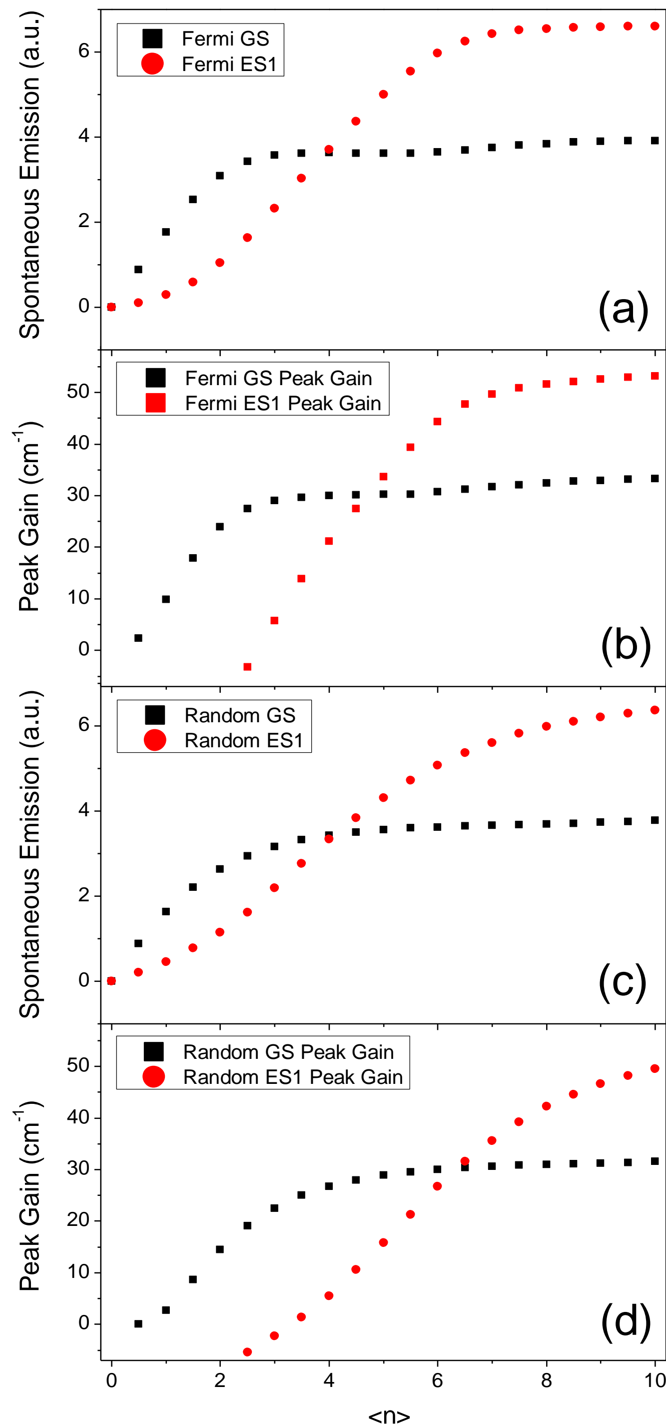

Figure 4.13 (a) &(c) Spontaneous emission as a function of carrier occupancy of both Fermi and random models, (b) peak gain for Fermi distribution model, (d) peak gain for random population model.

For the Fermi model, the ES gain is larger than the GS gain when <n> is bigger than ~4.7, which is ~6.4 in the random model. Previous investigations on 1.3μm quantum dot laser device [11] have suggested the carrier is a random population. However, in terms of dot occupancy, there is little difference (~50%) between models for carrier distribution.

In the following, I assume a random population distribution. For a random population, the probability of a particular dot to have 0, 1, 2, 3…electron-hole pairs (<n>) is determined by Poisson statistics, which indicates the probabilities of the number of carriers in one quantum dot for a given average number of e-h pairs per QD. Based on random filling of the QD and state saturation via the Pauli exclusion principle, it then enables the modelling and calculation of the gain from the ensemble of quantum dots at a given current.

Based on the A, B, C coefficients obtained from Figure 4.9, the carrier lifetime (excluding thermal escape), τ_c, at 20°C and 60°C as a function of carrier occupancy can be calculated based on equation 4-(2):

$$\frac{1}{\tau_c} = A + B\left(\frac{<n>}{V_{Dots}}\right) + C\left(\frac{<n>}{V_{Dots}}\right)^2 \qquad \text{4-(2)}$$

Where *<n>* is the average dot occupancy, V_{dot} is the dot volume. Then, based on the calculated τ_c, the relationship between the current density *J* and the carrier occupancy *<n>* is given by equation 4-(3) based on random population model [12]:

$$J = \frac{<n> qN_{qd}N_{layer}}{\tau_c \cdot \eta_i} \quad 4\text{-}(3)$$

Where the electron charge q=1.6×10^{-19}, areal dot density N_{qd}=4×10^{10}, number of layers N_{layer}=8 and the internal quantum efficiency η_i =0.24 (calculated from Figure 4.5). From 4-(2) and 4-(3) the carrier occupancy as a function of current density J is plotted in Figure 4.14. It shows a highly non-linear <*n*>: J relationship.

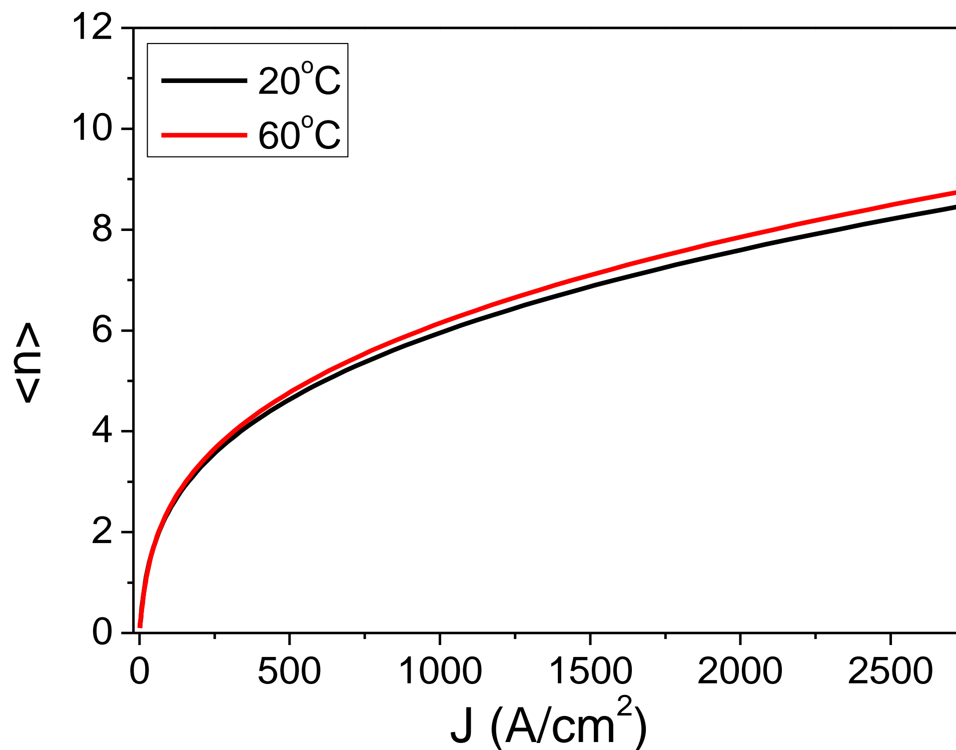

Figure 4.14 The relationship between current density (J) and the carrier occupancy (<*n*>) obtained from the model.

4.5.2. Peak Gain Model

The relationship between the peak gain from the ground/excited state of the QDs and the carrier occupancy can be determined based on the property of Poisson statistics. At the current where the peak gain from the GS and ES are equal, there are equal numbers of carriers in both levels and then the mean

dot occupancy can be deduced. Based on the model [6], the GS peak gain and the ES peak gain vs. carrier occupancy is simulated, which is shown in Figure 4.15. The inset is the gain model based on the Poisson distribution [13] (random population) theory (simulated by Professor Richard Hogg).

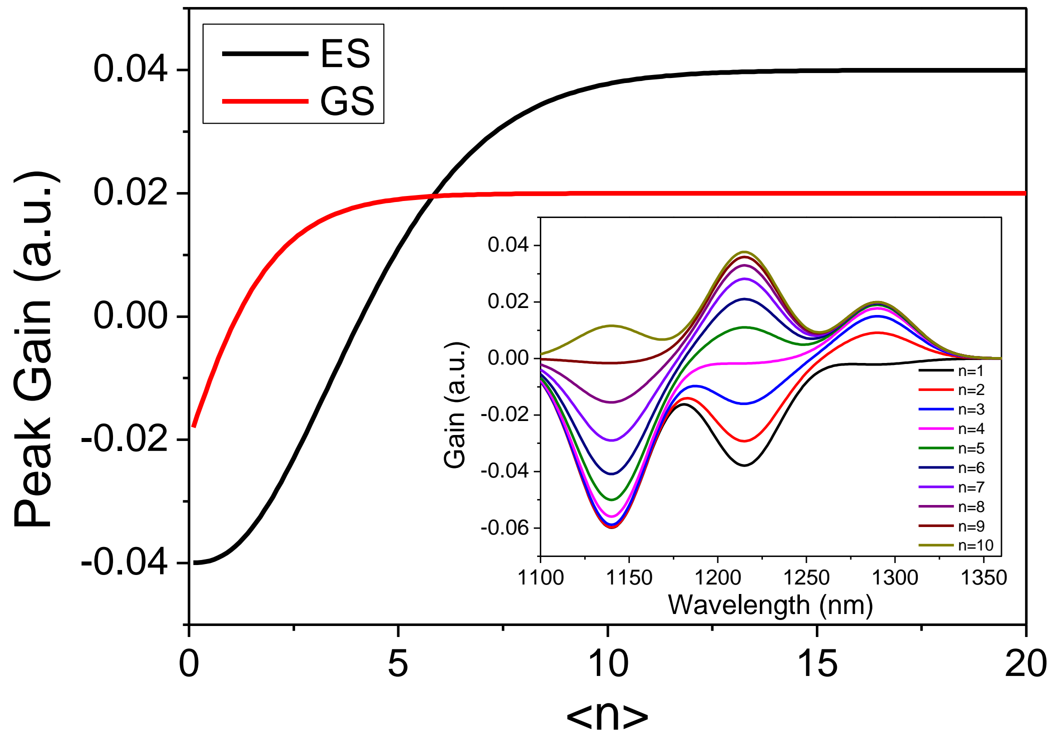

Figure 4.15 The simulated GS and ES gain vs. carrier occupancy, the inset shows the plot based on the random population model (modelled by Professor Richard Hogg).

From this Figure, it can be seen that the GS peak gain increases with increasing carrier occupancy, and it saturates when carrier occupancy is bigger than about 7 electron-hole pairs per dot. For the ES, the peak gain increases with increasing carrier occupancy and it saturates when carrier occupancy is bigger than about 14 electron-hole pairs per dot. Figure 4.14 and Figure 4.15 are used as a look-up table when the peak gain versus the current density is plotted in Figure 4.16 without the consideration of the thermal escape coefficient of the carriers.

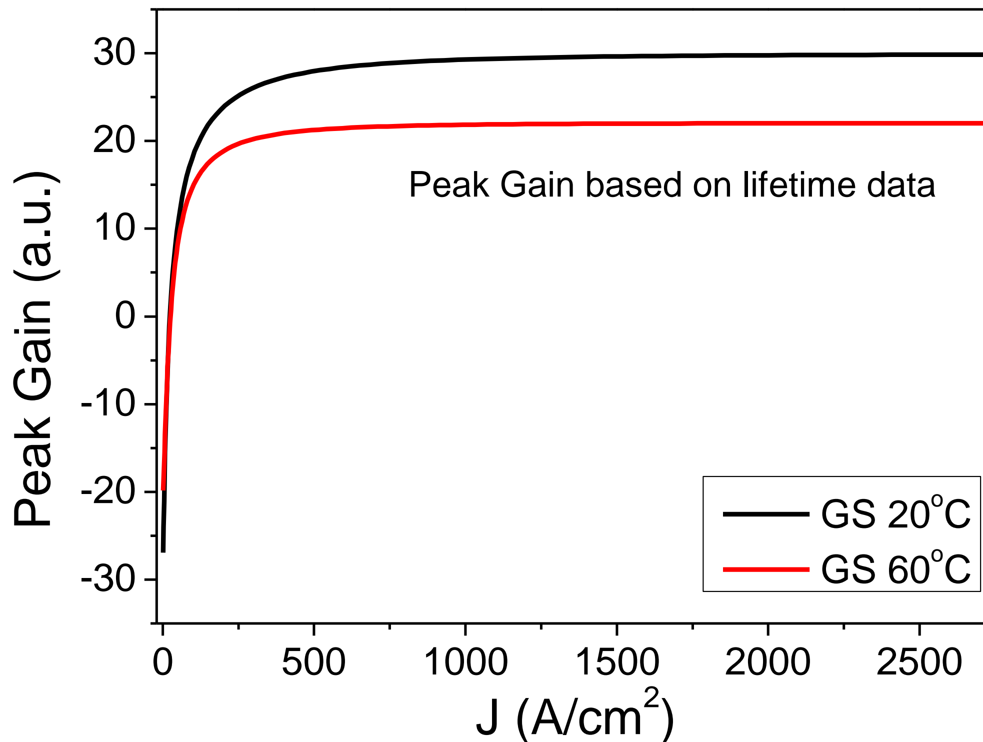

Figure 4.16 The calculated GS peak gain based on the random population model.

To further investigate this device, in the following section, the thermal escape process of the carrier will be considered and analysed. Based on the experimental GS and ES gain measured by the Hakki-Paoli method. The thermal escape coefficient will be discussed based on the difference between the calculated peak gain from the carrier lifetime which excludes thermalisation effects and the experimentally measured peak gain.

4.5.3. Empirical Fit

Based on the experimental data in Figure 4.11 and 4.12, the symbols in Figure 4.17 plot the GS peak gain as a function of injection current at two temperatures (20°C and 60°C), with the junction temperature being maintained constant as described in chapter 2. At 20°C the GS peak gain saturates while the current density is beyond ~1250A/cm^2. At 60°C the GS peak gain is saturated when the current density reaches ~1750A/cm^2.

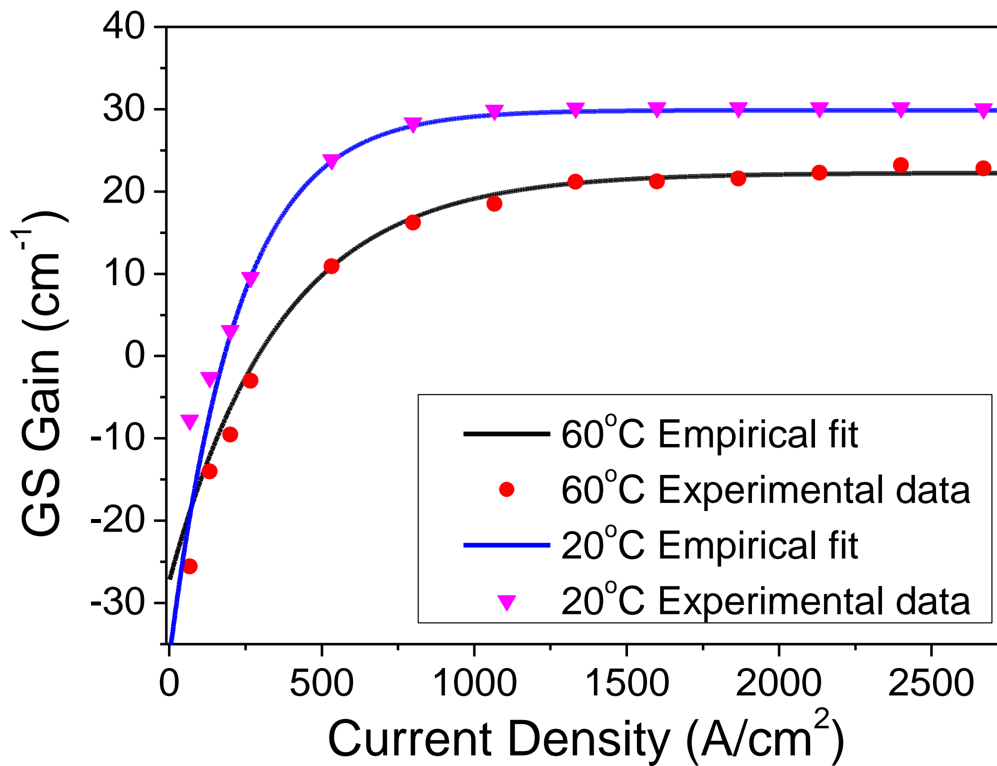

Figure 4.17 Peak net modal gain for the ensemble of GS at 20°C and 60°C as a function of carrier density.

The peak gain data is fitted by using the empirical model described by Zhukov *et al*. [14]. The fitting result is also shown in Figure 4.17 in solid line. The equation for this empirical fit is shown in 4-(4):

$$G = G_{sat}[1 - EXP(-\gamma \frac{J - J_0}{J_0})] \qquad 4\text{-}(4)$$

Where J is the current density and J_0 is the transparency current density of the device and γ is a fit parameter. The parameters used during fitting are shown in table 4.2:

Empirical fit	Gain parameters		
	G_{sat} (cm^{-1})	J_0 (Acm^{-2})	γ
20°C GS	30±1	180±9	0.8±0.05
60°C GS	22±1	290±15	0.8±0.05

Table 4.2 Parameters used for the empirical model.

Here G_{sat} is measured from the gain plot in Figure 4.11 and 4.12, J_0 data is calculated from length dependant data by plotting the threshold density versus the inverse cavity length, the intercept of the linear fit gives us the J_0 and γ is chosen for the best fit of the experimental data. J_0 at 20°C is comparable to the device discussed in the previous chapter which showed J_0=75±5Acm^{-2} for the 15μm ridge laser with 18acc/QD [11]. The number of QDs in the present sample is almost double that of the previous sample (~48×10^{10}cm^{-2}: ~28×10^{10}cm^{-2}) and increased internal loss (3μm compared to 15μm ridge)

The fitted GS peak gain curve in Figure 4.17 should be comparable to the peak gain curve calculated based on the differential carrier lifetime data in Figure 4.16. The comparison of two peak gain curves is plotted in Figure 4.18. The calculated GS gain based on the differential carrier lifetime data does not include the carrier escape process. In the thermal escape process, the electron from the QD GS is thermally activated to an intermediate state, and the thermal activation energy may indicate the energy difference between GS and ES or GS and 2D states [15].

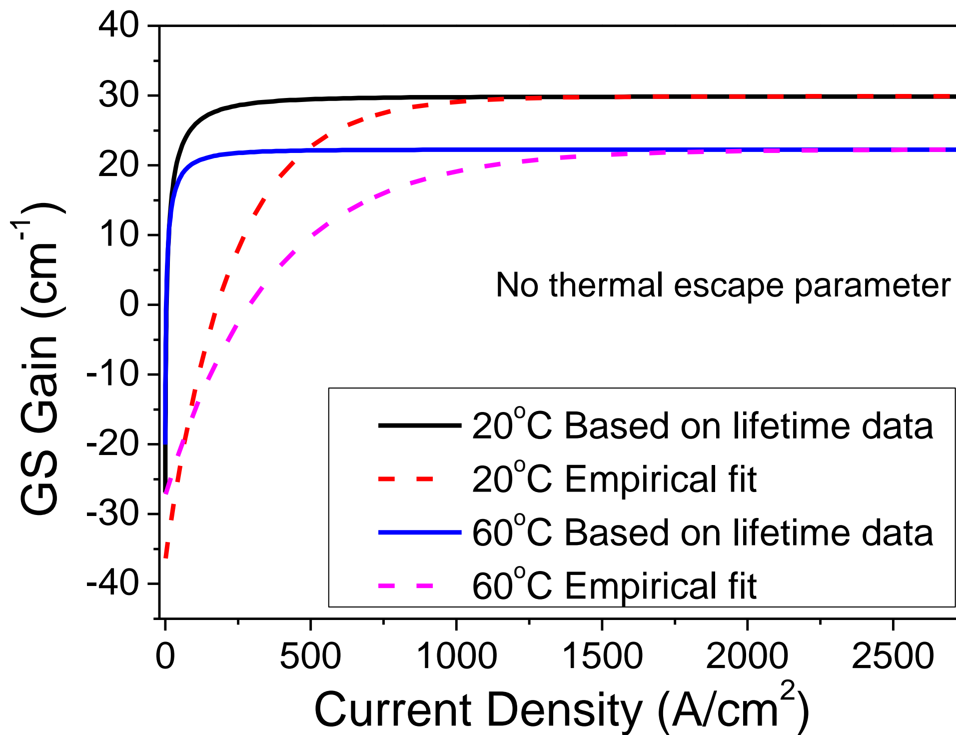

Figure 4.18 Calculated GS peak gain compared to the empirical gain fit based on the experimental GS gain data.

The difference between the modelled differential carrier lifetime based data and the empirical fit is attributed to be exclusively due to the carrier escape process. In order to determine the carrier thermal escape coefficient (τ_{escape}), the carrier life τ_c with the thermal escape process can be write in the format of equation 4-(5):

$$\frac{1}{\tau_c} = \frac{1}{\tau_{noescape}} + \frac{1}{\tau_{escape}} \qquad 4\text{-}(5)$$

This carrier lifetime data which includes the carrier thermal escape process is used in equation 4-(3) to re-calculate the corresponding current density. Then following the steps in section 4.5.2 again, a new plot of the calculated GS peak gain as a function of the current density is made at two temperatures. In this case the carrier thermal escape process is considered, with a best fit of the carrier thermal escape coefficient.

Figure 4.19 shows the re-calculated GS peak gain as a function of the current density (solid line). It is in a good agreement with the experimental data based on the empirical fit of Zhukov *et.al.,* when the carrier thermal escape is included. The carrier thermal escape coefficients are found to be 0.6ns and 0.3ns at 20°C and 60°C, respectively.

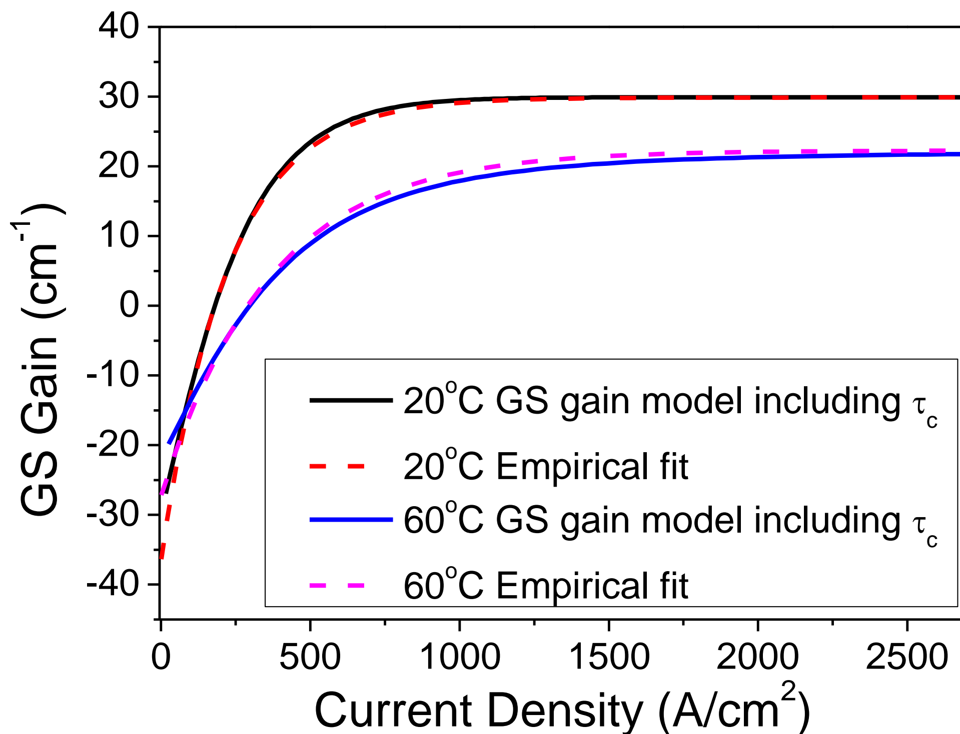

Figure 4.19 Calculated GS peak gain including carrier escape effect compared to the empirical fit based on the experimental GS gain data.

It has been reported that in a QW device, the thermal escape coefficient, τ_0^{TE}, is determined by equation 4-(6) [15]:

$$\tau_0^{TE} = d\sqrt{\frac{2\pi m^*}{kT}}e^{+\Delta E_b(F)/kT} \qquad 4\text{-}(6)$$

Where *d* is the well width, m* is the effective mass, *k* is the Boltzmann coefficient, *T* is temperature (K), $\Delta E_b(F)$ is the effective barrier height which is one of the key coefficients in equation 4-(6). The well width is assumed to be

8nm in the following calculation. Figure 4.20 (a) is an energy band diagram reproduced from [16], the effective barrier height is ~250meV (in agreement with [17]) for electrons and ~190meV for holes.

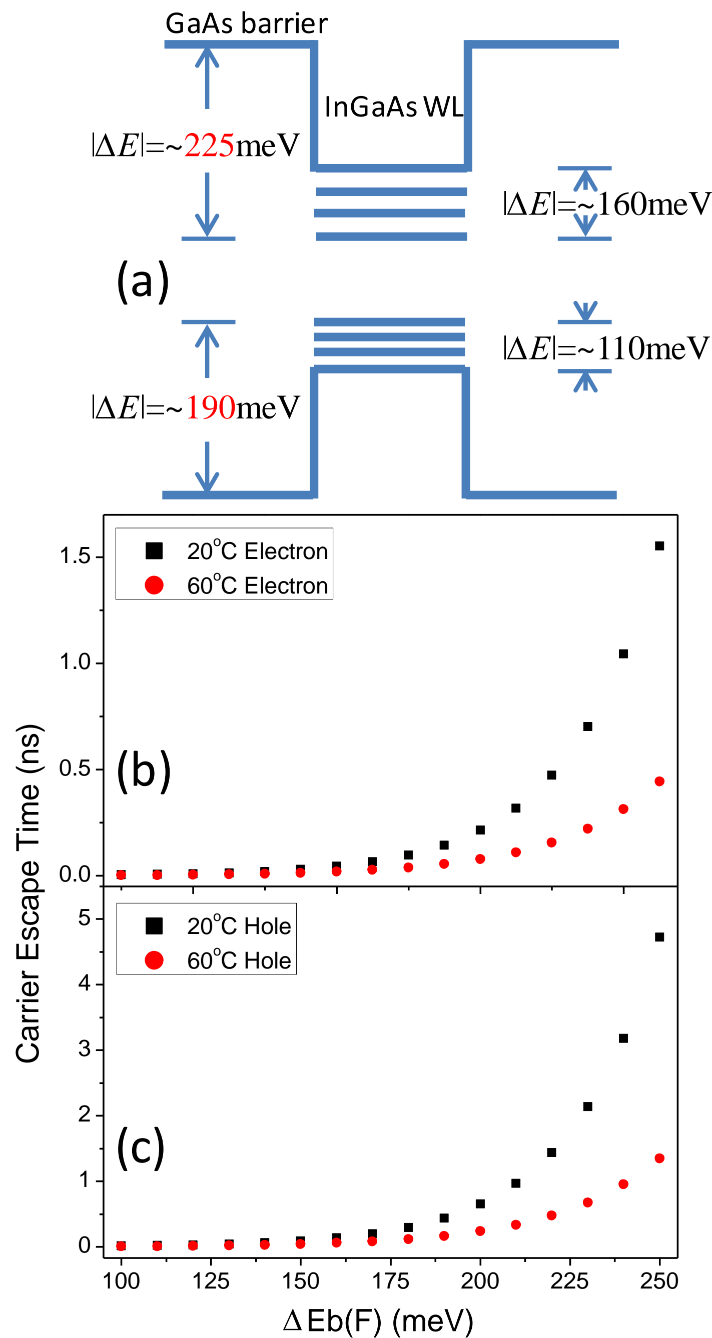

Figure 4.20 (a) Band energy diagram of QD [16] and the carrier escape time for (b) electrons and (c) holes as a function of the effective barrier height.

Since the barrier height of the electron and the hole are not measured for my

device, the carrier (electron or hole) escape time at 20°C and 60°C as a function of $\Delta E_b(F)$ is plotted in Figure 4.20(b) &(c). Whilst the barrier height and effective mass is uncertain, good agreement between the experimentally determined τ_{escape} (0.6ns, 0.3ns) and calculations is obtained.

Inspecting Figure 4.20, if electron escape dominates the thermal escape process, from Figure 4.20(b) the effective barrier height is ~230meV when the result based on equation 4-(5) is similar to the coefficients obtained from Figure 4.19. If hole escape dominates the thermal escape process, from 4.20(c) the effective barrier height is ~190meV. These values for effective barrier height are close to the parameters obtained based on Figure 4.19. These calculations and observations suggest that the thermal escape process is from the GS to GaAs layers.

4.5.4. Explore Possibility of Obtaining Infinite T_0

Comparing the previously calculated GS peak gain Figure 4.19, for a laser device, if it is operated at a current density with the gain curves at two different temperatures cross each other in the positive region, then the gain in the laser cavity is the same at each temperature and the laser device will be insensitive to the temperature [7]. For the present device, this is not the case.

Figure 4.19 shows that the crossing point is in the negative gain region, it is therefore important to explore the possibility to “move” the crossing point up to the positive gain region in order to make a temperature insensitive laser device. The infinite T_0 operating current position (crossing point) is

investigated by varying the Auger recombination coefficient. Based on the previous experimental result in Figure 4.10, the Auger recombination coefficient at 60 degree C is about 70% of the value at 20 degree C one. In Figure 4.21, the Auger recombination coefficient is varied in different orders and the C coefficient used at 60 degree C is set to be 70% of the 20 degree C value.

In Figure 4.21, the temperature dependent gain curves intersect each other in the positive gain region when the Auger recombination coefficient increases up to $8\times10^{-27}cm^6/s$. The crossing point further increases to the positive gain region with increasing Auger recombination coefficient. It is known that the Auger recombination coefficient increases with increasing p-doping level [18].

Based on the modelling in Figure 4.21, the GS saturation gain is observed to decrease with increasing p-doping level. The GS peak net gain for the p-doped device is less than that of the un-doped device at low injection ($<1300A/cm^2$) [19]. At high injection, due to the reduced gain saturation effect by p-doping, the GS net gain is higher for the p-doped sample, as shown in Figure 4.22 [19]. So the deduced Auger coefficient of $8\times10^{-27}cm^6/s$ from the modelling may be over estimated in the real case as this factor is not considered. The previous results in chapter 3 showed that, the Auger coefficient increased from $4.8\times10^{-29}cm^6/s$ to $9.8\times10^{-29}cm^6/s$ with doping level increased from 0 to 18acc/dot. The trend in [20] indicates that the lifetime ratio decreases (corresponding to the increase of the Auger coefficient) with increasing doping level up to 30acc/dot.

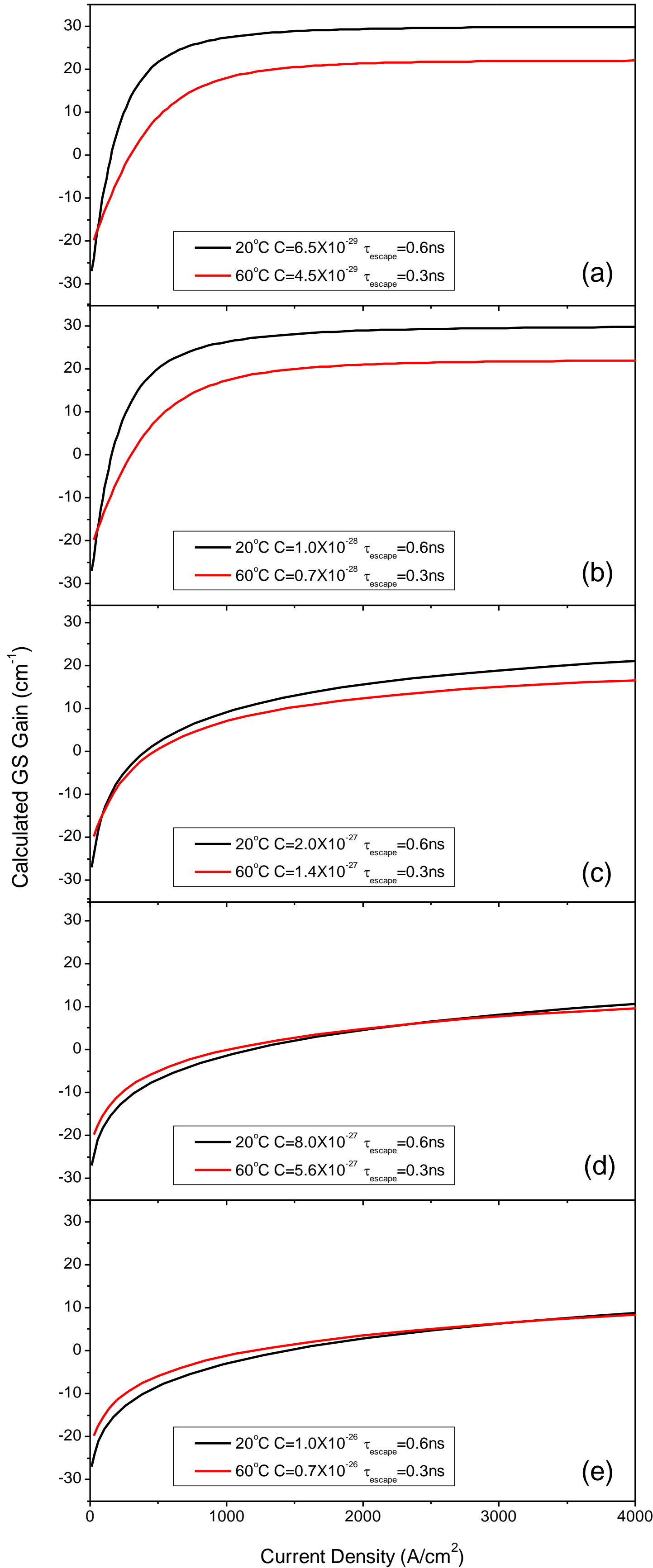

Figure 4.21 Calculated GS peak gain including carrier escape effect as a function of Auger recombination coefficients.

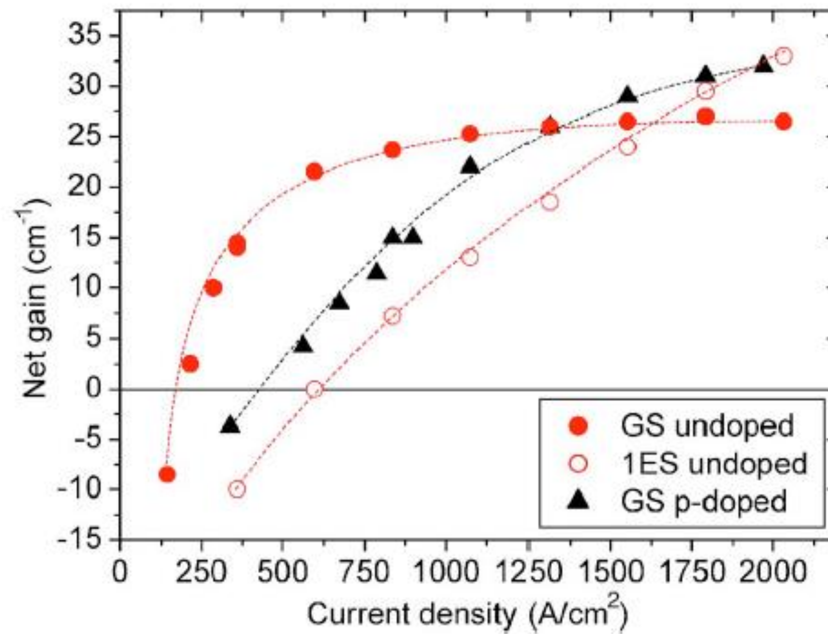

Figure 2.22 Peak net gain as a function of current density at room temperature [19].

4.6. Conclusion

In this chapter, the growth structure is illustrated, the static characteristic of the laser device is investigated such as L-I, EL, temperature dependent L-I and the differential external efficiency. The characteristic temperature, T_0, is measured and discussed. The lasing peak FWHMs at $2J_{th}$ and $1.2J_{th}$ as a function of temperature are investigated. In order to improve the temperature insensitive performance, firstly the dynamic properties of this device is analysed such as the differential carrier lifetime (A, B, C coefficients are also determined), then the gain at different temperatures are measured using Hakki-Paoli method. The difference between the Fermi distribution model and random population model is briefly discussed. The device discussed in this chapter is assumed to follow the random population model. The peak gain as a function of current density is plotted based on the random population model. By comparing the modelling data to the experimental data, the carrier thermal

escape coefficients are found. Finally, based on modelling, with increased Auger coefficient (by increasing doping level in this kind of device), it is suggested that temperature stable operation is possible.

4.7. Future Work

Future possible work is to grow a series of wafers under identical growth conditions except the variation of the modulation p-doping levels. Samples should be fabricated into narrow ridge device. The L-I, Hakki-Paoli gain measurement, differential carrier lifetime and the modelling discussed in this chapter should be followed in the future run, in order to confirm whether the temperature insensitive laser device is possible to achieve based on higher p-doping levels. The relative roles of Auger, thermal escape and homogenous linewidth can then be deduced.

Reference

1. O. B. Shchekin and D. G. Deppe, "1.3μm InAs quantum dot laser with To=161 K from 0 to 80 degrees C," Appl. Phys. Lett. 80, 3277-3279 (2002).
2. O. B. Shchekin and D. G. Deppe, "Low-threshold high T_0 1.3μm InAs quantum-dot lasers due to P-type modulation doping of the active region," IEEE Photon. Technol. Lett. 14, 1231-1233 (2002).
3. M. Sugawara, K. Mukai, Y. Nakata, H. Ishikawa, and A. Sakamoto, "Effect of homogeneous broadening of optical gain on lasing spectra in self-assembled $In_{(x)}Ga_{(1-x)}As$/GaAs quantum dot lasers," Phys. Rev. B. 61, 7595-7603 (2000).
4. M. Gurioli, A. Vinattieri, M. Colocci, C. Deparis, J. Massies, G. Neu, A. Bosacchi, and S. Franchi, "Temperature dependence of the radiative and nonradiative recombination time in GaAs/$Al_{(x)}Ga_{(1-x)}As$ quantum-well structures," Phys. Rev. B. 44, 3115-3124 (1991).
5. G. Park, O. B. Shchekin, and D. G. Deppe, "Temperature dependence of gain saturation in multilevel quantum dot lasers," IEEE J. Quantum Electron. 36, 1065-1071 (2000).
6. M. Grundmann and D. Bimberg, "Theory of random population for quantum dots," Phys. Rev. B. 55, 9740-9745 (1997).
7. S. Fathpour, Z. Mi, P. Bhattacharya, A. R. Kovsh, S. S. Mikhrin, I. L. Krestnikov, A. V. Kozhukhov, and N. N. Ledentsov, "The role of Auger recombination in the temperature-dependent output characteristics ($T_0=\infty$) of p-doped 1.3μm quantum dot lasers," Appl. Phys. Lett. 85, 5164 (2004).
8. B. W. Hakki and T. L. Paoli, "Gain spectra in GaAs double-heterostructure injection lasers," J. Appl. Phys. 46, 1299-1306 (1975).
9. H. Shahid, D. T. D. Childs, B. J. Stevens, and R. A. Hogg, "Negative differential gain due to many body effects in self-assembled quantum dot lasers," Appl. Phys. Lett. 99(2011).
10. V. Zeghbroeck, Principles of semiconductor devices and heterojunctions (Prentice Hall PTR, 2007).

11. R. R. Alexander, "GaAs based quantum dot lasers for 1.3μm optical communications," (University of Sheffield, Sheffield, 2009).
12. L. A. Coldren, S. W. Corzine, and M. L. Mashanovitch, Diode lasers and photonic integrated circuits (Wiley. com, 1995), Vol. 218.
13. L. Schrottke, M. Giehler, M. Wienold, R. Hey, and H. T. Grahn, "Compact model for the efficient simulation of the optical gain and transport properties in THz quantum-cascade lasers," Semiconduct. Sci. Technol. 25(2010).
14. A. E. Zhukov, A. R. Kovsh, V. M. Ustinov, A. Y. Egorov, N. N. Ledentsov, A. F. Tsatsul'nikov, M. V. Maksimov, S. V. Zaitsev, Y. M. Shernyakov, A. V. Lunev, P. S. Kop'ev, Z. I. Alferov, and D. Bimberg, "Gain characteristics of quantum-dot injection lasers," Semiconduct. Sci. Technol. 33, 1013-1015 (1999).
15. D. J. Moss, T. Ido, and H. Sano, "Calculation of photogenerated carrier escape rates from GaAs/$AlGa_{1-x}As$ quantum wells," IEEE J. Quantum Electron. 30, 1015-1026 (1994).
16. J. Kim and S. L. Chuang, "Theoretical and experimental study of optical gain, refractive index change, and linewidth enhancement factor of p-doped quantum-dot lasers," IEEE J. Quantum Electron. 42, 942-952 (2006).
17. C. M. A. Kapteyn, F. Heinrichsdorff, O. Stier, R. Heitz, M. Grundmann, N. D. Zakharov, D. Bimberg, and P. Werner, "Electron escape from InAs quantum dots," Phys. Rev. B. 60, 14265-14268 (1999).
18. R. R. Alexander, D. Childs, H. Agarwal, K. M. Groom, H. Y. Liu, M. Hopkinson, R. A. Hogg, M. Ishida, T. Yamamoto, M. Sugawara, Y. Arakawa, T. J. Badcock, R. J. Royce, and D. J. Mowbray, "Systematic study of the effects of modulation p-doping on 1.3μm InAs/GaAs dot-in-well lasers," IEEE J. Quantum Electron. 43, 1129-1139 (2007).
19. N. F. Masse, S. J. Sweeney, I. P. Marko, A. R. Adams, N. Hatori, and M. Sugawara, "Temperature dependence of the gain in p-doped and intrinsic 1.3μm InAs/GaAs quantum dot lasers," Appl. Phys. Lett. 89(2006).
20. Y. D. Jang, T. J. Badcock, D. J. Mowbray, M. S. Skolnick, J. Park, D. Lee, H. Y. Liu, M. Hopkinson, R. A. Hogg, and A. D. Andreev,

"Enhanced nonradiative Auger recombination in p-type modulation doped InAs/GaAs quantum dots," Appl. Phys. Lett. 93, 101903 (2008).

5. Quantum Dot Selective Area Intermixing for Broadband Light Sources (Material Investigation)

In this chapter, the intermixing technique is introduced and discussed based on both QW and QD structures. Firstly a comparison of different capping materials and temperatures on the intermixing of an un-doped 8 layer InAs/In(Ga)As QD structure is investigated. Then, to further investigate the intermixing effect on different wafer structures, the intermixing of 5 layer of un-doped and modulation p-doped DWELL structures is discussed based on their PL results. It is found that QD materials with different caps exhibit significant differences in their optical properties following the annealing process. And modulation p-doped sample annealed at 700°C is considered to be the optimum setting.

5.1. Introduction of Selective Intermixing Technique

In chirped [1] or the hybrid QW/QD structures [2, 3] (as shown schematically in Figure 5.1(a)), different layers within the device (positioned vertically) emit at different wavelengths. The selective area post-growth intermixing technique modifies the emission wavelength in each selected area laterally, in order to realise a spatial variation of the bandgap energy of quantum dot materials across a single wafer, as shown in Figure 5.1(b).

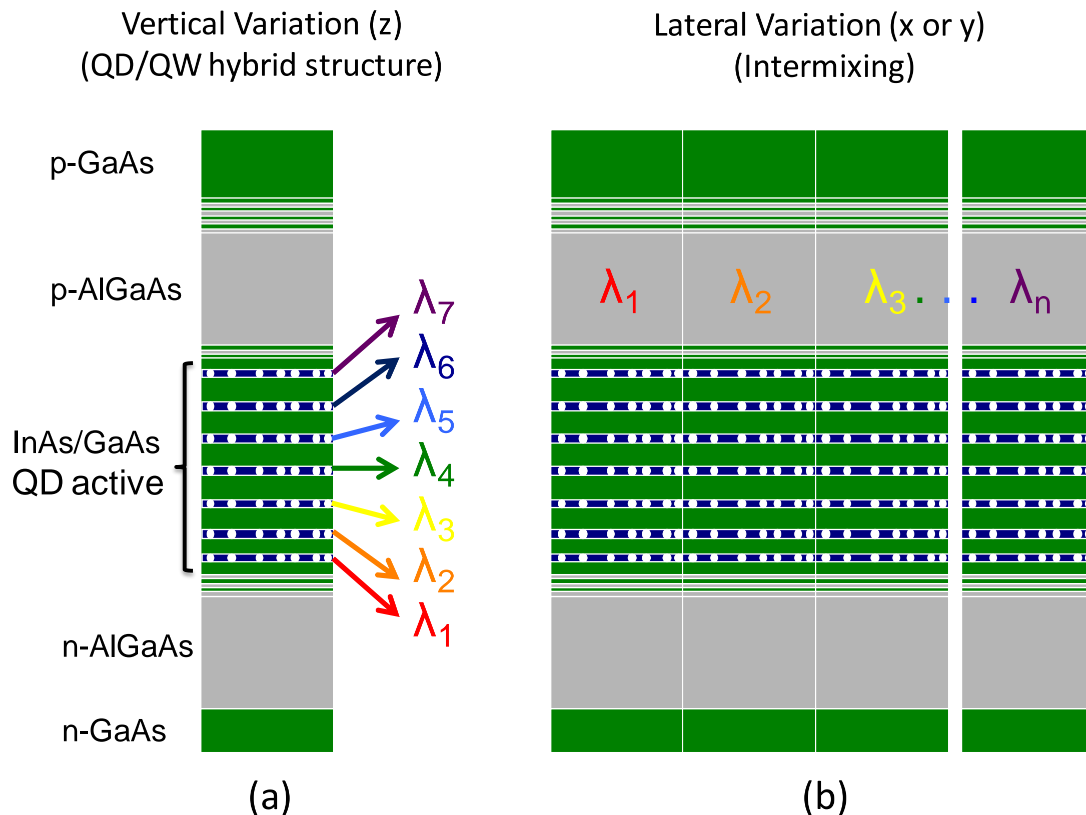

Figure 5.1 (a) Shows the integration of different wavelengths in vertical direction (such as multilayer stacks with different emission wavelength and a hybrid QW/QD structure), (b) shows the integration of different wavelengths by using selective area intermixing technique.

In a wavelength integrated device, each spectrum should be overlapped complementarily to obtain the broadband emission. However, if a strong spectral overlap of the two different regions appears, the selective area intermixed device may not exhibit enhanced emission bandwidth [4].

5.2. QW Intermixing

Post-growth annealing processes have been investigated for ~30 years, and have been widely used to modify the optical properties of semiconductor materials and devices [5].

The process of QW intermixing can be explained as atoms interdiffuse

between QWs and their surrounding matrix, which can cause the modification of the shape and composition (depth) of the QW, and hence changes of the quantized energy state [6]. In general, a blue shift of the peak wavelength is observed after the intermixing process, this is because of the interdiffusion process between the QW materials and the barrier materials, results in a change in the composition profile of the QW leading to an increase in its average band gap energy.

By using high annealing temperature, long annealing time or other intermixing techniques the interdiffusion process can be enhanced. For example, the impurity-induced disordering (IID) process which breaks the defect concentration equilibrium in the crystal. The self-diffusion of the group-*III* or group-*V* materials can then be enhanced, which in turn promotes the intermixing degree [7]. Similarly, by annealing with different dielectric materials capped on sample surface, the impurity-free vacancy disordering (IFVD) process can create vacancies, such as gallium vacancy, near the *III*-*V* semiconductor sample surface. A demonstration of the interdiffusion process is shown in Figure 5.2.

Typically, in the GaAs systems, a dielectric film such as SiO_2 is widely used during the annealing process. Gallium atoms are dissolved in the SiO_2 cap and create group *III* vacancies which then diffuse through the QW structure and cause intermixing [8]. Because it is essentially free of impurities, it can produce a low optical loss waveguide, and the electrical properties and performance of the device can be maintained [5]. The IFVD process provides

the opportunity to modify the QW band structure after epitaxial growth and design flexibility for many integrated opto-electronic devices.

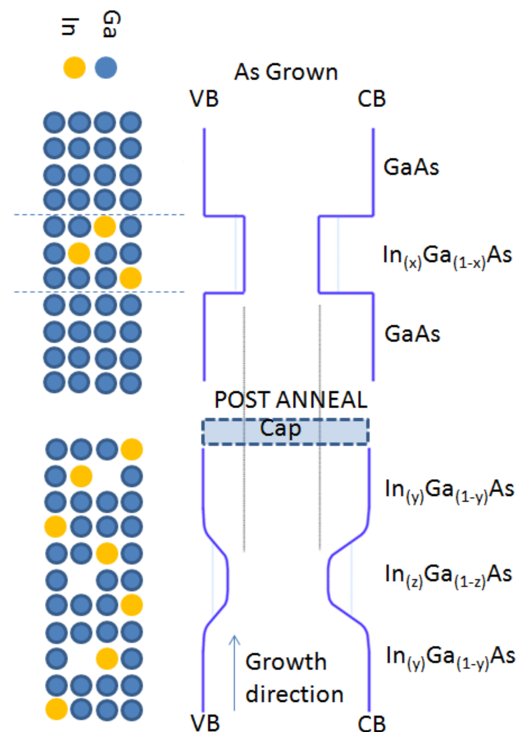

Figure 5.2. A demonstration of the intermixing process, during the annealing process the Ga vacancies defused between different materials. And different caps have different effects on the wafer.

Selective area QW intermixing (QWI) techniques have been used for the fabrication of photonic integrated circuits (PICs) [5], and have also been used to realize high power single mode lasers by introducing non-absorbing mirror facets [9].

5.3. QD Intermixing

More recently, quantum dot intermixing (QDI) has been used to fabricate wavelength tunable QD lasers [10]. Similar to the QWI, during the QDI process, the atoms interdiffuse between the QDs and the surrounding barrier layers. QDI is more complicated than QWI because the intermixing process is not only influenced by the difference in thermal expansion coefficients

between the QDs and the surrounding materials which causes the In/Ga interdiffusion, but is also strongly affected by the shape, size and strain distribution in/around the QDs [11]. Compared to QWI, because of the lack of precise material characterization methods, (although TEM can provide images before/after QDI process with resolution at atomic level [12]) the QDI process is still difficult to be accurately understood and controlled. As a result, there are fewer reports in the literature on QDI as compared to QWI. Furthermore, the high thermal sensitivity of QD structures makes the optimised annealing parameters (e.g. annealing temperature and time duration) very difficult to trace.

For QD devices, after the intermixing process, normally, a narrowing of the PL linewidth, a blue shift of the emission spectrum and a reduction of electronic state energy separation is observed (details in 5.3.1.2). Two main techniques are widely used for realizing the intermixing process: one is to use the RTA system which heats the wafer up in an airtight chamber under nitrogen, the other is to use a laser-induced annealing (LIA) system [13], in which a high power laser is focussed on the capped or uncapped wafer surface in order to increase the wafer temperature.

As a consequence, the intermixing technique can be used to vary the linewidth and the emission wavelength of QD devices, and the development of selective area QDI (SAQDI) shows the potential to spatially vary the bandgap of the QD device and allow the integration of a single contact, multi-wavelength device.

5.3.1. Introduction & Theory

5.3.1.1. Post-growth Annealing Process and Epitaxial Growth

Recently, the QDI technique has been reviewed and summarized by Zhang *et. al*. [14]. The optical properties from a strained InGaAs/InAs QDs ensemble was initially investigated by Leon *et al.,* [15] and Kosogov *et al.,* [12] by post-growth annealing (PGA) and high temperature upper cladding layer growth. They suggested that the interdiffusion (intermixing) process around the QD interface causes the emission wavelength shifts rather than strain effects from the capping layer thickness variation. The PGA process has a similar thermal effect to the high temperature growth of the waveguide and upper cladding layers. The results from both processes are comparable. Temperature dependant PL is a powerful tool which is commonly used to analyse PGA and epitaxial processes. It indicates the shape and confining potential depth changes of the QDs, which correspond to a linewidth change and a wavelength shift of the PL emission, details can be seen in section 5.3.1.2.

The schematic of a typical QD based laser diode (QD-LD) structure is shown in Figure 5.1. It is a typical p-i-n structure and there are seven InGaAs QD layers in the active region, sandwiched by a top p-AlGaAs cladding layer and a bottom n-AlGaAs cladding layer. High temperature growth is used for the top and bottom cladding layers, which in turn acts as a high temperature annealing process to the QD layers in the active region. Furthermore, if the growth/annealing temperature is too high, or the high temperature time duration is too long, it will induce “dissolution” of the dots and/or the dislocations in the material caused by large strain relaxation.

Thermal interdiffusion of the QD devices has been investigated by several research groups [10, 11, 16-19], they found that in addition to the blue-shift of the emission spectrum, in InGaAs/GaAs QDs, the PL emission linewidth and the energy spacing between the confined states were reduced, which is discussed in the next section. Figure 5.3 shows a schematic diagram combined with the TEM images [17] of the evolution of the QD structure with different annealing parameters (reproduced and modified from [14]).

Figure 5.3(a) and (f) show the TEM image and the schematic of the as-grown InAs/GaAs quantum dot, illustrating sharp interfaces, different shapes and inhomogeneous QD sizes.

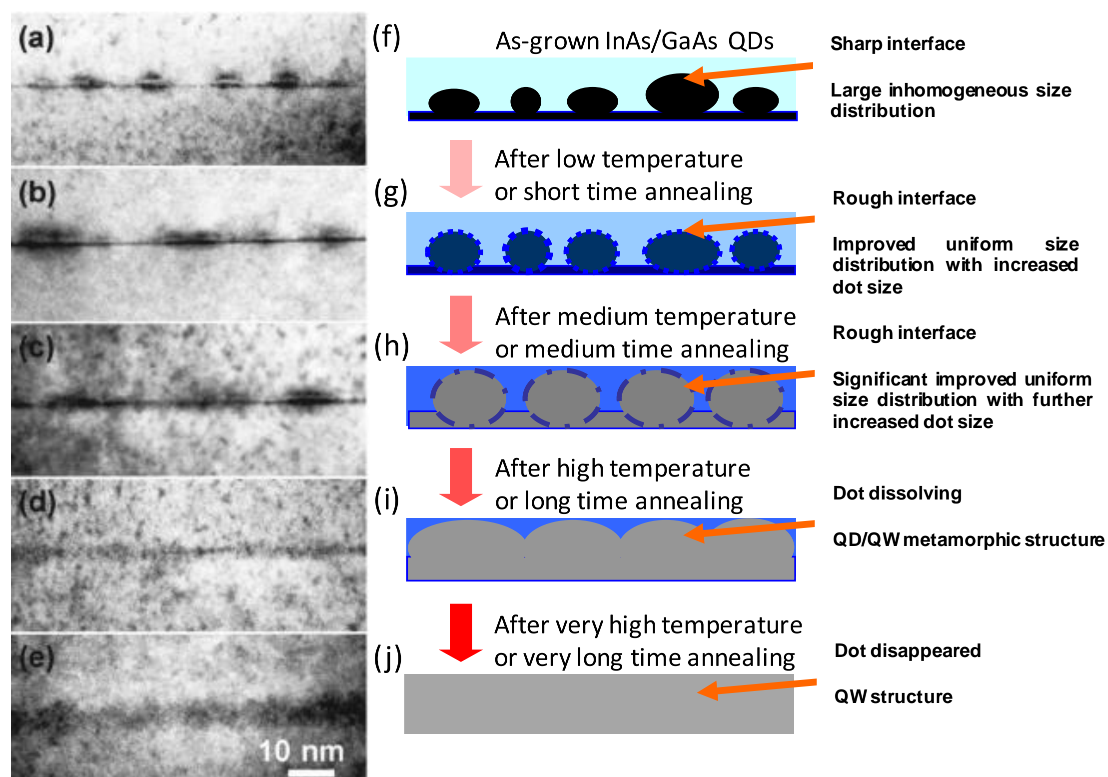

Figure 5.3 A schematic diagram of the evolution of the InAs/GaAs QDs annealed with different temperatures and time duration, a series of TEM images are shown corresponding to this process [17].

In Figure 5.3(g) and (h), during the intermixing process, due to the interdiffusion effect, the interface of the QDs and their surrounding matrix becomes rough and the dot size uniformity is improved with increased dot volume (confirmed by the TEM images in Figure 5.3(b) and (c)). Figure 5.3(i) demonstrates the situation when a high temperature or/and a long time duration is applied to the annealing process. In this case, a 2D InGaAs layer or a QD/QW metamorphic structure (Figure 5.3(d)) may be formed in the wafer caused by strong lateral In/Ga interdiffusion. Finally in Figure 5.3(j), the QDs are disappeared after an excessive intermixing process and the whole structure will be similar to a bulk like alloy of InGaAs, the corresponding TEM image is shown in Figure 5.3(e).

5.3.1.2. Key Parameters of the PL Result Based on the PGA Sample

As mentioned previously, the PL measurement is a powerful tool to investigate the intermixing process. To investigate the PL results, there are several main parameters should be considered [14]:

(1) PL emission energy. Two main factors contribute to the emission wavelength shift during the intermixing process. One is the increased QD size, shown in Figure 5.3(g) & (h), which will cause a red-shift of the quantized energy states due to the reduced confinement energy. The other factor is the Ga composition increase in the QDs, due to the In-Ga interdiffusion at the QD interface. Because the QD becomes more Ga rich and In deficient, a blue-shift of the emission wavelength is observed. An example is shown in Figure 5.4, at 77K, the detected PL emission wavelength of the InGa(Al)As/GaAs QD sample is continuously blue-shifting with increasing annealing temperature. Compared to the wavelength tuning range of ~110nm in QWI [20], the tuning

range of a QDI device is broader (~200nm in Figure 5.4 [21]), which indicates the flexibility and potential of wavelength tuning using QDI.

(2) PL FWHM. During the high temperature annealing process, the PL emission linewidth of the sample broadens first and then narrows. The reason for this is illustrated in Figure 5.3. In an as-grown QD sample, the inhomogeneous emission linewidth is governed by the dot size distribution and composition variations. During the intermixing process, at low temperatures, the PL linewidth broadening effect is dominant, which is promising for fabricating broadband QD light sources and amplifiers [10, 22]. When the annealing temperature is relatively high, the dot size uniformity effect becomes dominant and the PL linewidth narrows with increasing annealing degree (temperature) before the disappearance of the quantum dot.

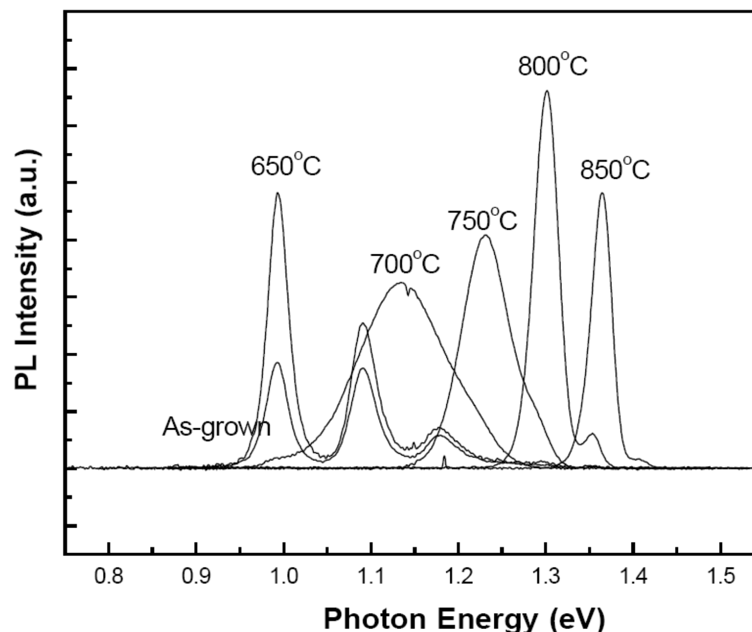

Figure 5.4 PL spectra from the InGa(Al)As/GaAs QD samples (as-grown sample and samples annealed at different temperatures), measured at 77K [21].

(3) The spacing of QD energy transitions. The InGaAs/GaAs QDs have an asymmetric shape with the height of the QD is smaller than the length and width. The emission energy is therefore mainly determined by the height of the dot, and the energy state separation is decided by the QD width [22]. The In/Ga interdiffusion takes place in both vertical and horizontal directions. The anisotropic strain distribution around the interface of the QD is caused by the small height to width ratio of the QD. During intermixing, a size increase in the base plane direction rather than the height direction leads to a reduced energy separation. Wang *et al.*, reported a widely tuned energy spacing of the QD optical transitions from 14.6meV to 90.9meV [23], Babinski *et al.*, demonstrated that the rapid disappearance of the QDs during the RTA process is due to the strong lateral interdiffusion [21].

5.3.1.3. Capping Materials

Recently, introducing p-type doping to QD active materials has been demonstrated to improve the thermal stability of QDs during the annealing process, leading to the realization of high performance intermixed QD devices [4, 24]. Several different capping films have been used during the annealing process, such as TiO_2 [25], aluminium (Al) [26] and SiO_2 [5].

Thin TiO_2 films have been demonstrated [25] to significantly reduce the intermixing degree due to its large thermal expansion coefficient. When a thin dielectric film is deposited onto a thick GaAs substrate [27], there is a thermal expansion coefficient mismatch between the film and the substrate at the annealing temperature, which causes a thermal stress near the interface region during the annealing process. The thermal expansion coefficient of

TiO_2 is ~8.2×10^{-6} $^{o}C^{-1}$ which is larger than that of the GaAs (~6.8×10^{-6} $^{o}C^{-1}$). During the annealing process TiO_2 is under compressive stress near the interface region when GaAs is under tensile stress, as a consequence the Ga atoms will be trapped which inhibits the interdiffusion process.

Moreover, Al has a much larger thermal expansion coefficient (~23.5×10^{-6} $^{o}C^{-1}$) [28], so it is also expected to inhibit intermixing by the same argument. Al capping has also been used to reduce the intermixing rate, with this being discussed in terms of an increased density of Ga interstitials on the sample surface due to atomic exchange between the Al film and Ga_2O_3 layer during the annealing process [26]. Such interstitials are expected to inhibit the formation of Ga vacancies which drives the intermixing process. A PECVD deposited SiO_2 layer (thermal expansion coefficient less than GaAs) behaves like a porous structure during the annealing process. Ga atoms readily diffuse into the SiO_2 matrix, leaving a number of Ga vacancies in the semiconductor structure which is expected to enhance the degree of interdiffusion.

Furthermore, the intermixing rate is found to be increased with increasing thickness of the SiO_2 films. Since there is always a limit of Ga solubility in the SiO_2 film, once it reaches this value, no more Ga vacancies can be generated. The solubility is higher in thicker SiO_2 films. Moreover, related to the mismatch of thermal expansion, the stress caused at the SiO_2/GaAs interface is larger with a thicker SiO_2 film, which also enhances the Ga atoms out-diffusion into the SiO_2 matrix [8].

5.3.1.4. Discussion

In the following sections, a comparative study of the intermixing of un-doped QD structures, the un-doped and modulation p-doped DWELL structures is discussed based on PL measurement. Various caps were used to promote and inhibit intermixing under the same annealing process conditions.

5.3.2. Intermixing of Un-doped QD sample

5.3.2.1. Experiments

Four different samples are investigated in this section, the as-grown sample, sample annealed with 200nm thickness of TiO_2 [25] film at 680^oC and samples annealed with 200nm thickness of SiO_2 film at 680^oC and 700^oC, respectively. The sample has 8 QD layers in the active region. The growth detail of the wafer was fully described in chapter 4.1 and the schematic of this structure is shown in the inset of Figure 5.5. The annealing process was performed in an N_2 ambient at temperatures of 680^oC and 700^oC for 5 minutes. By shining a 532nm solid-state laser on samples, the room temperature photoluminescence (RT-PL) signal was collected by a focusing lens and shone into a spectrometer and Ge detector system. All caps on the sample surface were removed by 10% concentration of hydrofluoric acid before the RT-PL test.

Figure 5.5 shows the RT-PL spectra of the as-grown sample and samples annealed with different caps with an excitation laser power density of 50W/cm^2. For the as-grown sample, the GS emission is located at ~1282nm, the TiO_2 capped sample has a similar GS emission wavelength at ~1275nm.

Compared to the as-grown sample, there is a small blue-shift of the GS emission peak wavelength for the TiO_2 capped sample. For the SiO_2 capped sample annealed at 680°C, the main peak blue shifted to ~1233nm after annealing. And for the SiO_2 capped sample annealed at 700°C, the GS peak is further blue shifted to ~1159nm with lower integrated PL intensity.

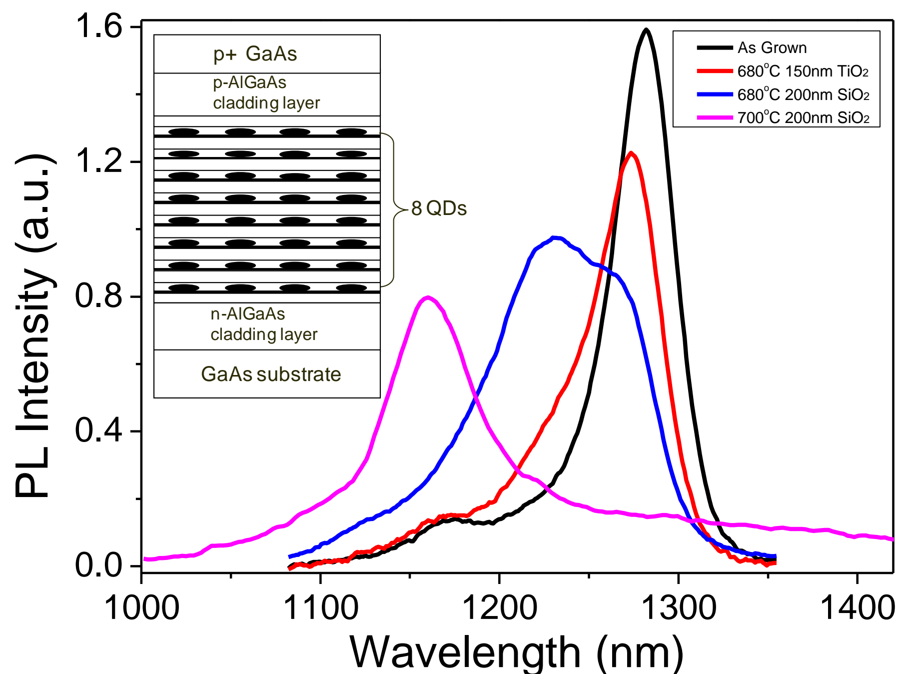

Figure 5.5 PL intensity vs. wavelength of the samples annealed with different caps, the inset shows the structural plot of the wafer.

In addition, the PC spectra were measured from a mesa device with a diameter of 400μm. The samples were measured at room temperature with no reverse bias, as shown in Figure 5.6 (a). The PC plot for the as-grown sample shows a number of well-defined peaks (eg GS-e_1hh_1, ES_1-e_2hh_2, ES_2-e_3hh_3…) from the InAs QD interband absorption. This is in agreement with the PL result in Figure 5.5.

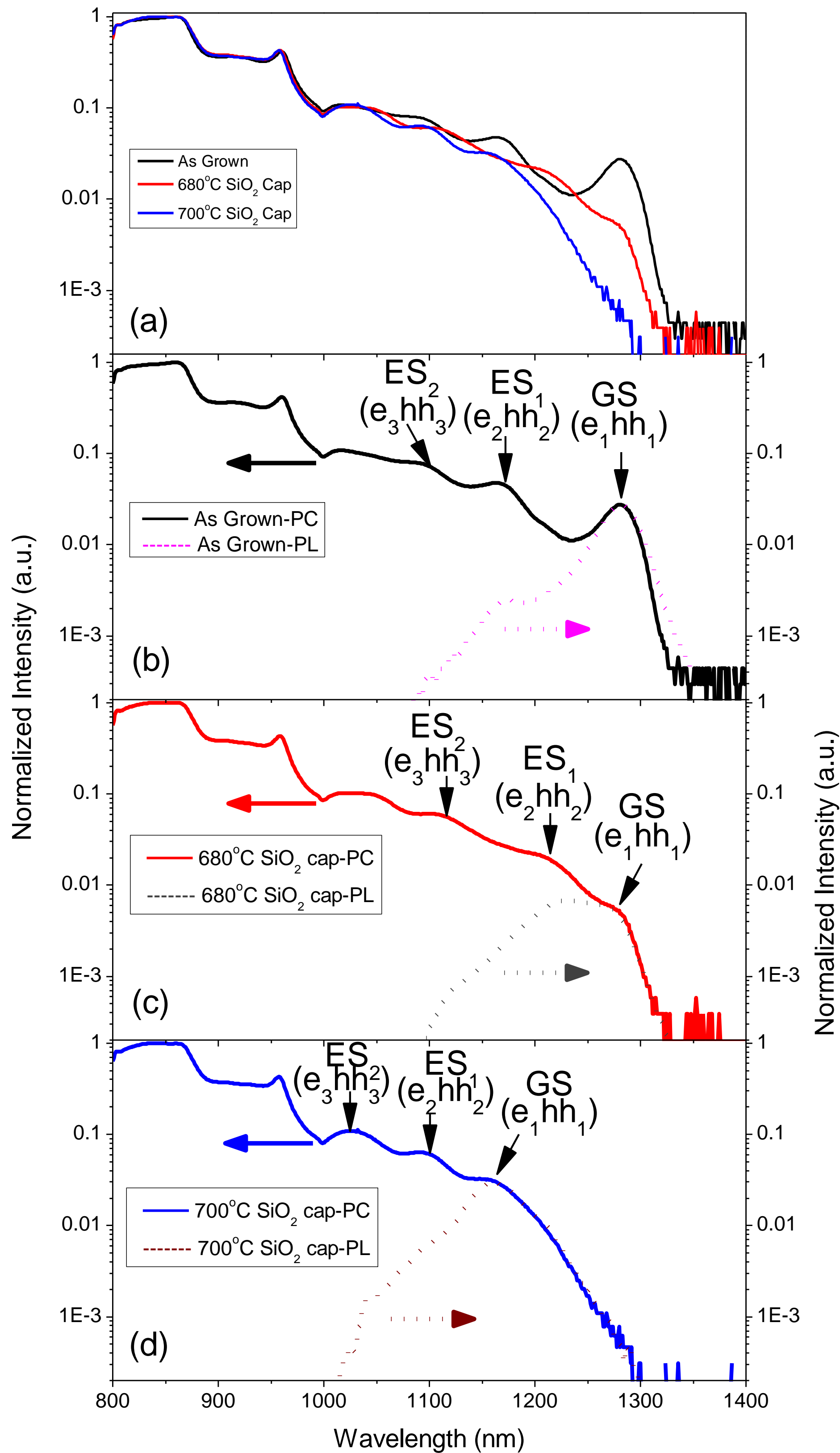

Figure 5.6 (a) Photocurrent plot of the as-grown QD sample and samples annealed with the SiO_2 cap at 680°C and 700°C respectively, (b) comparison of PC and PL of the as-grown sample, (c) comparison of PC and PL of the SiO_2 capped sample annealed at 680°C, (d) comparison of PC and PL of 700°C SiO_2 capped sample.

For the SiO_2 capped sample annealed at 680^oC, shown in Figure 5.6(b), the absorption peak intensity at ~1281nm is reduced by a factor of ~7 compared to the as-grown sample, also there is a peak which appears at ~1210nm, which is the ES_1. This red shift of ES_1 is attributed to the shallower quantum confinement caused by the In/Ga interdiffusion near the QD interface during the annealing process. The decrease of the splitting between the GS absorption peak and the ES_1 absorption peak is also in agreement with the PL result in Figure 5.5 [29]. As the PL shown in the dashed line in Figure 5.6(b), the GS absorption peak is located at ~1281nm, the overlap of the two GS peaks (from PC and PL) indicates the Stoke's effect is negligible in this QD sample [30]. Also, the PC of the device annealed with a SiO_2 cap at 700^oC shows low absorption value at ~1281nm and all the energy states blue shift, with further decreased separation between ES_1 and GS. Also, the PC and PL plot in Figure 5.6(c) show no Stoke's shift for this 700^oC intermixed sample. At the annealing temperature of 700^oC, there is almost no absorption peak at ~1281nm (shown in Figure 5.6(d)). All the absorption peaks in Figure 5.6(d) are shifted to higher energy due to the shallow confinement of the QDs. The GS peak of the PL result matches the GS absorption peak in Figure 5.6(d), which indicates the Stoke's shift is negligible for this sample up to the annealing temperature of 700^oC. Because it is easy to regrow In-P materials [31] but hard for GaAs, this intermixing technique offers another way of making active and passive integrated devices and circuits [5].

Further discussion is given to confirm the peak at ~1210nm is from ES_1 not the GS of a subset of QDs affected by the intermixing process. If the peak at

~1210nm is the GS peak of another dot, it should have its own PC absorption peaks independent to the original dot. In Figure 5.7, the GS of one of the as-grown PC is shifted to ~1210nm and then overlapped with the original as-grown spectrum, which is shown in red.

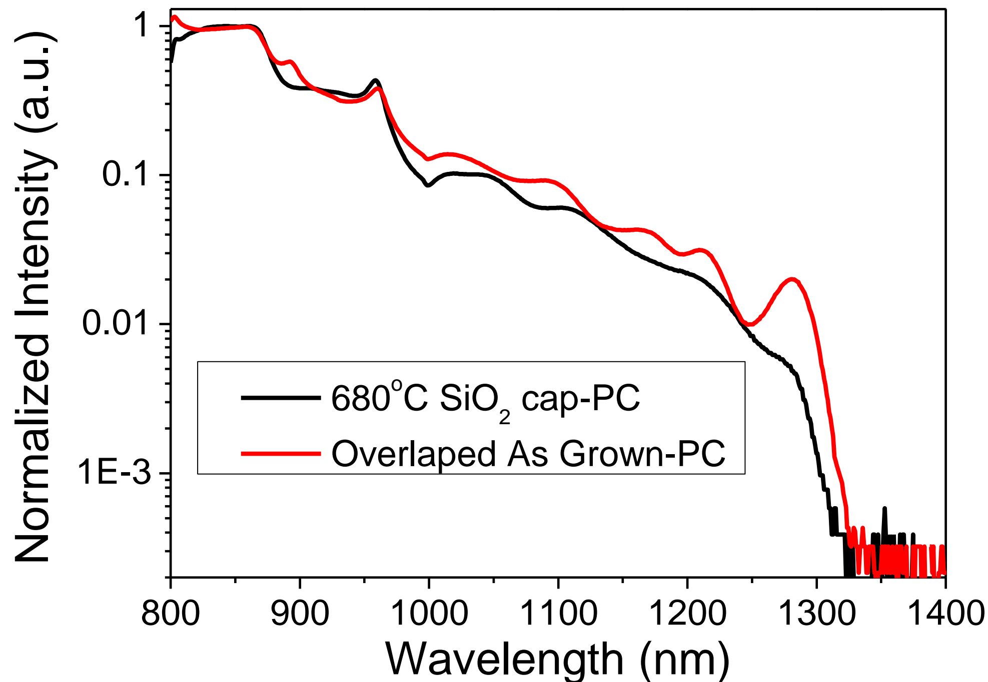

Figure 5.7 PC of the SiO_2 capped device annealed at 680°C compared to the shifted and overlapped PC of the as grown device.

In Figure 5.7, the shifted and overlapped PC of the as grown sample is very different to the spectrum measured from the SiO_2 capped device annealed at 680°C. This suggests that the absorption peak at ~1210nm is probably not from the GS of a subset of QDs.

5.3.2.2. Discussion

Based on the PL result of the QD sample, the TiO_2 capped sample only shifted a few nm in wavelength after the annealing process. Therefore it is considered to be one of the suitable materials to suppress interdiffusion during the annealing process. The SiO_2 cap acts as an interdiffusion

promoting material as discussed in the previous sections. Its wavelength is heavily blue shifted after the annealing process. The characteristics of the TiO_2 cap and the SiO_2 cap show that different capping materials can cause different emission wavelength after the same annealing process which has potential application in forming an integrated light source.

5.3.3. Intermixing Based on DWELL Samples

In this section, I try to compare the PL results based on the samples with/without p-doping. Two different samples are investigated with different capping materials during the annealing process, they are nominally identical with one sample being un-doped and the other being modulated p-doped with 20 accepters per dot.

5.3.3.1. Un-doped DWELL Sample

5.3.3.1.1. Epitaxy

In this section, an un-doped 5 layer InAs DWELL structure is discussed. Efforts are made to broaden the emission bandwidth. The comparison of the FWHM and the separation between GS and ES_1 for two different samples is shown in Figure 5.8. The separation of GS and ES_1 for the DWELL is ~81nm compared to ~110nm for the 8 layer QD sample (investigated in section 5.3.2), and the FWHMs for these two samples are ~41nm and ~44nm respectively.

The un-doped DWELL sample was grown in a molecular beam epitaxy (MBE) Veeco Gen 2 system on a Si-doped GaAs (100) substrate by Prof. Huiyun Liu. In each QD layer, 3 monolayer (ML) of InAs is grown on a 2nm InGaAs layer, covered by a 5nm InGaAs layer. The 5 DWELL structures were separated by

44nm GaAs spacers. The whole active region was sandwiched by lower n-$Al_{0.4}Ga_{0.6}As$ and upper p-$Al_{0.4}Ga_{0.6}As$ cladding layers, which is shown schematically in the inset of Figure 5.8.

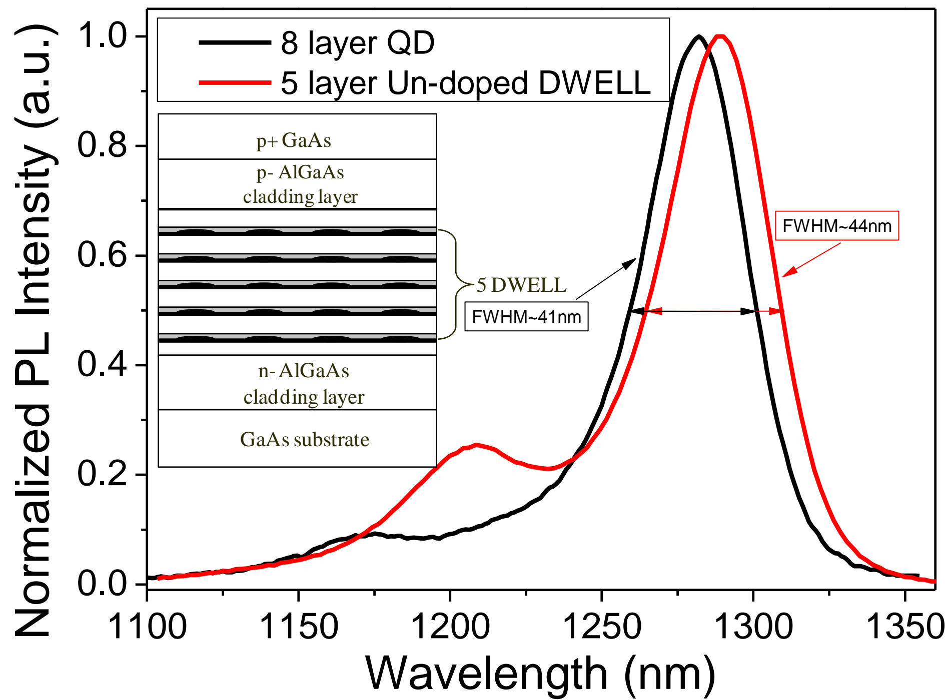

Figure 5.8 PL comparisons between the 8 layer QD as-grown sample and the 5 layer un-doped DWELL as-grown sample. The inset shows the schematic of the wafer structure, there are 5 dot-in-well structures in the active region.

5.3.3.1.2. PL Measurement Comparison & Analysis

Five different kinds of metal and dielectric caps were initially trialled on the un-doped DWELL sample, including a 200nm thick e-beam evaporated TiO_2 film, a 200nm thick e-beam evaporated Al film, a GaAs proximity cap (a small piece of GaAs substrate placed upside down on top of the sample during annealing), a 200nm thick PECVD deposited SiO_2 film and a 200nm thick PECVD deposited Si_3N_4 film. The annealing process was performed in an N_2 ambient at temperatures of 700°C or 750°C for 5 minutes in order to optimise the annealing temperature. Samples for PL measurement were prepared by

etching off ~1μm of the p-AlGaAs cladding on top of the samples. The RT-PL result was obtained via excitation using a diode-pumped solid-state laser emitting at 532nm and the light was collected by a lens and then fed into a spectrometer and Ge detector system.

Figure 5.9 shows the RT-PL spectra of un-doped samples annealed at 700°C with different caps under an excitation laser power density of $50W/cm^2$. For the as-grown sample, the GS is located at ~1288nm and the ES is located at ~1209nm; For the TiO_2 capped sample, the intensity of the GS drops dramatically while the wavelength stays at ~1287nm and the ES is located at ~1204nm. For the GaAs proximity sample, the GS is located at ~1288nm and the ES cannot be well defined. The un-shifted GS peak wavelength with a reduced PL intensity for the TiO_2 capped and GaAs proximity sample may be due to an increase of the dot volume compensating the shallow confinement caused by intermixing.

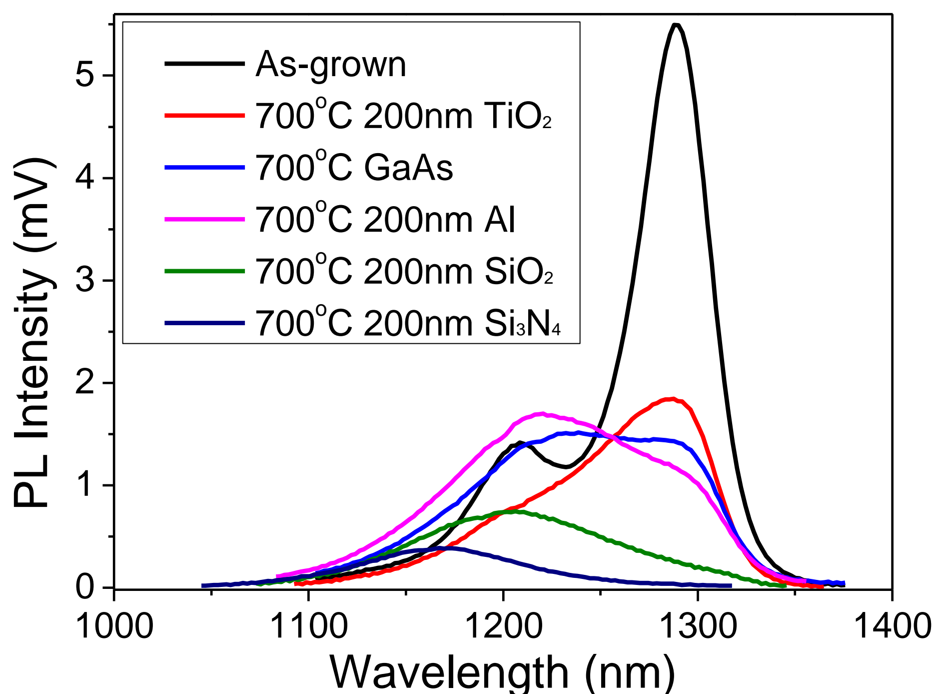

Figure 5.9 PL spectra of the un-doped samples with different caps annealed at 700°C for 5 minutes.

For the Al capped sample, the GS is located at ~1288nm and the ES is located at ~1219nm; For the SiO_2 capped sample, there is only one peak which can be observed at ~1204nm, For the Si_3N_4 capped sample, the shape of the spectrum is similar to that of the SiO_2 sample with its peak further blue shifted to ~1170nm.

To optimise the annealing temperature, samples with the identical caps were annealed at 750°C for 5 minutes to make a comparison to the results of the 700°C annealed samples. The result is shown in Figure 5.10, the GS and the ES cannot be well distinguished for all the 750°C annealed samples, because the interdiffusion caused shallow confinement.

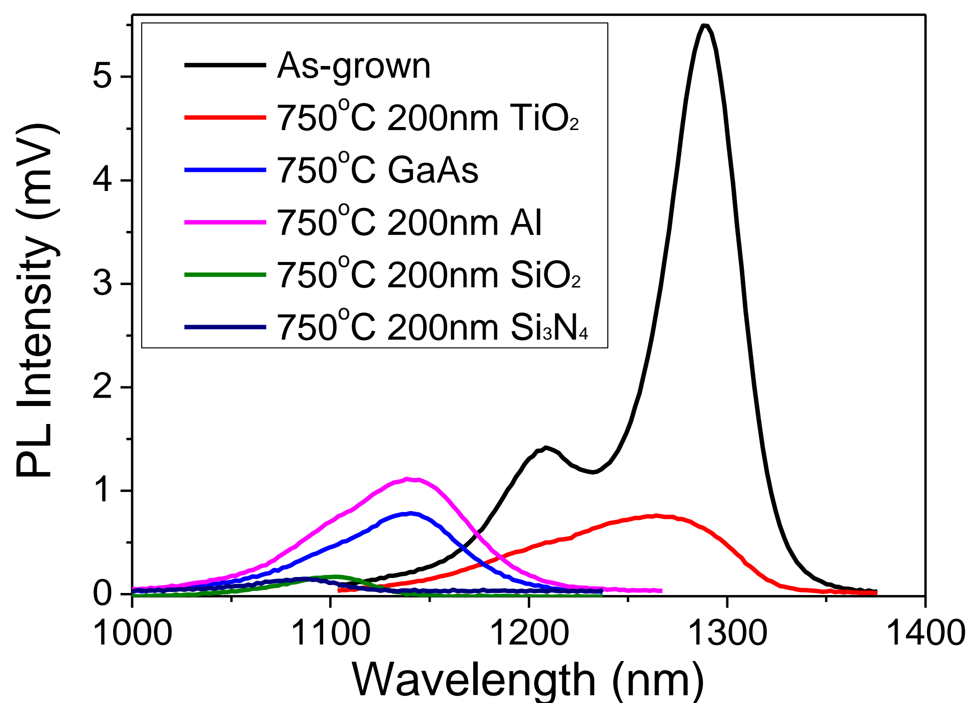

Figure 5.10 PL spectra of the un-doped samples with different caps annealed at 750°C for 5 minutes.

For the TiO_2 capped sample the peak is located at ~1267nm; For the GaAs capped sample, the peak blue shifted to ~1141nm and the Al capped sample has the similar peak wavelength at ~1142nm with a higher intensity. For the

SiO_2 and Si_3N_4 capped samples, the peak wavelengths are further blue shifted to ~1104nm and ~1087nm, respectively. The wavelength change as a function of different caps is plotted in Figure 5.11.

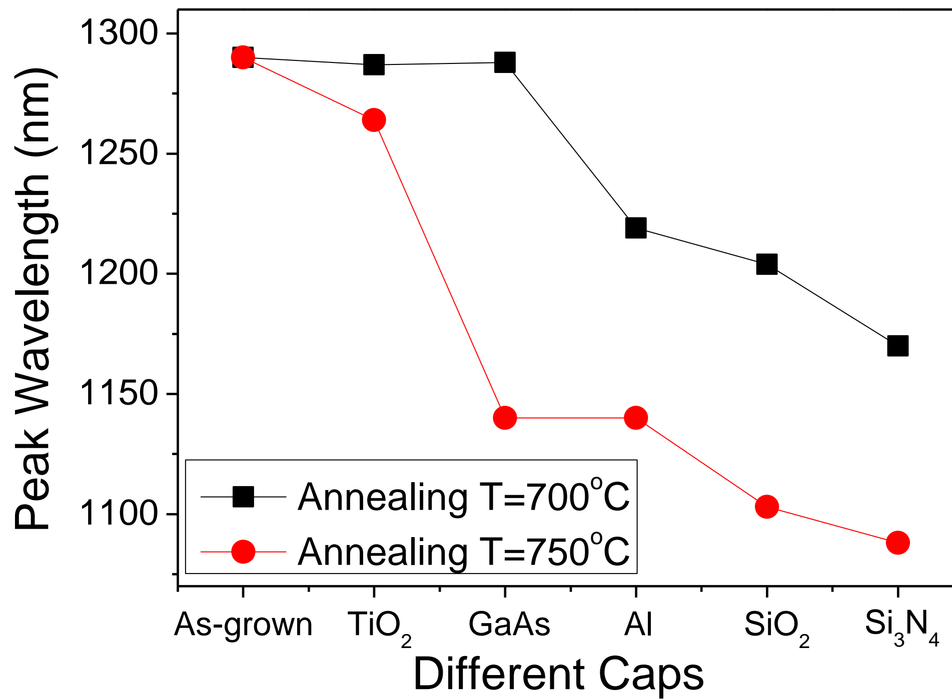

Figure 5.11 Peak wavelength plotted as a function of different caps for the un-doped samples, the annealing temperatures are 700°C and 750°C respectively.

Figure 5.11 shows that there are two different caps which can efficiently suppress interdiffusion during the annealing process at 700°C, they are the TiO_2 cap and the GaAs cap. But at the annealing temperature of 750°C, the TiO_2 cap is shown to be more effective compared to the GaAs cap. For the Al cap, at both 700°C and 750°C the peak wavelength is blue shifted by ~70-140nm. Both SiO_2 and Si_3N_4 caps caused a blue-shift of the peak wavelength at 700°C and the peak wavelength further blue shifted at the higher annealing temperature (750°C).

5.3.3.2. Modulation p-doped Sample

Modulation p-doped samples have previously shown potential for suppressing

the interdiffusion process with a high device performance [29]. Therefore, in this section the modulation p-doped sample is investigated. It is nominally identical to the un-doped sample except the modulation p-doping with beryllium (Be) to a concentration of 20 acceptors per dot located in the 9nm wide GaAs spacer layer, 6nm beneath each DWELL.

5.3.3.2.1. PL Measurement & Discuss

In an identical manner as the un-doped sample, the modulation p-doped samples with same capping materials and preparation were annealed at 700°C and 750°C for 5 minutes. The PL results of 700°C annealed samples (under an excitation laser power density of 50W/cm^2) are shown in Figure 5.12.

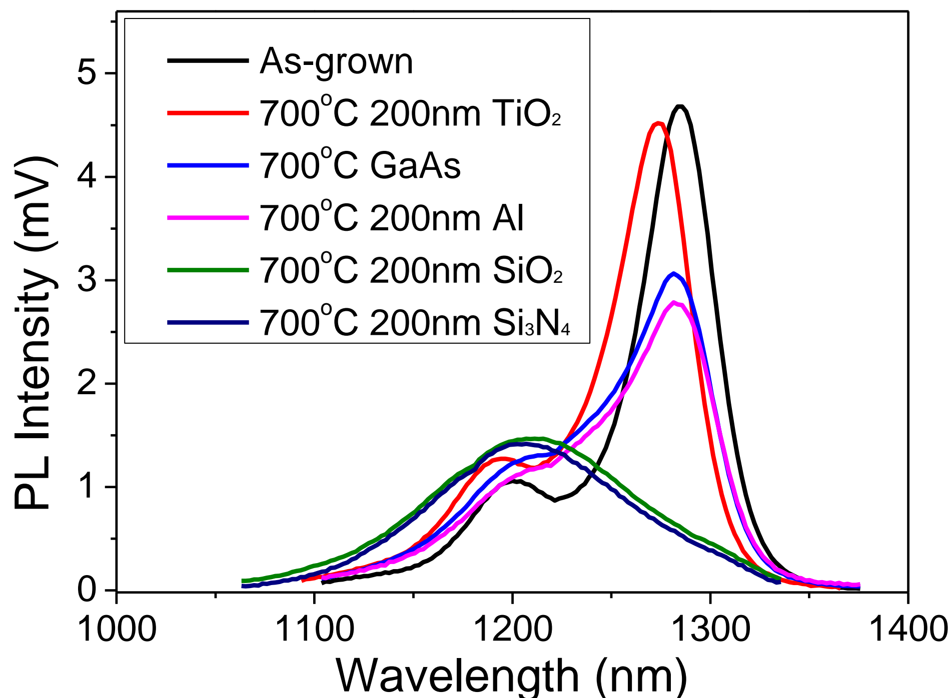

Figure 5.12 PL spectra of the modulation p-doped samples with different caps annealed at 700°C for 5 minutes.

Compared to the as-grown sample, there is a small blue-shift of the GS

emission peak wavelength for the TiO_2, GaAs and Al capped samples. This confirms that the TiO_2 and Al caps provide an effective way to suppress the interdiffusion for p-doped sample. The GaAs cap suppresses the interdiffusion by providing a Ga atom rich environment on top of the sample which suppresses the Ga vacancy formation [17]. The 200nm SiO_2 capped sample and the 200nm Si_3N_4 cap have the similar shape. More characteristics for this p-doped sample will be further discussed in the next chapter.

Also, the samples were annealed at 750°C with the same kinds of caps to optimise the annealing temperature. The PL result is shown in Figure 5.13.

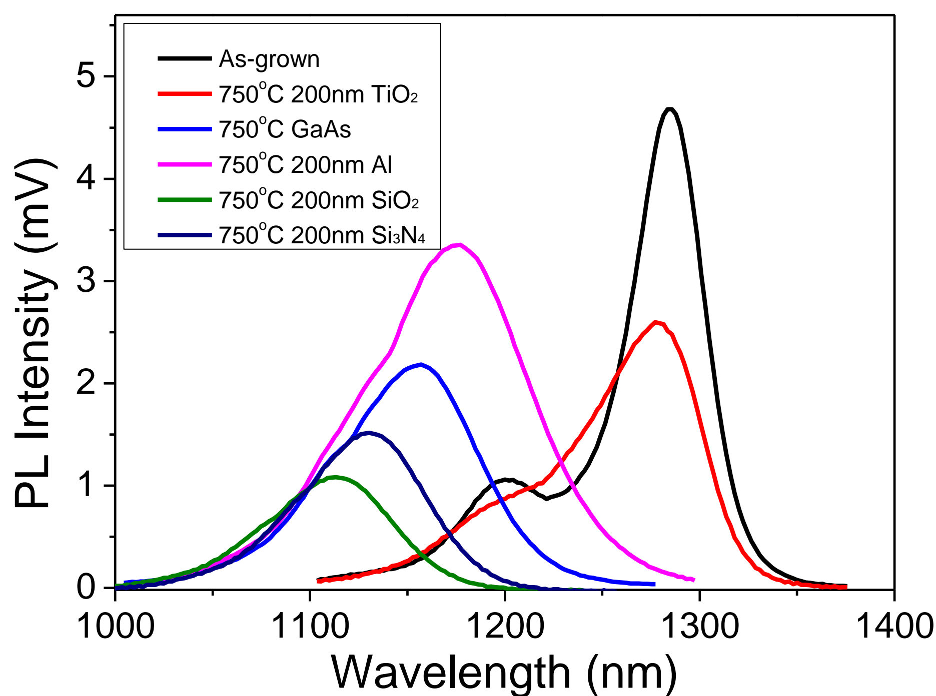

Figure 5.13 PL spectra of the modulation p-doped samples with different caps annealed at 750°C for 5 minutes.

It shows the TiO_2 cap is still effective in suppressing interdiffusion process even with higher annealing temperature (750°C). The GS of the TiO_2 capped sample is slightly blue-shifted to ~1278nm with an intensity drop to half of the as-grown value. For the Al capped sample, the peak wavelength blue shifted

to ~1175nm. The Al cap did not efficiently suppress the interdiffusion at the annealing temperature of 750°C compared to its performance when the annealing temperature was 700°C. The GaAs capped sample shows its peak wavelength blue shifted to ~1157nm. For the SiO_2 and Si_3N_4 capped samples, the peak wavelength blue shifted to ~1113nm and ~1131nm respectively.

In order to optimise the annealing temperature and chose the suitable caps for the device fabrication process, the peak wavelength vs. different caps at two annealing temperatures is plotted in Figure 5.14.

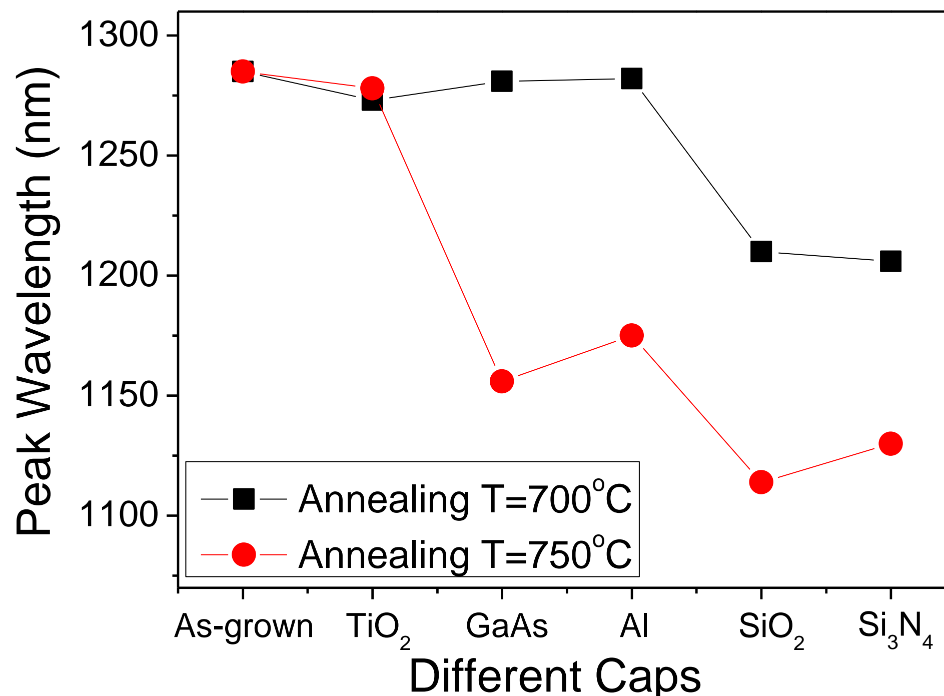

Figure 5.14 Peak wavelength plotted as a function of different caps for the modulation p-doped samples, the annealing temperatures are 700°C and 750°C respectively.

It shows for the modulation p-doped sample, the TiO_2 cap is also a promising material to suppress the intermixing process as it was for the un-doped sample; it also has a relative high PL intensity after annealing. The GaAs cap and the Al cap were efficient at 700°C but failed to effectively suppress the

interdiffusion at 750°C. Both SiO_2 and Si_3N_4 caps show the dramatic blue shift of the peak wavelength at 700°C and their peak wavelengths further blue shifted at higher annealing temperature (750°C).

5.4. Conclusion

In conclusion, the intermixing techniques such as QWI and QDI have been introduced. Compared to the hybrid QW/QD technique, which varies the wavelength in the vertical direction, the intermixing technique varies the wavelength laterally. The key parameters during the PL measurement were discussed refer to Zhang *et.al*. [14]. For three different QD structures, a number of capping materials were investigated at two annealing temperatures, 700°C and 750°C, respectively. The PC from un-doped 8 layer QD sample shows the Stoke's shift is negligible. Compared to the un-doped InAs/InGaAs/GaAs DWELL structure, the modulation p-doped DWELL structure with post-growth annealing treatments is promising for broadband QD devices. Moreover, the technique of IFVD should be highlighted, as it is a simple and low-cost method.

5.5. Future work

Future possible work is to anneal the sample with the capping materials not included in this chapter. Annealing temperatures could be varied with a smaller step (e.g. a 10°C step). Wafers with higher doping levels (>20acc/QD) could be grown in the next run. To investigate, with reduced intermixing rate in a heavily p-doped sample, if the wavelength shift can be controlled more accurately. Analysis could be carried out with the same experimental method discussed in this chapter.

Reference

1. Y. C. Yoo, I. K. Han, and J. I. Lee, "High power broadband superluminescent diodes with chirped multiple quantum dots," Electron. Lett. 43, 1045 (2007).
2. S. M. Chen, K. J. Zhou, Z. Y. Zhang, D. T. D. Childs, M. Hugues, A. J. Ramsay, and R. A. Hogg, "Ultra-broad spontaneous emission and modal gain spectrum from a hybrid quantum well/quantum dot laser structure," Appl. Phys. Lett. 100, 041118 (2012).
3. S. M. Chen, K. J. Zhou, Z. Y. Zhang, J. R. Orchard, D. T. D. Childs, M. Hugues, O. Wada, and R. A. Hogg, "Hybrid quantum well/quantum dot structure for broad spectral bandwidth emitters," IEEE J. Sel. Topics Quantum Electron. 19, 1900209-1900209 (2013).
4. Z. Y. Zhang, Q. Jiang, M. Hopkinson, and R. A. Hogg, "Effects of intermixing on modulation p-doped quantum dot superluminescent light emitting diodes," Opt. Express 18, 7055-7063 (2010).
5. J. H. Marsh, "Quantum well intermixing," Semiconduct. Sci. Technol. 8, 1136 (1993).
6. D. Sengupta, V. Jandhyala, S. Kim, W. Fang, J. Malin, P. Apostolakis, K. C. Hseih, Y. C. Chang, S. L. Chuang, S. Bandara, S. Gunapala, M. Feng, E. Michielssen, and G. Stillman, "Redshifting and broadening of quantum-well infrared photodetector's response via impurity-free vacancy disordering," IEEE J. Sel. Topics Quantum Electron. 4, 746-757 (1998).
7. D. G. Deppe and N. Holonyak, "Atom diffusion and impurity-induced layer disordering in quantum well III-V semiconductor heterostructures," J. Appl. Phys. 64, R93-R113 (1988).
8. B. S. Ooi, K. McIlvaney, M. W. Street, A. S. Helmy, S. G. Ayling, A. C. Bryce, J. H. Marsh, and J. S. Roberts, "Selective quantum-well intermixing in GaAs-AlGaAs structures using impurity-free vacancy diffusion," IEEE J. Quantum Electron. 33, 1784-1793 (1997).
9. C. L. Walker, A. C. Bryce, and J. H. Marsh, "Improved catastrophic optical damage level from laser with nonabsorbing mirrors," IEEE

Photon. Technol. Lett. 14, 1394-1396 (2002).

10. H. S. Djie, Y. Wang, D. Negro, and B. S. Ooi, "Postgrowth band gap trimming of InAs/InAlGaAs quantum-dash laser," Appl. Phys. Lett. 90, 031101 (2007).
11. X. C. Wang, S. J. Xu, S. J. Chua, Z. H. Zhang, W. J. Fan, C. H. Wang, J. Jiang, and X. G. Xie, "Widely tunable intersubband energy spacing of self-assembled InAs/GaAs quantum dots due to interface intermixing," J. Appl. Phys. 86, 2687-2690 (1999).
12. A. O. Kosogov, P. Werner, U. Gosele, N. N. Ledentsov, D. Bimberg, V. M. Ustinov, A. Y. Egorov, A. E. Zhukov, P. S. Kopev, N. A. Bert, and Z. I. Alferov, "Structural and optical properties of InAs-GaAs quantum dots subjected to high temperature annealing," Appl. Phys. Lett. 69, 3072-3074 (1996).
13. J. J. Dubowski, C. N. Allen, and S. Fafard, "Laser-induced InAs/GaAs quantum dot intermixing," Appl. Phys. Lett. 77, 3583-3585 (2000).
14. Z. Y. Zhang and R. A. Hogg, "Post-growth intermixing of GaAs based quantum dot devices," in Quantum Dot Devices (Springer, 2012).
15. R. Leon, Y. Kim, C. Jagadish, M. Gal, J. Zou, and D. J. H. Cockayne, "Effects of interdiffusion on the luminescence of InGaAs/GaAs quantum dots," Appl. Phys. Lett. 69, 1888-1890 (1996).
16. S. Fafard and C. N. Allen, "Intermixing in quantum-dot ensembles with sharp adjustable shells," Appl. Phys. Lett. 75, 2374-2376 (1999).
17. A. Babinski, J. Jasinski, R. Bozek, A. Szepielow, and J. M. Baranowski, "Rapid thermal annealing of InAs/GaAs quantum dots under a GaAs proximity cap," Appl. Phys. Lett. 79, 2576-2578 (2001).
18. D. Bhattacharyya, A. S. Helmy, A. C. Bryce, E. A. Avrutin, and J. H. Marsh, "Selective control of self-organized $In_{0.5}Ga_{0.5}As$/GaAs quantum dot properties: Quantum dot intermixing," J. Appl. Phys. 88, 4619-4622 (2000).
19. C. Lobo, R. Leon, S. Fafard, and P. G. Piva, "Intermixing induced changes in the radiative emission from III-V quantum dots," Appl. Phys. Lett. 72, 2850-2852 (1998).
20. C. K. Chia, J. R. Dong, S. J. Chua, and S. Tripathy, "Bandgap engineering in semiconductor quantum dots," J. Cryst. Growth 288, 57-

60 (2006).

21. Z. Y. Zhang, P. Jin, C. M. Li, X. L. Ye, X. Q. Meng, B. Xu, F. Q. Liu, and Z. G. Wang, "The evolution of InAs/InAlAs/InGaAlAs quantum dots after rapid thermal annealing," J. Cryst. Growth 253, 59-63 (2003).
22. C. K. Chia, S. J. Chua, J. R. Dong, and S. L. Teo, "Ultrawide band quantum dot light emitting device by postfabrication laser annealing," Appl. Phys. Lett. 90(2007).
23. Z. Y. Zhang, Z. G. Wang, B. Xu, P. Jin, Z. Z. Sun, and F. Q. Liu, "High-performance quantum-dot superluminescent diodes," IEEE Photon. Technol. Lett. 16, 27-29 (2004).
24. Z. Y. Zhang, Q. Jiang, and R. A. Hogg, "Tunable interband and intersubband transitions in modulation C-doped InGaAs/GaAs quantum dot lasers by postgrowth annealing process," Appl. Phys. Lett. 93, 071111 (2008).
25. L. Fu, P. Lever, H. H. Tan, C. Jagadish, P. Reece, and M. Gal, "Suppression of interdiffusion in InGaAs/GaAs quantum dots using dielectric layer of titanium dioxide," Appl. Phys. Lett. 82, 2613-2615 (2003).
26. R. M. Cohen, G. Li, C. Jagadish, P. T. Burke, and M. Gal, "Native defect engineering of interdiffusion using thermally grown oxides of GaAs," Appl. Phys. Lett. 73, 803-805 (1998).
27. A. Pepin, C. Vieu, M. Schneider, H. Launois, and Y. Nissim, "Evidence of stress dependence in SiO_2/Si_3N_4 encapsulation-based layer disordering of GaAs/AlGaAs quantum well heterostructures," J. Vac. Sci. Technol. B 15, 142-153 (1997).
28. S. Alexey, "Properties of pure aluminum," in Handbook of Aluminum (CRC Press, 2003).
29. Z. Y. Zhang, Q. Jiang, I. J. Luxmoore, and R. A. Hogg, "A p-type-doped quantum dot superluminescent LED with broadband and flat-topped emission spectra obtained by post-growth intermixing under a GaAs proximity cap," Nanotechnology 20, 055204 (2009).
30. P. W. Fry, I. E. Itskevich, S. R. Parnell, J. J. Finley, L. R. Wilson, K. L. Schumacher, D. J. Mowbray, M. S. Skolnick, M. Al-Khafaji, A. G. Cullis, M. Hopkinson, J. C. Clark, and G. Hill, "Photocurrent spectroscopy of

InAs/GaAs self-assembled quantum dots," Phys. Rev. B. 62, 16784-16791 (2000).

31. P. G. Hofstra, D. A. Thompson, B. J. Robinson, and R. W. Streater, "Application of an in situ hydrogen plasma to the epitaxial regrowth of InP grown by molecular beam epitaxy," J. Vac. Sci. Technol. B 11, 985-988 (1993).

6. Quantum Dot Selective Areas Intermixing for Broadband Light Sources (Device Investigation)

In this chapter, the QDI technique is demonstrated, based on the modulation p-doped sample, to laterally integrate two and three different QD light emitting devices with a single electrical contact. In an OCT system, the bandwidth of the light source is a critical parameter, which dictates the axial resolution. In this chapter, a light source with spectral bandwidth of ~240nm centred at ~1188nm is obtained in a device with two selective area intermixed sections, corresponding to an OCT axial resolution of ~3.5µm. Then, a three section selective area intermixed device is realized with a spectral bandwidth of ~310nm centred at ~1145nm, which corresponding to an OCT axial resolution of ~2.4µm. Such a small predicted axial resolution is highly desirable in an OCT system.

6.1. Introduction to Broadband Sources

Broadband light sources are vital components for wavelength division multiplexing (WDM) [1] and OCT systems [2] (introduced in section 1.3). The spectral shape of the broadband source is of critical importance in determining the axial resolution of the OCT system. The spectral bandwidth of the light source determines the coherence length which in turn determines the resolution of imaging [3]. Figure 6.1 shows an image taken from an OCT system [4]. It can be seen that different layers of the human skin are distinguishable, but due to the limitation of the bandwidth (~85nm) of the broadband light source, more details of the layers are not available (such as

the clear interface of different layers or the structure of a single cell).

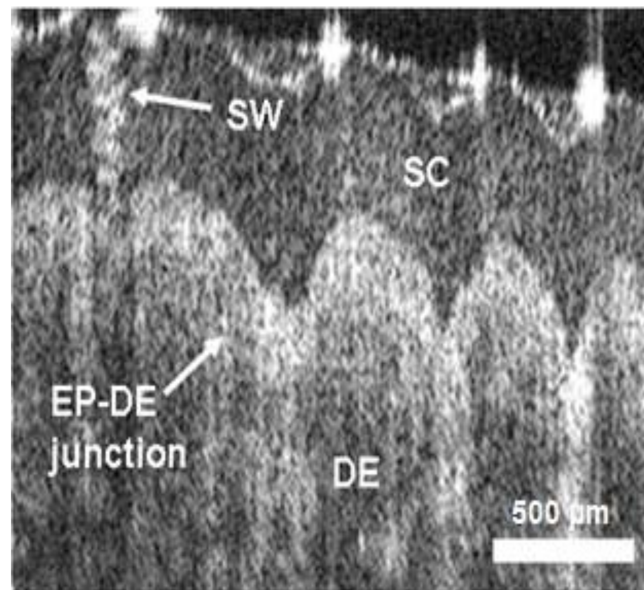

Figure 6.1. An image of human skin achieved from an OCT system [4].

In the past ~10 years, self-assembled quantum dot structures have attracted considerable attention for the realization of broadband optical sources due to their inhomogeneously broadened emission spectra [5, 6]. Various methods have been proposed and utilized to achieve broad spectral bandwidth light emission from QD devices, such as using multilayer stacks of QDs with different emission wavelength for each layer [7], or hybrid quantum well (QW)/quantum dot structures [8, 9] (as shown schematically in Figure 5.1(a)), optimizing the growth conditions to increase the inhomogeneous dot size distribution [10], or using multi-contact device structures [11]. In addition to QD epitaxial growth and device fabrication techniques, most recently, post-growth intermixing processes are emerging as a very effective method to broaden the emission spectrum [12], by increasing the effect of interdiffusion between In/Ga near the interface of the QDs and their surrounding barrier layer materials [13]. Subsequently, a selective area post-growth intermixing

technique has been successfully demonstrated to laterally integrate two different optical elements (quantum dot superluminescent diodes) by realizing a spatial variation of the bandgap energy of quantum dot materials across a single wafer, a demonstration was shown in Figure 5.1(b). Due to the difficulty of the fabrication process and the complexity of the intermixing process, only 3 different wavelengths can be integrated on one single contact device so far [14].

6.1.1. Broadband Emission Discussion Based on PL

In order to achieve a broadband light source, the spontaneous emission from different capped sections should complement each other. A demonstration is shown schematically in the inset of Figure 6.2.

Based on the PL results in previous sections, the modulation p-doped sample is found to have shorter wavelength shift and less integrated intensity decrease compared to the un-doped sample. TiO_2 and Al caps were shown to be effective in suppressing the wavelength shift during the intermixing process at an annealing temperature of 700°C.

Therefore, the 200nm TiO_2 cap, the 200nm Al cap and the 200nm SiO_2 cap on the modulation p-doped samples were annealed at 700°C, they were chosen to be further investigated for broadband source application, and the PL result is shown in Figure 6.2. Also a 500nm SiO_2 cap was deposited on the p-doped sample and then annealed at 700°C to further blue shift the wavelength, the purpose of this is schematically shown in the inset of Figure 6.2 and the theory was introduced at the end of section 5.3.1.3.

For the 500nm SiO_2 capped modulation p-doped sample annealed at 700°C, the GS peak is further blue shifted to ~1089nm, also its integrated PL intensity drops compared to other capped samples, it is plotted in Figure 6.2.

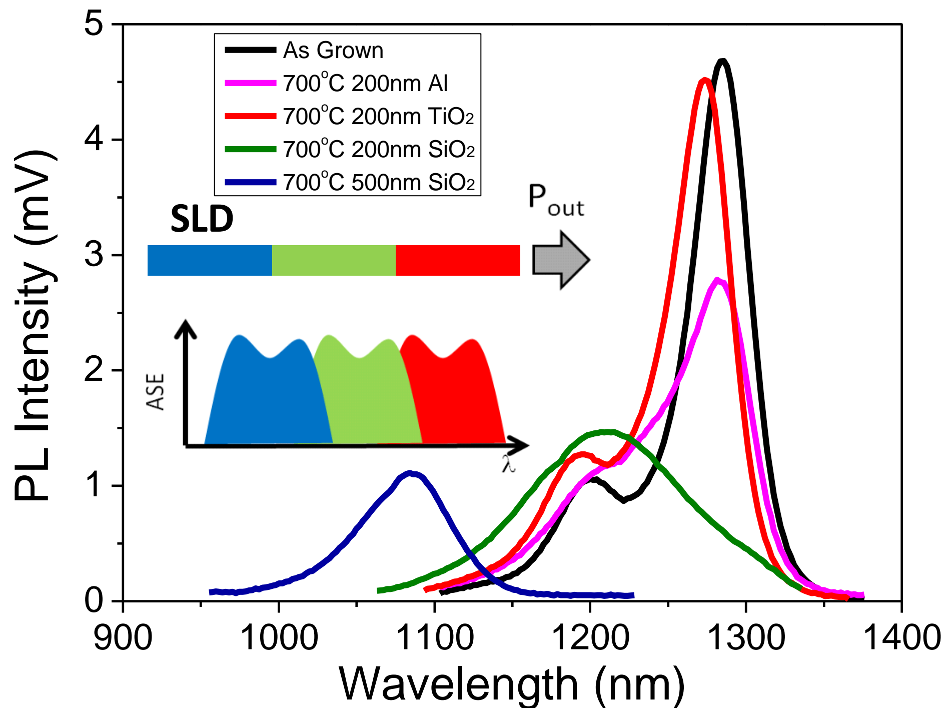

Figure 6.2 PL intensity versus wavelengths of different caps used on the modulation p-doped sample during the annealing process. The annealing temperature was 700°C and the inset shows a demonstration of the emission components of a broadband light source.

6.1.2. Power-Dependent PL & Analysis

The room temperature power-dependent PL is shown in Figure 6.3, for the identical samples measured in Figure 6.2. For the as-grown sample, at a pump power (~10W/cm^2) the GS is located at ~1285nm, the FWHM of the GS is ~41nm.

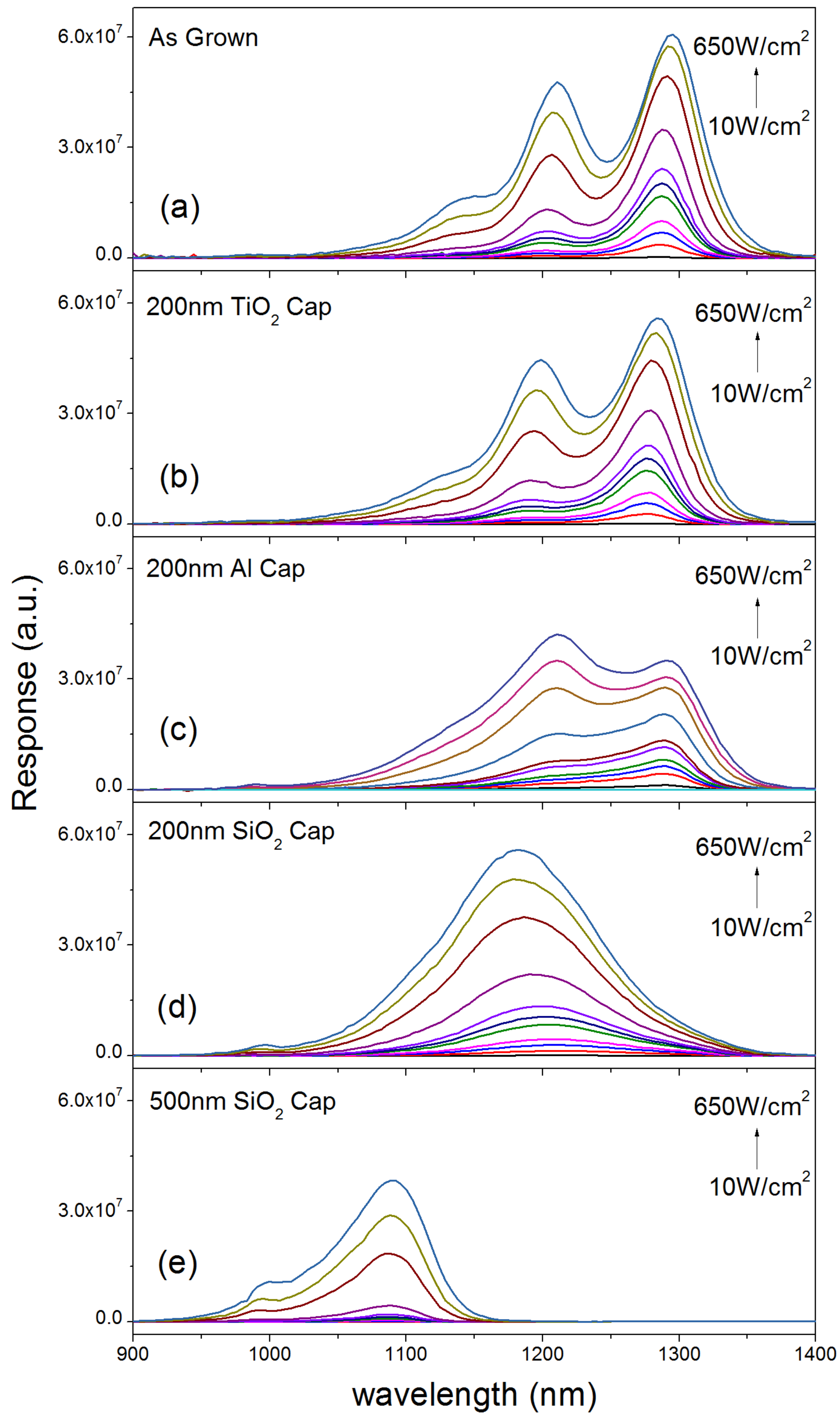

Figure. 6.3. Power-dependent PL for (a) As-grown sample, (b) sample annealed with 200nm thick TiO_2 film, (c) sample annealed with 200nm thick Al film, (c) sample annealed with 200nm SiO_2 film, (d) sample annealed with 500nm SiO_2 film [14].

At higher pump power (~20W/cm^2), the GS saturates due to state filling [15] and the ES_1 is observed at ~1202nm with FWHM of ~58nm. At the pump power of ~650W/cm^2, the ES_2 starts to appear at ~1146nm with FWHM of ~68nm. The power-dependent PL data of the TiO_2 caped sample annealed at 700°C is plotted in Figure 6.3(b). At pump power (~10W/cm^2) the GS is slightly blue-shifted (~10nm) to ~1275nm compared to the as-grown sample, the FWHM of the GS is ~42nm. At higher pump power (~20W/cm^2), the GS saturates and the ES_1 is observed at ~1191nm with a FWHM of ~63nm. At the pump power of ~650W/cm^2 ES_2 starts to appear at ~1134nm with FWHM of ~68nm. It has been predicted [16] that by using a TiO_2 cap, long wavelength emission of QDs can be preserved during the selective area intermixing process, which is very important for broadband emission light source fabrication. As expected, the spectral shape of the TiO_2 capped sample is very similar to that of the as-grown sample and the PL integrated intensities are essentially the same at the maximum pump power density.

The result for the Al capped sample is shown in Figure 6.3(c), at pump power (~10W/cm^2) the GS is located at ~1285nm and the FWHM of the GS is ~43nm. At higher pump power (~20W/cm^2), the GS is observed to saturate and the ES_1 is observed at ~1211nm with FWHM of ~74nm. At the pump power of ~650W/cm^2 ES_2 starts to appear at ~1140nm with FWHM of ~80nm. A reduction in ES-GS splitting has been observed in the early stage of QD intermixing [17], the RT-PL spectra of the SiO_2 capped sample shows such a reduction in state splitting.

In Figure 6.3(d), the spectra of the sample annealed at 700°C with 200nm SiO_2 is plotted, at pump power (~10W/cm^2) the GS exhibits a large blue-shift of ~75nm (from ~1285nm to ~1210nm), the FWHM of the GS is ~124nm. There is no clear second peak appearing with increasing excitation power. The apparent blue-shift of the peak can be attributed to state filling effects when the split in energy is smaller than the inhomogeneous broadening. Also, the enhanced interdiffusion observed for the SiO_2 capped QD sample is in a good agreement with previous reports [18]. At the pump power of ~650W/cm^2 the GS and ES combined peak is located at 1182nm with FWHM of ~132nm.

Figure 6.3(e) shows the sample annealed at 700°C capped with a 500nm SiO_2 film, at pump power (~10W/cm^2) its GS emission peak blue shifted from ~1285nm to ~1087nm (~198nm) with FWHM of ~42nm, and the PL integrated intensity drops to ~50% of the as-grown sample. There is no significant blue-shift with increasing pump power, this may due to a transition from QD-like to more QW-like behaviour with increasing degree of intermixing.

Furthermore, the reduced PL intensity is suggestive of a reduced carrier lifetime which may also act to inhibit state-filling effects. At the pump power of ~650W/cm^2 the GS is located at ~1090nm with the FWHM of ~58nm. To a greater or lesser degree, a feature is observed in all spectra at ~990nm. This is attributed to recombination in the QW in which the QDs are encapsulated. It is observed that this emission becomes more pronounced as the confinement energy of the QDs is reduced.

Although an Al mask is a good candidate to preserve the emission wavelength and intensity of the QDs during the annealing treatment, a very rough surface was observed after the Al was removed. Further processing of the sample was not pursued. The other three capping materials were investigated further as a smooth sample surface was maintained, ideal for device fabrication.

6.1.3. PC Measurement & Analysis

In the previous sections, based on the PL result, the TiO_2 cap and the SiO_2 cap were used on the p-doped sample annealed at 700°C. The SiO_2 capped un-doped QD samples with two different annealing temperatures were further investigated with the PC technique in 5.3.2.1. Here, the room temperature PC results of the TiO_2 and SiO_2 capped samples with no reverse bias are shown in Figure 6.4.

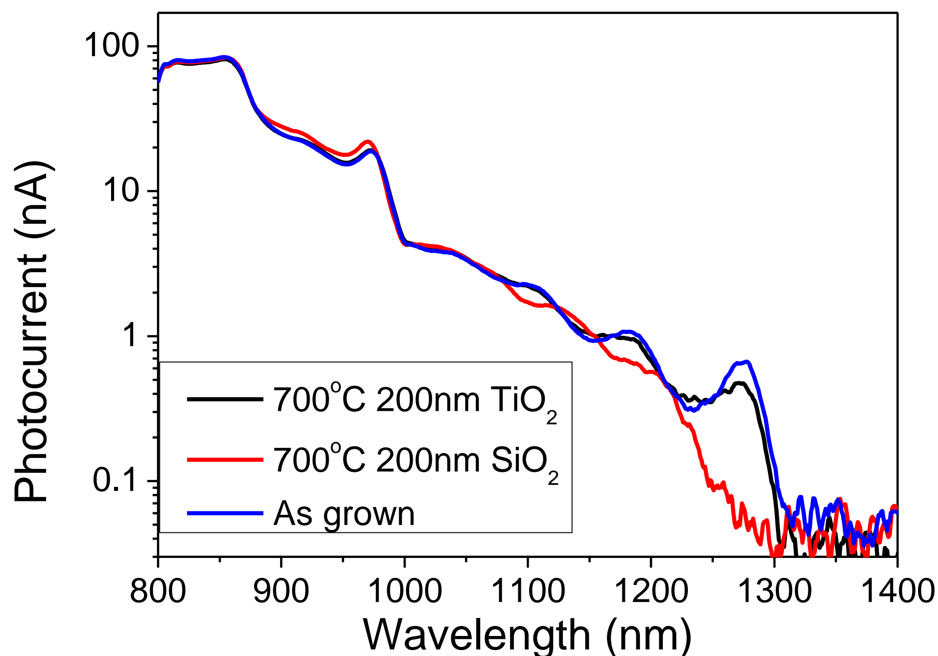

Figure 6.4 The PC results of the mesa devices with different caps during the annealing process.

The samples were annealed at 700°C. The PC of the as-grown sample shows the well confined absorption peaks of the GS (~1274nm), ES_1 (~1185nm), ES_2 (~1106nm)….

The PC plot for the 200nm TiO_2 capped sample is similar to the as-grown sample. The intensity of the GS is lower than that of the as-grown sample with a slight blue-shift. For the 200nm SiO_2 capped sample, the GS absorption peak is blue shifted by ~71nm and there is almost no absorption at the original wavelength, indicating the shape of the quantum dot may had been changed as described in previous sections. The PC shows agreement with the PL result, after annealing process the intensity of the TiO_2 capped sample is slightly lower than the as-grown sample with its GS slightly blue shifted, this may due to the compensation of the increase of the dot volume and the shallow quantum confinement, which is discussed previously. The GS of the SiO_2 capped sample blue shifted to ~1204nm. Figure 6.4 demonstrates the potential for using a TiO_2 cap associated with a SiO_2 cap for active/passive QD devices. The next step is to fabricate the integrated broadband device based on the previous investigation.

6.1.4. Device Fabrication and Result

The selective area intermixed QD samples were fabricated into 5μm wide ridge waveguide devices by a dry etch through the QD active region. A thin layer of Au-Zn-Au and In-Ge-Au was thermally evaporated on the top and the bottom of the device to provide p and n-side ohmic contacts, respectively. The waveguide structure is 7 degree off from normal to the facet. A schematic of this process is shown in Figure 6.5 and the detailed fabrication process has been discussed in chapter 2.

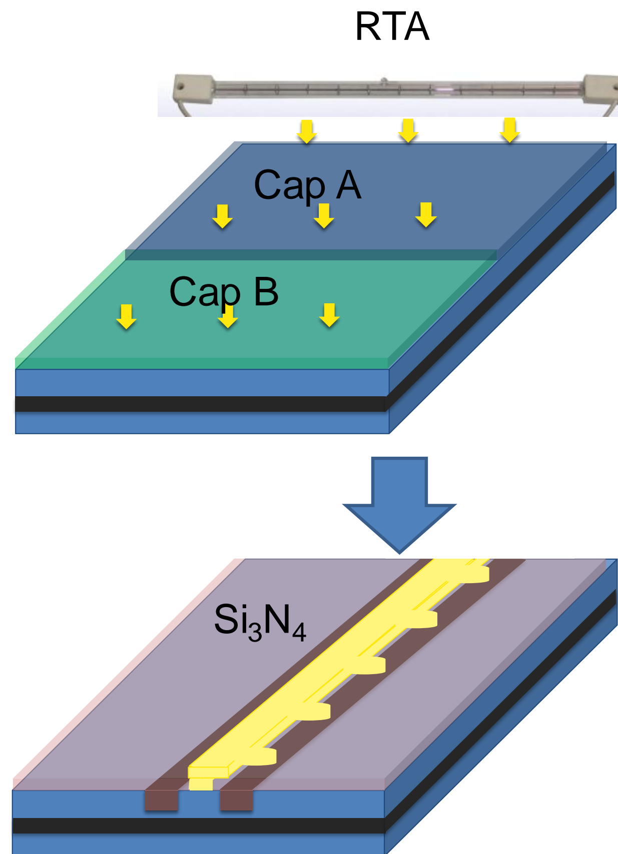

Figure 6.5 The demonstration of the annealing process and the 7 degree off normal ridge device structure.

6mm long as-cleaved devices were mounted on ceramic titles and tested at room temperature under pulsed operation with 5μs pulse width and 5% duty cycle to reduce the effect of self-heating.

6.1.4.1. Two Section Integrated Device

Firstly, a device was fabricated containing two light emitting elements realized using a 200nm TiO_2 cap and a 200nm SiO_2 cap. A 5 minute, 700°C anneal was then applied to this sample to create two regions with different emission wavelengths. A 5μm wide 7 degree off ridge waveguide device was fabricated, as described previously. The top view of the device is plotted as an inset in Figure 6.6, the TiO_2 capped section is chosen to be 2mm and the SiO_2 capped section is chosen to be 4mm.

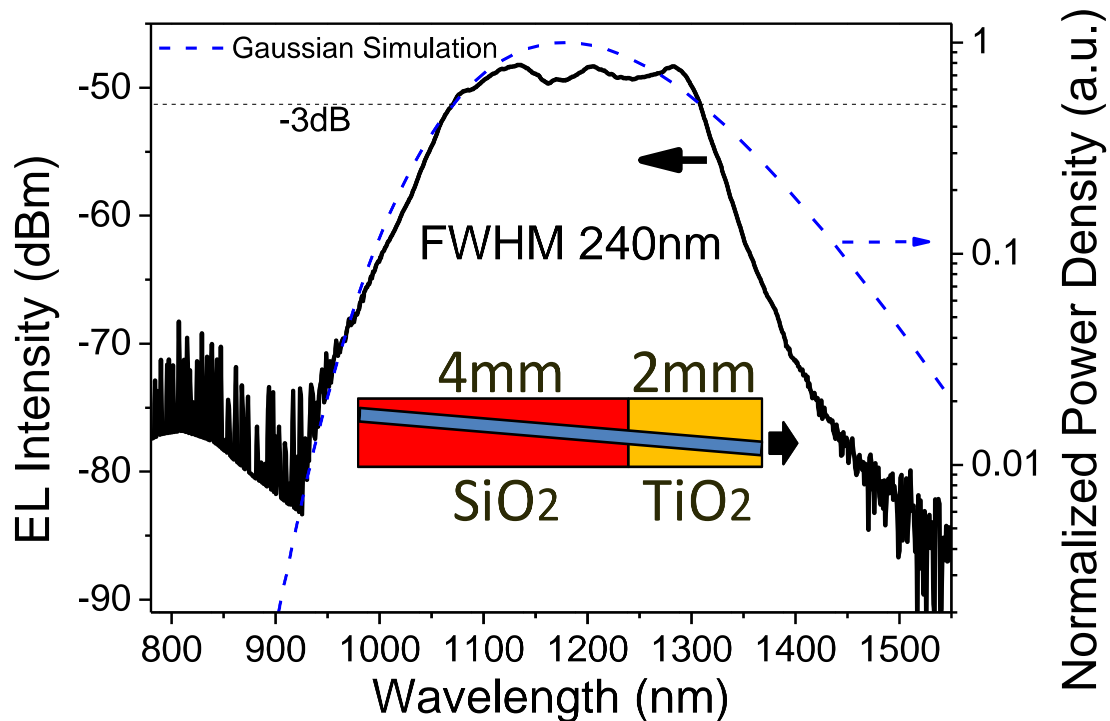

Figure 6.6 The EL spectrum of the two section integrated device, the dash line shows the Gaussian power spectral density (PSD) simulation and the inset shows the top view of the integrated device.

The EL spectrum of the device under pulse mode is shown in Figure 6.6 with a maximum ex-facet power of ~2.25mW at a drive current density of 3.67kA/cm^2. An emission spectrum of ~240nm -3dB band-width centred at ~1188nm is obtained at this maximum power. As there is a large differential shift of the emission wavelengths of the two intermixed QD regions, a broader spectrum is obtained compared to the previous work in [16], where the spectra from the two intermixed regions were strongly overlapped.

The power spectral density (PSD), which is fully characterized by the spectral shape, the spectral bandwidth, and the centre wavelength, is usually used to estimate the resolution of an optical coherence imaging systems [19-22]. A general expression for a normalized Gaussian PSD *S(λ)* is shown in equation 6-(1) [3]:

$$S_{Gaussian}(\lambda)=\frac{2\sqrt{\ln 2}\lambda_0^2}{\sqrt{\pi}c\Delta\lambda}\exp\left\{-\left[2\sqrt{\ln 2}\frac{\left(\frac{1}{\lambda}-\frac{1}{\lambda_0}\right)}{\left(\frac{\Delta\lambda}{\lambda_0^2}\right)}\right]^2\right\} \quad 6\text{-}(1)$$

and its inverse Fourier transform *Γ(λ)* is shown in equation 6-(2) [3]:

$$\Gamma_{Gaussian}(\tau)=\exp\left[-\left(\frac{\pi c\Delta\lambda\tau}{\lambda_0^2 2\sqrt{\ln 2}}\right)^2\right]\exp\left[-j\left(\frac{2\pi c\tau}{\lambda_0}\right)\right] \quad 6\text{-}(2)$$

Where λ_0 is the centre wavelength and $\Delta\lambda$ is the -3dB spectral bandwidth. The Gaussian PSD spectrum is plotted based on equations 6-(1) compared to the experimental spectrum in Figure 6.6. The λ_0 and $\Delta\lambda$ were set to 1188(nm) and 240(nm) respectively.

If the PSD of a light source is a Gaussian spectral shape, the coherence lengths l_{cFWHM} of an OCT system can be theoretically represented as [3]:

$$l_{cFWHM}=\frac{4\ln 2}{\pi}\times\frac{\lambda_0^2}{\Delta\lambda} \quad 6\text{-}(3)$$

where λ_0 is the centre wavelength of the spectrum and $\Delta\lambda$ is the -3dB bandwidth of the spectrum. Based on equation 6-(3), $l_{cFWHM}/2$ is ~2.6μm if the experimentally determined bandwidth value of 240nm is used. Such resolution may be used to visualize the details of *e.g.* the human skin tissues, retina, and choroid where features have typical scales between ~10 and 30μm [23, 24]. However, equation 6-(3) is only satisfied when the spectrum is a pure Gaussian shape. For more complex emission spectra the resolution of an OCT system may be estimated through the complex temporal coherence function (CTCF) which can be regarded as the point spread function (PSF) of the imaging system [3].

Figure 6.7 plots the modulus of the CTCF for the experimental spectrum in Figure 6.6 and the CTCF of a Gaussian peak with $\Delta\lambda = 240\mathrm{nm}$, obtained using an inverse fast Fourier transform in equation 6-(2). For the Gaussian spectrum (from equation 6-(2)), as expected we obtain a system resolution similar to the calculated one based on equation 6-(3). There is almost no side-lobe on the simulated system resolution, shown by the red line in Figure 6.7(a). Based on this data, for a light source with Gaussian shape with 240nm -3dB bandwidth, the theoretical resolution is ~3.2um when the Rayleigh criterion is satisfied [3], shown in Figure 6.7(b).

For the experimental data, side-lobes are observed in the CTCF and half of the FWHM of the peak corresponding to ~3.2μm axial resolution. However, side-lobes in the CTCF close to the main lobe will act to decrease image resolution. The impact of the side-lobes in resolution is explored in Figure 6.7(c), where the experimentally obtained CTCF is applied to two layers separated by Δz (the optical path-length difference). Here, in order to achieve the Rayleigh criterion for resolution Δz is ~3.5μm. The non-Gaussian emission spectrum of the device may therefore be considered to introduce a 0.3μm penalty to system axial resolution. In addition, ~35% of the energy is lost in the side-lobe.

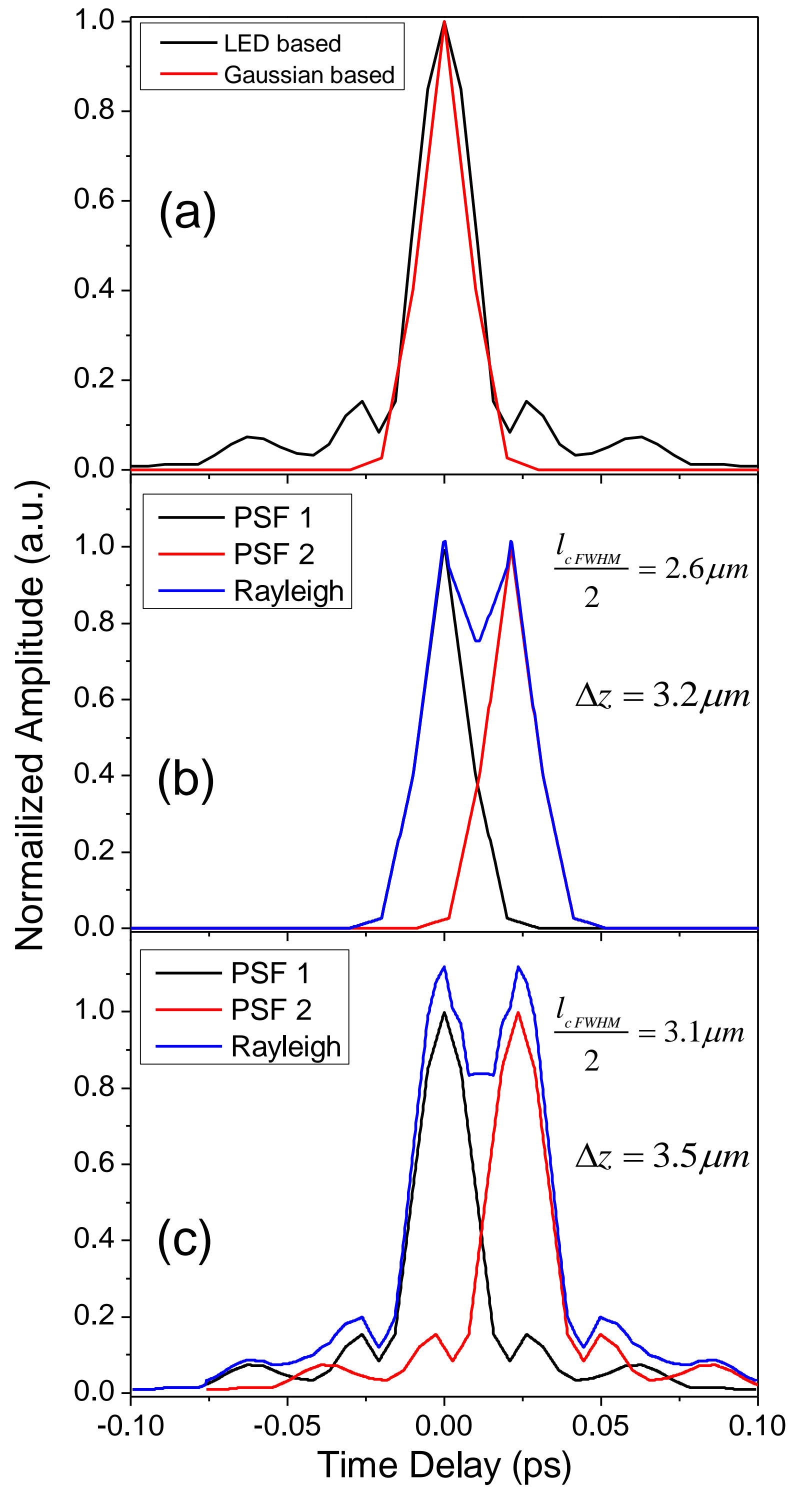

Figure 6.7 (a) The computed CTCF in time domain, (b) the plot when the two Gaussian PSF functions satisfy the Rayleigh criterion, (c) the plot when the two experimental CTCF functions satisfy the Rayleigh criterion.

6.1.4.2. Three Section Integrated Device

In order to further increase the -3dB bandwidth of the light emission spectrum,

a three section intermixed device was fabricated. Again it is a 5μm wide 7 degree off ridge waveguide device. This device consists of a 200nm TiO_2 film covered region (1mm section), a 200nm SiO_2 film covered region (2mm section) and a 500nm SiO_2 film covered region (3mm section) incorporated in one device during the annealing process at 700°C for 5 minutes. The EL spectrum of the device is shown in Figure 6.8 with a maximum ex-facet power of ~1.81mW at a drive current density of 3.5kA/cm^2. A spectrum with ~310nm -3dB bandwidth centred at ~1145nm is obtained at this maximum power.

Moreover, the Gaussian PSD spectrum is plotted compared to the experimental spectrum in Figure 6.8 based on equations 6-(1). The λ_0 and $\Delta\lambda$ were set to 1145(nm) and 310(nm) respectively. The top view of the device is also shown as an inset in Figure 6.8.

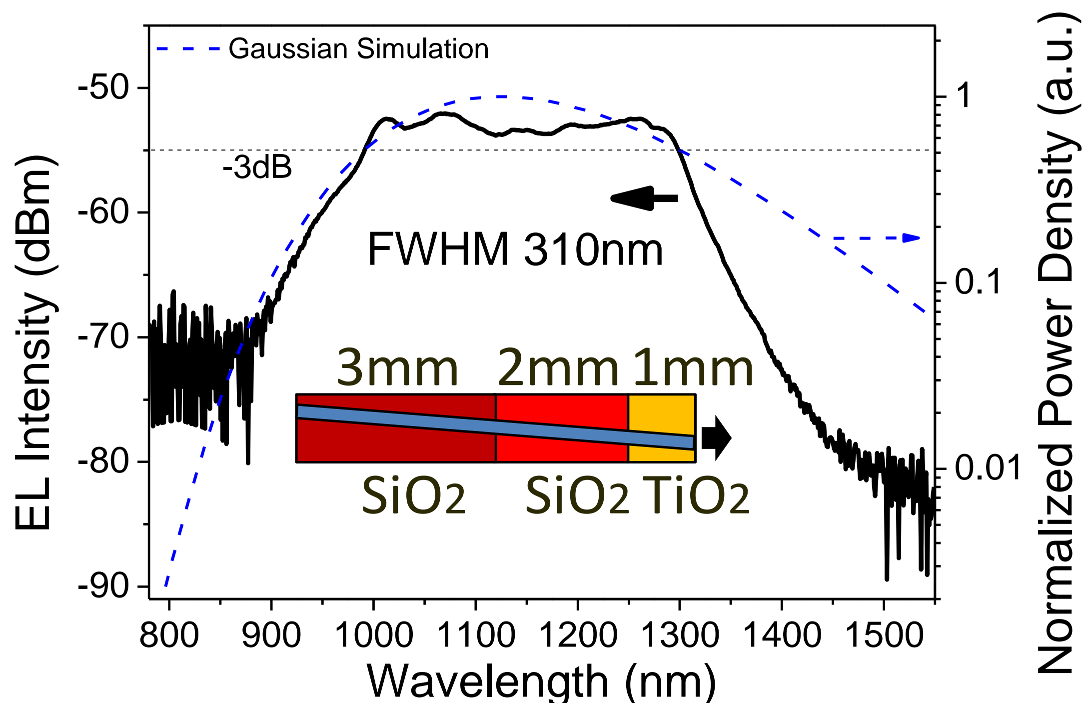

Figure 6.8 The EL spectrum of the three section integrated device, the dash line shows the Gaussian PSD simulation and the inset shows the top view of the integrated device.

As expected, from the PL data presented previously, the spectrum from the

TiO_2 caped section and the spectra from the other two SiO_2 caped sections overlap to form an emission spectrum with a flat top.

Figure 6.9(a) plots the CTCF of a Gaussian peak with $\Delta\lambda = 310\text{nm}$ which obtained using an inverse fast Fourier transform in equation 6-(2) and it also shows the CTCF based on the experimental data in Figure 6.8. Based the experimental data, half of the FWHM of the peak corresponding to a ~2.2μm axial resolution.

For the simulated Gaussian spectrum, the measured system resolution (~1.9μm) is similar to the calculated one based on equation 6-(3). And there is almost no side-lobe on the simulated system resolution, shown the red line in Figure 6.9(a). Therefore, for a light source in Gaussian shape with 310nm -3dB bandwidth, the theoretical resolution is 2.1um when the Rayleigh criterion is satisfied, as shown in Figure 6.9(b).

Again, for the experimental spectrum, the effect of the side-lobes on axial resolution is explored in 6.9(c), where the experimentally obtained CTCF is applied to two layers separated by Δz. Here, in order to achieve the Rayleigh criterion the axial resolution is ~2.4μm. This gives us a corrected axial resolution of ~2.4μm for the three section intermixed device. These theoretical values for OCT system resolution are promising for sub-cellular resolution imaging.

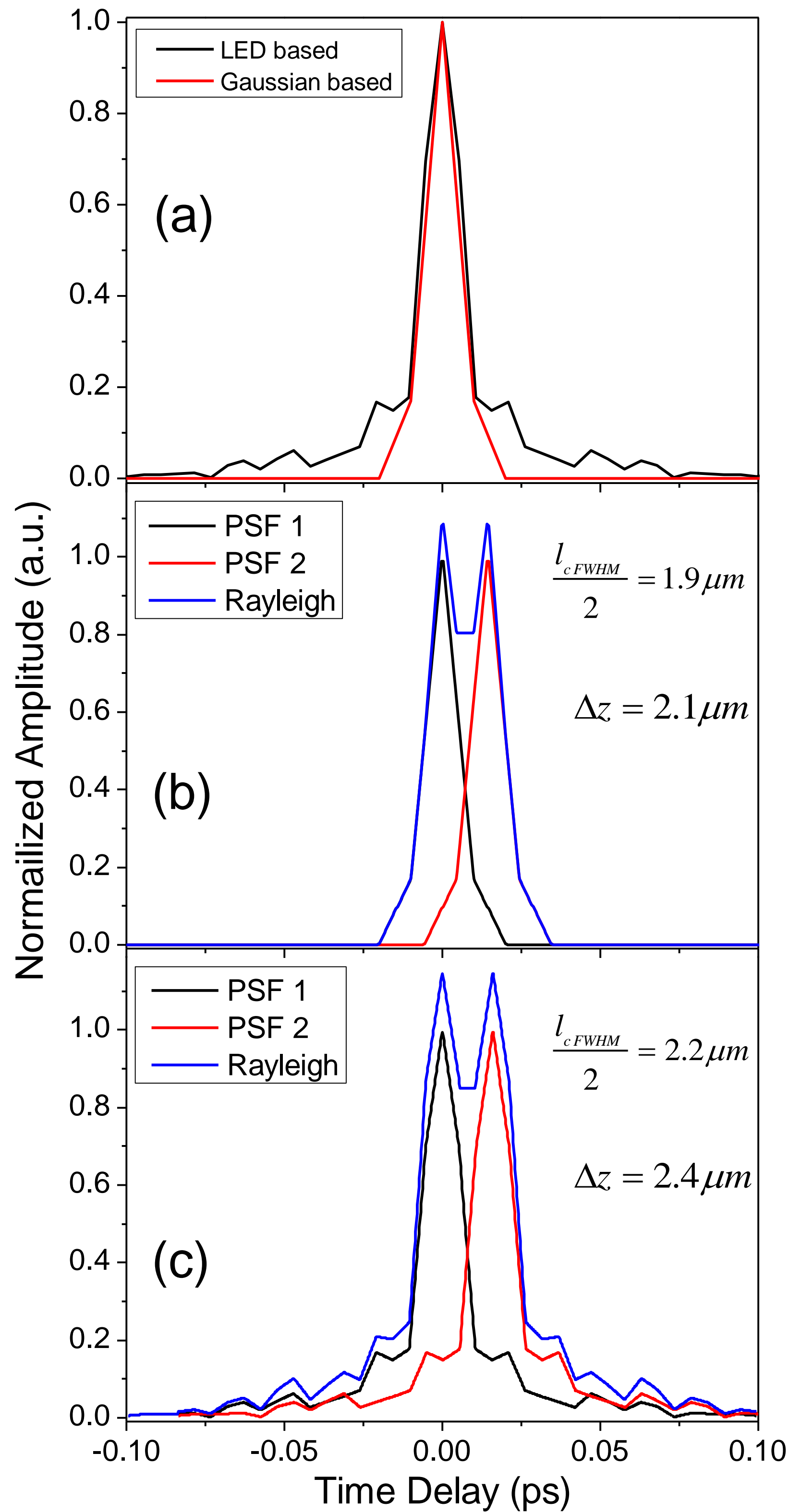

Figure 6.9 (a) Shows the computed CTCF in time domain, (b) shows the plot when the two Gaussian PSF functions satisfy the Rayleigh criterion, (c) shows the plot when the two experimental CTCF functions satisfy the Rayleigh criterion.

6.2. Conclusion

In summary, OCT applications for broadband sources were introduced in this chapter. Then, power dependent PL and photocurrent were used to investigate the optical properties of varies intermixed samples. By fabricating samples annealed at 700°C with suitable caps and choosing suitable device length, devices with two and three differentially intermixed regions are realized. FWHMs of ~240nm and ~310nm with ex-facet mW power levels were obtained for the two and three intermixed region devices, respectively. Based on the experimental spectra, the theoretical system axial resolution in an OCT system is discussed. The resolutions of ~3.5μm and ~2.4μm were deduced using the Rayleigh criterion, for the two and three intermixed region devices, respectively.

6.3. Further work

In this work, because the ridge was etched through active region, it has a strong light confinement which tends to make these device lase. In future device fabrication, it is better to stop the etch depth above the active region to prevent this lasing. Furthermore, both devices discussed in section 6.2.3 failed under CW operation. This may be because of the thick substrate left in the device and the deep etching of the ridge, which prevents heat extraction from the active region. In the next fabrication runs, the substrate should be thinned down to less than ~100μm instead of ~180μm. The shallower ridge etch and thinner substrate should help in heat extraction from the junction.

Also, instead of fabricating and testing the two/three section integrated device

directly, devices with different capping materials in each section could be investigated under CW mode in advance. This process is helpful for detecting the failure mode in the integrated devices. This may be due to the modification in the diode characteristics of the different intermixed regions. In such a case, the majority of current is passed through the “best” intermixed diode. A segmented contact device, with a corresponding intermixing mask would allow this effect to be ameliorated.

Also, in order to further investigate the gain measured by the Hakki-Paoli method, for each capping material, the samples can be annealed at different temperatures and then fabricated into 3μm edge-emit devices. Then the temperature dependent gain for this capping material can be achieved. This method can be repeated for all the promising capping material. The simulation of the LED devices with a spatial variation in band-gap has not been discussed. A comprehensive set of empirical data is required to allow this modelling to be meaningful.

Reference

1. R. D. Feldman, E. E. Harstead, S. Jiang, T. H. Wood, and M. Zirngibl, "An evaluation of architectures incorporating wavelength division multiplexing," J. Lightwave Technol. 16, 1546-1559 (1998).
2. W. Drexler, U. Morgner, F. X. Kartner, C. Pitris, S. A. Boppart, X. D. Li, E. P. Ippen, and J. G. Fujimoto, "In vivo ultrahigh-resolution optical coherence tomography," Opt. Lett. 24, 1221-1223 (1999).
3. C. Akcay, P. Parrein, and J. P. Rolland, "Estimation of longitudinal resolution in optical coherence imaging," Appl. Optics 41, 5256-5262 (2002).
4. P. D. L. Greenwood, D. T. D. Childs, K. Kennedy, K. M. Groom, M. Hugues, M. Hopkinson, R. A. Hogg, N. Krstajic, L. E. Smith, S. J. Matcher, M. Bonesi, S. MacNeil, and R. Smallwood, "Quantum Dot Superluminescent Diodes for Optical Coherence Tomography: Device Engineering," IEEE J. Sel. Topics Quantum Electron. 16, 1015-1022 (2010).
5. Z. Y. Zhang, Z. G. Wang, B. Xu, P. Jin, Z. Z. Sun, and F. Q. Liu, "High-performance quantum-dot superluminescent diodes," IEEE Photon. Technol. Lett. 16, 27-29 (2004).
6. Z. Y. Zhang, R. A. Hogg, X. Q. Lv, and Z. G. Wang, "Self-assembled quantum-dot superluminescent light-emitting diodes," Adv. Opt. Photon. 2, 201-228 (2010).
7. L. H. Li, M. Rossetti, A. Fiore, L. Occhi, and C. Velez, "Wide emission spectrum from superluminescent diodes with chirped quantum dot multilayers," Electron. Lett. 41, 41-43 (2005).
8. S. M. Chen, K. J. Zhou, Z. Y. Zhang, D. T. D. Childs, M. Hugues, A. J. Ramsay, and R. A. Hogg, "Ultra-broad spontaneous emission and modal gain spectrum from a hybrid quantum well/quantum dot laser structure," Appl. Phys. Lett. 100, 041118 (2012).
9. S. M. Chen, K. J. Zhou, Z. Y. Zhang, J. R. Orchard, D. T. D. Childs, M. Hugues, O. Wada, and R. A. Hogg, "Hybrid quantum well/quantum dot structure for broad spectral bandwidth emitters," IEEE J. Sel. Topics

Quantum Electron. 19, 1900209-1900209 (2013).

10. X. Q. Lv, N. Liu, P. Jin, and Z. G. Wang, "Broadband emitting superluminescent diodes with InAs quantum dots in AlGaAs matrix," IEEE Photon. Technol. Lett. 20, 1742-1744 (2008).
11. Y. C. Xin, A. Martinez, T. Saiz, A. J. Moscho, Y. Li, T. A. Nilsen, A. L. Gray, and L. F. Lester, "1.3μm quantum-dot multisection superluminescent diodes with extremely broad bandwidth," IEEE Photon. Technol. Lett. 19, 501-503 (2007).
12. Q. Jiang, Z. Y. Zhang, M. Hopkinson, and R. A. Hogg, "High performance intermixed p-doped quantum dot superluminescent diodes at 1.2μm," Electron. Lett. 46, 295-U249 (2010).
13. Z. Y. Zhang, R. A. Hogg, B. Xu, P. Jin, and Z. G. Wang, "Realization of extremely broadband quantum-dot superluminescent light-emitting diodes by rapid thermal-annealing process," Opt. Lett. 33, 1210-1212 (2008).
14. K. J. Zhou, Q. Jiang, Z. Y. Zhang, S. M. Chen, H. Y. Liu, Z. H. Lu, K. Kennedy, S. J. Matcher, and R. A. Hogg, "Quantum dot selective area intermixing for broadband light sources," Opt. Express 20, 26950-26957 (2012).
15. S. Grosse, J. H. H. Sandmann, G. von Plessen, J. Feldmann, H. Lipsanen, M. Sopanen, J. Tulkki, and J. Ahopelto, "Carrier relaxation dynamics in quantum dots: scattering mechanisms and state-filling effects," Phys. Rev. B. 55, 4473-4476 (1997).
16. Z. Y. Zhang, Q. Jiang, M. Hopkinson, and R. A. Hogg, "Effects of intermixing on modulation p-doped quantum dot superluminescent light emitting diodes," Opt. Express 18, 7055-7063 (2010).
17. Z. Y. Zhang, Q. Jiang, I. J. Luxmoore, and R. A. Hogg, "A p-type-doped quantum dot superluminescent LED with broadband and flat-topped emission spectra obtained by post-growth intermixing under a GaAs proximity cap," Nanotechnology 20, 055204 (2009).
18. B. S. Ooi, K. McIlvaney, M. W. Street, A. S. Helmy, S. G. Ayling, A. C. Bryce, J. H. Marsh, and J. S. Roberts, "Selective quantum-well intermixing in GaAs-AlGaAs structures using impurity-free vacancy diffusion," IEEE J. Quantum Electron. 33, 1784-1793 (1997).

19. A. F. Fercher, "Optical coherence tomography," J. Biol. Opt. 1, 157-173 (1996).
20. J. A. Izatt, M. D. Kulkarni, H. W. Wang, K. Kobayashi, and M. V. Sivak, "Optical coherence tomography and microscopy in gastrointestinal tissues," IEEE J. Sel. Topics Quantum Electron. 2, 1017-1028 (1996).
21. B. Bouma, G. J. Tearney, S. A. Boppart, M. R. Hee, M. E. Brezinski, and J. G. Fujimoto, "High-resolution optical coherence tomographic imaging using a mode-locked Ti:Al_2O_3 laser source," Opt. Lett. 20, 1486-1488 (1995).
22. Y. T. Pan, R. Birngruber, J. Rosperich, and R. Engelhardt, "Low-coherence optical tomography in turbid tissue -theoretical analysis," Appl. Optics 34, 6564-6574 (1995).
23. Y. H. Zhao, Z. P. Chen, C. Saxer, S. H. Xiang, J. F. de Boer, and J. S. Nelson, "Phase-resolved optical coherence tomography and optical doppler tomography for imaging blood flow in human skin with fast scanning speed and high velocity sensitivity," Opt. Lett. 25, 114-116 (2000).
24. W. Drexler, U. Morgner, R. K. Ghanta, F. X. Kartner, J. S. Schuman, and J. G. Fujimoto, "Ultrahigh-resolution ophthalmic optical coherence tomography," Nature Medicine 7, 502-507 (2001).

7. Summary

In this thesis, I have analysed and discussed results related to the development of both QD laser and devices.

In chapter 1 and 2 the background and the basic experimental techniques were introduced and discussed.

In chapter 3, the dynamic characteristic (differential carrier lifetime) of two 15μm wide laser devices (an un-doped device and a modulation p-doped device) were investigated based on the small signal modulation method. It has been found for both un-doped and modulation p-doped samples all the recombination coefficients reduce with increasing temperature. Auger recombination is observed to be enhanced in the modulation p-doped sample compared to the un-doped sample.

In chapter 4, the L-I curve and the EL spectrum of a 3μm ridge laser device was shown. The differential external efficiency was introduced and discussed. T_0 of the device was also analysed and discussed, which is not very high for this device. Gain from a 250μm device at 20°C and 60°C were measured. The thermal escape coefficients at different temperatures were achieved by comparing the experimental gain data to the modelled gain data (based on the differential carrier lifetime). The possibility of obtaining a temperature insensitive laser was discussed at the end of the chapter by varying the Auger coefficient.

In chapter 5, the intermixing technique was introduced and discussed based on both QW and QDs. The important parameters during the PL measurement were also discussed. PL measurements were used to investigate a number of capping materials based on the QD and DWELL samples at temperatures of 700°C and 750°C. By comparing the PL results from different samples, at the end of the chapter, modulation p-doped sample annealed at 700°C was chosen to be further investigated.

In chapter 6, the power-dependent PL measurement was used to further investigate the modulation p-doped sample annealed at 700°C. After the analysis, the TiO_2 film and two different SiO_2 films were chosen to be used to fabricate LED devices. Firstly, a two-section device with mili-watt ex-facet powers was achieved with FWHM of ~240nm. Then a three-section device was obtained with a FWHM of ~310nm. By implementing a fast Fourier transform and applying the Rayleigh criterion to the PSF, a theoretical imaging system resolution of ~3.5μm (FWHM=240nm) and ~2.4μm (FWHM=310nm) were achieved if these LED devices are used in an OCT system.

By comparing to a combined broadband superluminescent diode (SLED) [1], the devices discussed in this thesis have a reduced complexity of the current driving system. Because the devices in chapter 6 have a single metal contact, this only needs one current source instead of 4 in [1]. Compared to the hybrid QW/QD technology [2], the broadband source achieved in this thesis has wider emission bandwidth (FWHM of ~213nm: ~310nm). Also the advantage

for this selective area intermixing technique is that there is no need for special design of the wafer structure, where in the QW/QD wafer the emission wavelength is carefully engineered. In previous intermixing investigation [3], although the output power was relatively high, the compensation of the spectrum emitted from two different sections was not successfully demonstrated. This has been successfully demonstrated in this thesis, details in chapter 6. Moreover, based on the discussion in chapter 5, the combination of TiO_2 cap and SiO_2 caps is considered to be an upgrade to the combination of GaAs proximity cap and SiO_2 cap [3] in realising broadband emitters, due to a better contact between capping material and the sample surface.

The potential impact this work may have is to offer a simple and cheap broadband light source for the OCT system. Moreover this work shows the possibility of integrating more than two individual sections into a single metal contact device. In the future, maybe more sections (>3) could be integrated in the device to provide a broader emission spectrum.

Reference

1. H. Wang, M. W. Jenkins, and A. M. Rollins, "A combined multiple-SLED broadband light source at 1300nm for high resolution optical coherence tomography," Opt. Commun. 281, 1896-1900 (2008).
2. S. M. Chen, K. J. Zhou, Z. Y. Zhang, J. R. Orchard, D. T. D. Childs, M. Hugues, O. Wada, and R. A. Hogg, "Hybrid quantum well/quantum dot structure for broad spectral bandwidth emitters," IEEE J. Sel. Topics Quantum Electron. 19, 1900209-1900209 (2013).
3. Z. Y. Zhang, Q. Jiang, M. Hopkinson, and R. A. Hogg, "Effects of intermixing on modulation p-doped quantum dot superluminescent light emitting diodes," Opt. Express 18, 7055-7063 (2010).

8. Appendix

8.1. 5µm and 15µm Narrow Ridge Lasers

Prepared by: Kristian Groom & Kejia Zhou

Proc. No.	Equipment / Chemicals	Notes	Process/Parameter Information					Achieved	Sign/Date
1	HCl Ultrasonic bath	Only for samples with In on back	**INDIUM REMOVAL FROM BACKSIDE**						
			Protect front side with resist and large slide and agitate in HCl. May take a long time.						
2	Scriber 1) n-Butyl 2) Acetone 3) IPA		**CLEAVE and CLEAN**						
			< one particle per field of view on 100 x magnification						
3	MJB3 mask aligner	Remove edge beads	**RIDGES PHOTOLITHOGRAPHY** Mask number: RIDGES (RFLAS - MASK1)						
	Resist: BPRS 100 (PLSI) or SPR350 (MF26A)	Clean mask.	Dimensions:	MIN	AIM	MAX	UNIT		
			Wide ridge:	14.5	15	15.5	µm		
		Require perfectly straight lines!	Narrow ridge:	4.5	5	5.5	µm		
	Align to cleaved edge		Follow lithography with 1 minute O_2 plasma ash , and 1min at 100°C hotplate.						
4	ICP Etcher	Approx 1µm per minute	**SEMICONDUCTOR RIDGE ETCH**						
				MIN	AIM	MAX	UNITS		
			$SiCl_4$ =		21		sccm		
			Cl_2 =		9		sccm		
			RF =		100		W		
			ICP =		500		W		
			Pressure =		4		mTorr		
			Temp =		20		degC		
	Dektak		Etch depth=	1.8	1.85	1.9	µm		
5	MJB3 mask aligner Resist: BPRS		**CONTACTS PHOTOLITHOGRAPHY** Mask number: CONTACTS (RFLAS - MASK1)						

	200 (PLSI)			MIN	AIM	MAX	UNITS		
			Wide ridges:	10.5	11	11.5	µm		
			Narrow:	2.5	3	3.5	µm		
			Follow lithography with 1 minute O_2 plasma Ash and 30 sec rinse in 19:1 DIW:Ammonia solution .						
6	Thermal Evaporator		**METAL DEPOSITION**						
				MIN	AIM	MAX	UNITS		
			Gold:	3	5	8	nm		
			Zinc:	8	10	12	nm		
			Gold:	180	200	220	nm		
			Lift off in acetone Follow lift-off with a 3 stage clean						
7	RTA Prog: Furn 360		**ANNEAL**						
				MIN	AIM	MAX	UNITS		
			Temperature:		360		degC		
			Ramp/Hold time:		3		sec		
8	Plasmatherm-PECVD Silicon Nitride	Rate = 10 nm/min	**DEPOSIT DIELECTRIC** Program STDSIN						
				MIN	AIM	MAX	UNIT		
			Thickness:		500		nm		
9	MJB3 Resist : BPRS 200 (PLSI) or SPR220 (MF26A)	Remove edge beads first	**CONTACT WINDOW NITRIDE PHOTOLITH** Mask number: WINDOWS (RFLAS- MASK 2)						
			Dimensions	MIN	AIM	MAX	UNIT		
			Wide ridge:	7	7.5	8	µm		
			Narrow ridge:	1.5	2	2.5	µm		
10	RIE Took 49mins on 21/11/2011	Etch until endpoint curve flattens, then add 30sec. Check window is clear.	**CONTACT WINDOW NITRIDE ETCH**						
			Critical Dimensions	MIN	AIM	MAX	UNIT		
			CHF_3		35		sccm		
			O_2		5		sccm		
			Pressure		35		mTorr		
			RF		75		W		
			Follow etch with 10 mins O_2 plasma Ash, heat in resist stripper, and 3 stage clean. Inspect that all resist removed.						

<table>
<tr><td>11</td><td>MJB3.

BPRS200 (PLSI)

No HMDS

Hard contact</td><td>Edge bead removal</td><td>BOND PADS PHOTOLITH
Mask number: S/I ETCH (RFLAS- MASK 1)<hr>Align normally. Expose. Move sample so ridges are just inside the open area of mask pattern. Expose again. Use longer exposure than necessary to make sure resist is well exposed at bottom of ridges.
Follow lithography with 2min O_2 plasma ash.</td><td></td><td></td></tr>
<tr><td>12</td><td>Thermal Evaporator</td><td>Half each thickness evaporated from either side of ridge</td><td>BOND PAD METAL DEPOSITION and LIFT-OFF<table><tr><td>From each side</td><td>MIN</td><td>AIM</td><td>MAX</td><td>UNIT</td></tr><tr><td>Titanium:</td><td>13/13</td><td>15/15</td><td>17/17</td><td>nm</td></tr><tr><td>Gold:</td><td>140/140</td><td>150/150</td><td>160/160</td><td>nm</td></tr></table></td><td></td><td></td></tr>
<tr><td>13</td><td>MJB3
SPR220 (MF26A)</td><td>Remove edge beads</td><td>ELECTROPLATED BOND PADS PHOTOLITH
Mask number: RFLAS e-plate (in “Groomguide” box)

Nb: Homemade mask so fit as best you can

Or use the Bond pad mask again (K. Zhou did)</td><td></td><td></td></tr>
<tr><td>14</td><td>ELECTROPLATING KIT.

DEKTAK</td><td>mount on gold slide & contact with Ag paint</td><td>ELECTROPLATED BOND PADS<table><tr><td></td><td>MIN</td><td>AIM</td><td>MAX</td><td>UNIT</td></tr><tr><td>Plated Thickness:</td><td>1.5</td><td>2</td><td>2.5</td><td>μm</td></tr></table></td><td></td><td></td></tr>
<tr><td>15</td><td>MINIMET 1000
FORCE: 006lbs
Speed :030</td><td>3μm paste</td><td>THINNING<table><tr><td></td><td>MIN</td><td>AIM</td><td>MAX</td><td>UNIT</td></tr><tr><td>Wafer thickness:</td><td>160</td><td>170</td><td>180</td><td>μm</td></tr></table>Be aware of uniformity, and allow for wax in thickness measurement.
Followed by 3 stage clean (using carriers).</td><td></td><td></td></tr>
<tr><td></td><td></td><td></td><td></td><td></td><td></td></tr>
<tr><td>16</td><td>Thermal evaporator</td><td></td><td>BACKCONTACT METAL<table><tr><td>Thickness</td><td>MIN</td><td>AIM</td><td>MAX</td><td>UNIT</td></tr><tr><td>InGe:</td><td>17</td><td>20</td><td>23</td><td>nm</td></tr><tr><td>Gold:</td><td>280</td><td>300</td><td>320</td><td>nm</td></tr></table></td><td></td><td></td></tr>
<tr><td>17</td><td>RTA
Program: FURN340</td><td></td><td>ANNEAL<table><tr><td></td><td>MIN</td><td>AIM</td><td>MAX</td><td>UNIT</td></tr><tr><td>Temperature:</td><td></td><td>340</td><td></td><td>DEG</td></tr><tr><td>Wait time</td><td></td><td>3</td><td></td><td>sec</td></tr></table></td><td></td><td></td></tr>
<tr><td>18</td><td></td><td></td><td>SCRIBE AND BREAK</td><td></td><td></td></tr>
</table>

<table>
<tr><td></td><td></td><td></td><td><table><tr><td></td><td>MIN</td><td>AIM</td><td>MAX</td><td>UNIT</td></tr><tr><td>Bar width</td><td>0.95</td><td>1.0</td><td>1.05</td><td>mm</td></tr><tr><td>Bar width</td><td>1.95</td><td>2.0</td><td>2.05</td><td>mm</td></tr><tr><td>Bar width</td><td>2.95</td><td>3.0</td><td>3.05</td><td>mm</td></tr><tr><td>Bar width</td><td>4.95</td><td>5.0</td><td>5.05</td><td>mm</td></tr></table></td><td></td><td></td></tr>
<tr><td>19</td><td>K&S Ultrasonic Ball Bonder</td><td></td><td>MOUNT and BOND
Mount on TO5 headers with Au epoxy (150°C, 1hour)
Bond 15s and 5s.</td><td></td><td></td></tr>
</table>

8.2. 3µm trench lasers

Prepared by: Ben Stevens Siming and Zhou

<table>
<tr><th>Proc. No.</th><th>Equipment/ Chemicals</th><th>Notes</th><th colspan="5">Process/Parameter Information</th><th>Achieved</th><th>Sign/ Date</th></tr>
<tr><td rowspan="2">1</td><td rowspan="2">Scriber
1) n-Butyl
2) Acetone
3) IPA</td><td rowspan="2"></td><td colspan="5">SCRIBE and CLEAN</td><td rowspan="2"></td><td rowspan="2"></td></tr>
<tr><td colspan="5">< one particle per field of view on 100 x magnification</td></tr>
<tr><td rowspan="5">2</td><td rowspan="5">UV300
MJB3 mask aligner
~8.7sec
Resist: SPR350
(MF26A)

Align to stripe pattern</td><td rowspan="5">Remove edge beads CLEAN MASK.

Prepare a test piece for etch also</td><td colspan="5">TRENCH PHOTOLITHOGRAPHY
Mask number: 3UMTRENCH (Vacuum contact)
Device: FILCS
Layer: TRENCH OXIDE ETCH</td><td></td><td></td></tr>
<tr><td>Dimensions:</td><td>MIN</td><td>AIM</td><td>MAX</td><td>UNIT</td><td></td><td></td></tr>
<tr><td>3 µm Ridge:</td><td>2.8</td><td>3</td><td>3.2</td><td>µm</td><td></td><td></td></tr>
<tr><td>2 µm Trench :</td><td>1.8</td><td>2</td><td>2.2</td><td>µm</td><td></td><td></td></tr>
<tr><td colspan="5">Follow lithography with 1 minute O_2 plasma ash, and 1min at 100°C hotplate.</td><td></td><td></td></tr>
<tr><td rowspan="9">3</td><td rowspan="9">ICP Etcher

Small drop of fomblin oil on back

Dektak</td><td rowspan="9">Approx 1µm per minute

Use test piece first for etch rate Stop etch @2.3 µm</td><td colspan="5">SEMICONDUCTOR TRENCH ETCH</td><td rowspan="9">5min 10sec 1.58um at Allen key</td><td rowspan="9"></td></tr>
<tr><td></td><td>MIN</td><td>AIM</td><td>MAX</td><td>UNITS</td></tr>
<tr><td>$SiCl_4$ =</td><td></td><td>5</td><td></td><td>sccm</td></tr>
<tr><td>RF =</td><td></td><td>100</td><td></td><td>W</td></tr>
<tr><td>ICP =</td><td></td><td>250</td><td></td><td>W</td></tr>
<tr><td>Pressure =</td><td></td><td>2</td><td></td><td>mTorr</td></tr>
<tr><td>Temp =</td><td></td><td>20</td><td></td><td>degC</td></tr>
<tr><td>Etch depth=</td><td>1.75</td><td>1.8</td><td>1.9</td><td>µm</td></tr>
<tr><td colspan="5"></td></tr>
<tr><td>4</td><td>Wet etch 20:1 Citric acid:H_2O_2</td><td></td><td colspan="5">WET ETCH

Mount samples on large glass slide with wax (to tie up Fomblin oil).

30 second etch

Follow etch with 3 mins O_2 plasma Ash, before heating in resist stripper, and 3 stage clean. Inspect that all resist removed.</td><td>Make side of the ridge smooth</td><td></td></tr>
</table>

<table>
<tr><td>5</td><td>Plasmatherm-
PECVD

Silicon Nitride</td><td>Rate = 10 nm/min</td><td>DEPOSIT DIELECTRIC
Program STDSIN
<table><tr><td></td><td>MIN</td><td>AIM</td><td>MAX</td><td>UNIT</td></tr><tr><td>Thickness:</td><td></td><td>1000</td><td></td><td>nm</td></tr></table></td><td></td><td></td></tr>
<tr><td>6</td><td>RIE
Only use if it has a history of SiO2 or SiN etching. If TiO2 or strange polymer etching evident, don't use!</td><td>Etch until endpoint curve flattens, then add 30sec.</td><td>CONTACT WINDOW NITRIDE ETCH
<table><tr><td>Critical Dimensions</td><td>MIN</td><td>AIM</td><td>MAX</td><td>UNIT</td></tr><tr><td>CHF_3</td><td></td><td>35</td><td></td><td>sccm</td></tr><tr><td>O_2</td><td></td><td>5</td><td></td><td>sccm</td></tr><tr><td>Pressure</td><td></td><td>35</td><td></td><td>mTorr</td></tr><tr><td>RF</td><td></td><td>60</td><td></td><td>W</td></tr></table></td><td></td><td></td></tr>
<tr><td>7</td><td>Plasmatherm-
PECVD

Silicon Nitride</td><td>Rate = 10 nm/min</td><td>DEPOSIT DIELECTRIC
Program STDSIN
<table><tr><td></td><td>MIN</td><td>AIM</td><td>MAX</td><td>UNIT</td></tr><tr><td>Thickness:</td><td></td><td>500</td><td></td><td>nm</td></tr></table></td><td></td><td></td></tr>
<tr><td>8</td><td>MJB3

Resist : SPR350 (MF26A)</td><td>Remove edge beads first</td><td>CONTACT WINDOW NITRIDE PHOTOLITH
Mask number: (same mask as layer 2)
<table><tr><td>Dimensions</td><td>MIN</td><td>AIM</td><td>MAX</td><td></td></tr><tr><td>Window:</td><td>2.8</td><td>3</td><td>3.2</td><td></td></tr></table></td><td></td><td></td></tr>
<tr><td>9</td><td>ICP
Only use if it has a history of SiO2 or SiN etching. If TiO2 or strange polymer etching evident, don't use!</td><td>Etch until endpoint curve flattens, then add 30sec. Check window is clear.</td><td>CONTACT WINDOW NITRIDE ETCH
<table><tr><td>Critical Dimensions</td><td>MIN</td><td>AIM</td><td>MAX</td><td>UNIT</td></tr><tr><td>CHF_3</td><td></td><td>35</td><td></td><td>sccm</td></tr><tr><td>O_2</td><td></td><td>5</td><td></td><td>sccm</td></tr><tr><td>Pressure</td><td></td><td>35</td><td></td><td>mTorr</td></tr><tr><td>RF</td><td></td><td>200</td><td></td><td>W</td></tr></table>
Follow etch with 6 mins O_2 plasma Ash, heat in resist stripper, and 3 stage clean. Inspect that all resist removed. Check for any strange polymer/depositions etc.</td><td></td><td></td></tr>
<tr><td>10</td><td>MJB3

SPR350 (MF-26A)</td><td></td><td>N – CONTACT PHOTOLITH
N-etch mask (Filtronic)

1 min 100C bake prior to etching</td><td></td><td></td></tr>
<tr><td>11</td><td>1:1:1 etchant Hydrobromic:acetic : Potassim dichromate</td><td>Etch rate ~2 µm/min</td><td>N – CONTACT ETCH
<table><tr><td></td><td>MIN</td><td>AIM</td><td>MAX</td><td>UNIT</td></tr><tr><td>Etch depth</td><td>3.8</td><td>4</td><td>4.5</td><td>µm</td></tr></table></td><td></td><td></td></tr>
</table>

<table>
<tr><td>12</td><td>MJB3.

BPRS200 (PLSI)</td><td>Edge bead removal</td><td>CONTACTS PHOTOLITHOGRAPHY
Mask number: (Filtronic - MASK)
FILTRONICS MASK 3 LAYER 1um metal (soft contact)<table><tr><td></td><td>MIN</td><td>AIM</td><td>MAX</td><td>UNITS</td></tr><tr><td>50 ridge:</td><td colspan="4">Make sure contact is within top surface of ridge and not shorting down side!</td></tr></table>Follow lithography with 1 minute O_2 plasma Ash.</td><td></td><td></td></tr>
<tr><td>13</td><td>Thermal Evaporator</td><td>30 sec rinse in 19:1 DIW:Ammonia solution prior to loading.</td><td>METAL DEPOSITION<table><tr><td></td><td>MIN</td><td>AIM</td><td>MAX</td><td>UNITS</td></tr><tr><td>Gold:</td><td>3</td><td>5</td><td>8</td><td>nm</td></tr><tr><td>Zinc:</td><td>8</td><td>10</td><td>12</td><td>nm</td></tr><tr><td>Gold:</td><td>90</td><td>100</td><td>110</td><td>nm</td></tr></table>Lift off in acetone
Follow lift-off with a 3 stage clean

Then RTA furn 360</td><td></td><td></td></tr>
<tr><td>14</td><td>MJB3.

BPRS200 (PLSI)</td><td>Edge bead removal</td><td>BOND PADS PHOTOLITH
Mask number: MCbondpads (Filtronic - MASK ?)
Netch (Filtronic - MASK ?)
Expose both masks on same resist in order to get correct pattern (ignore netch if no n-contact).

Use longer exposure than necessary to make sure resist is well exposed at bottom of ridges.
Follow lithography with 1.5 min O_2 plasma ash.</td><td></td><td></td></tr>
<tr><td>15</td><td>Thermal Evaporator</td><td>Half of each thickness evaporated from either side of ridge</td><td>BOND PAD METAL DEPOSITION and LIFT-OFF<table><tr><td>From each side</td><td>MIN</td><td>AIM</td><td>MAX</td><td>UNIT</td></tr><tr><td>Titanium:</td><td>13/13</td><td>15/15</td><td>17/17</td><td>nm</td></tr><tr><td>Gold:</td><td>140/140</td><td>150/150</td><td>160/160</td><td>nm</td></tr></table>Lift off in acetone

Follow lift-off with a 3 stage clean</td><td></td><td></td></tr>
<tr><td>16</td><td>MJB3

SPR220 (MF-26A)</td><td>Edge bead removal</td><td>ELECTROPLATE PHOTOLITH
Mask: Electroplate</td><td></td><td></td></tr>
<tr><td>17</td><td>Electroplate kit (in semi-clean room)</td><td>Work out time required</td><td>ELECTROPLATE<table><tr><td></td><td>MIN</td><td>AIM</td><td>MAX</td><td></td></tr><tr><td>Au Thickness:</td><td>2.5</td><td>3</td><td>3.5</td><td></td></tr></table></td><td></td><td></td></tr>
<tr><td>18</td><td>MJB3

SPR350 (MF26A)</td><td></td><td>MULTI-SECTION ETCH PHOTOLITH
Mask: MSEtch (Filtronic)</td><td></td><td></td></tr>
</table>

<table>
<tr><td>19</td><td>KI/I$_2$ etchant</td><td></td><td>MS GOLD ETCH
Etch for 12 seconds, then check no gold in windows</td><td></td><td></td></tr>
<tr><td>20</td><td>H_2O_2:Citric acid 5:1 by volume</td><td></td><td>MS SEMICONDUCTOR ETCH
Highly selective etch, etch for 1:30 mins then check resistance on curve tracer >1 kΩ</td><td></td><td></td></tr>
<tr><td>21</td><td>RTA Program: FURN360</td><td></td><td>ANNEAL
<table>
<tr><td></td><td>MIN</td><td>AIM</td><td>MAX</td><td>UNIT</td></tr>
<tr><td>Temperature:</td><td></td><td>360</td><td></td><td>DEG</td></tr>
<tr><td>Wait time</td><td></td><td>3</td><td></td><td>sec</td></tr>
</table></td><td></td><td></td></tr>
<tr><td>22</td><td>Logitech lapper polisher</td><td></td><td>THINNING
<table>
<tr><td></td><td>MIN</td><td>AIM</td><td>MAX</td><td>UNIT</td></tr>
<tr><td>Wafer thickness:</td><td>160</td><td>170</td><td>180</td><td>μm</td></tr>
</table></td><td></td><td></td></tr>
<tr><td>23</td><td>Thermal Evaporator</td><td></td><td>BACK CONTACT
<table>
<tr><td>Thickness</td><td>MIN</td><td>AIM</td><td>MAX</td><td>UNIT</td></tr>
<tr><td>InGe:</td><td>17</td><td>20</td><td>23</td><td>nm</td></tr>
<tr><td>Gold:</td><td>280</td><td>300</td><td>320</td><td>nm</td></tr>
</table></td><td></td><td></td></tr>
<tr><td>24</td><td>RTA Program: FURN340</td><td></td><td>ANNEAL
<table>
<tr><td></td><td>MIN</td><td>AIM</td><td>MAX</td><td>UNIT</td></tr>
<tr><td>Temperature:</td><td></td><td>340</td><td></td><td>DEG</td></tr>
<tr><td>Wait time</td><td></td><td>3</td><td></td><td>sec</td></tr>
</table></td><td></td><td></td></tr>
<tr><td>25</td><td></td><td></td><td>CLEAVE ETC</td><td></td><td></td></tr>
</table>

8.3. QD Multi-section SLDs

Prepared by: Kristian Groom, Siming Chen and Kejia Zhou

Pr. no.	Equipment/ Chemicals	Notes	Process/Parameter Information	MIN	AIM	MAX	UNIT	Achieved	Sign/Date
1	Scriber 1) n-Butyl 2) Acetone 3) IPA	Take a quarter wafer	**CLEAVE and CLEAN**						
			< one particle per field of view on 100 x magnification Check orientation of wafer: crucial for v-etch						
2	MJB3 aligner Resist: SPR350 (MF26A) **NB:** Align to cleaved edge **perpendicular to major flat**	1. Clean mask 2.Remove edge beads 3.Perfectly straight lines!	**TRENCHES PHOTOLITHOGRAPHY** Mask number: TRENCHES (MultiSLED - MASK1)						
			Dimensions:	MIN	AIM	MAX	UNIT		
			Ridge widths:	6.5	7	7.5	µm		
			Follow lithography with 1 minute O_2 plasma ash, and 1min at 100°C hotplate.						
3	ICP Etcher Fomblin oil Dektak	Approx 700nm per minute Resist etches ~130nm per min	**SEMICONDUCTOR TRENCH ETCH**						
				MIN	AIM	MAX	UNITS		
			$SiCl_4$ =		5		sccm		
			RF =		100		W		
			ICP =		400		W		
			Pressure =		2		mTorr		
			Temp =		20		degC		
			He=		8		mTorr		
			Etch depth=	2.5	2.75	3.0	µm		
			Cover Fomblin with wax to prevent it coming off in acid						
4	Wet chemical station		**SEMICONDUCTOR TRENCH WET TICKLE**						
				MIN	AIM	MAX	UNITS		
			Citric acid		20		ml		
			H_2O_2		1		ml		
			Etch time:		30		sec		
			Follow with O_2 ash, resist stripper if necessary, and 3-stage clean. Inspect that all resist has been removed						
5	PECVD Silicon Nitride	19.1 ammonia rinse Rate =	**DEPOSIT DIELECTRIC** Program STDSIN						
				MIN	AIM	MAX	UNIT		

		10 nm/min	Thickness:		900		nm		
6	RIE	Etch back to semi-conductor on top (leaves SiN on sidewalls)	**DIELECTRIC ETCH BACK**						
				MIN	AIM	MAX	UNITS		
			CHF_3 =		35		sccm		
			O_2 =		5		sccm		
			Pressure =		35		mTorr		
			RF power =		80		W		
7	PECVD Silicon Nitride	Rate = 10 nm/min	**DEPOSIT DIELECTRIC** Program STDSIN						
				MIN	AIM	MAX	UNIT		
			Thickness:		450		nm		
8	MJB3 Resist : SPR350 (MF26A) or BPRS100/200 (PLSI)	Remove edge beads first **Alignment is critical**	**CONTACT WINDOW PHOTOLITHOGRAPHY** Mask number: WINDOWS (MultiSLED- MASK 1)						
			Dimensions	MIN	AIM	MAX	UNIT		
			Window width:	6	7	8	µm		
			Window must not extend beyond the SiN sidewalls						
9	RIE	Overetch beyond endpoint by ~1min so window opens over whole ridge width	**CONTACT WINDOW NITRIDE ETCH**						
				MIN	AIM	MAX	UNIT		
			CHF_3 =		35		sccm		
			O_2 =		5		sccm		
			Pressure =		35		mTorr		
			RF =		70		W		
			Follow etch with 5 mins O_2 plasma Ash, heat in resist stripper, and 3 stage clean. Inspect that all resist removed.						
10	MJB3 mask aligner		**CONTACTS PHOTOLITHOGRAPHY** Mask number: P+ METAL (MultiSLED – MASK2)						

<table>
<tr><td></td><td>Resist:
BPRS 100
(PLSI)</td><td></td><td><table><tr><td></td><td>MIN</td><td>AIM</td><td>MAX</td><td>UNITS</td></tr><tr><td>Width =</td><td>6</td><td>7</td><td>8</td><td>µm</td></tr></table>Follow lithography with 1.5 minute O_2 plasma ash</td><td></td><td></td></tr>
<tr><td>11</td><td>Thermal Evaporator</td><td>19.1 ammonia rinse prior to dep.</td><td>CONTACT DEPOSITION and LIFT-OFF<table><tr><td></td><td>MIN</td><td>AIM</td><td>MAX</td><td>UNITS</td></tr><tr><td>Gold:</td><td>3</td><td>5</td><td>8</td><td>nm</td></tr><tr><td>Zinc:</td><td>8</td><td>10</td><td>12</td><td>nm</td></tr><tr><td>Gold:</td><td>180</td><td>200</td><td>220</td><td>nm</td></tr></table>Lift off in acetone

Follow lift-off with a 3 stage clean</td><td></td><td></td></tr>
<tr><td>12</td><td>RTA
Prog:
Furn 360</td><td></td><td>ANNEAL<table><tr><td></td><td>MIN</td><td>AIM</td><td>MAX</td><td>UNITS</td></tr><tr><td>Temperature:</td><td></td><td>360</td><td></td><td>degC</td></tr><tr><td>Ramp/Hold time:</td><td></td><td>3</td><td></td><td>sec</td></tr></table></td><td></td><td></td></tr>
<tr><td>13</td><td>MJB3 mask aligner

Resist:
BPRS 100
(PLSI)</td><td>Remove edge beads</td><td>BONDPAD PHOTOLITHOGRAPHY

Mask number: BONDPADS (MultiSLED – MASK2)<table><tr><td></td><td>MIN</td><td>AIM</td><td>MAX</td><td>UNITS</td></tr><tr><td>Isolation gap:</td><td>10</td><td>13</td><td>14</td><td>µm</td></tr></table>Follow lithography with 2 minute O_2 plasma ash</td><td></td><td></td></tr>
<tr><td>14</td><td>Thermal Evaporator</td><td></td><td>BOND PAD METAL DEPOSITION and LIFT-OFF<table><tr><td></td><td>MIN</td><td>AIM</td><td>MAX</td><td>UNIT</td></tr><tr><td>Titanium:</td><td>15</td><td>20</td><td>25</td><td>nm</td></tr><tr><td>Gold:</td><td>180</td><td>200</td><td>220</td><td>nm</td></tr></table>Lift off in acetone
Follow lift-off with a 3 stage clean</td><td></td><td></td></tr>
<tr><td>15</td><td>Thermal Evaporator</td><td></td><td>BLANKET DEPOSITION<table><tr><td></td><td>MIN</td><td>AIM</td><td>MAX</td><td>UNIT</td></tr><tr><td>Gold =</td><td>3</td><td>5</td><td>7</td><td>nm</td></tr></table></td><td></td><td></td></tr>
<tr><td>16</td><td>MJB3
SPR220 (MF26A) or BPRS200 (PLSI)</td><td>Remove edge beads</td><td>ELECTROPLATED BOND PADS PHOTOLITH
Mask number: BONDPADS (MultiSLED – MASK2)<table><tr><td></td><td>MIN</td><td>AIM</td><td>MAX</td><td>UNITS</td></tr><tr><td>Isolation gap =</td><td>10</td><td>13</td><td>14</td><td>µm</td></tr></table>Follow lithography with 1 minute O_2 plasma ash</td><td></td><td></td></tr>
<tr><td>17</td><td>ELECTRO-PLATING</td><td>mount on gold</td><td>ELECTROPLATED BOND PADS<table><tr><td></td><td>MIN</td><td>AIM</td><td>MAX</td><td>UNIT</td></tr></table></td><td></td><td></td></tr>
</table>

<table>
<tr><td></td><td>KIT

DEKTAK</td><td>slide & contact with Ag paint</td><td><table><tr><td>Thickness:</td><td>0.75</td><td>1</td><td>1.5</td><td>µm</td></tr><tr><td colspan="5">Full clean up after plating</td></tr></table></td><td></td><td></td></tr>
<tr><td>18</td><td>Wet chemical station

Curve tracer</td><td>Check resistance between devices. Make sure Au has gone</td><td><table><tr><td colspan="5">GOLD ETCH BACK</td></tr><tr><td></td><td>MIN</td><td>AIM</td><td>MAX</td><td>UNIT</td></tr><tr><td>KI/I_2 =</td><td></td><td></td><td></td><td>ml</td></tr><tr><td>H_2O =</td><td></td><td></td><td></td><td>ml</td></tr><tr><td>Time =</td><td></td><td></td><td></td><td>min</td></tr><tr><td colspan="5">Clean afterwards</td></tr></table></td><td></td><td></td></tr>
<tr><td>19</td><td>MJB3 mask aligner BPRS200 (PLSI)</td><td>Remove edge beads</td><td><table><tr><td colspan="5">ISOLATION PHOTOLITHOGRAPHY
Mask number: ISOLATION (MultiSLED – MASK1)</td></tr><tr><td></td><td>MIN</td><td>AIM</td><td>MAX</td><td>UNITS</td></tr><tr><td>Isolation gap:</td><td>3</td><td>4</td><td>5</td><td>µm</td></tr><tr><td colspan="5">Follow lithography with 1 minute O_2 plasma ash</td></tr></table></td><td></td><td></td></tr>
<tr><td>20</td><td>Wet chemical station</td><td>Etchnt is ~300nm per min in GaAs ~3nm per min in AlGaAs</td><td><table><tr><td colspan="5">ISOLATION ETCH</td></tr><tr><td></td><td>MIN</td><td>AIM</td><td>MAX</td><td>UNITS</td></tr><tr><td>Citric acid</td><td></td><td>20</td><td></td><td>ml</td></tr><tr><td>H_2O_2</td><td></td><td>5</td><td></td><td>ml</td></tr><tr><td>Etch time:</td><td></td><td>90</td><td></td><td>sec</td></tr><tr><td>Resistance:</td><td>1</td><td></td><td></td><td>kΩ</td></tr><tr><td colspan="5">Follow with O_2 ash, and 3-stage clean.
Check resistance between contacts.</td></tr></table></td><td></td><td></td></tr>
<tr><td>21</td><td>MJB3 mask aligner BPRS200 (PLSI)</td><td>Remove edge beads</td><td><table><tr><td colspan="5">V-ETCH PHOTOLITHOGRAPHY
Mask number: V-ETCH (MultiSLED – MASK2)</td></tr><tr><td></td><td>MIN</td><td>AIM</td><td>MAX</td><td>UNITS</td></tr><tr><td>V-width:</td><td>4</td><td>6</td><td>8</td><td>µm</td></tr><tr><td colspan="5">Follow lithography with 1 minute O_2 plasma ash</td></tr></table></td><td></td><td></td></tr>
<tr><td>22</td><td>Wet chemical station</td><td>~2µm per min</td><td><table><tr><td colspan="5">V-ETCH</td></tr><tr><td></td><td>MIN</td><td>AIM</td><td>MAX</td><td>UNITS</td></tr><tr><td>H_2SO_4 =</td><td></td><td>1</td><td></td><td>ml</td></tr><tr><td>H_2O_2 =</td><td></td><td>8</td><td></td><td>ml</td></tr><tr><td>H_2O =</td><td></td><td>40</td><td></td><td>ml</td></tr><tr><td>Depth =</td><td>3</td><td>4</td><td>5</td><td>µm</td></tr><tr><td colspan="5">Follow with O_2 ash, and 3-stage clean.</td></tr></table></td><td></td><td></td></tr>
<tr><td>23</td><td>MINIMET 1000 FORCE: 006lbs Speed :030

Alternatively, ask Qi about the Logitec lapper</td><td>Protect with resist, mount with wax, make sure wax thickness is</td><td><table><tr><td colspan="5">THINNING</td></tr><tr><td></td><td>MIN</td><td>AIM</td><td>MAX</td><td>UNIT</td></tr><tr><td>Wafer thickness:</td><td>150</td><td>160</td><td>170</td><td>µm</td></tr><tr><td colspan="5">Be aware of uniformity, and allow for wax in thickness measurement.
Followed by 3 stage clean (using carriers).</td></tr></table></td><td></td><td></td></tr>
</table>

		unifor m. 3µm paste			
24	Thermal evaporator		**BACKCONTACT METAL** <table><tr><td>Thickness</td><td>MIN</td><td>AIM</td><td>MAX</td><td>UNIT</td></tr><tr><td>InGe:</td><td>17</td><td>20</td><td>23</td><td>nm</td></tr><tr><td>Gold:</td><td>280</td><td>300</td><td>320</td><td>nm</td></tr></table>		
25	RTA Program: FURN340		**ANNEAL** <table><tr><td></td><td>MIN</td><td>AIM</td><td>MAX</td><td>UNIT</td></tr><tr><td>Temperature:</td><td></td><td>340</td><td></td><td>DEG</td></tr><tr><td>Wait time</td><td></td><td>3</td><td></td><td>sec</td></tr></table>		
26	Loomis LSD-100		**SCRIBE AND BREAK** Scribe/break according to arrows, ie: whole 10mm device length		
27	Ceramic tiles, K&S Ultrasonic Ball Bonder		**MOUNT and BOND** TBA		